UNIVERSITY OF BIRMINGHAM

Pair Distribution Function Studies of Inorganic Materials Under Extreme Conditions

By

Tim Lucas

Supervisor: Dr J A Hriljac

A thesis submitted to the University of Birmingham for the degree of DOCTOR OF PHILOSOPHY

The School of Chemistry

College of Engineering and Physical Sciences

The University of Birmingham

August 2013

ABSTRACT

This study concentrates on pair distribution function (PDF) analysis of various related systems under extreme conditions using variable temperatures and pressures. The local structure of $BaTiO_3$ (BTO) was investigated using x-rays (xPDF) between 0 and 8.78 GPa and x-rays and neutrons (nPDF) between 100 and 500K. Evidence is presented that indicates that the “Comes model” of Ti disorder is too simplistic to describe the local structure of BTO at variable temperature but results from the high pressure xPDF study are inconclusive due to the inability to observe the very weak first Ti-O peak. The ambient structure of related $Ba_{1-x}Bi_xTi_{1-x}Yb_xO_3$ was also investigated using both nPDF and xPDF between $x = 0$ and 0.15, with PDFs indicating significant local disorder present on both A and B sites. Cubic $ZrMo_2O_8$ undergoes pressure induced amorphisation at ~0.7 GPa and this was investigated up to 11.02 GPa using xPDF which showed an increase in Mo coordination with pressure but no significant change around Zr. Iron undergoes a bcc-hcp phase transition between 10 and 20 GPa and xPDF was used to investigate this phase transition and the local structure of the hcp phase up to 50.07 GPa, but texture in the sample at high pressures hindered analysis.

ACKNOWLEDGEMENTS

I feel that Joe Hriljac probably deserves more praise that can be written in this acknowledgement but I will have a go. It took me several months to actually start my PhD due to factors out of my control but Joe waited patiently for these issues to be resolved taking me down to Diamond for a trip before my PhD started to get me invaluable experience. He continually supported me in my studies, pushing and challenging me when I needed it and supporting me through some difficult problems, be they health or personal. I have been extremely lucky to have Joe as my supervisor and being able to undertake my research. Each and every day I have felt privileged to carry out my research, even if it was sometimes very repetitive. Although I am glad to not have to do any more refinements on $BaTiO_3$ for a while at least.

I would also like to thank the people who I have been lucky to have worked with over the past few years. Peter Chupas and Karena Chapman provided invaluable help of getting to grips with some of the software associated with PDF analysis. I am also grateful for Diamond Light Source providing some of the funding for this project and it has been enjoyable working there, be it working at I-15 or helping run their total scattering training school. I would to thank all the people who I collaborated with it, be it on work presented here or on other projects, particularly staff at Diamond Light Source and ISIS.

My family, Liz, Barry and Jane have also given me vital support throughout this project, without them I would never have made it to the end. Jenny Readman also gave me some very early help getting to grips with Fit2D and while I did not have much chance to work with her, her support was invaluable early on. I would also like to thank the other members of the research group and floor. Special mention to Tom Carey for breaking a diamond anvil cell I needed to use, for not telling me his sample had gone off before I ran an overnight high pressure PDF experiment for him and for not scoring a single goal for our Chemistry football team.

Dedicated to:

Sam Dix

Joe Alderman
Daisy Lindlar
Robert Bradshaw
Emma Packham
Frankie Greenwell
Sam Delacruz
James Kendrick
Beth Dovey
Ash Green
Zuki Majuqwana
Dave Charles
Callum Gosling

Jack Dart
Laura Graham
Sam Loveridge
Steph Young
Midge Price
Carly Thomas
James Farley
George Derbyshire
Daisy Lindlar
Adam Paigge
Luke Reynolds
Jez Boyd

TABLE OF CONTENTS

Tables

Figures

Page

Page

Page

Page

Page

Page

Page

Page

AIMS OF THE STUDY

This project was part funded by Diamond Light Source (DLS) and began in September 2009. The aims of the project were to develop the methodology of producing and analysing high pressure pair distribution (PDF) data. The work was conducted on various systems, along with supporting the development of the I-15 beamline for collecting high energy x-ray scattering data in order to produce high quality PDFs at both ambient and extreme conditions. Much of the early work was carried out at the 11-ID-B beamline at the Advanced Photon Source, which is a long established dedicated PDF beamline where the Staff have a lot of expertise in collecting and analysing PDF data. In the latter half of the project, data collections were conducted exclusively at Diamond and work was undertaken to help with the development of I-15 for collecting PDF data including, software development, detector integration and experimental set up (*i.e.* creation of an automatic sample changer).

While the focus of this project was initially to concentrate on high pressure studies of various systems, the study also expanded to studies at variable temperatures and also structures at ambient temperatures and pressures. As a result of extensive work on $BaTiO_3$ the project concentrated on perovskite related systems along with a study designed to push the envelope in high pressure PDF analysis, going to higher pressures that previously presented in literature (Chapter 7).

1. INTRODUCTION

1.1 Why Is Structure Determination Important?

Structure determination is an absolutely vital component of modern chemistry and all types of compounds can be analysed using various structural determination techniques. Solving unknown structures provides insights into the physical and chemical properties of materials. Graphite and diamond show how the structure of a material can impact properties, both consist of only carbon atoms but possess different structures and wildly different properties. When new materials are synthesised, understanding their structures and how these impact on chemical and physical behaviour is an essential component of scientific research. Another example of where structure determination is important is when materials undergo transformations under extreme conditions such as high pressures and temperatures. Iron possesses several different structures at varying pressures and temperatures, understanding phase transitions can help scientists understand the structure and behaviour of the Earth's inner core which is made up primarily of iron.[1]

Diffraction techniques have been used to study crystallographic systems for a long time and in 1969 the Rietveld method revolutionised data analysis of powder diffraction patterns.[2] Powder diffraction by neutrons and x-rays is widely used for structural characterisation of microcrystalline samples.

1.2 Bragg Diffraction

Bragg diffraction occurs when a beam of electromagnetic radiation (x-rays) or particles (neutrons and elections) possessing a wavelength similar to the interatomic spacings are fired at crystalline samples. X-rays are scattered by atoms through interactions with the electron cloud, neutrons are scattered by the nucleus of atoms (neutrons can also be scattered by

magnetic moments) and electrons interact with both the electron cloud and nucleus due to them being charged particles.

If the diffracted x-rays, neutrons or electrons are in phase (the path difference of the scattered radiation, *n*, is an integer of wavelengths), resulting in constructive interference, this results in the production of a diffraction pattern that can be used to investigate the structure of a material. Bragg's law expresses this

$$n\lambda = 2d_{\mathrm{hkl}}\sin\theta \tag{1.1}$$

where λ is the wavelength of the incident beam, *d* is the plane spacing and θ is the angle between the incident rays and the surface of the crystal.

Bragg's law can be used to work out how atoms are arranged inside a solid crystal and diffraction can be used to probe the structure of mono- and polycrystalline materials.

Crystals are randomly oriented in a powder which leads to the production of diffraction rings which correspond to a specific lattice vector (*Q*) in the sample. *Q* is defined as:

$$Q = \frac{4\pi \sin(\theta)}{\lambda} \tag{1.2}$$

As atoms in crystals are vibrating this means that a crystal structure may never be static and thus "truly perfect". These thermal vibrations diminish the scattering intensity of Bragg peaks by the Debye-Waller (DW) factor $\exp(-\frac{1}{2}Q^2\langle u^2\rangle)$, where u is the displacement of the atom. As a result, at larger values of *Q* Bragg peaks are small.

1.3 Non-Bragg Diffraction

Despite being an extremely powerful method for structure determination in crystalline materials the Rietveld method has several limitations, such as only describing long range structure, meaning it is unable to describe local disorder.[3] The method is also not useful for "cystallographically challenged" materials such as highly disordered materials, liquids, nano-particles and glasses.

If a crystal is not perfectly periodic, then this can give rise to diffuse scattering of x-rays. Diffuse scatter can also be observed in non-crystalline samples that possess no long-range periodicity such as glasses and liquids which will show no Bragg reflections. At larger values of *Q* diffuse scattering dominates the pattern and the Bragg peaks are small (Section 1.2).

In materials possessing disorder, diffuse scattering occurs when the average space group no longer provides a good description of all of the local structure. As a result, diffuse scattering can be used to investigate various types of disorder in crystals, such as static disorder (vacancies and stacking faults), dynamic disorder (reorientation of molecules and disorder due to vibrations), orientational disorder and magnetic disorder (in neutron diffraction).[4] Diffuse scatter is observed throughout the diffraction pattern however and is typically disregarded as "background" in traditional crystallographic analysis, meaning Rietveld analysis of diffraction data is limited by the fact it only produces a long range average of the structure of a material.

1.4 From Diffraction Pattern to Pair Distribution Function

While the theory behind the atomic pair distribution function (PDF) was known since the 1920's, the power of the Rietveld method, coupled with the lack of experimental facilities to produce high quality PDFs, meant there appeared to be little point in using PDFs for structure determination.[5, 6] Since the advent of high-energy x-ray and spallation neutron sources

(Section 1.6) and better computer analysis, neutron PDF (nPDF) and x-ray PDF (xPDF) analysis have become viable methods for structure determination. While PDF analysis is not in its infancy by any means, experimental techniques and new data reduction and analysis software are still being developed and advanced.[7, 8] Indeed a lot of the work presented in this thesis would not have been possible if it had not been for the relatively recent advances in high-pressure PDF experimental techniques and data analysis that are outlined by Chapman *et al* (2010).[7]

In the production of a pair distribution function we consider both the Bragg and the diffuse scatter which is why it often described as a "total scattering technique". The PDF gives the opportunity to investigate local structure and is defined as "the probability of finding two atoms separated by the distance, *r*".[9] This allows the PDF to simultaneously contain information about the average, longer range structure and the local structural disorder. The PDF $G(r)$, is defined as

$$G(r) = \frac{2}{\pi}\int_0^\infty Q[S(Q) - 1]\sin(Qr)\,dQ = 4\pi r[\rho(r) - \rho_0] \qquad (1.3)$$

where $\rho(r)$ is the microscopic pair density, ρ_0 is the average number density and r is the radial distance. The function oscillates around zero at larger values of r and trends to zero when $r = 0$ with a negatively sloping baseline, $-4\pi r\rho_0$ which is only valid for bulk materials and as r increases ρ_0 tends to zero. On a basic level, the $G(r)$ will give information about how many atoms are found in a spherical distance (r) from any given atom (co-ordination number). It will give information about any local disorder present in the system and atom pair distances can be measured from the PDF pattern. Once a PDF has been produced it can be fitted with an experimental model by computer programs (Section 2.3). Even if the structure of the sample

is unknown, analysis can be conducted by simply obtaining atom-atom distances and co-ordination numbers directly from the PDF.

The PDF is produced *via* a sine Fourier transform of the total scattering function S(*Q*). The S(*Q*) is produced from the normalised scattering intensity *I*(*Q*) and is defined as:

$$S(Q) = \frac{I(Q) - \sum c_i |f_i(Q)|^2}{|\sum c_i f_i(Q)|} + 1 \quad (1.4)$$

where c_i is the atomic concentration and f_i the atomic form factor for atoms of type *i* which is dependent on *Q*.[6] For neutrons the equation becomes:

$$S(Q) = \frac{I(Q) - \sum c_i |b_i|^2}{|\sum c_i b_i|} + 1 \quad (1.5)$$

where b_i is the neutron scattering length, which is independent of *Q* (Section 1.6).

The *I*(*Q*) must be corrected for a number of factors such as the number of atoms in the sample and the experimental background. As it is essential to measure the diffuse scattering, the PDF technique is very sensitive to background subtractions, particularly when the sample is weakly scattering in comparison to the background. A background measurement typically includes an empty sample container situated in the same place in the experimental set up, although it may be necessary to conduct further measurements such as just the empty beam with no container and the container with any pressure transmitting fluid. This background is then subtracted from the data collected on a sample so that any diffuse scatter is retained in the final measured *S(Q)* and all the scatter present is exclusively from the sample.

The *I*(*Q*) must also be corrected for any inelastic scattering, in XRD this is called Compton scattering and in neutron diffraction this is accounted for by Placek corrections. Also

corrections must be made from the neutrons or x-rays that are scattered multiple times within the sample or with the container (multiple scattering) and also sample absorption.

Once these corrections have been made, a PDF can be produced by the Fourier transform of the $S(Q)$.

1.5 Termination Errors

The Fourier transform in Equation 1.4 requires data from $Q = 0$ Å^{-1} to $Q = \infty$ Å^{-1}, but experimental constraints means that it is not possible to access this data range. This has an impact on the PDFs that are produced from the total scattering patterns. As a result we need to consider what Q_{max} and Q_{min} we are accessing in our experiments and what impact these data ranges can have on our measured PDFs.

1.5.1 Q_{max}

While it is not experimentally possible to access $Q_{max} = \infty$ it is possible to produce high quality PDFs as long as the value of Q_{max} is sufficiently high. Accurate data analysis can be conducted on PDFs produced $Q_{max} \geq 20$Å^{-1} and this is potentially a conservative estimate with it being acceptable to publish PDFs using $Q_{max} \leq 20$Å^{-1}.

Accessing finite values of Q_{max} results in termination ripples at low r that reduce in amplitude as r increases (Figure 1.1). These ripples are worse with lower values of Q_{max} and will contribute to the pattern at low r, making it vital to ensure that this effect is as small as possible, particularly when investigating atom-atom distances at short atomic distances.

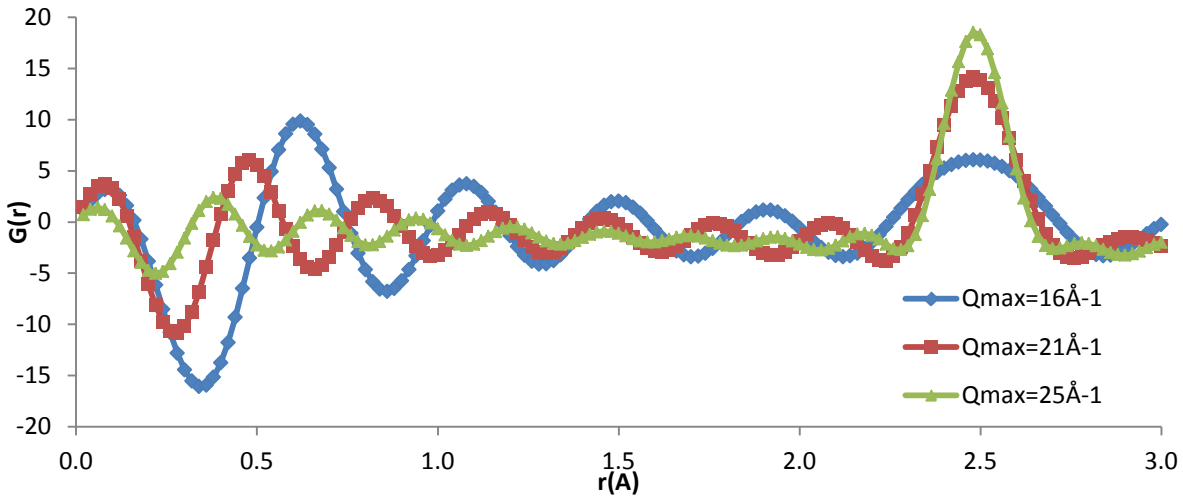

Figure 1.1: xPDF of Ni collected in a capillary produced using varying values of Q_{max}.

On the other hand, using very high values of Q_{max} can also introduce noise into the PDF if counting statistics become too poor.[10] For this reason, it may necessary not to use the full Q range collected, thus ensuring statistical errors are not introduced into the PDF. In practice the S(Q) can be examined to investigate at what point scattering from the sample is lost in the noise from the detectors and different values of Q_{max} can be used to produce the highest quality PDF possible.

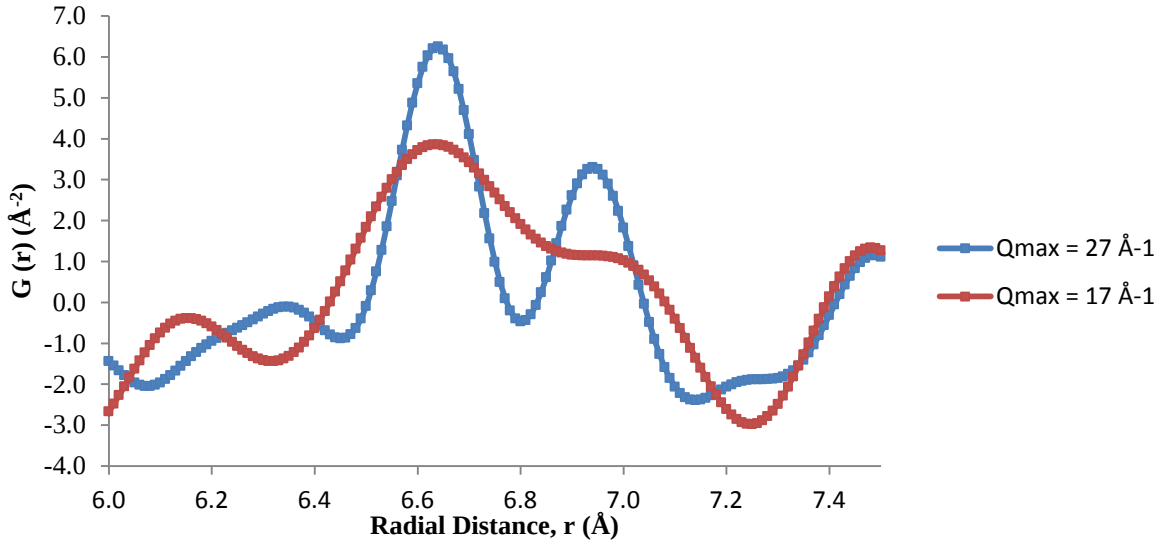

Figure 1.2: Comparison of xPDF patterns of $BaTiO_3$ using different values of Q_{max}.

The value of Q_{max} used for the Fourier transform will also determine the real space resolution of the PDF. The higher the value of Q_{max}, the higher the resolution in the PDF (Figure 1.2). Higher peak resolutions are clearly beneficial for PDF analysis, particularly when considering subtle changes in overlapping peaks.

1.5.2 Q_{min}

Experimental considerations will result in not being able to measure sample scattering down to $Q = 0$ **Å**$^{-1}$. For example, a beam stop prevents the beam hitting the detector directly in x-ray diffraction measurements, but the beam stop then blocks scattering at very low values of Q. This will introduce errors around the first peak in the PDF (shortest atom-atom distance).[11]

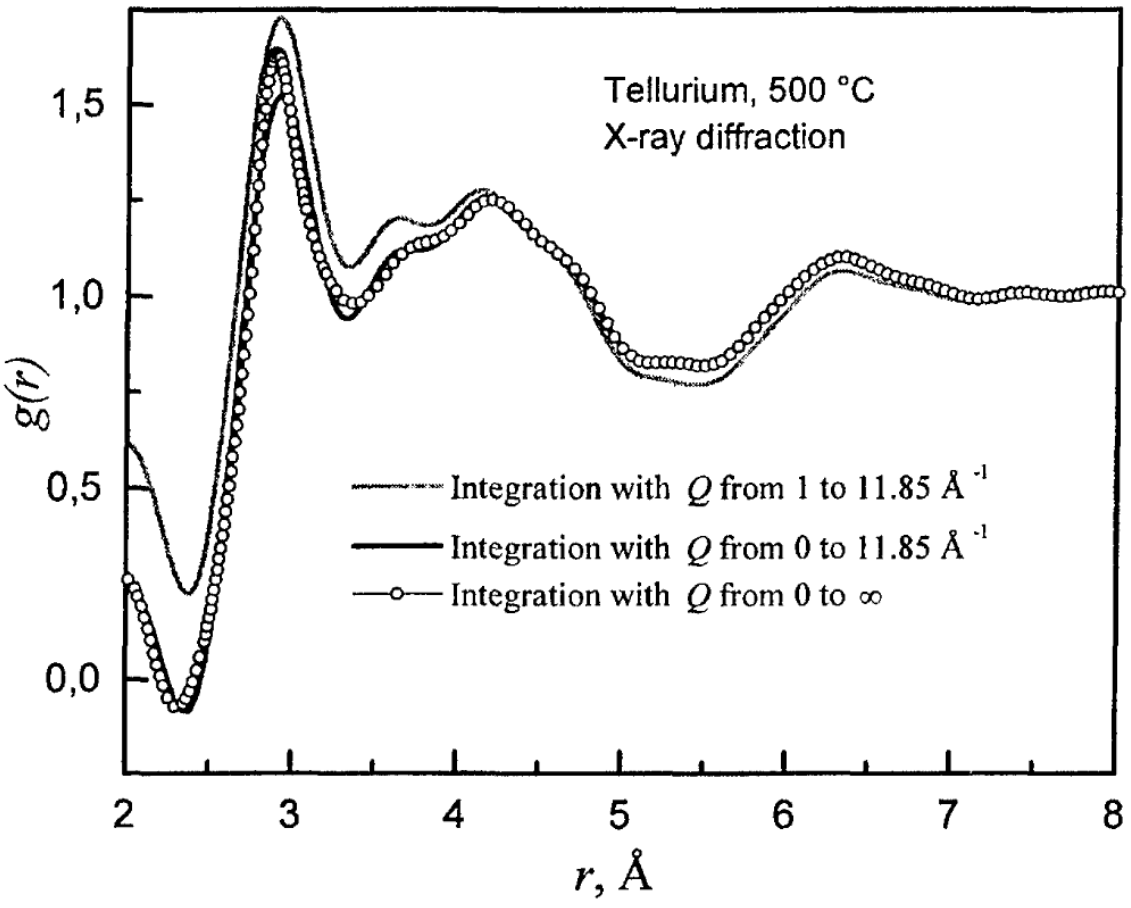

Figure 1.3: $G(r)$s of liquid Te calculated with different integration limits (Hoyer *et al* 2001).

If $Q_{min} > 0$ Å^{-1} then termination errors are introduced that along with termination errors introduced by $Q_{max} < \infty$ will lead to overestimation of co-ordination numbers.

In the absence of experimental data at low Q, it is possible to extrapolate data to $Q_{min} = 0$, reducing termination errors.[11]

1.6 xPDF vs nPDF

While Bragg's law is applicable to both neutron and x-ray diffraction, there are clearly differences in how both neutrons and x-rays are produced. How they interact with matter also leads to some subtle advantages and disadvantages between the two techniques and analysis of both nPDF and xPDFs can be complementary.

As sin $\theta \leq 1$ then the Q range accessible by laboratory sources is very limited, with Cu K-alpha radiation only giving a Q_{max} of roughly 8 Å^{-1}. Other laboratory radiation sources can provide better Q ranges, such as Mo K-alpha (~ 17 Å^{-1}) and Ag K-alpha (~ 22 Å^{-1}) but low intensities make the production of high quality PDFs problematic, often taking several days of data collection to obtain sufficiently good statistics to produce high quality PDFs.[10] As a result, synchrotron radiation sources are used to provide x-rays of high enough energy to obtain effective Q ranges (~30 Å^{-1}).

Neutrons can be produced by a variety of methods but the two most common for use in neutron diffraction are by using a reactor or a spallation source. All the data presented here are from ISIS which is a spallation source (Section 3.2.1). A pulsed neutron beam is produced by accelerating H^- ions, stripping off the electrons and then bombarding a tungsten target with these high energy protons. These neutrons are then slowed to useful speeds by moderators. Spallation sources are particularly useful for production of high quality PDFs due to epithermal neutrons which exit the neutron moderator before reaching thermal equilibrium,

resulting in them possessing shorter wavelengths and higher Q ranges.[10] Diffractometers can be time-of-flight or angle-dispersive. If the time of pulse generation is known then the time-of-flight of a neutron can be calculated by the arrival of the scattered neutron on the detector. The relationship between time-of-flight and Q is given by

$$Q = \frac{2mL}{ht} sin\theta \tag{3}$$

where t is time-of-flight, L is the path, $\hbar$ *is* Planck constant divided by 2π and m is momentum. Detectors at various scattering angles are then grouped together in banks and data from these banks can be used to produce PDFs.

Neutron diffraction can provide several advantages (and disadvantages) in comparison to x-ray diffraction. There is an angular dependence on the scattering of X-rays with the scattering power of an atom decreasing as (sin θ) increases. Electrons are not at fixed points in space and are spread out, meaning they are not all scattering is in phase which results in a reduction of peak intensities as Q increases as the scattering power of each atom is angle dependant. As neutrons are scattered by the nucleus and not the electron cloud, there is no drop off in scattering intensity with sin θ, which is an obvious advantage when trying to access the highest values of Q_{max} that are experimentally possible

In XRD, generally the scattering power of an atom increases as atomic number meaning it is not very sensitive to light elements such as hydrogen and oxygen, particularly in the presence of elements with much larger atomic numbers. In neutron diffraction, scattering power varies irregularly with atomic number and as a result it is much more sensitive to light elements. Some elements can strongly absorb neutrons such as boron and mercury however and cannot be easily studied using neutron diffraction. Some elements such as titanium even have

negative scattering lengths, where the scattered neutrons are 180^{o} out of phase in comparison to the neutrons scattered by other elements.

While epithermal neutrons and intensity of scattering being independent of *Q* make neutron diffraction an attractive alternative to x-ray scattering methods for PDF analysis, it also has several disadvantages in comparison to its x-ray counterpart. With the relatively low fluxes associated with neutrons in comparison to x-rays it results in data collection times much longer in order to produce high quality PDFs (hours for neutrons *vs* minutes for X-rays). Also it is not currently possible to conduct very high pressure (>2GPa) PDF measurements using neutron diffraction due to issues in normalising the background of the high pressure cells used.

As a result of the relevant differences to this study outlined above, neutron PDF (nPDF) and X-Ray PDF (xPDF) can be used as complimentary techniques, used to investigate different elements in samples and thus increase validity in conclusions.

1.7 Summary of Literature

While nPDF and xPDF methods are based on the same basic diffraction principles, the different qualities they offer make them powerful tools in structural determination. While combining both diffuse and Bragg scattering is a clear advantage of the PDF method, it leads to a slightly more complicated experimental methodology in comparison to traditional diffraction techniques (background subtractions, stable experimental conditions *etc*).

References

1. S. Anzellini, A. Dewaele, M. Mezouar, P. Loubeyre and G. Morard, *Science*, 2013, **340**, 464-466.
2. H. Rietveld, *Journal of Applied Crystallography* 1969, **2**, 65-71.
3. T. Proffen, S. J. L. Billinge, T. Egami and D. Louca, *Zeitschrift für Kristallographie*, 2003, **2003**, 132-143.

4. V. M. Nield and D. A. Keen, *Diffuse Neutron Scattering from Crystalline Materials*, Oxford University Press, 2001.
5. F. P. Zernike, J, *Z. Phys.*, 1927, **41**, 184.
6. S. J. L. Billinge, *Zeitschrift für Kristallographie*, 2004, **219**, 117-121.
7. K. W. Chapman, P. J. Chupas, G. J. Halder, J. A. Hriljac, C. Kurtz, B. K. Greve, C. J. Ruschman and A. P. Wilkinson, *Journal of Applied Crystallography*, 2010, **43**, 297-307.
8. P. Juhas, T. Davis, C. Farrow and S. Billinge, *ArXiv e-prints*, 2012.
9. T. Egami and S. Billinge, in *Underneath the Bragg Peaks: Structural Analysis of Complex Materials*, 2003, p. 56.
10. T. Egami and S. J. L. Billinge, *Underneath the Bragg Peaks: Structural Analysis of Complex Materials*, Elsevier, 2003.
11. W. Hoyer, I. Kaban and T. Halm, *Journal of Optoelectronics and Advanced Materials*, 2001, **3**, 255-264.

2. EXPERIMENTAL AND METHODOLGY

2.1 xPDF

As mentioned in Section 1.6, in order to obtain the highest quality xPDFs possible, synchrotron radiation must be used. In a synchrotron, electrons are generated by an electron gun and are then accelerated to high speed by a series of particle accelerators. These high speed electrons are then injected into a large storage ring and are steered around the ring by bending magnets. As the electron passes through each bending magnet it loses energy as light, which is then channelled out of the storage ring into the beamline stations. Each beamline is optimised for different experiments and the light is filtered and focused into the experiment hutch.

All x-ray data presented in Chapters 3 to 7 were collected from either the Advanced Photon Source (APS) in Chicago at beamline 11-ID-B or Diamond Light Source (DLS) in Didcot, Oxford at beamline I 15. 11-ID-B is dedicated to PDF work and is capable of running routine variable temperature and pressure work. It operates at fixed energies of 58 and 90KeV and uses a silicon crystal as a monochromator.[1] In comparison to 90KeV, at 58KeV more flux is available and the Compton scattering from diamond anvil cells is reduced and elastic scattering is increased.[2] As a result 58KeV is the energy routinely used for PDF measurements but 90KeV can be used to avoid absorption edges or access higher values of Q_{max}.

I-15 on the other hand is not a dedicated PDF line but none the less is still capable of producing high energy X-rays with PDF studies. It is Diamond Light Sources' "extreme conditions" beamline, studying materials under high-pressures and variable temperatures.[3] It

is capable of providing tuneable energies up to 80KeV using a double crystal monochromator and focusing mirrors.

2.1.1 Detector

Large flat panel area detectors built from an amorphous array of silicon (with a scintillator layer) are well suited to PDF experiments. They are available from Perkin-Elmer or General Electric Healthcare and are optimised for work using high energy x-rays. Due to their size, sensitivity and quick read out rates they are ideal for quick time-resolved PDF measurements.[4] The rapid readout allows for several images to be collected quickly (making experiments more efficient) and then averaged together to provide better statistics on collected patterns by reducing signal-to-noise ratios. The same model PE flat panel detector was used at both the APS and DLS (containing 2048 x 2048 pixels that are 200 x 200μm in size). For PDF experiments sample-to-detector distances are kept small (~200mm) to allow for maximum Q-ranges to be collected (Figure 2.1).

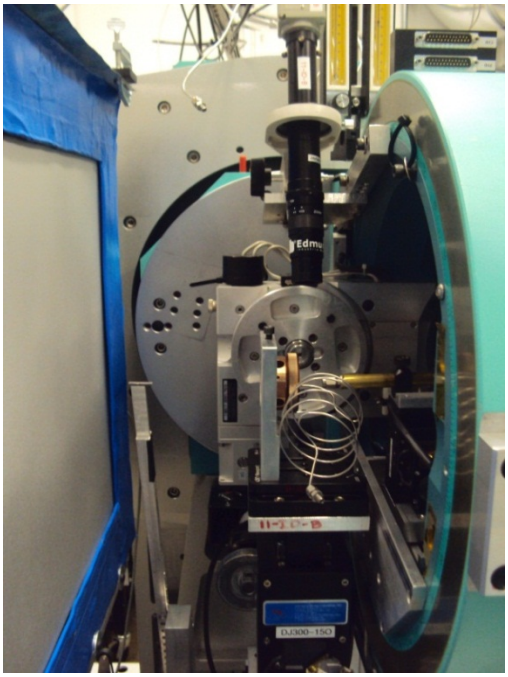

Figure 2.1: Experimental Set up for High Pressure Work at the APS.

There is also a trade-off to be made between *Q*-range and detector resolution, however with *Q* resolution decreasing as sample-to-detector distance decreases. This is due to the number of pixels integrated for each value of *Q*; at lower values of *Q*, less pixels are integrated and thus resolution is reduced. It is possible to move the detector "off-centre" to access a higher values of *Q*-max, where resolution is maintained at low-*Q*, but this approach has not been taken in any studies presented in this thesis. It is possible to move the detector *via* motors and it is possible to move the detector away from the sample to allow for better data quality for Rietveld analysis (not needing to access such a high theta value).

2.1.2 Diamond Anvil Cells

For collecting ambient and variable temperature data, the samples were contained within a 1mm diameter kapton tube. Kapton capillaries are easy to load and provide very little scatter, resulting in good sample-to-background ratios. For high pressure work however, we must use something more sophisticated in order to reach the high pressures required.

Diamond anvil cells (DAC) were used, which apply pressure to a sample by compressing it between two diamonds (Figure 2.2). A metal gasket to hold the sample is pre-indented to the required depth using the DAC itself and then this gasket is drilled with the required hole size.

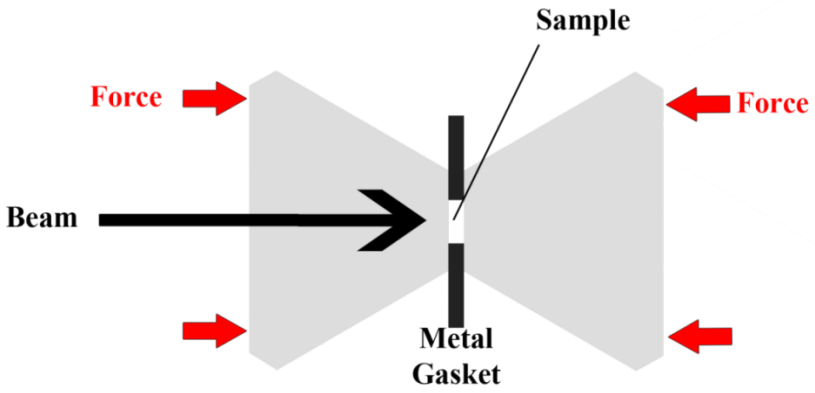

Figure 2.2: The basic principles of a DAC.

The diamonds contribute to a significant amount of the observed scattering pattern. This is because the beam path is a lot longer through the diamonds than the sample and a large component of this diamond scattering is as a result of Compton scattering from the carbon atoms. To minimise this, a drilled diamond can be used to reduce the beam path through, and hence Compton scatter from, the upstream diamond. Unfortunately this weakens the strength of the diamond resulting in a lower working pressure range for the DAC.

There are many types of DACs and different ways to apply pressures. Screws in the DAC body that force together both diamonds when turned can be used to apply pressure. Or another method is to use a DAC with a membrane containing a fluid under pressure that transmits force onto the sample *via* the diamonds can be used. Both of these methods have been used to apply pressure to a sample in the work presented in this thesis.

In order to measure the applied pressure, ruby crystals can be loaded into the gasket hole with the sample. Then the pressure in the sample can be calculated using ruby fluorescence manometry.[5]

2.1.3 Data Reduction

2.1.3.1 Integrating Images

Although the experimental set up for collecting high temperature and high pressure work varies, the data processing for both approaches is largely the same. The images produced by the detector at each pressure and temperature were averaged and integrated in a program called Fit2D.[6] This program is a general purpose program capable of analysing 1- and 2-dimensional data. It is also able to calibrate certain experimental details from standards, such as sample to detector distance, beam centre and detector tilt.

In order to integrate and produce useable data, some regions of the image need to be masked (Figure 2.3), for example areas blocked by the beam stop, dead pixels and the large amount of scatter from the diamonds in a DAC. In kapton capillaries, the sample-to-background ratio is high enough that masking is not a lengthy or intricate task, but this is not the case for data collected in a DAC. As the sample-to-background ratio is so poor, a good mask may take several hours and a significant amount of the image may be masked in order to remove diamond scatter.

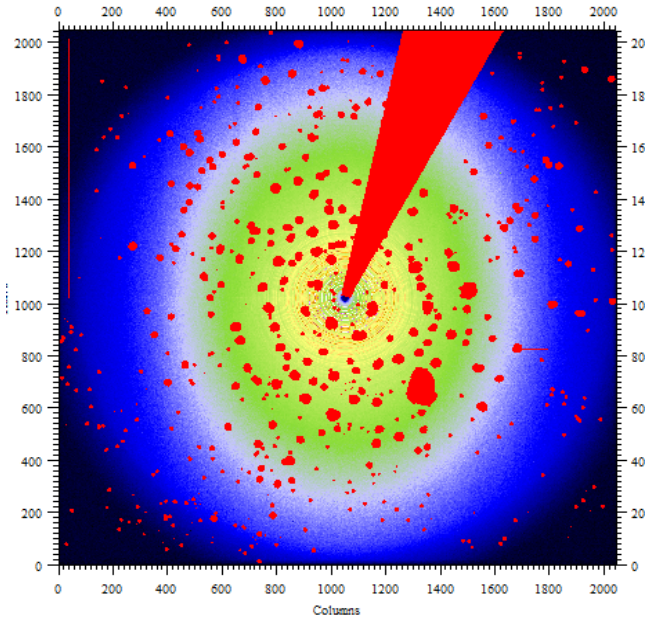

Figure 2.3: An example of a mask of a sample in a DAC used in Fit2D.

This masking is required as the scattering from the diamonds changes as pressure is varied. This is due to the diamond positions changing as pressure is increased, extra strain in the diamonds and the secondary diffraction from backing plates changing. It is not possible to measure a background at each pressure but a background can be masked at ambient and then this mask can be grown for each data set collected. The final mask is then used to integrate all the data sets collected, including the background.

A method for easily identifying non-radial features in scattering patterns (Bragg and diffuse scatter) has been developed where the image is rotated by an arbitrary amount (±5º) around the beam centre and this rotated image is then subtracted from the original.[2] This then makes spotting these features much easier, allowing for much more comprehensive masks to be made.

Once the mask has been produced, the image is integrated into a one dimensional pattern based on the information provided by the calibration to produce $I(Q)$ files in a .chi format.

2.1.3.2 Normalising Diffraction Patterns

These .chi files were then inputted into a program called PDFgetX2, which is capable of producing the $S(Q)$ for the data and in turn, produce the $G(r)$ files (PDF).[7] It should be noted that PDFGetX3 has recently been released, giving some improvements in ability to handle numerous data sets.[8] Due to its very recent release, PDFGetX3 was not used to produce any of the PDFs used in the studies presented in this thesis and the discussion here will concern PDFGetX2. It is also possible to normalise the data in GudrunX, which works on the same principles as PDFGetX2, as a test the same diffraction data was normalised *via* both GudrunX and PDFGetX2 and both PDFs produced were essentially identical. This is clearly reassuring but also highlights the robust nature of both programs to produce reliable PDFs.

PDFGetX2 is capable of applying all the corrections outlined in Section 1, but it also has to correct for other experimental conditions. The penetration of the diffracted beam into the detector varies with the angle between the detector surface and the diffracted beam.[9] The use of area detectors requires PDFGetX2 to be able to apply an oblique incident-angle correction to the data which is dependent of wavelength and sample-to-detector distance. The sensitivity of the detector is also dependent on the energy of the x-rays with the detector becoming more

efficient at lower energies than those used for PDF analysis.[10] As a result energy dependent corrections are also conducted in PDFGetX2.

PDFGextX2 is also capable of artificially smoothing and damping data but this approach has not been taken with any data presented in this thesis.

Once the images have been properly integrated in Fit2D the .chi files are inputed into PDFGetX2 and an appropriate *Q* range is chosen for use with the Fourier transform to a PDF. As seen in Figure 2.4, there is a drop off in scattering intensity at the edges of the detector (high *Q*) and thus care must be made to ensure the selected Q_{max} excludes this region in the raw data.

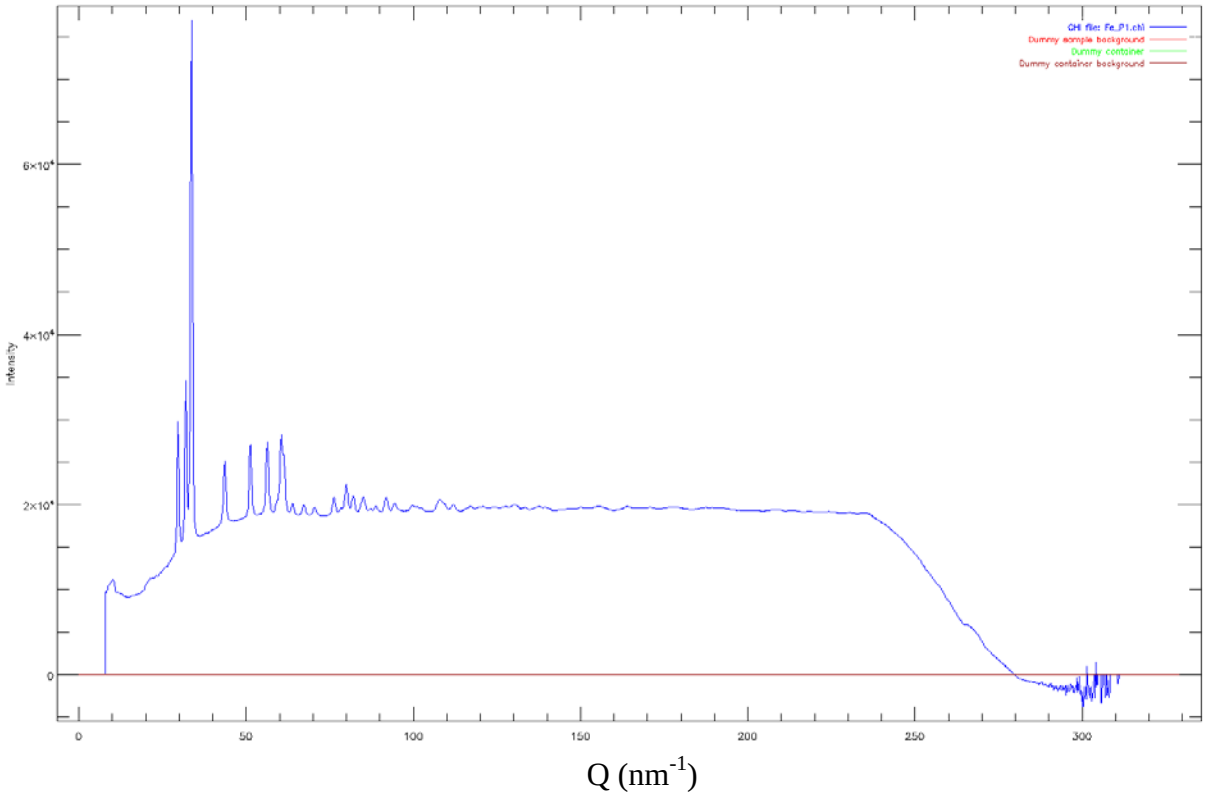

Figure 2.4: Integrated Pattern *I(Q)* inputted into PDFGetX2.

As can be seen in Figure 2.4, the beam stop hinders the accessing of the very low *Q* region of the diffraction pattern. The correct energy and sample information is then inputted and the

background is scaled to the sample to ensure an accurate background subtraction. The intensity of the beam can vary during a run so it is important to scale the background to the sample (Figure 2.5).

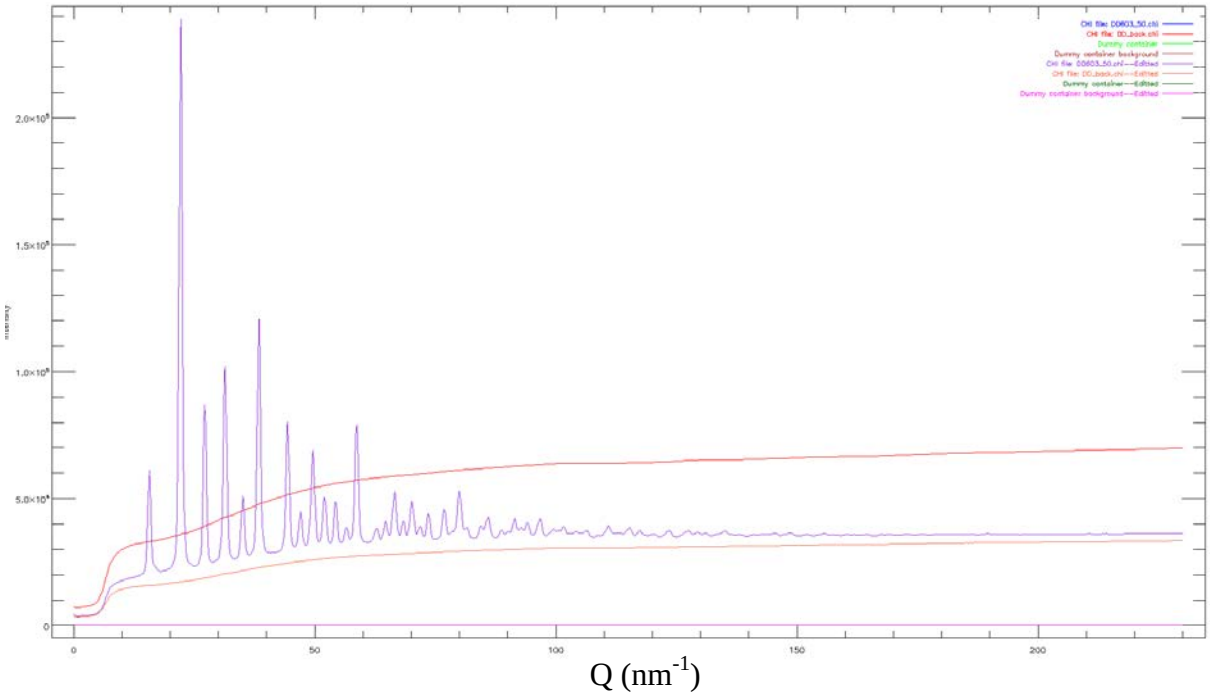

Figure 2.5: Scaling the Background for subtraction.

The *S*(*Q*) is then produced and appropriate corrections are made (Section 1.4). It is very quick to calculate the PDF from the *S*(*Q*) and a good way of ensuring accurate normalisations is to simply check the quality of the PDFs that are being produced. If normalisations are poor then there will be large termination errors in the PDF or the PDF may not drop out at all. In Figure 2.6a the energy dependent corrections for the detector have not been applied, resulting in the *S*(*Q*) not trending to unity at high (*Q*). Even though in this instance the effect on the normalised *S*(*Q*) appears small, the effect on the PDF is very clear, with large spurious oscillations at low r as shown in Figure 2.6b.

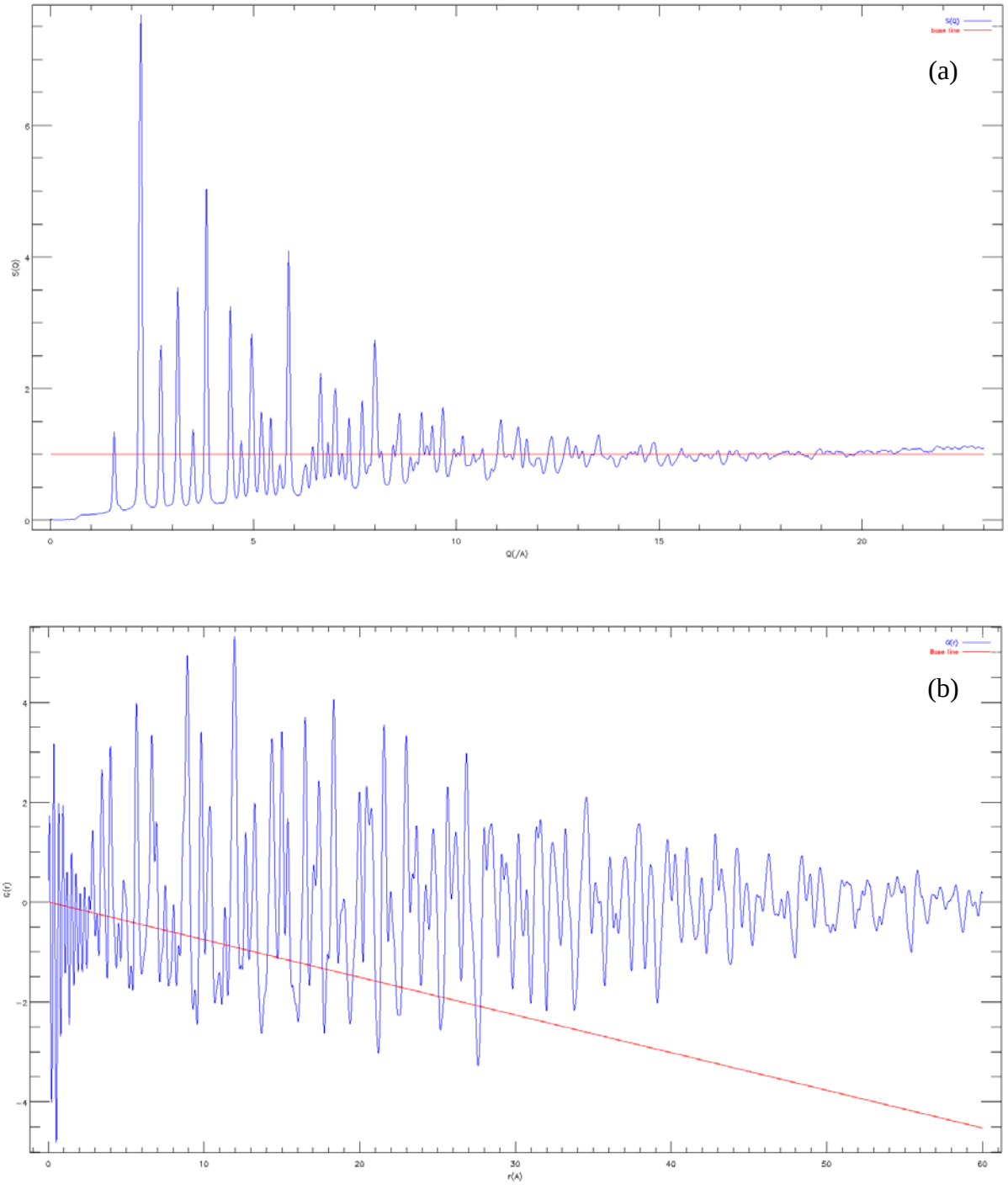

Figure 2.6 (a): $S(Q)$ without energy dependant corrections applied. (b): Resulting PDF.

You would expect PDFs produced from DAC data to be of worse quality than capillary data owing to lower obtainable Q_{max} values and lower sample-to-background ratios, but as seen in Figure 2.7, high quality PDFs can be produced from DAC data.

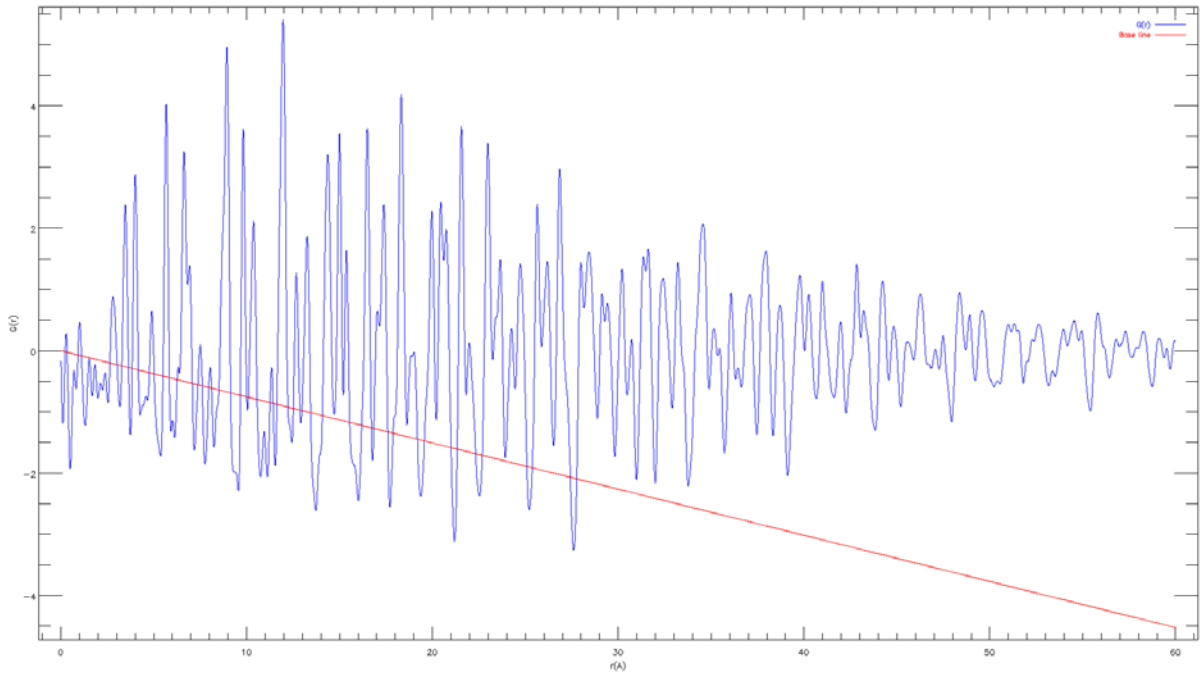

Figure 2.7: PDF of $BaTiO_3$ in a DAC (with drilled upstream diamond) at ambient conditions.

Once the first PDF has been normalised, if one background is used for the whole experiment, it is relatively easy to input data for each pressure/temperature and use similar (if not identical) corrections for each. In some cases it is necessary to collect multiple backgrounds, for example if the cell slips in its holder during a run or if using a sample container whose background changes with temperature. In these instances, data corrections are more laborious, but nonetheless they are relatively straight forward.

2.2 nPDF

All neutron PDFs were measured at ISIS, on the GEM (General Material) diffractometer.[11] GEM has the ability to collect high quality data on samples in a variety conditions, up to very high values of Q_{max} (up to $Q = 55$ Å^{-1}). The large range of momentum transfers, coupled to high count rates make GEM ideal for conducting very high quality PDF experiments.

Neutrons are moderated using liquid methane and exit the moderator at temperatures between 100 and 110K. The primary flight path of these neutrons to the sample is 17m (which is relatively long) and this results in a high *Q* resolution. The flight path is also evacuated so that there is no air scattering present in as part of the background, further increasing data quality. The beam size is defined by a series boron carbide slits and choppers are also used to prevent frame overlap.

2.2.1 Detector

There are eight banks of detectors on GEM, all of which contain strips of ZnS/^{6}Li and these banks are situated so they cover a large range of scattering angles (from 1.20 to 171.4^{o}). This arrangement allows for small values of Q_{min} (Section 1.5.2) and high values of Q_{max} (Section 1.5.1) to be accessed. Coupled with high count rates, this results in a detector well suited to collected PDF data.

The detector banks were designed to be as stable as possible, with little variation in efficiency over varying temperatures and protection against any magnetic fields present. This stability is clearly ideal when measuring PDFs, making background subtractions a lot more accurate due to the stability of conditions between background and sample scans.

With optimised conditions for PDF measurements the limiting factor when considering what value of Q_{max} can be obtained is the Debye–Waller factor (Section 1.2). The detectors can provide data up to a Q_{max} of 100 Å^{-1} but in practice the Debye–Waller factor means that sample scattering has disappeared much before these values of *Q*.

2.2.2 Sample Environment

The samples were loaded into vanadium cans and the sample height was measured for each can so that the “packing fraction” could be calculated (Figure 2.8). They were then sealed

using indium metal, squashed between the sample and the sample lid *via* a series of screws. This ensured that samples would not pick up moisture from the air over time. Vanadium is chosen because almost all of the scattering is incoherent resulting in a flat background with only very weak Bragg peaks.

Figure 2.8: Vanadium Can Used in nPDF experiments.

High temperatures were accessed by loading the sample can into a furnace and temperatures below room temperature were accessed using a cryostat, closed cycle refrigerator (CCR).

2.2.3 Data Reduction

Gudrun was used to normalise the data in the neutron diffraction experiments and takes information about the detector (detector angles and positions, flight path, detector grouping etc), the beam (geometry), the sample (packing fraction, composition, scattering lengths), the container (Thickness, density and composition) and then uses this information to produce a PDF from the inputted diffraction data.

The basic processes are the same as with PDFGetX2 (subtracting measured background and running the various corrections required). Four measurements are taken, the empty instrument with nothing in the beam, a vanadium standard, an empty container in the beam and finally the sample within the container.

In order to produce a PDF, Gudrun needs information about the detector used; a deadtime corrections file, a detector grouping file and a detector calibration file. Gudrun is able to throw out bad detectors from analysis (of time-of-flight diffraction) by running a purge on the data files, which will exclude these detectors from the final corrections and Fourier transform.

In order to conduct multiple scattering corrections Gudrun must be provided with the sample geometry and composition as well as the beam size and position.

The container thickness, density and composition (vanadium) is inputted and the total neutron transmission cross-section is calculated from tables. Information about the sample composition (atom types and relative abundances) and density is then inputted and if there are multiple data sets corresponding to the same sample data collection then these can be combined in Gudrun.

Once Gudrun has this information it can subtract the background from the sample and this background can be scaled to the sample pattern if required using the "container tweak factor". When a purge has been run by using the "run gudrun" command Gudrun with perform the necessary background subtracts and normalisations which will produce the $S(Q)$. The *"Top Hat"* function can be used to bring the $S(Q)$ to oscillate about 0 and the PDF produced to required r range.

2.3 Analysing PDFs

2.3.1 PDFGui

Once the PDFs have been measured, there are several methods to extract structural information. One such method is a “down-hill least squares” refinement, which was implemented on PDF data by a program called PDFfit.[12] Like the Rietveld technique and the GSAS program, the structural parameters are all adjusted to obtain the best fit to the experimental data. As a result, the program allows the structural refinement of PDF data providing information on a variety of variables, such as atom positions and thermal parameters. More recently a program called PDFfit2 was developed which was based on the original PDFfit program.[13] The developers of PDFfit2 re-wrote the original PDFfit engine, and intended it to provide a wide range of upgrades over the original program, such as removing bugs and adding several new features.[13]

PDFgui is a graphical user interface built on the PDFfit2 engine, containing all of the functionality of PDFfit2 but simplifying various tasks for the user.[13] It allows users to refine various parameters using their experimental PDF data. It can also fit PDFs using multiple phases if required and can easily produce partial PDFs from the fitted models. The *Phase Configuration* tool allows users to input a theoretical structural model, with the addition of a number of variables as seen in Figure 2.9.

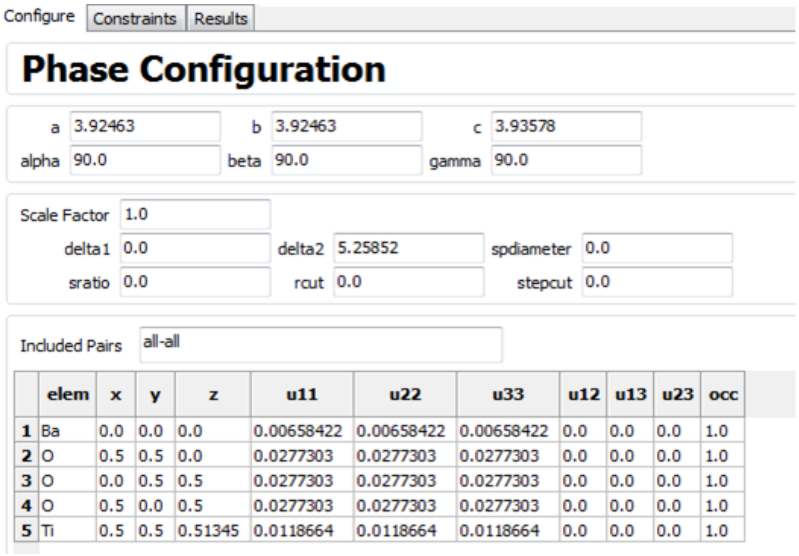

	elem	x	y	z	u11	u22	u33	u12	u13	u23	occ
1	Ba	0.0	0.0	0.0	0.00658422	0.00658422	0.00658422	0.0	0.0	0.0	1.0
2	O	0.5	0.5	0.0	0.0277303	0.0277303	0.0277303	0.0	0.0	0.0	1.0
3	O	0.0	0.5	0.5	0.0277303	0.0277303	0.0277303	0.0	0.0	0.0	1.0
4	O	0.5	0.0	0.5	0.0277303	0.0277303	0.0277303	0.0	0.0	0.0	1.0
5	Ti	0.5	0.5	0.51345	0.0118664	0.0118664	0.0118664	0.0	0.0	0.0	1.0

Figure 2.9: PDFgui phase construction screen.

These may be fixed to certain values or be set as variables to be refined by PDFgui. The program will then produce a theoretical fit to the experimental data, producing a *Rw* value which corresponds to how well the theoretical model fits the observed data. The weighted *R*-value is calculated as follows

$$R_w = \sqrt{\frac{\sum_{i=1}^{N} w(r_i) - [G_{obs}(r_i) - G_{calc}(r_i)]^2}{\sum_{i=1}^{N} w(r_i) G_{obs}^2(r_i)}} \tag{2.1}$$

Where N is the number of points, $w(r_i)$ is the weight of each data point and G_{obs} the experimental PDF.

The program also includes a number of parameters that account for correlated atomic motion. At shorter distances, the motion of atoms can be highly correlated which leads to a sharpening in the first few peaks in the experimental PDF. [14] Likewise, at longer distances, the motion of two atoms is uncorrelated. Overall, peak width is defined as

$$\sigma_{ij} = \sigma'_{ij}\sqrt{1 - \frac{\delta_1}{r_{ij}} - \frac{\delta_2}{r_{ij}^2} + Q_{broad}^2 r_{ij}^2} \tag{2.2}$$

Where σ_{ij}' is the width of a peak without correlated motion, $\frac{\delta_1}{r_{ij}}$ and $\frac{\delta_2}{{r_{ij}}^2}$ are terms which correct for the effect of correlated motion. The term $\frac{\delta_2}{{r_{ij}}^2}$ describes the low temperature behaviour and $\frac{\delta_1}{r_{ij}}$ describes the high temperature behaviour. These terms are highly correlated, so it is only necessary to refine one of these terms. An alternative method to correct for the effects of correlated motion is to include the parameters *rcut* and *sratio* into a refinement. The parameter *sratio* defines low- to high-r PDF peak ratios and *rcut* defines what r-range *sratio* is applied (for example if rcut=3.1 then *sratio* will be applied up to 3.1Å). The user should decide which method should be used to correct for correlated motion, both methods should not be used simultaneously. The final term in Equation 2.2, $Q_{broad}^2 r_{ij}^2$, deals with the effects of peak broadening as a result of the *Q*-resolution of the diffractometer and is only significant in the PDF at larger *r*-ranges. This *Q* resolution also results in exponential dampening of the PDF peaks, which is modelled by the parameter *qdamp*. When running refinements as the *Q*-resolution is the same for all data sets collected at any given time, *qdamp* should not be refined. It can be obtained by refining a known standard (CeO_2) in PDFGui or by refining a model that accurately describes the experimental data. This parameter is one example of instances where it does not make physical sense to refine it for each PDF, despite giving lower *Rw* values if refined. As it is highly correlated with other parameters such as correlated motion and thermal parameters, refining it for each model may not provide accurate refinement results. Deciding what to refine and what to fix is an essential consideration when refining models at different length scales and in different conditions. An attempt will be made to justify the refinement approaches in each of the experimental chapters.

The final parameters in PDFgui that deal with peak width are *spdiameter* and *stepcut.* The parameter *spdiameter* is concerned with the diameter of nano particles and *stepcut* truncates the PDF to zero at r values above the value set as *steptcut*.

Whilst these numerous parameters deal with modelling the peak widths, *scalefactor* deals with the relative peak intensities. It keeps the ratio between the intensities of the peaks the same, relative to the total pattern intensity.

If a parameter flag is set to zero, it is not included in a refinement. Parameters can either be fixed to set values, or alternatively, refined by PDFgui. Once a user has inputted the desired phase and variables, PDFgui can refine the theoretical structure to the observed data. The values of the calculated parameters are presented and the program is able to plot the calculated PDF on top of the experimental PDF (Figure 2.10).

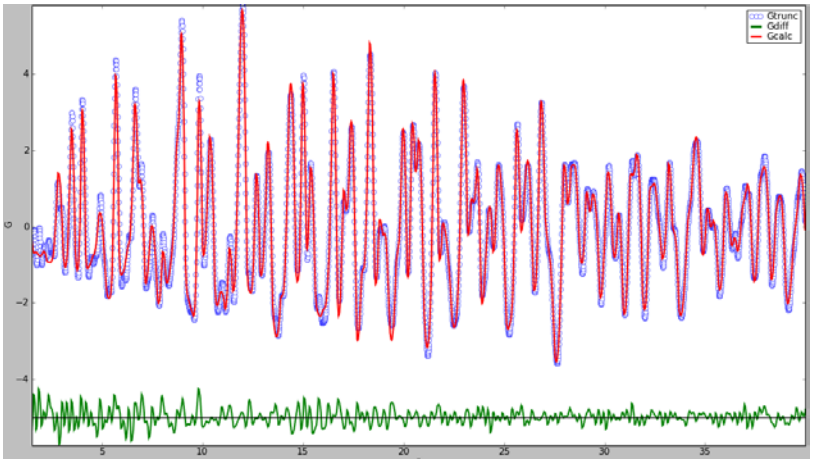

Figure 2.10: A calculated fit for experimental PDF of $BaTiO_3$ in PDFgui.

The red line in Figure 2.10 represents the theoretical PDF, the blue circles represent the experimental data and the green line at the bottom of the plot represents the difference between the two.

PDFgui has an inbuilt feature (macro) designed to deal with sequential fitting of data sets corresponding to different temperatures. This feature speeds up the fitting of a large number of data sets of the same sample over a range of temperatures. Once the user has set up a refinement for the initial temperature, the program will then apply this refinement set-up to the rest of the series and fit them sequentially. Once the file series has been fit, the program is able to produce the refinement results for the whole temperature range in text and graphical format.

PDFGui is capable of refining models containing large numbers of atoms (>100) over large r ranges but as complexity of refinements are increased, more care must be taken in setting up a refinement. As refinements are conducted *via* a "down-hill least squares" method, it is helpful that all parameters (both those refined and fixed) are as close to expected as possible. It is often necessary to keep refinements basic at the start and then increase the complexity as the model starts to more accurately describe the experimental data. For example, only initially refining the scale factor and lattice parameters over a shorter r range than will be eventually used. This keeps refinements quick and makes for much more efficient approach to refinements that simply "throwing in" all required variables at once, indeed PDFGui may not initially be able to handle all the parameters at once.

Care must also be taken to inspect results of refinements beyond simply the R_w values. It is possible that PDFGui will produce a very good fit to experimental data (R_w < 10%) but it has achieved this by one parameter being changed beyond something that is physically reasonable, such as U_{iso} values above 1 $Å^{-3}$ or atoms being moved to nonsensical positions.

Ultimately a lot of time was spent on developing acceptable refinement approaches to the measured PDFs. An attempt will be made to discuss how each given approach was developed

but it not possible to present every single approach used in detail this thesis due to the sheer volume of data that is produced for the numerous approaches used for each system.

2.3.2 Error Estimation

Currently it is not possible to produce reliable estimated standard deviations (ESDs) from any of the refined parameters in PDFGui for 2D detector data. The problem lies with Fit2D not producing uncertainties on any of the data points produced from integrating the 2D images, resulting in any uncertainties being produced by PDFGui being non-realistic. While progress is apparently being made on addressing this problem[15], it remains an issue for all the refined parameters presented in this thesis.

Due to the relatively quick data collections associated with xPDF collections, it was possible to take several measurements of a sample over the space of a few minutes, with no conditions changing between each collection. This meant that the standard deviation in refined parameters on each of each PDF produced could be calculated, hopefully giving at least a basic insight into the magnitude of error for each refined parameter.

Nineteen xPDFs were collected of $BaTiO_3$ (BTO) in a kapton capillary at 500K over the space of roughly 20 minutes (each PDF was produced from an image of 120 x 0.5 second exposures). For more information on the experimental set up see Section 3.2.1 and for information regarding the refinement approach see Section 3.2.2. The images collected were integrated using the same mask and PDFs were produced using PDFGetX2. The PDFs produced can be seen in Figure 2.11.

a

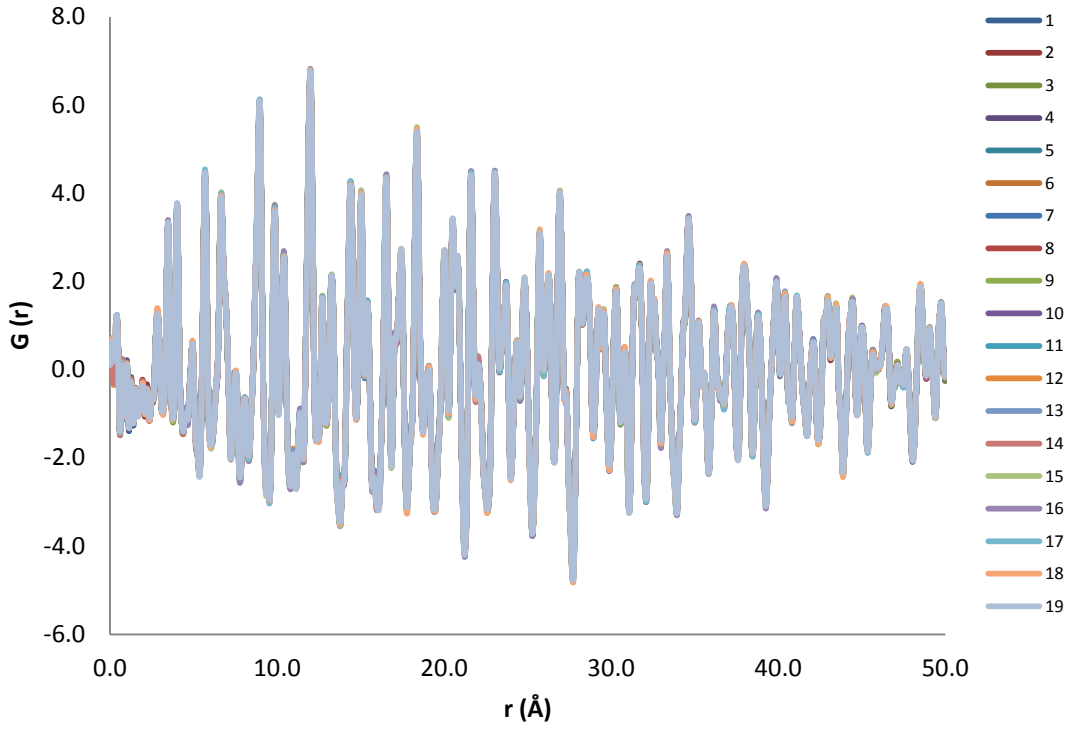

b

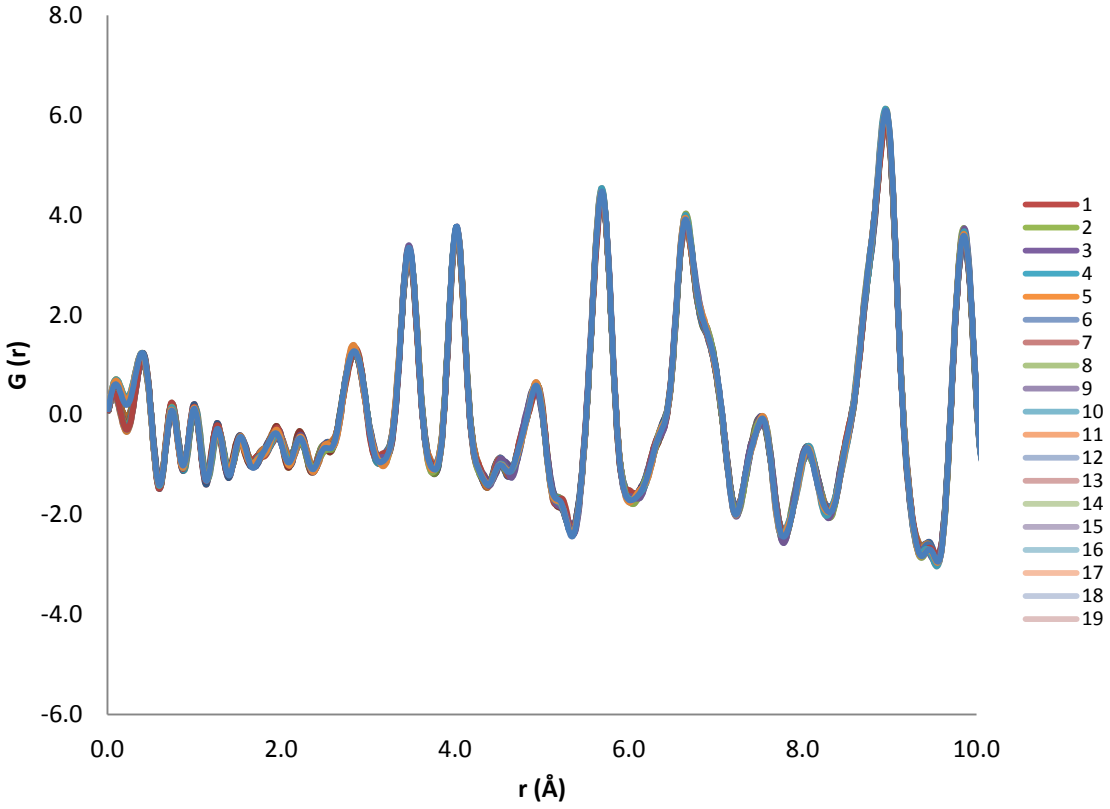

Figure 2.11(a): PDFs of $BaTiO_3$ at 500K from 0 to 50 Å (b): from 0 to 10 Å.

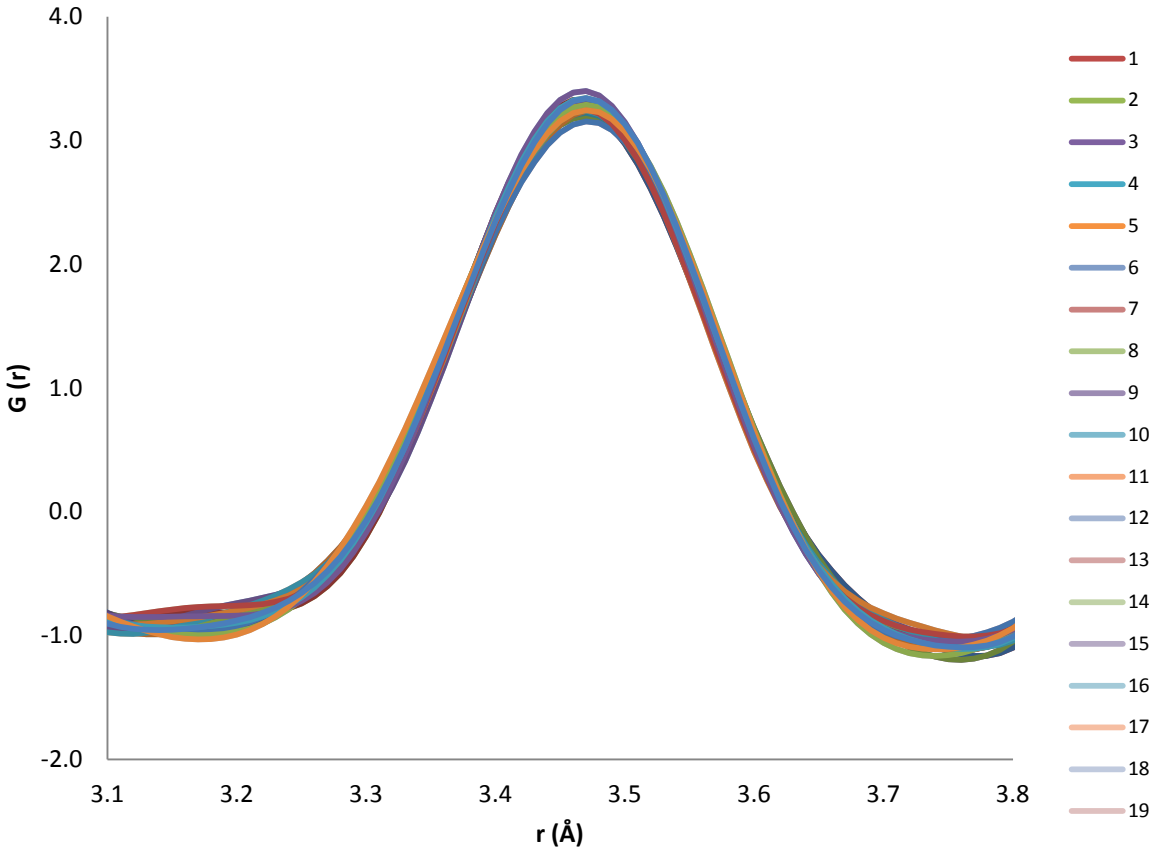

Figure 2.12: The first Ba-Ti peak for the PDFs of $BaTiO_3$ at 500K.

As can be seen from Figures 2.11a and b and Figure 2.12, the PDFs do not track perfectly over the top of each other, there is variation in one to the next. In order to investigate the effect these variations have on refined parameters in PDFGui a cubic model of BTO was fitted to the PDFs on a length scale of 2.5 to 50Å (Table 2.1).

Table 2.1: Refined parameters for a cubic model of BTO fit to 19 PDFs of BTO at 500K.

			Atomic Displacement Parameters (ADPs)		
File No.	R_w	a (Å)	Ba ($Å^2$)	Ti ($Å^2$)	O ($Å^2$)
101	0.10670964	4.01742956	0.0087132	0.01663085	0.03445382
102	0.10761012	4.01745947	0.00875889	0.01660216	0.03444449
103	0.10842311	4.0174958	0.00873399	0.01664441	0.03436771
104	0.10749822	4.01752524	0.00879591	0.01666475	0.03462517
105	0.10904267	4.0175298	0.00878272	0.01668112	0.03475159
106	0.10602047	4.01756048	0.0088034	0.01667439	0.03469825
107	0.11046233	4.01753513	0.00879312	0.01668983	0.03456403
108	0.10718856	4.01758536	0.00878643	0.01665683	0.03450465
109	0.10875253	4.01757205	0.00878295	0.01665922	0.03450468
110	0.10801459	4.01760906	0.00877444	0.01673226	0.03457562
111	0.10908151	4.0175803	0.00877634	0.0167148	0.03460195
112	0.10857071	4.01757166	0.00879927	0.0166553	0.0346423
113	0.10603227	4.01761606	0.00879007	0.01667063	0.03463267
114	0.11086166	4.0175944	0.00877157	0.01668455	0.03448999
115	0.10675128	4.01759636	0.00876829	0.01673387	0.03445808
116	0.10985629	4.01759042	0.00879642	0.01670002	0.0346986
117	0.10640536	4.01759341	0.0088267	0.01674158	0.03479656
118	0.10913705	4.01757876	0.00881373	0.01671193	0.03464924
119	0.1062082	4.01759052	0.00882716	0.01674158	0.03468956

In order to investigate the amount of variation in the results of refinement on each PDF the standard deviation (σ) for each refined was calculated:

$$\sigma = \sqrt{\frac{1}{N}\sum_{i=1}^{N}(x_i - \mu)^2} \quad (2.3)$$

Where N is the population size, x_i is the individual values and μ is the mean. In statistics the three-sigma rule states that almost all values (99.7%) will lie within three standard deviations of the mean in a normal distribution. As a result the calculated standard deviations presented in Tables 2.2 to 2.4 should potentially be tripled in order to more accurately describe the errors associated with the data analysis in PDFGui.

The standard deviations for refined parameters for a cubic model of BTO fit to these data be seen in Table 2.2, along with several other models of $BaTiO_3$ (Table 2.1) being fit to the same data, at the same length scale.

Table 2.2: Standard deviations of refined parameters on xPDF data of BTO at 500K from 2.5 to 50A.

	Cubic	Disordered Tetragonal	Tetragonal	Orthorhombic	Rhombohedral
Rw	**0.00149**	0.00150	0.00152	0.00152	0.00150
a (Å)	**0.00005**	0.00012	0.00012	0.00021	0.00005
b (Å)				0.00027	
c (Å)		0.00019	0.00020	0.00034	
Ti co-ordinate		0.00027	0.00024	0.00018	0.00024
Ba *U* (Å^2)	**0.00003**	0.00004	0.00004	0.00004	0.00004
Ti *U* (Å^2)	**0.00004**	0.00010	0.00013	0.00010	0.00013
O *U* (Å^2)	**0.00012**	0.00012	0.00010	0.00012	0.00015

For the cubic model the *Rw* values appear to be accurate to the 3rd decimal place, meaning a change/difference of 1% in *Rw* values could be seen to be "real" and not within errors. The cubic lattice parameters and atomic displacement parameters (ADPs) (excluding the oxygen atom) appear to be accurate to the 4th decimal place and the error in the oxygen atoms ADPs possessing a higher standard deviation and potentially accurate to the 3rd decimal place. Due to various parameters being compared for different models over phase transitions it is appropriate to look at what standard deviations are present for parameters from other models of BTO at 500K. Clearly there is a certain variation between models, which is perhaps to be expected with only one model truly representing the correct structure at this temperature. There appears to be less variation is lattice parameters when a = b = c then when than when this is not the case, which is perhaps to be expected with models that have more degrees of freedom when it comes to refining multiple values for the lattice parameters. *Rw* values appear to remain accurate to the 3rd decimal place however, even with each model possessing differing numbers of refined parameters (Section 3.2.2). The refined position of the Ti-atom appears to be reliable to 4th decimal place as well, which is true of all models.

Of course one of the advantages of the PDF technique is that the structure of materials can be studied at different length scales and it likely that refining models to different length scales will affect ESDs (if we could produce them). This would be due to decreasing the number of data points available for refinement if smaller length scales or a "sliding box" method were used. A "sliding box" method being where a "refinement box" of a fixed length is moved through the data to investigate structures at different length scales, for example a 10Å "box" refined at 0-10, 5-15, 10-20Å etc.

Two length scales used in Chapters 3 and 4 were 2.2 to 13Å and 37 to 50Å. In order to investigate potential errors on refined parameters at these length scales the same process was

repeated for the PDFs collected at 500K but models were refined at these length scales. Results from refinement for each PDF at each length scale can be seen in Appendix 1. The standard deviations in the refined parameters can be seen in Table 2.3.

Table 2.3: Standard deviations of refined parameters on xPDF data of BTO at 500K from 2.5 to 13Å.

	Cubic	Disordered Tetragonal	Tetragonal	Orthorhombic	Rhombohedral
Rw	**0.00237**	0.00245	0.00249	0.00244	0.00240
a (Å)	**0.00008**	0.00107	0.00026	0.00246	0.00008
b (Å)				0.00246	
c (Å)		0.00216	0.00056	0.00406	
Ti co-ordinate		0.00055	0.00036	0.00029	0.00029

Table 2.4: Standard deviations of refined parameters on xPDF data of BTO at 500K from 37 to 50Å.

	Cubic	Disordered Tetragonal	Tetragonal	Orthorhombic	Rhombohedral
Rw	**0.00498**	0.00516	0.00509	0.00510	0.00508
a (Å)	**0.00005**	0.00010	0.00010	0.00018	0.00005
b (Å)				0.00047	
c (Å)		0.00013	0.00013	0.00035	
Ti co-ordinate		0.00079	0.00083	0.00054	0.00050

It can be seen from Tables 2.3 and 2.4 that *Rw* values vary more for refinements at shorter length scales, with variation smaller from refinements at 2.5 to 13Å than 37 to 50Å. *Rw* values will be more sensitive to slight variations in the PDFs when there are fewer data points. On the whole lattice parameters appear to be more accurate from refinements between 37 and 50Å and it is difficult to draw any firm conclusions from variation in Ti positions, apart from to say they are roughly comparable.

While standard deviations calculated in this way do not present precise values for ESDs on the data presented in subsequent chapters, they give a rough guide to the order of magnitude or errors that could be present on the data presented. They may be useful to refer back to when attempting to discuss trends in the data presented but they may not be used to draw firm conclusions.

Based on the standard deviations presented in Tables 2.2 to 2.4 *Rw* will be presented to 3 decimal places and lattice parameters, thermal parameters and atom positions to four.

2.3.3 Fityk

It is possible to fit Gaussian peaks to the PDF pattern using a program called Fityk.[16] It can be used on various different types of data such as powder diffraction data, chromatography and Raman spectroscopy to name a few (Figure 2.13)

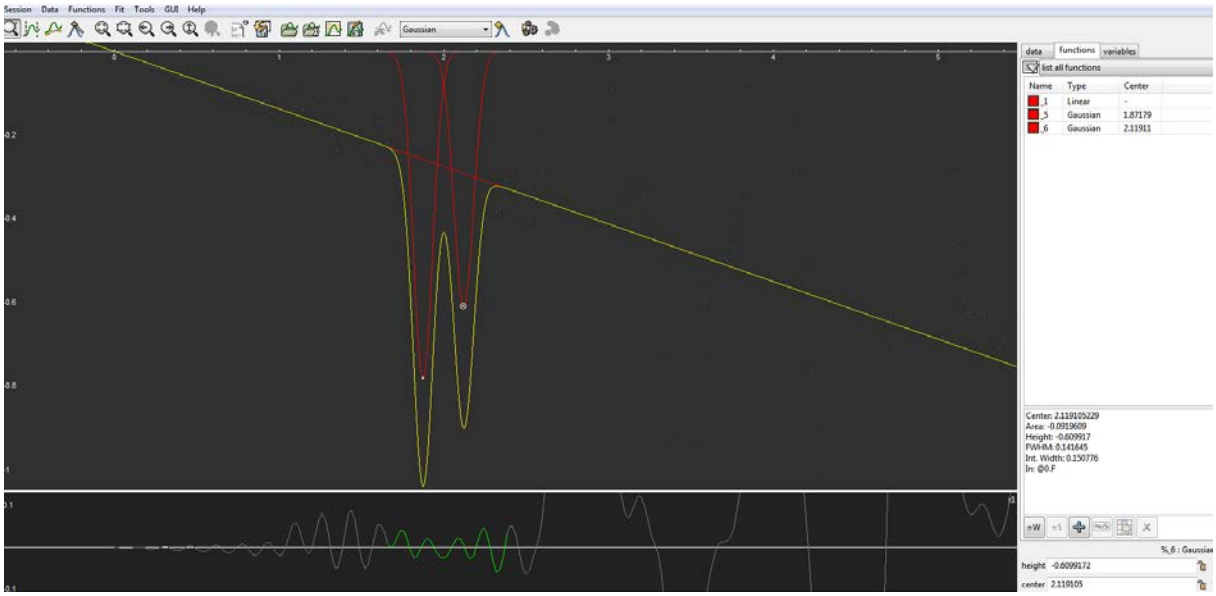

Figure 2.13: Fityk GUI.

Gaussian peaks can be fit to the experimental PDFs and the program will produce various peak parameters such as full width at half maxima (FWHMs), area and peak centre. If the average number density (ρ_0) is known (PDFGui will estimate this value using the model provided) then the PDF can be converted into the radial distribution function (RDF) and co-ordination numbers can be calculated. The radial distribution function $R(r)$ is related to the $G(r)$ by

$$R(r) = r[G(r) + 4\pi r\rho_0] \tag{2.4}$$

In order to correctly model the PDF peaks, it is possible to fix peaks to have the same FWHM and thus to set relative areas of peaks. This is useful when considering peaks that have contributions from different atom-atom distances. In order to model the baseline a linear function was applied so that its intercept on the y-axis was zero and it was given a negative slope based on examining the experimental data. Data ranges can be excluded and as many

peaks can be added to fit as required. Once an acceptable fit is achieved, the fits can be exported into other plotting programs such as excel.

2.4 Rietveld Refinements

There are several programs capable of carrying out Rietveld refinements on diffraction data and the one utilised in this study was GSAS v*ia* the EXPGUI user interface.[17-20] GSAS has similarities with PDFGui in that it can fit crystallographic models to a variety of different experimental data and does this by a least squares refinement to obtain the best possible fit. It can fit neutron diffraction and x-ray diffraction data but it only considers Bragg diffraction and not diffuse scattering. As there is no need to model diffuse scattering there is no need for accurate backgrounds to be measured and the background is modelled in GSAS.

Models in GSAS are constructed from a variety of parameters that are essentially identical to those available in PDFGui. For example the size, shape and symmetry of the unit cell is defined along with atom positions, atom occupancies and thermal parameters (U_{iso}). Peak width and peak shapes are also modelled as they are affected by experimental set ups, beam characteristics and sample size and shape. The width of Bragg peaks broaden at larger Bragg angles and this angular dependency is also modelled in GSAS. Some parameters may be fixed and some refined during the modelling and the parameters will be varied in an attempt to provide the best fit to experimental data.

In order to measure how well the theoretical model fits the experimental data a weighted-profile *R*-factor (R_{wp}) which is defined as:

$$R_{wp} = 100\sqrt{\left[\frac{\sum w_i[y_i(obs)-y_i(calc)]^2}{\sum w_i[y_i(obs)]^2}\right]} \qquad (2.5)$$

where $y_i(obs)$ is the observed intensity at the ith step, $y_i(calc)$is the calculated intensity at the ith step and $w_i=1/y_i(obs)$. During the refinement process the R_{wp} should converge with the expected *R*-factor (R_{exp}) which gives the best possible *R*-value obtainable for the data set being examined. It is affected by the number of data points (*N*), refined paramters (*P*) and constraints (*C*) used in the refinements and is defined by:

$$R_{exp} = 100\left[\frac{N-P-C}{\sum w_i[y_i(obs)]^2}\right] \tag{2.6}$$

When the refinement has been completed then a graphical plot of the fit to experimental data is produced (Figure 2.14). Tick marks corresponding to peak positions for the phase(s) are also provided with each tick corresponding to certain reflection.

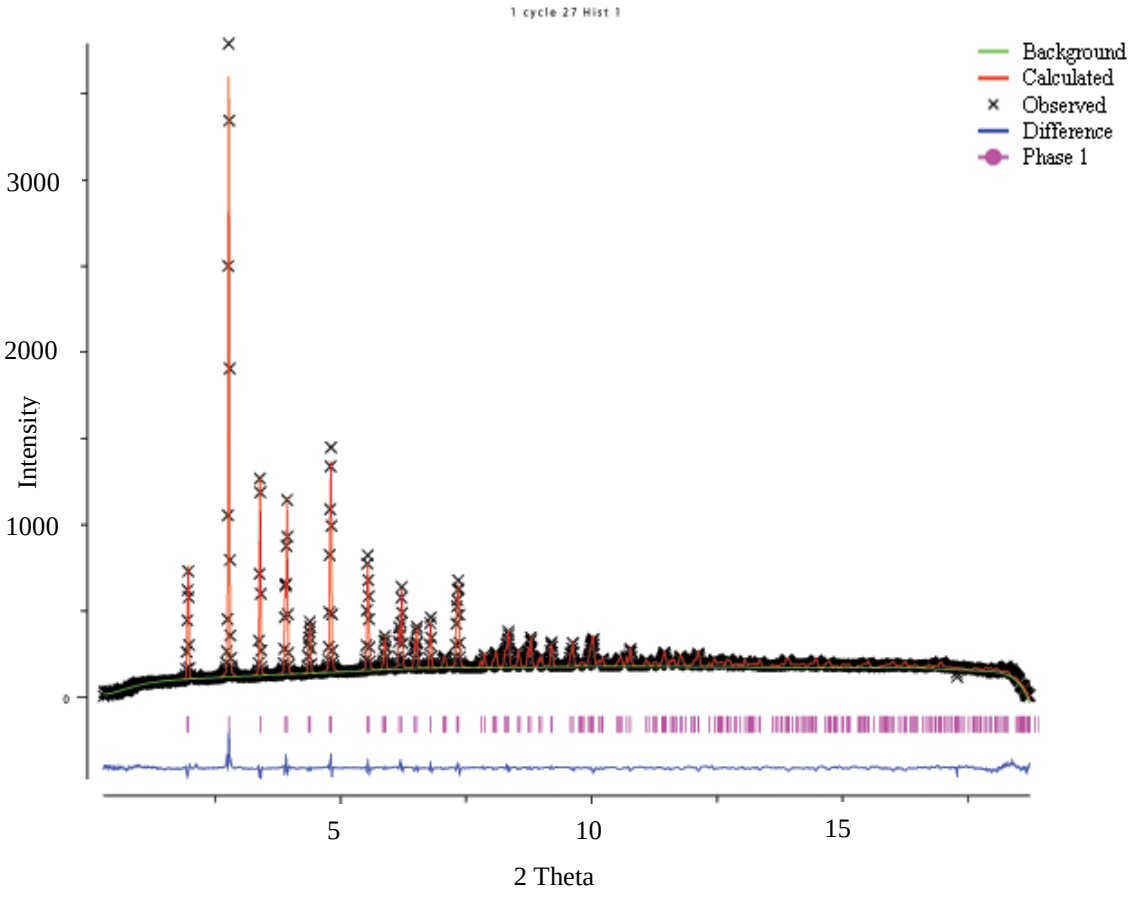

Figure 2.14: Example of a Rietveld fit to experimental data.

Preferred orientation (texture) can also be modelled in GSAS. Preferred orientation is where the orientations of crystals in a sample are not random with some crystals aligned along certain axis. This can affect the intensities of Bragg peaks, making some more intense and some less intense than expected. A correction factor can be applied by GSAS using a March-Dollase correction[21] which requires knowing the specific plane of preferred orientation.

It should be noted that GSAS-II has been released[22] but due to the relatively recent release no data presented in this thesis was analysed using the new program. This new program is aimed at replacing the existing GSAS software that was originally released in the 1980s.

References

1. P. J. Chupas, X-ray Science Division, APS, vol. 2013.
2. K. W. Chapman, P. J. Chupas, G. J. Halder, J. A. Hriljac, C. Kurtz, B. K. Greve, C. J. Ruschman and A. P. Wilkinson, *Journal of Applied Crystallography*, 2010, **43**, 297-307.
3. DLS, Diamond Light Source Ltd, 2012, vol. 2013.
4. P. J. Chupas, K. W. Chapman and P. Lee, *Journal of Applied Crystallography*, 2007, **40**, 463-470.
5. G. J. Piermarini, S. Block and J. D. F. Barnett, R. A, *Journal of Applied Physics*, 1975, **46**, 2774-2780.
6. A. P. Hammersley, S. O. Svensson, M. Hanfland, A. N. Fitch and D. Hausermann, *High Pressure Research*, 1996, **14**, 235-248.
7. X. Qui, J. W. Thompson and S. J. L. Billinge, *Journal of Applied Crystallography*, 2004, **37**, 678.
8. P. Juhas, T. Davis, C. L. Farrow and S. J. L. Billinge, *ArXiv e-prints*, 2012.
9. G. Zaleski, G. Wu and P. Coppens, *Journal of Applied Crystallography*, 1998, **31**, 302-304.
10. M. Ito and Y. Amemiya, *Nuclear Instruments and Methods in Physics Research: Section A*, 1991, **310**, 369-372.
11. A. C. Hannon, *Nuclear Instruments and Methods in Physics Research A*, 2005, **551**, 88-107.
12. T. Proffen and S. J. L. Billinge, *Journal of Applied Crystallography*, 1999, **32**, 572-575.
13. C. L. Farrow, P. Juhas, J. W. Liu, D. Bryndin, E. S. Bozin, J. Bloch, T. Proffen and S. J. L. Billinge, *Journal of Physics: Condensed Matter*, 2007, **19**, 335219-335226.
14. I. Jeong, T. Proffen, F. Mohiuddin-Jacobs and S. J. L. Billinge, *Journal of Physical Chemistry A*, 1999, **103**, 921-924.
15. P. Juhas, T. Davis, C. Farrow and S. Billinge, *ArXiv e-prints*, 2012.
16. M. Wojdyr, *Journal of Applied Crystallography*, 2010, **43**, 1126-1128.

17. B. H. Toby, *Journal of Applied Crystallography*, 2001, **34**, 210-213.
18. A. C. Larson and R. B. Von Dreele, *General Structure Analysis System (GSAS)*, Los Alamos National Laboratory, 2000.
19. H. Rietveld, *Journal of Applied Crystallography*, 1969, **2**, 65-71.
20. H. Rietveld, *Journal of Applied Crystallography*, 1967, **22**, 151-152.
21. W. A. Dollase, *Journal of Applied Crystallography*, 1986, **19**, 267-272.
22. B. H. Toby and R. B. Von Dreele, *Journal of Applied Crystallography*, 2013, **46**, 544-549.

3. LOCAL STRUCTURE AND PHASE TRASITIONS OF $BaTiO_3$ AT VARYING TEMPERATURE.

3.1 Introduction

3.1.1 Average Structure of $BaTiO_3$

Barium Titanate ($BaTiO_3$, BTO) has been one of the most studied materials since the discovery in 1945 of its ferroelectric behaviour.[1] Upon its initial discovery it was found that it had a dieletric constant more than ten times greater than other known ceramics. This high dielectric constant, coupled with low loss characteristics has led to $BaTiO_3$ being used in various electronic devices. It can be found in, amongst other things capacitors and thermistors.

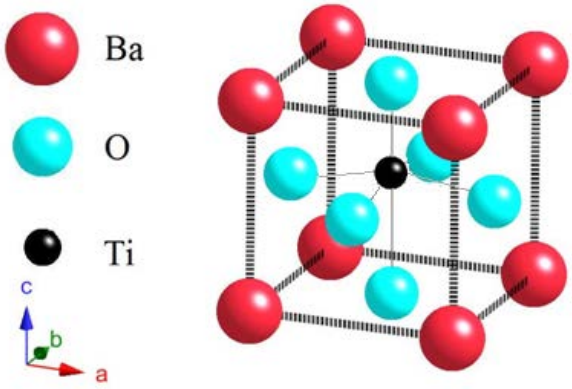

Figure 3.1: Unit cell of the average tetragonal structure of $BaTiO_3$.

Despite being widely used in electronic devices and extensive research, there is still debate on the nature of the local structure of $BaTiO_3$. At ambient conditions, it possesses the ABO_3 perovskite structure.[2] An ideal perovskite structure has a cubic lattice with the A atoms at the corners of the unit cell, B atoms at the body centre and oxygen atoms which are face centred. Megaw (1945) conducted the first detailed study of the structure of $BaTiO_3$ using powder x-

ray diffraction (pXRD) and showed that $BaTiO_3$ possesses a tetragonal structure (*P4mm* space group) where a = 3.986Å and c = 4.026Å (Figure 3.1).[3]

It is accepted that $BaTiO_3$ possesses several different phases over a range of temperatures and each of these phases shows a particular dielectric behaviour. As temperature decreases, the average structure becomes orthorhombic between 278 and 183K and then finally rhombohedral below 183K.[4] Above 393K, $BaTiO_3$ undergoes a ferroelectric to paraelectric phase transition to a cubic structure (Figure 3.2).

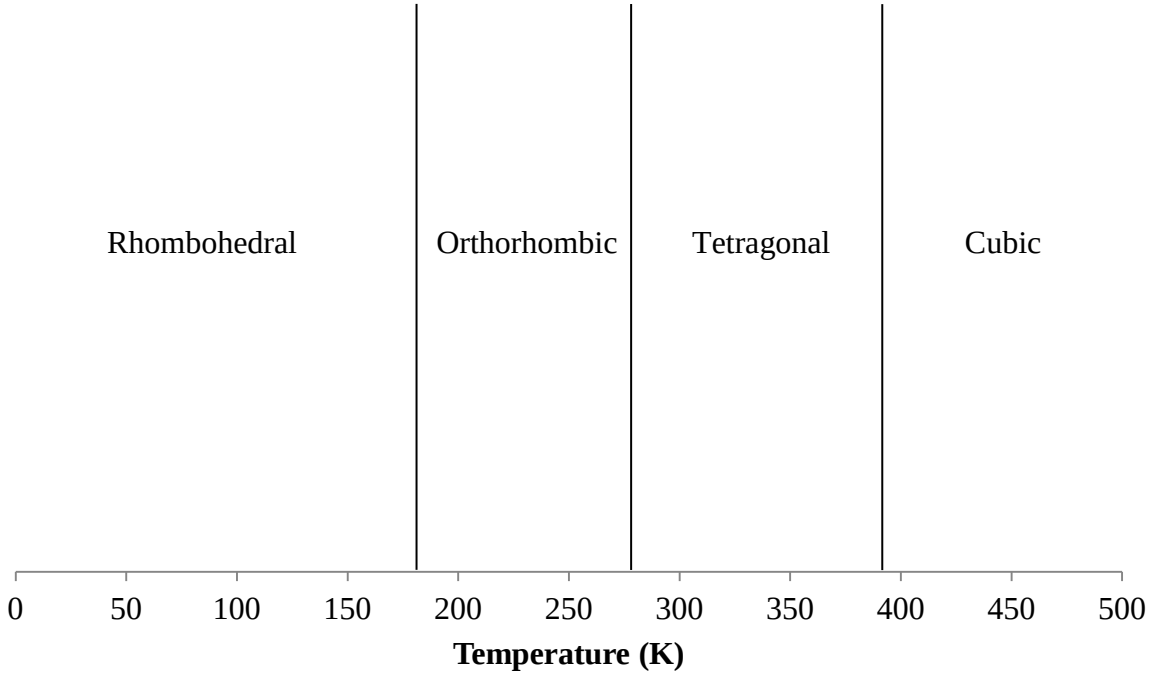

Figure 3.2: Temperatures of the phase transitions of $BaTiO_3$.

Each of these average structures is a result of a distortion of the cubic unit cell. pXRD shows that in the rhombohedral phase the Ti is displaced along [111], in orthorhombic along [011] and in tetragonal along [001]. These distortions arise due to the displacement of the Ti^{4+} cation from the centre of the oxygen octahedra, giving rise to spontaneous polarisation (Figure 3.3).[5]

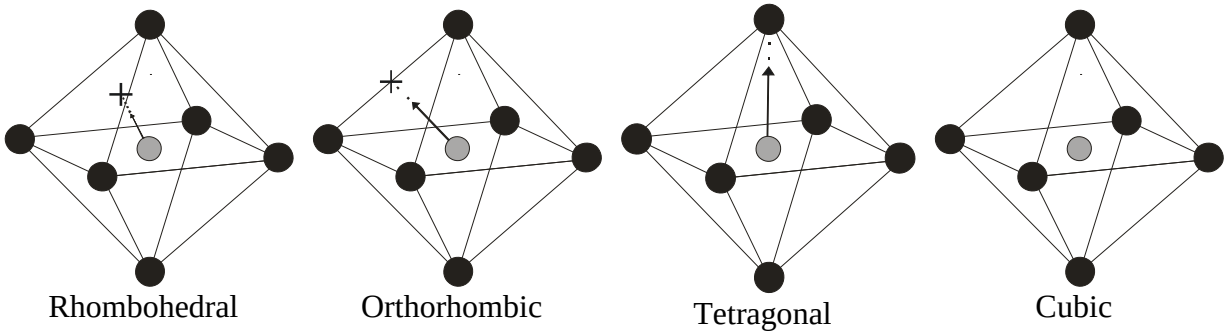

Figure 3.3: Fragments of the average structures of $BaTiO_3$.

3.1.2 Local Disorder in $BaTiO_3$

As mentioned in Section (1.2), techniques such as Rietveld analysis of x-ray diffraction data of Bragg peaks only consider the long range average structure of crystals. Diffuse scattering of x-rays was observed in diffraction patterns of $BaTiO_3$ at room temperature suggesting that the ambient structure is partially disordered.[6] This diffuse scattering (Section 1.3) was also observed in electron scattering, adding weight to the theory that $BaTiO_3$ contains local disorder.[7] Diffuse scatter is not observed in the rhombohedral phase however, indicating that this phase is perfectly ordered. This led to Comes *et al* (1968) suggesting that the Ti atom is locally displaced in one or more of the [111] directions at all temperatures and it is the ordering of these displacements (consisting of eight potential off-centre sites) that is different in each phase.[8] As shown in Figure 3.4, in the tetragonal phase four of the eight sites would be occupied to give the observed tetragonal symmetry.

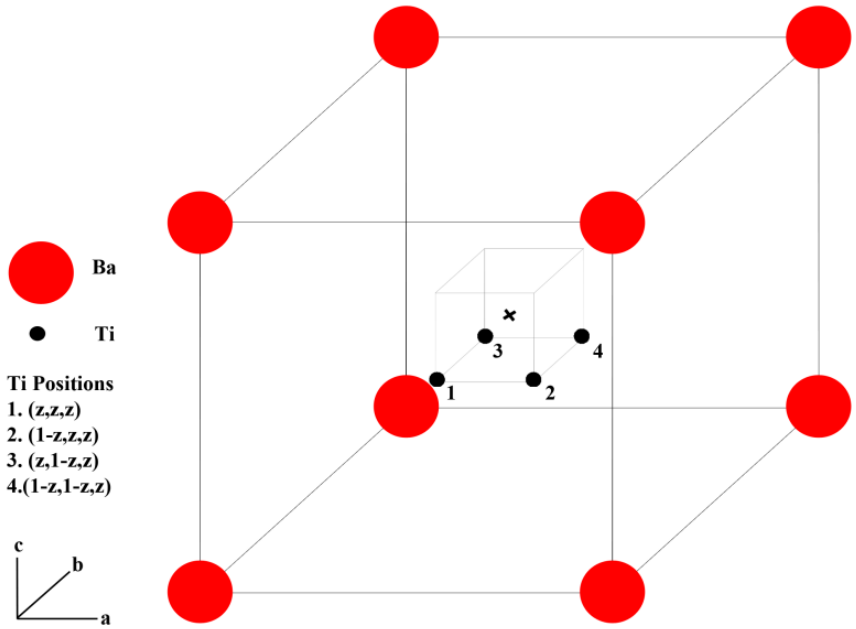

Figure 3.4: Model of $BaTiO_3$ used for modelling the tetragonal phase in an "eight-site" system. For clarity, oxygen atoms have been excluded from the diagram.

The eight-site model initially proposed by Comes was then discussed in more detail by Chaves *et al* (1976) who showed that this model was thermodynamically possible.[9]

Soon after the publication of the Comes model, Haranda and Honjo (1967) proposed that the observed x-ray and electron diffuse scattering could be explained by dynamic disorder due to low-energy phonons.[10] Shirane *et al* (1970) also supported this purely displacive model for the phase transitions in $BaTiO_3$ using inelastic neutron scattering.[11] Shirane *et al's* conclusions were later challenged by D. Heiman and S. Ushioda who were using Raman spectroscopy to investigate local structure.[12]

The Comes model has been subject to a lot of debate in the literature since its first proposal, a debate which has still not been resolved to this day. There are a large number of studies published in the literature, using a wide variety of experimental techniques, an attempt will be made to discuss some of the *"key"* techniques in turn.

The first technique to be considered is nuclear magnetic resonance spectroscopy (NMR), which is capable of investigating local structure by applying a magnetic field to nuclei and looking at the electromagnetic radiation that is emitted. The first NMR (^{137}Ba and ^{47,49}Ti) spectra of $BaTiO_3$ were reported by Forbes *et al* (1987) and since then there have been several studies on single crystal and polycrystalline $BaTiO_3$.[13] NMR studies have also shown evidence for the Comes model at ambient and variable temperature, in agreement with other techniques which will be discussed later. [14-17] In an initial study of single crystal $BaTiO_3$ Zalar *et al* (2003) suggested that there is dynamic tetragonal breaking of the cubic symmetry of the unit cell above T_c and also showed evidence for off-centre sites consistent with the Comes model of $BaTiO_3$.[18] However several authors cast doubt on the presence of tetragonal distortions in the cubic phase due to the time scales of NMR measurements.[15, 17] The observed tetragonal displacements could potentially have been time averaged from the eight-site model, with the Ti atom jumping between the available displacement sites. Ravel *et al* (2005) followed up their initial study suggesting that the tetragonal nanodomains could still be observed by NMR spectroscopy due the slow motion of the exchange between these tetragonal sites.[16] The "cubic" phase consists of a Comes model for Ti displacement along with small, randomly orientated tetragonal nonoclusters.[16] These order-disorder and displacive components in the cubic phase would explain why the electric field gradient (EFG) is non-zero. The Comes model of $BaTiO_3$ would result in a zero value for the EFG tensor.[16] These results suggest the co-existence of order-disorder and displacive components in the "cubic phase" and indicate a more complicated model for the local order/disorder in $BaTiO_3$ than what was suggested by Comes.

Other techniques that have been used to investigate the local structure of $BaTiO_3$ are x-ray absorption fine structure (XAFS) and x-ray absorption near-edge structure (XANES)

techniques. XAFS is a much faster measurement than NMR with an averaging time of 10^{-15} s in comparison to roughly 10^{-8} s for NMR spectroscopy.[15] Ravel *et al* stated that "it is sensitive to order below an Angstrom scale, thus directly measures local effects that are inaccessible to many other experimental techniques"[19], thus making it an ideal technique for investigating the local structure of $BaTiO_3$. By examining the extended XAFS region of the barium edge and the XANES region of the titanium edge Ravel *et at* showed agreement with the Comes model at all temperatures.[19] They also demonstrated the presence of dynamic "jumping" between the off-centre sites, as opposed to the static disorder suggested initially by Comes. The results also indicated that the displacement of the Ti atom in the "tetragonal" phase was not perfectly rhombohedral with the Ti atom displaced from the [111] direction by 12^{o} towards the *c*-axis.

Raman spectroscopy involves the inelastic scattering of monochromatic light, where the light interacts with molecular vibrations or phonons and leads to a shift in energy in the emitted light. The selection rules for Raman (and IR) spectra are based on group theory and in the cubic phase (O_h symmetry) all optical modes are forbidden. While the Raman spectra show the expected phase transitions over temperature, the Raman spectra of the high temperature "cubic" phase shows two forbidden broad bands which would be consistent with the Comes model. [20, 21]

3.1.3 Previous PDF Studies of $BaTiO_3$ at Variable Temperatures.

Finally there have been several previous studies that utilised total scattering to investigate the local structure of $BaTiO_3$ at both ambient and variable temperature.[22-28] There is strong evidence that the local structure of $BaTiO_3$ is affected by particle size so PDF analysis of nano-BTO is not discussed in this Section.

A comprehensive variable temperature study was conducted by Kwei *et al* (1995) using neutron PDF (nPDF) and a Q_{max} of 25^{-1}Å.[5] They did not make any firm conclusions based on both fitting theoretical models to experimental data and simply examining the first Ti-O peak (~2Å). The lack of firm conclusions was attributed to the poor resolution of this peak. The resolution could be improved by collecting neutron diffraction data to a higher value of Q_{max} (Section 1.5.l). They did however state that the shape of the Ti-O peak for the orthorhombic phase at 190K closely resembled the same peak in the rhombohedral phase, potentially in agreement with a pure order-disorder model. Despite this the orthorhombic-to-tetragonal (O-T) transition was not as clear with the Ti-O peak not resembling that from a rhombohedral distortion above or below this transition.[23] The shape of this first Ti-O peak has also been discussed by Laulhe *et al* (2009). [26] Using a nPDF produced from a Q_{max} of $23.4Å^{-1}$, they observed a poor fit on the Ti-O peak using a tetragonal model. While there was evidence of local rhombohedral distortions, the resolution of this peak was deemed too low to draw firm conclusions. This was particularly true when trying to investigate the proposed dual component model of Ravel (1998).[19]

RMC modelling of partial x-ray PDFs for "cubic" and "tetragonal" phases have provided further evidence for dynamic tetragonal displacements in the Ti atom in the paraelectric phase.[24] Furthermore this analysis found no evidence of static tetragonal displacements in the ferroelectric phase.

Page *et al* (2010) later presented a PDF of $BaTiO_3$ produced from neutron diffraction and a $S(Q)$ of $Q_{max} = 30Å^{-1}$ resulting in better resolution of the first Ti-O peak than in previous studies.[29] They again demonstrated that a rhombohedral displacement of the Ti atom better described the first Ti-O peak. There was no detailed analysis of this peak however due to the main focus of the study being on nano-$BaTiO_3$.

X-ray PDFs have been shown to have poor sensitivity to the Ti-O peak, making them less desirable for investigating local structure.[27] This has been further emphasised by Laulhe *et al* (2009) who stated that it was not possible to investigate the true local displacements of the Ti atom without the first Ti-O peak. This assertion was based on an excellent agreement between a tetragonal model and experimental data on data refined above 3.5Å. It is not clear however, what r_{max} Laulhe *et al* utilised when considering *Rw* values to give indications on local structure. While Yoneda and Kohara (2009) did not observe the first Ti-O peak using x-ray PDFs from a Q_{max} of 25Å^{-1}, they were still able to deduce that there is "remarkable" difference between the short- and long-range order of $BaTiO_3$ at various temperatures.[27]

3.1.4 Summary

There have been many studies of the local structure of $BaTiO_3$, using a wide variety of techniques over many years. It is clear from these various studies that the Comes model has a certain degree of validity at all temperatures. Despite this it is also apparent that this model may be too simplistic in order to accurately describe the true local structure of $BaTiO_3$ at all temperatures. For this reason, despite the vast number of studies, these issues remain an area of debate and further investigation is required.

3.2 xPDF

3.2.1 Experimental Set Up

The sample of $BaTiO_3$ for use in the xPDF study was provided by Neil Hyatt, Professor of Nuclear Materials Chemistry at the University of Sheffield.

The data were collected at the Advanced Photon Source (APS) in Chicago at beamline 11-ID-B. A flat panel area detector based on an amorphous silicon (a-Si) array was used to obtain the high energy x-ray scattering and a wavelength of 0.1370Å (90KeV) was used. A kapton

tube 1mm in diameter was used as the sample container and variable temperatures were achieved by using an *Oxford Cryosystems Cryostream 700 plus* that can operate between 80K and 500K. The sample to detector distance was 211.224 mm which at 90 KeV allowed for a useable Q_{max} of 27Å^{-1} in the Fourier transform of the *S(Q)*. This value of Q_{max} is comparable to previous PDF studies using both neutron and x-ray scattering data (Section 3.1.3).

The cryostream gas flow was cooled to 100K and allowed to dwell for 15 minutes before collecting data. The cryostream continuously ramped up at 240K an hour from 100K to 500K and 120 images were collected over this time. Each image produced was a result of 120 x 0.5 second exposures summed together, resulting in a total collection time of one minute for each temperature recorded. The images were then integrated using the same mask and then these integrated images were then inputted in PDFGetX2 in order to produce the PDF for each temperature. PDFGui was then used to refine models to the experimental data.

3.2.2 Refinement Approach

Due to the relative ease of being able to sequentially fit a model to a temperature series, it was possible to relatively quickly fit each model of $BaTiO_3$ to the whole temperature series. The four average structures of BTO were fit (Section 3.1.1) along with disordered tetragonal and cubic models based on an eight-site model of $BaTiO_3$.

For the disordered tetragonal model, four quarterly occupied Ti sites at (*z,z,z*), (*1-z,z,z*), (*1-z,1-z,z*) and (*z,1-z,z*) were used (as depicted by Figure 3.4). In the disordered cubic model eight Ti sites equally occupied within a cubic unit cell were used. All these sites were linked so that each Ti site was equally displaced away from the centre of the unit cell. For each model the refined parameters can be seen in Table 3.1.

Table 3.1 Refined parameters for each model of BTO.

	Cubic (Pm-3m)	**Tet** (P4mm)	**Ortho** (Amm2)	**Rhom** (R3m)	**Dis-Tet**	**Dis-Cubic**
	Scale Factor Delta 1 a $Ba\ U_{iso}$ $Ti\ U_{iso}$ $O\ U_{iso}$	*Scale Factor Delta 1 a c Ti z* $Ba\ U_{iso}$ $Ti\ U_{iso}$ $O\ U_{iso}$	*Scale Factor Delta 1 a b c Ti z* $Ba\ U_{iso}$ $Ti\ U_{iso}$ $O\ U_{iso}$ $O\ U_{iso}$	*Scale Factor Delta 1 a α Ti (z,z,z)* $Ba\ U_{iso}$ $Ti\ U_{iso}$ $O\ U_{iso}$	*Scale Factor Delta 1 a c Ti (z,z,z)* $Ba\ U_{iso}$ $Ti\ U_{iso}$ $O\ U_{iso}$	*Scale Factor Delta 1 a Ti (z,z,z)* $Ba\ U_{iso}$ $Ti\ U_{iso}$ $O\ U_{iso}$
Refined Parameters	6	8	9	8	8	7
Fixed Parameters	*qdamp*	*qdamp O1 z O2 z*	*qdamp O1 z O2 x O2 y*	*qdamp O x O y*	*qdamp O1 z O2 z*	*qdamp*

There are several different refinement approaches that were taken when attempting to analyse the variable temperature xPDF data in PDFGui. An attempt will now be made to explain and justify the final approach that was taken, results from an alternative refinement approach is presented in Appendix 2.

The value of *qdamp* (Section 2.3.1) was obtained by refining a tetragonal model of BTO to the data collected at 300K (over the full r-range produced e.g. 2.2 to 50Å), this value was then fixed for each model at all length scales and temperatures.

In PDFGui it is possible to set up a refinement approach (length scale, refined parameters, fixed parameters, model etc) and then use a macro to sequentially fit a data series using the initial approach. Refinements at any given temperature start from the results of previous temperature's and then the results were checked to ensure no refinements were caught in false

minima. Sign of a false minimum are high *Rw* values and/or identical refinement results from the previous temperature (there will always be a small variation no matter how small).

Initially oxygen positions were refined for all models but it was found that the O1 position in the orthorhombic model was moving far from its ideal position at all temperatures (Figure 3.5). This was also the case in the temperature region where we would expect the average structure to be orthorhombic (183 -273K).

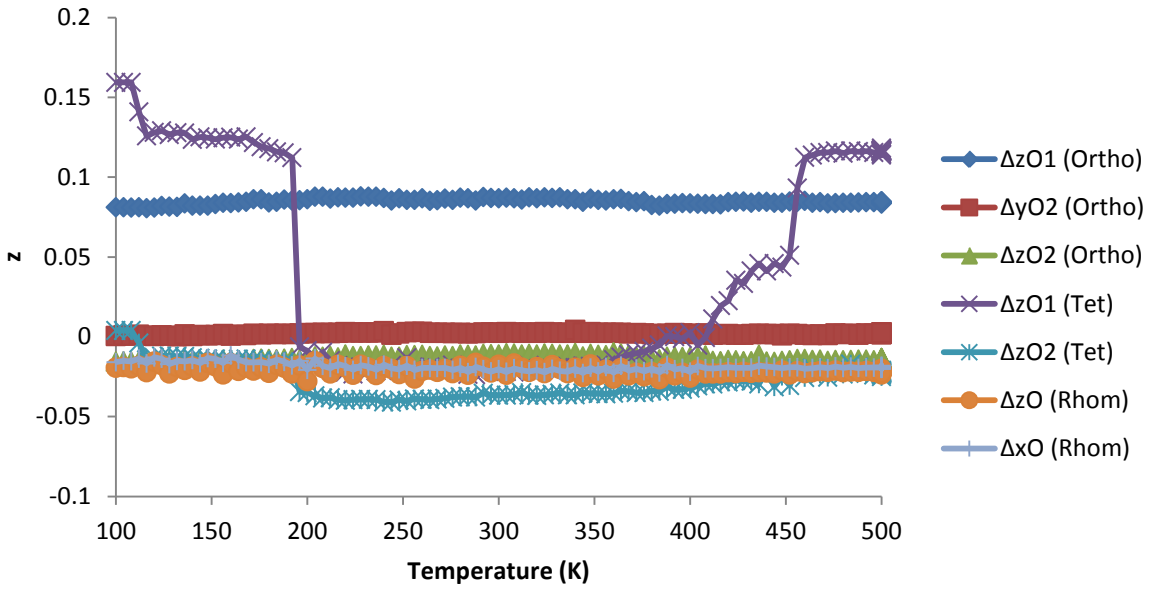

Figure 3.5: Refined oxygen positions from 100 to 500K using xPDF data between 2.5 to 50**Å**.

When oxygen positions from the literature powder neutron diffraction refinement values[5] were used (and not allowed to refine), the fit became worse so the fits of the two different refinement approaches (oxygen positions fixed and refined) were compared on a PDF produced from BTO at 200K (Figure 3.6a and b).

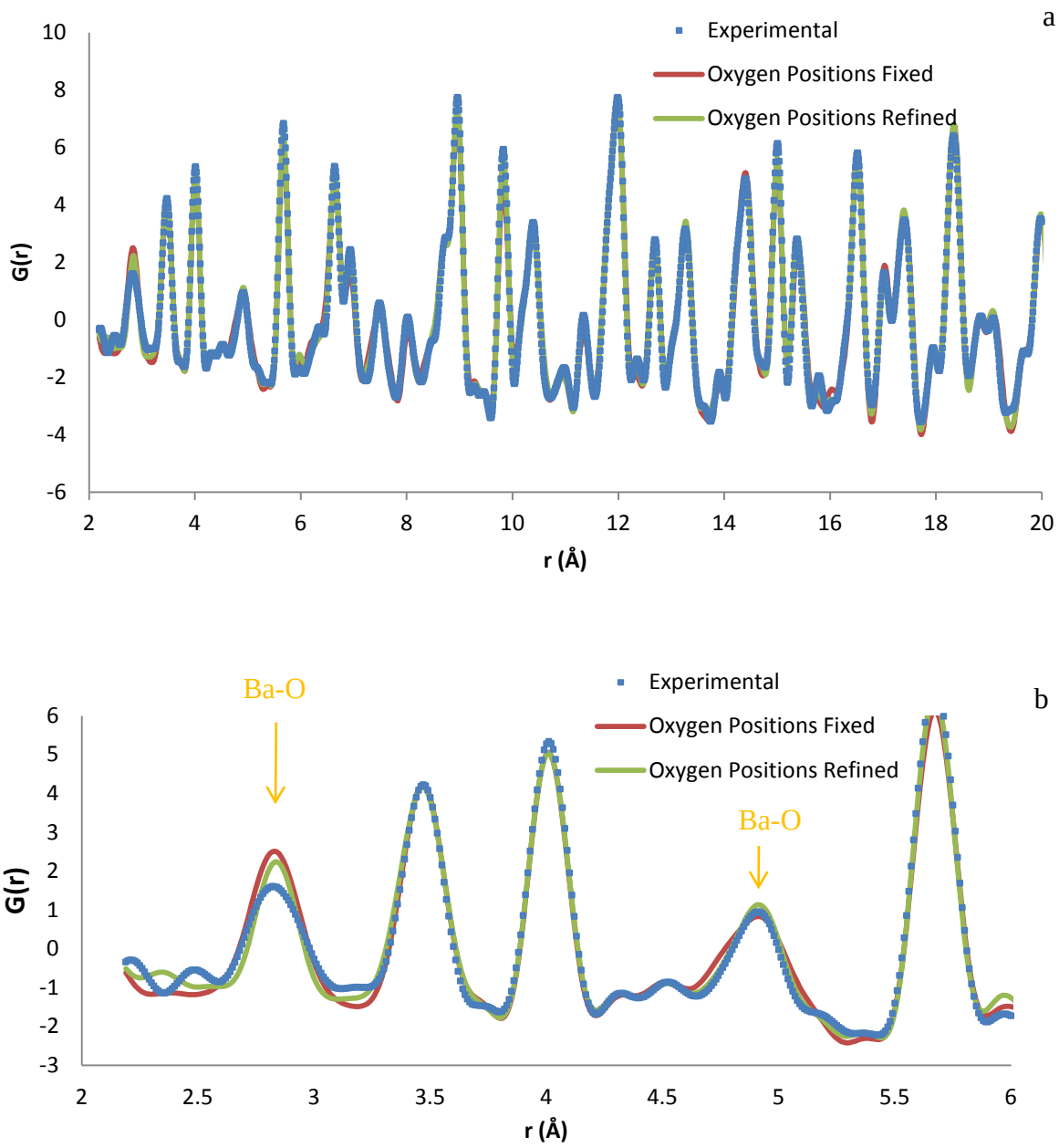

Figure 3.6a.and b Orthorhombic fits of two approaches to the experimental data from 2.2 to 50Å.

It is seen from Figure 3.6b that the orthorhombic fit to the Ba-O peak at ~4.9Å is much improved when oxygen positions are allowed to be refined, while the width of the first Ba-O peak is clearly incorrect with the atomic displacement parameter for the oxygen atoms ($0.0010Å^2$) reduced in comparison to fixing oxygen positions ($0.0263Å^2$) (value taken from Appendix 2).

With previous studies not reporting the orthorhombic *O1* position as displaced as our refinements, it was important to investigate the partial PDFs calculated from the PDFGui refinements (Figure 3.7). This was done to investigate the contribution of oxygen-atom distances to the overall PDF (2.2 to 50Å).

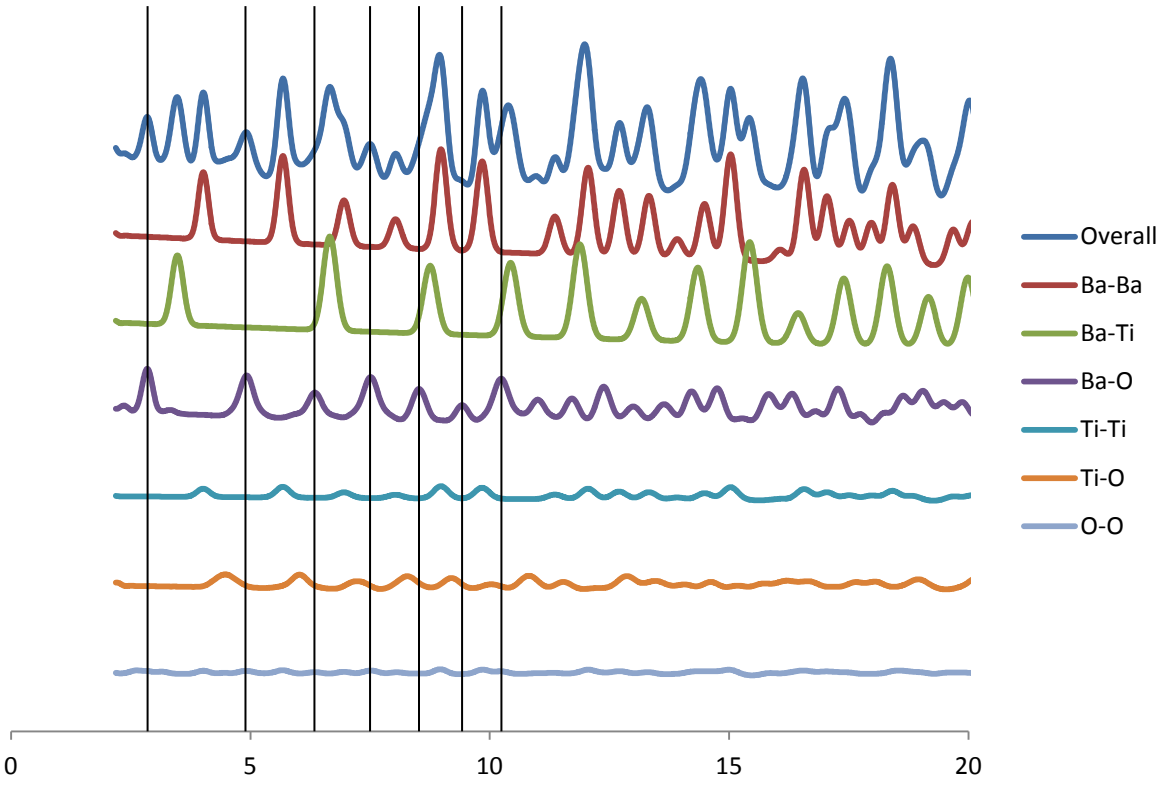

Figure 3.7: Calculated partial PDFs from a tetragonal model of BTO at 300K.

It is clear that Ba-atom distances dominate the PDF pattern, which is due to the relative scattering power of Ba in comparison to Ti and O. It is clear from looking at the partial PDFs that with the exception of the Ba-O peaks at ~2.7 and 4.9Å that the Ba-Ba and Ba-Ti distances dominate the PDF pattern. With this in mind, coupled with the *O1* position observed in the orthorhombic refinement and the fact the other models did not indicate any major deviations in oxygen positions, it was decided to fix oxygen positions for models at all temperatures and

length scales (Table 3.1). Also it was decided to give all three oxygens in the unit cell the same ADPs as there should not have been too much variation.

The first Ti-O peak is not observed in the PDF pattern and as seen from Figure 3.7b PDFGui was attempting to refine the artificial ringing in the PDF at ~2Å as the Ti-O peak. To ensure this was not affecting results, the PDFs were terminated at a r_{min} of 2.5Å.

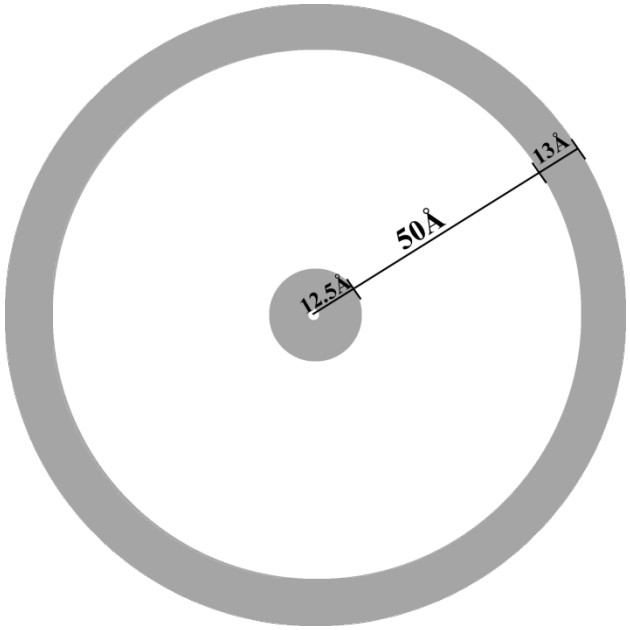

Figure 3.8: Representation of the different length scales refined in PDFGui (not to scale).

With a wide *r* range available for refinement it was decided to pick two arbitrary ranges to define “local structure” and “long range structure” (Figure 3.8) . In the absence of the first Ti-O peak, local structure was defined as 2.5 to 13Å (~3 unit cells excluding body diagonals), with long range structure being defined as 37 to 50Å. The long range refinements represent atoms between 37 and 50Å away from each atom in any given unit cell. At these length scales there are many overlapping atom-atom distances and the total amount of reciprocal space is much greater than the short range data (there are many more unit cells in the radial sample).

There are more data points available for refinements from 2.5 to 50Å, so thermal parameters were fixed from these refinements for use in refinements at long and short range. With uncertainty in the exact local structure of BTO it was important to limit the degrees of freedom available so that PDFGui did not create unrealistic models to fit the experimental data. It was decided that fixing thermal parameters in this fashion produced the most reliable refinement results at short and long range.

At longer ranges, the effect of correlated motion is negligible, so no corrections were used to model correlated for this effect in the long range refinements.

3.2.3 xPDF Results and Discussion

3.2.3.1 Refinements on Data from 2.5 to 50Å

As discussed in Section 3.1.3, *Laulhe* (2009) suggested that the first Ti-O peak was essential when investigating the local structure of BTO using nPDF. Despite this assertion *Yoneda and Kohara* (2009) stated that there was difference in the local and long range structure in the PDF patterns. As a result xPDF refinements were conducted of variable temperature diffraction data at different length scales.

The six models of BTO outlined in Table 3.1 were fit to xPDFs produced from diffraction data collected between 100 and 500K. There were numerous problems fitting the disordered cubic model to the data at all length scales and temperatures, with refinements becoming stuck in false minima. As a result this model is excluded from the sequential fitting. All refined parameters for each model can be seen in Appendix 3. The *Rw* values for each of the models fit between 2.5 and 50Å are presented in Figure 3.9. At this length scale the PDF contains some information about the local structure (below ~13 Å) but the medium and long range data will dominate the refinements.

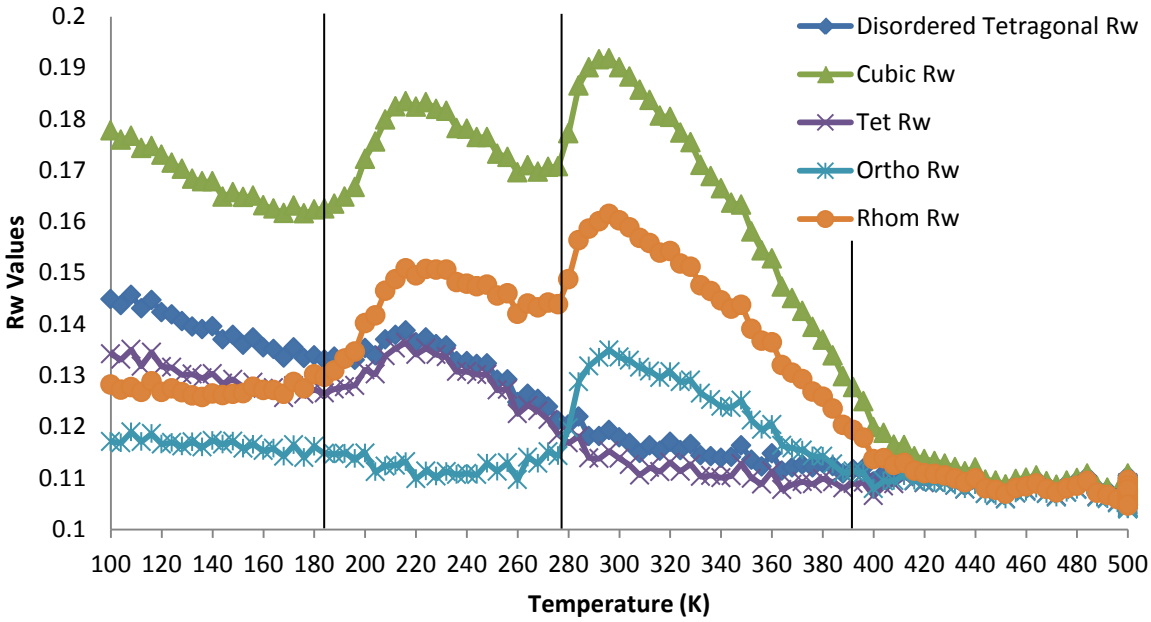

Figure 3.9: *Rw* values from xPDF refinements from 2.5 to 50Å for each theoretical model.

The model with lowest *Rw* value for the orthorhombic (183 to 278K) and tetragonal (278 to 393K) phases are as expected. Literature suggests that the rhombohedral model should best describe the experimental PDFs below 183K but this is not the case, with the orthorhombic model providing a better fit to the data. Fits of orthorhombic and rhombohedral fits to data collected at 100K can be seen in Figures 3.10 and 3.11.

The orthorhombic model continues to provide the best description of the experimental data until roughly 280K (the expected O-T transition temperature) where the tetragonal and disordered tetragonal model provide equally good fits.

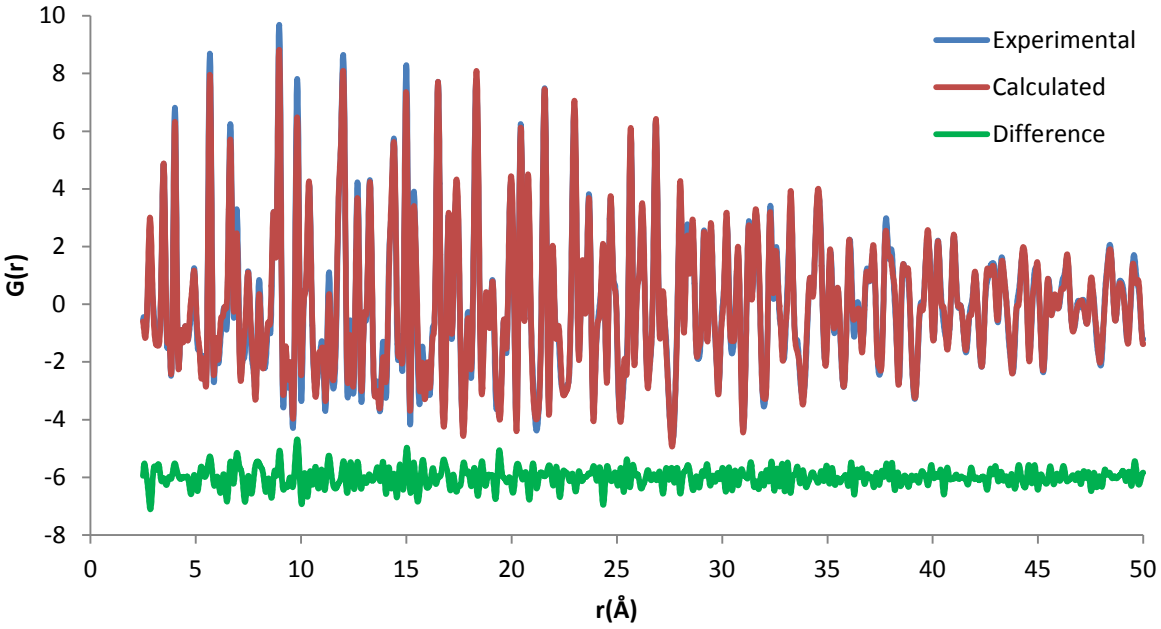

Figure 3.10: A rhombohedral model fit to experimental data of BTO at 100K between 2.5 and 50Å (*Rw* = 0.128).

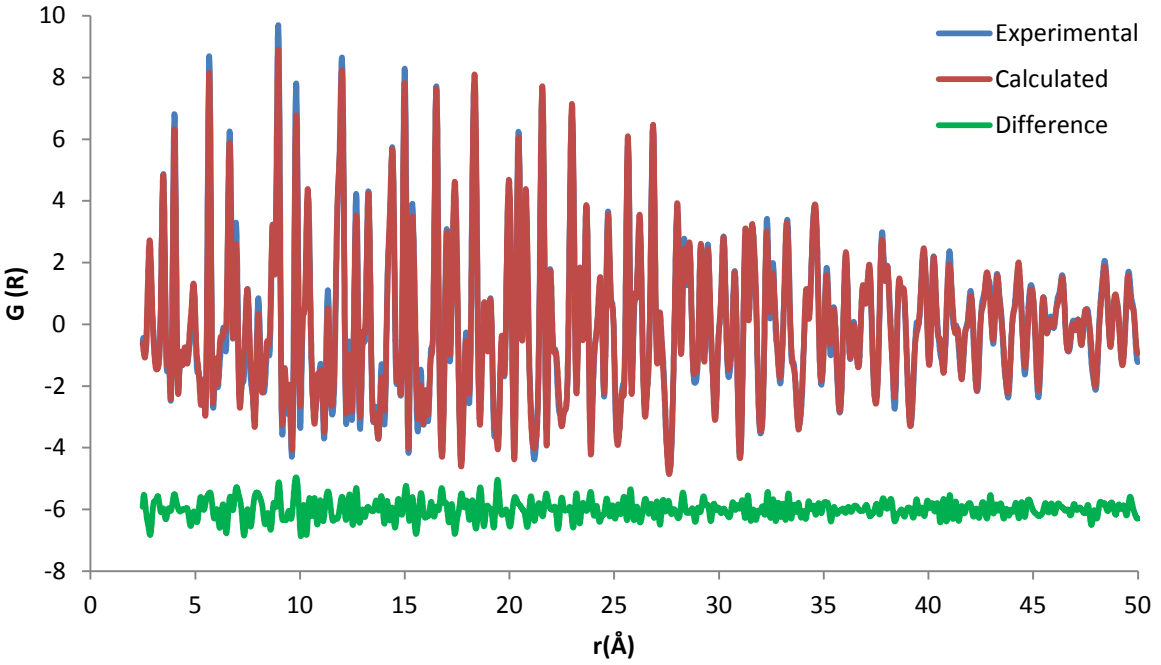

Figure 3.11: An orthorhombic model fit to experimental data of BTO at 100K between 2.5 and 50Å (*Rw* = 0.117).

Above the proposed T-C transition point (400K) the *Rw* for all models converge with each model providing an equally good fit. All the non-cubic models have the freedom to adopt a cubic structure ($a = b = c$ and Ti at 0.5,0.5,0.5) but this does not occur for any of these models, with the Ti atom still displaced above the phase transition point (Figure 3.12).

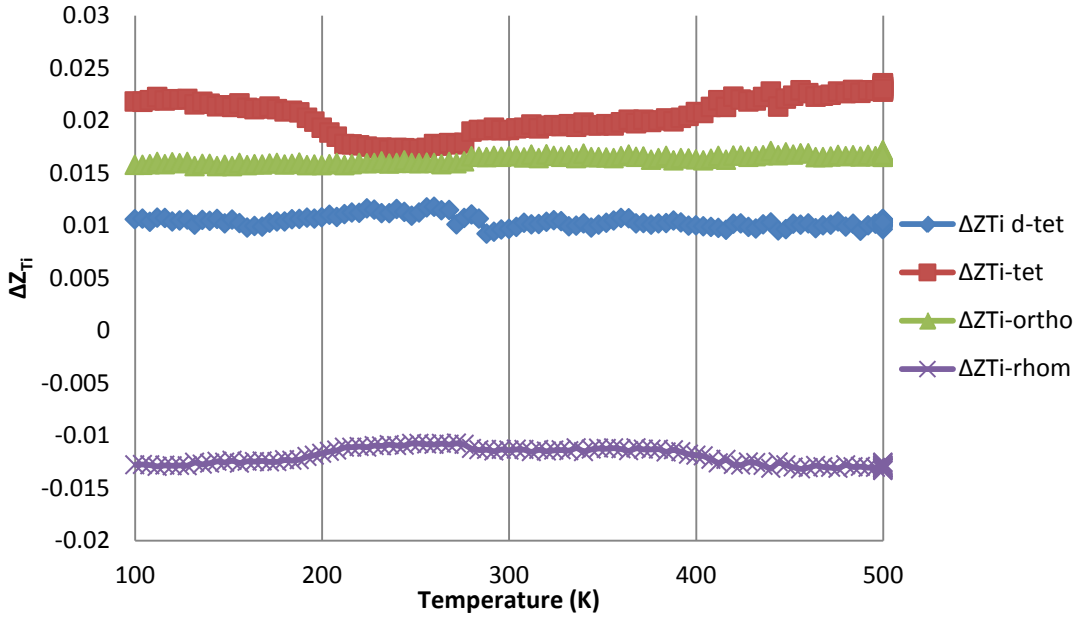

Figure 3.12: Δz_{Ti} for the rhombohedral (*z*,*z*,*z*), orthorhombic (*z*), tetragonal (*z*), disordered tetragonal (*z*,*z*,*z*) and disordered cubic (*z*,*z*,*z*) models.

While the Ti atom is still off-centre in the non-cubic models, as the cubic model has the fewest refined parameters (Table 3.1) and thus the fewest degrees of freedom in its refinement, it is possible to make the assertion that the cubic model best describes the experimental data above 400K (Figure 3.13).

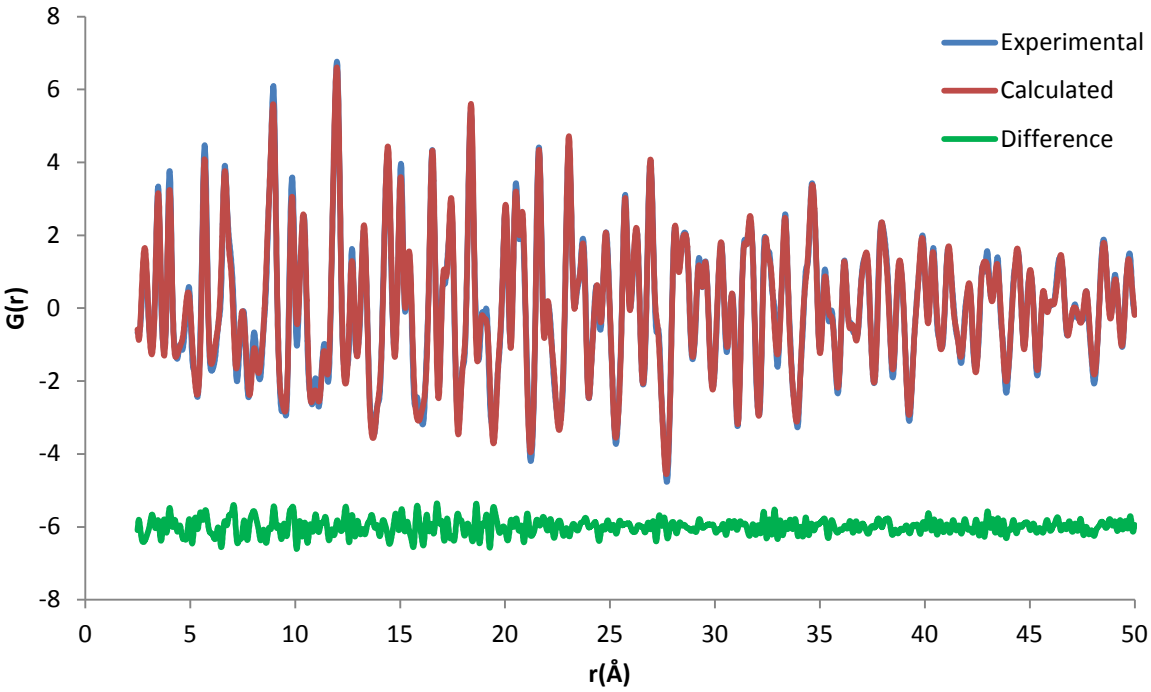

Figure 3.13: A cubic model fit to experimental data of BTO at 500K between 2.5 and 50Å (Rw = 0.106).

As mentioned previously, there were problems refining a disordered cubic model to the data with the Ti atom always remaining in the centre of the unit cell providing higher Rw values than the cubic model. Above the T-C transition point this was also true with the Rw values identical to the cubic fit meaning this model indicated that the Ti atom was not displaced above 400K. With most refinements stuck in false minima, with no change in any parameters it was not possible to refine this model to the experimental data.

With the refinements showing the orthorhombic, tetragonal and cubic phases in the expected temperature regions, the only anomaly is the fact that the rhombohedral model does not show the best fit to the data below 183K. This is unexpected as it is reported that there have been no reports in literature of diffuse scatter in the diffraction pattern of BTO below 183K, discounting the possibility of local disorder.

At these length scales (2.5 to 50Å) however, the PDF pattern includes information about both the short and long range structure and PDFGui will do its best to provide the best fit to the whole data range. As a result this length scale is not very useful for investigating local structure as the longer range data will affect refinement of peaks at low *r*.

3.2.3.2 Short Range Refinements (2.5 to 13Å)

In order to investigate short range structure, refinements were conducted on PDF data from 2.5 to 13Å (Figure 3.14). As mentioned in Section 3.2.2 the ADPs were fixed from the refinements on data from 2.5 to 50Å so each temperature had its own refined thermal parameters but these were not allowed to vary in the short range refinements, All the refined parameters can be found in Appendix 4 (along with fixed values of ADPs).

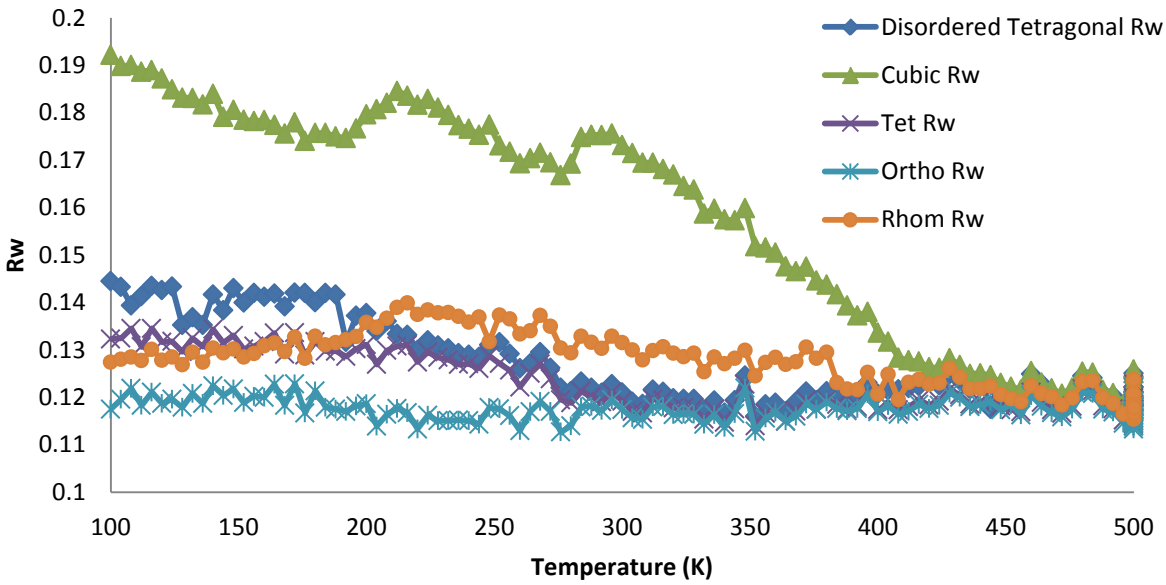

Figure 3.14: *Rw* values from refinements from 2.5 to 13Å for each theoretical model.

It is meaningless to compare *Rw* values observed in Figure 3.14 to 3.9, it is the relative *Rw* values of each model at the same length scale that are important. The orthorhombic model

still provides the best fit to experimental data below ~300K. The fits from both models to PDFs produced from data collected at 100K are presented in Figures 3.15 and 3.16.

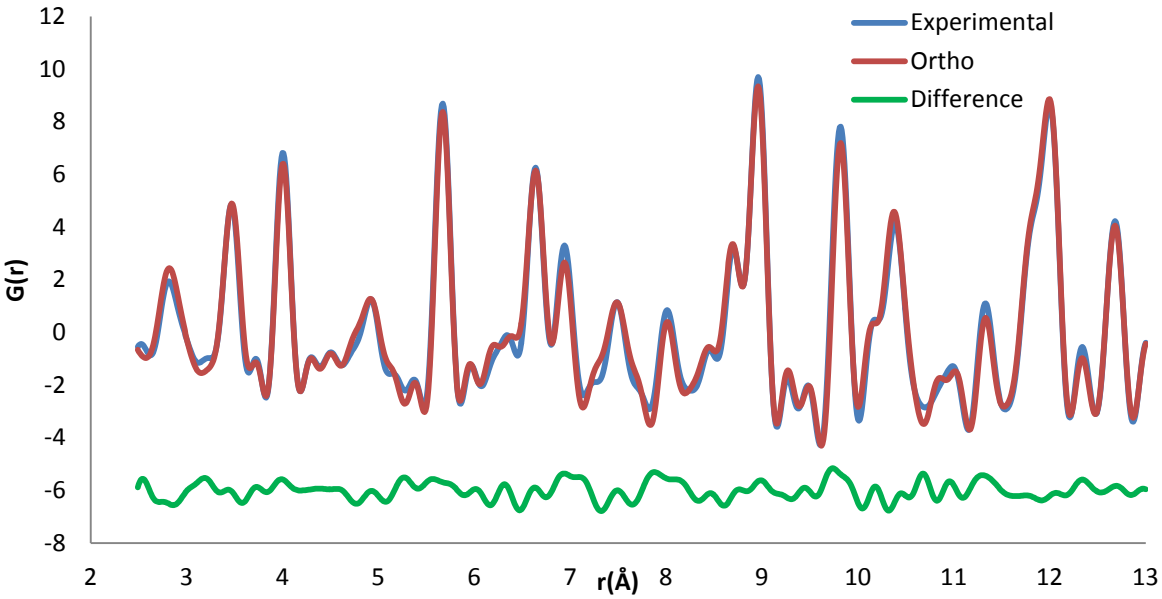

Figure 3.15: An orthorhombic model fit to experimental data of BTO at 100K between 2.5 and 13Å (*Rw* = 0.118).

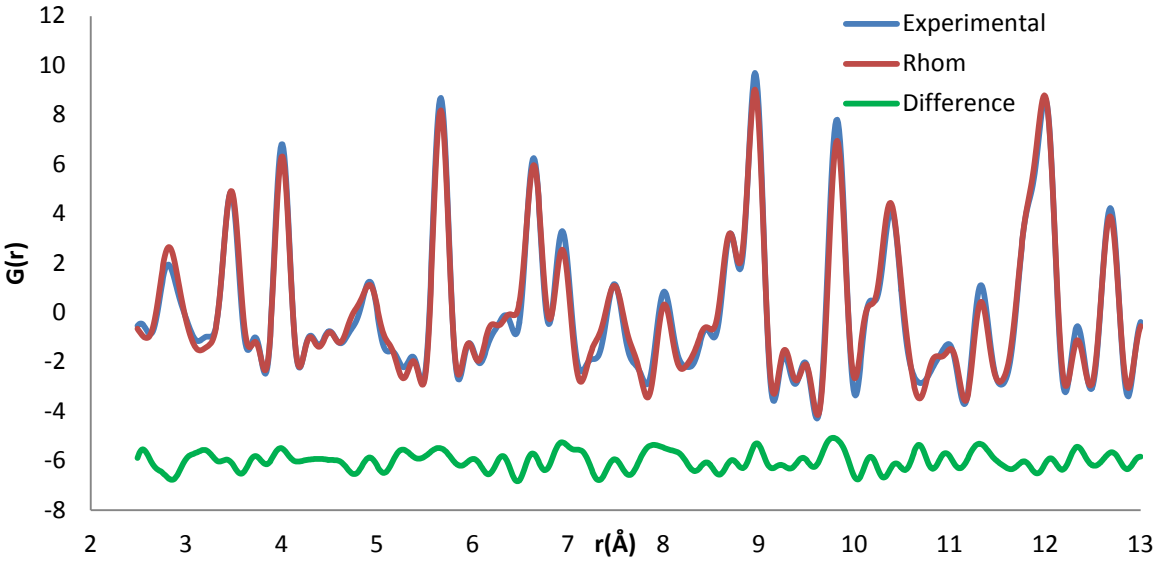

Figure 3.16: A rhombohedral model fit to experimental data of BTO at 100K between 2.5 and 13Å (*Rw* = 0.127).

It is clear that differences between the two fits are negligible, with small variations in fits providing more significant impacts on *Rw* values at this length scale due to the reduced number of data points. There is no evidence in literature for any disorder in the "rhombohedral" phase, so again the question is raised about the effect the number of refined parameters has on *Rw* values. With the orthorhombic model possessing the most number of refined parameters of all models (9 - taken from Table 3.1) it is possible that this leads to the best fits to the data. It is clear from diffraction data that BTO possesses rhombohedral unit cell at 100K so this would also cast serious doubt on the validity of this model describing the local structure at these temperatures.

Changes in *Rw* values across the whole temperature range are not as dramatic as seen in full data range refinements, apart from the cubic model. At first glance there appears to be slightly more variation between *Rw* values for each model above 400K. The *Rw* values for the respective models at 420K (an arbitrary value) are presented in Table 3.2. It was possible to obtain a disordered cubic refinement but once again the Ti atom sat in the centre of the unit cell ($Ti_z = 0.5004$).

Table 3.2: *Rw* values for each model of BTO refined against PDF data from 2.5 to 13Å at 420K.

Model	*Rw* Value
Cubic	0.126
Tetragonal	0.118
Orthorhombic	0.118
Rhombohedral	0.123
Disordered Tetragonal	0.124
Disordered Cubic	0.126

While there are no meaningful calculated ESDs, the work conducted in Section 2.3.2 suggests that these results may be within errors and thus essentially identical. For comparison, a tetragonal fit and a cubic fit (lowest and highest *Rw* respectively) from refinements at these length scales can be seen in Figures 3.18 and 3.19.

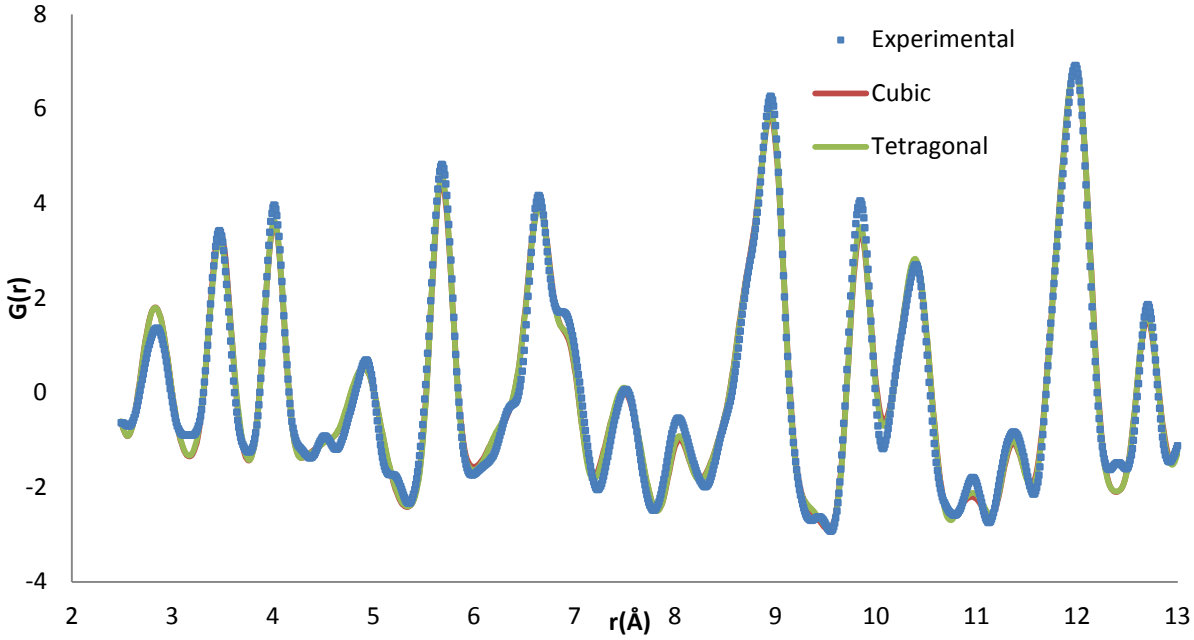

Figure 3.18: Comparison of Cubic and Tetragonal fits to xPDF of BTO at 420K.

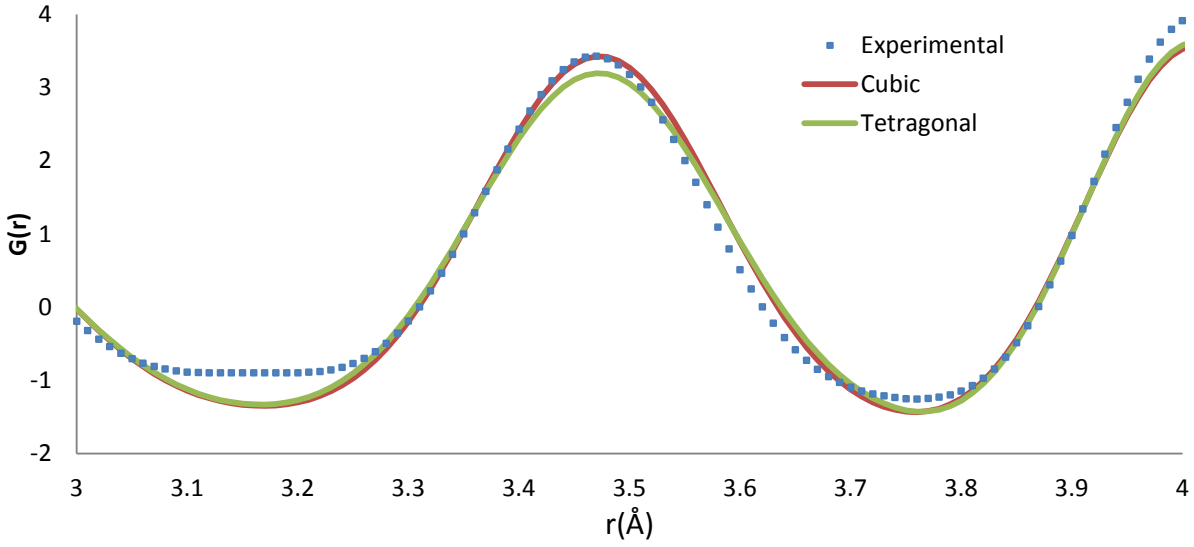

Figure 3.19: Comparison of Tetragonal and Cubic fits of the first Ba-Ti peak at 420K.

While fits appear essentially identical, in agreement with *Rw* values, there are still slight variations in fits for certain peaks. The first Ba-Ti peak should give an insight into the displacements of the Ti atom and it can be seen that the cubic model provides a better fit than the tetragonal model to this peak. This is perhaps unexpected but using the program Fityk (Section 2.3.3) it is possible to carry out peak fitting on individual peaks in the PDF patterns. It is clear from Figures 3.20 and 3.21 that a Ti atom displaced in the [111] direction better describes the shape of the first Ba-Ti peak than the Ti atom sat in the centre of the oxygen octahedra. As can be seen from Figure 3.20 and Table 3.3, the eight Ti distances are split into a ratio of 1:3:3:1.

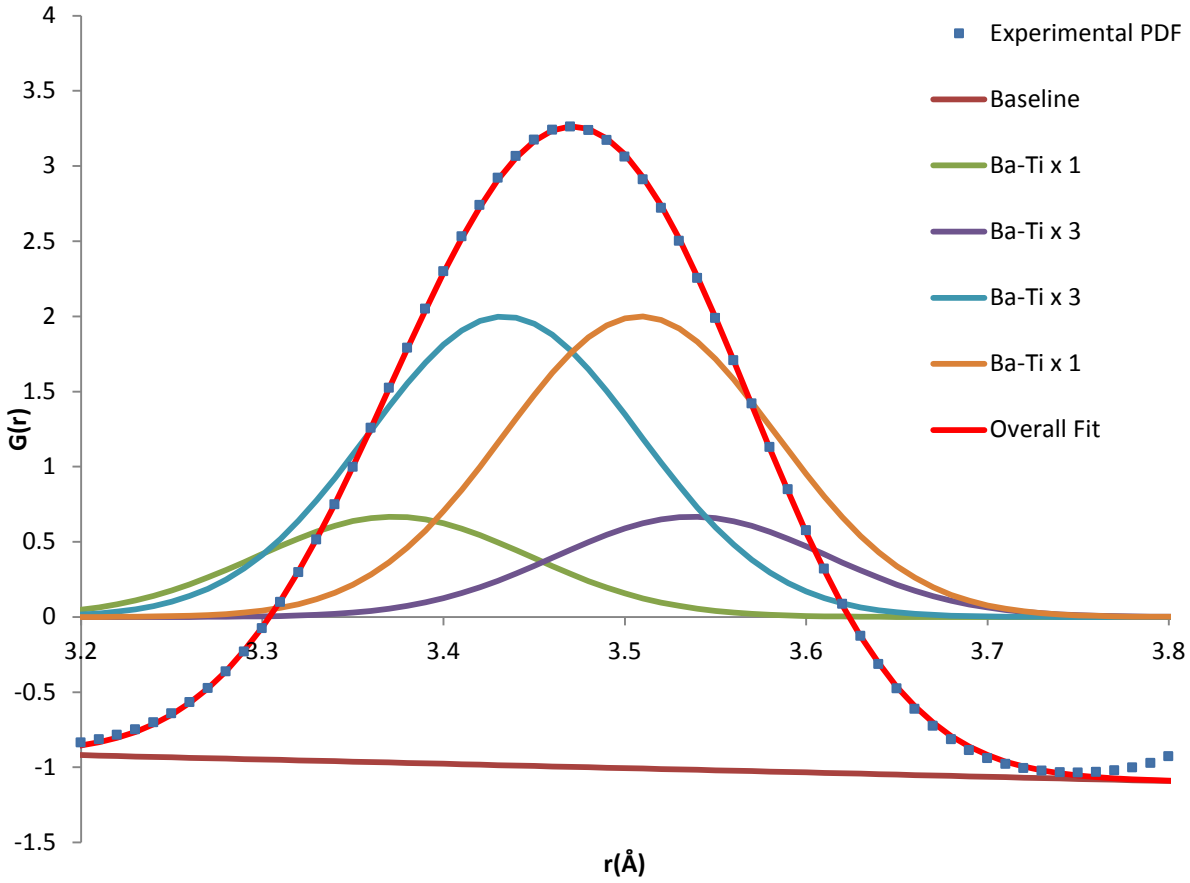

Figure 3.20: *"Rhombohedral"* peak fitting to the first Ba-Ti peak at 420K.

Table 3.3: Calculated peak positions for Figure 3.20.

Number of Ba-Ti distances	Peak Position (Å)
1	3.3749
3	3.4333
3	3.5100
1	3.5305

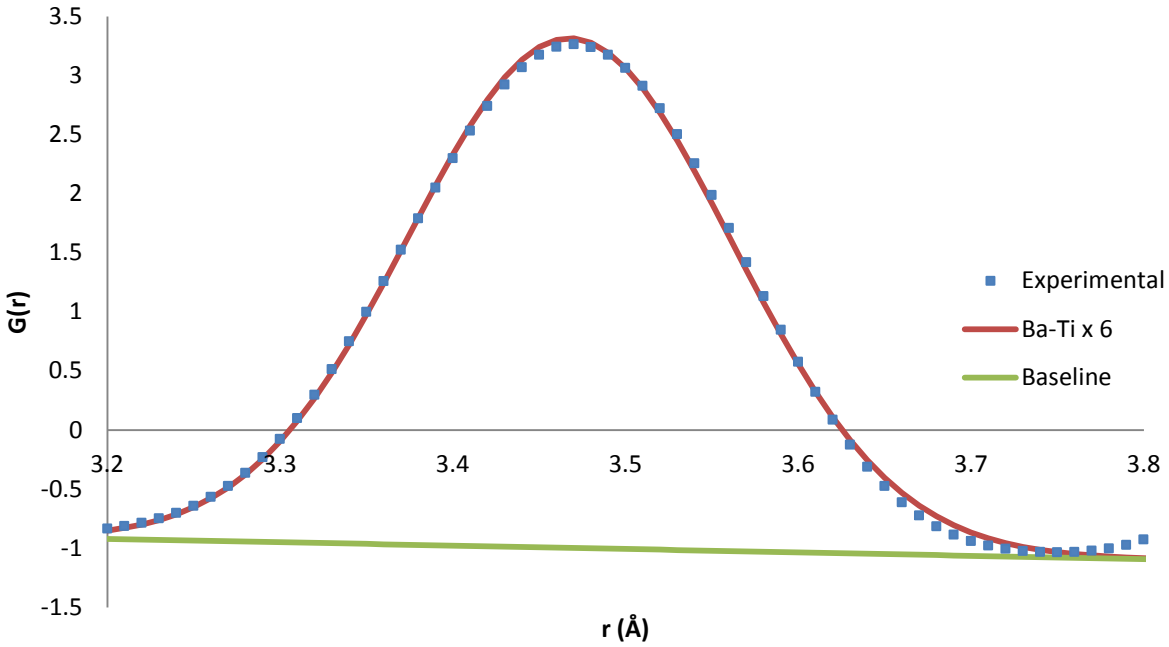

Figure 3.21: "*Cubic*" peak fitting to the first Ba-Ti peak at 420K.

While the intensities are set to the correct ratio and the FWHMs are identical (leading to the correct relative areas for each peak), the positions for each peak are not linked for the "*rhombohedral*" fitting. All the distances should be interconnected in this modelling. For example, if the Ti atom moves further off centre in the [111] direction then the shortening of one Ba-Ti peak will also equate in a lengthening of another. Furthermore the average of the two peaks with the same co-ordination number should give the same value and in this

instance it does not (3.4527Å vs. 3.4717Å). This shows that the peak fitting is not truly modelling a Ti atom displaced in the [111] direction but a method of linking the positions of each peak was not discovered. This obviously does not preclude there being a way of linking the peak positions relative to each other in Fityk.

A single peak was then fitted to the Ba-Ti peak above 400K to investigate the half width at half maxima (HWHM) (Figure 3.22). For comparison, the HWHMs of the first Ba-Ba/Ti-Ti peak at ~4Å were also investigated for comparison. ESDs are produced by fityk but with the baseline difficult to judge and affecting the ESDs they should be treated with caution.

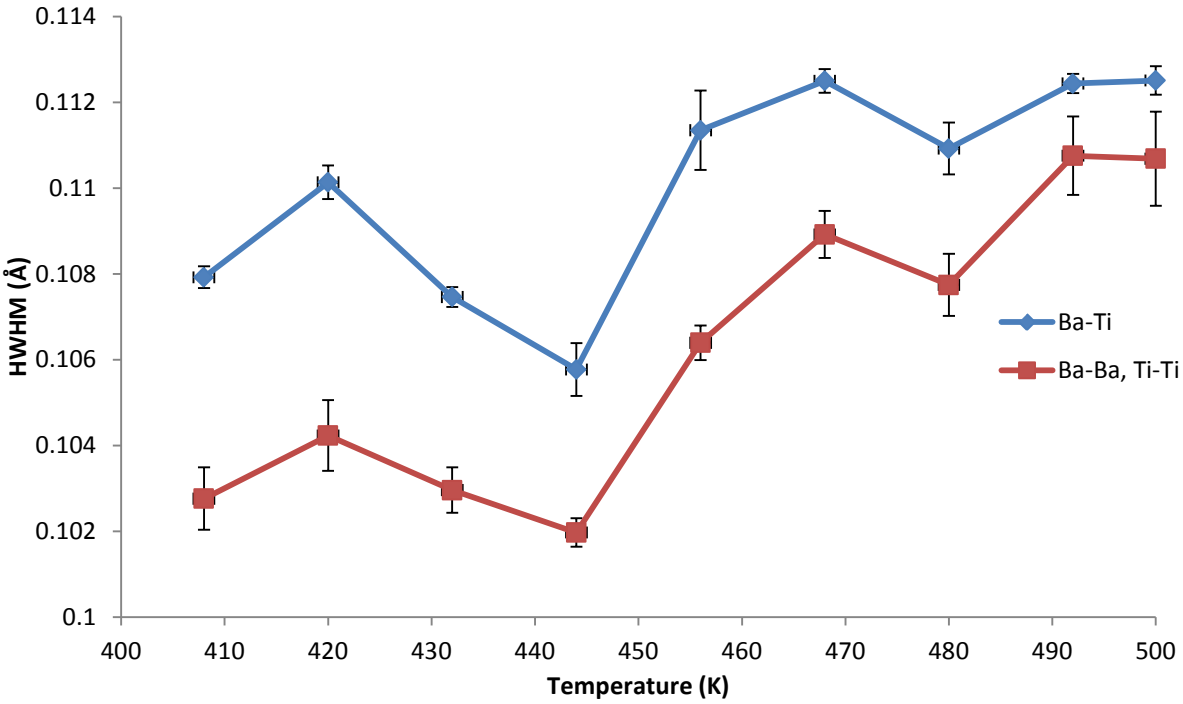

Figure 3.22: Peak fitting on the first Ba-Ti and Ba-Ba/Ti-Ti peaks for BTO over temperature (with ESDs for each data point).

As temperature is increased, the ADPs will increase, broadening the peaks. If the Ti-atom is becoming less displaced as temperature is increased, this will also affect the width of the Ba-

Ti peak however, with the distribution of distances decreasing and thus sharpening the peak (and *vice versa*).

The peak fitting is inconclusive, without reliable error bars it is impossible to make any firm conclusions although the difference between HWHMs for these two peaks appears to decrease as temperature increases. The major contribution to the peak at ~4Å will be the Ba-Ba distances within one unit cell, however there will be a contribution from Ti-Ti distances from one unit cell to the next, affecting the peak shape. The Ba-O peak was not modelled due to problems with termination ripples associated with the accessible Q_{min} in $S(Q)$ (Section 1.5.2).

When the Ti co-ordinates from refinements in PDFGui were examined it can be seen (Figure 3.23) they are comparable to the values produced from refinements over the full length scale.

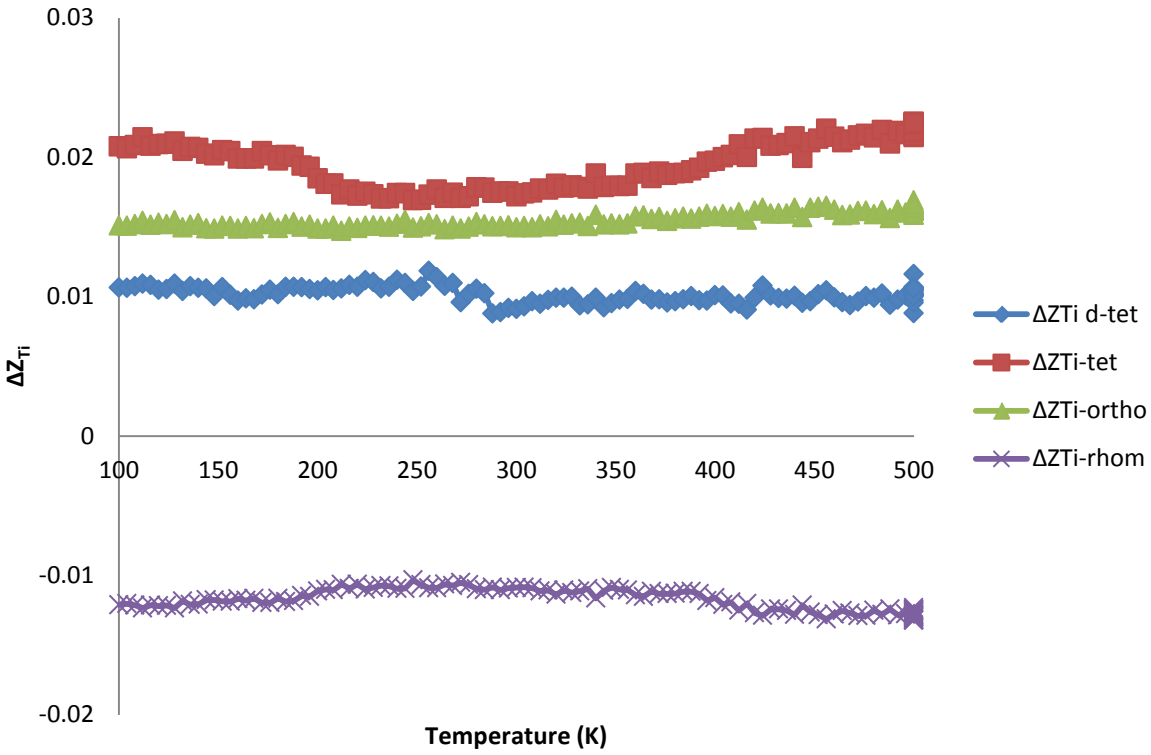

Figure 3.23: Δz_{Ti} for the rhombohedral (z,z,z), orthorhombic (z), tetragonal (z), disordered tetragonal (z,z,z) and disordered cubic (z,z,z) models.

Again the non-cubic models do not adopt cubic symmetry at any temperature and there are also no apparent trends in Ti co-ordinates over temperature.

3.2.3.3 Long Range Refinements (37 to 50Å)

In order to investigate long range structure, refinements were conducted on PDF data from 37 to 50Å (Figure 3.24). As discussed in Section 3.2.2 the ADPs were fixed from the refinements on data from 2.5 to 50Å so each temperature had its own refined thermal parameters but these were not allowed to vary in the short range refinements. All parameters can be found in Appendix 5.

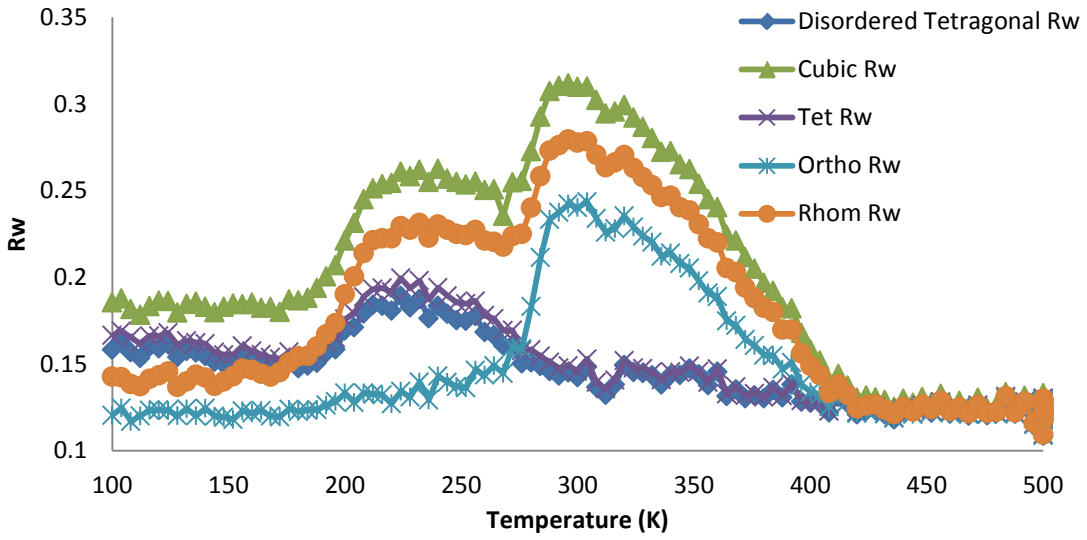

Figure 3.24: *Rw* values from refinements from 37 to 50Å for each theoretical model of BTO.

Long range refinements show more dramatic changes in *Rw* with temperature in comparison to Figure 3.9, with suggested phase transitions being indicated by the *Rw* values, with the exception of below 183K. The rhombohedral model still does not best describe the structure below this temperature which would give more evidence to this phenomena being attributed to the orthorhombic model possessing more refined parameters. This length scale (37 to 50Å) represents a more averaged view of the structure of BTO, which Rietveld shows possesses a

rhombohedral structure. Disordered-tetragonal and tetragonal models show very similar *Rw* values and provide the best fit to the longer range data in the expected tetragonal region 273 to 400K). Once again *Rw* values converge above 400K, but non-cubic models once more do not adopt cubic symmetry above this temperature (Figure 3.25).

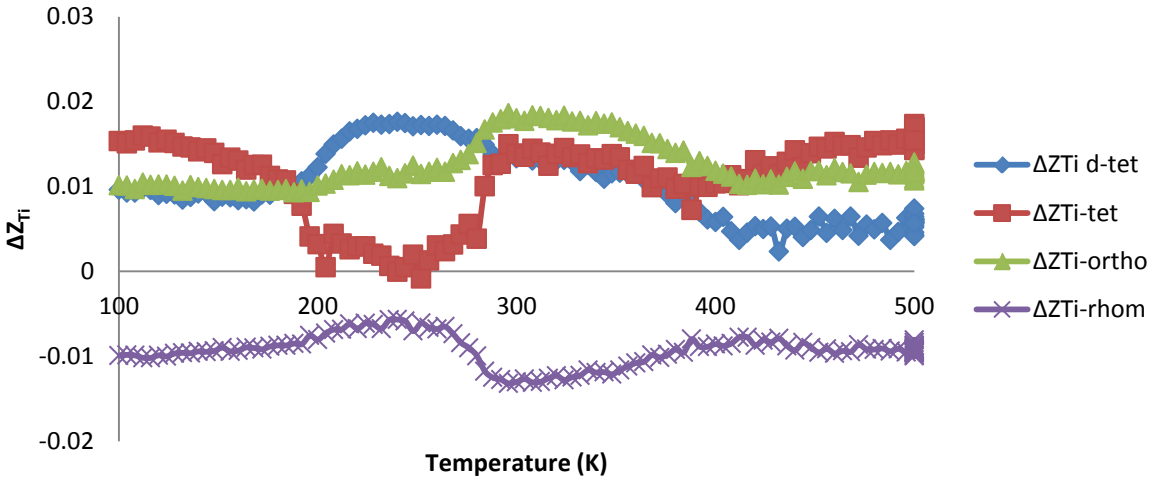

Figure 3.25: Δz_{Ti} for the rhombohedral *(z,z,z)*, orthorhombic (*z*), tetragonal (*z*), and disordered tetragonal (*z*,*z*,*z*) models.

There is more variation in the Ti co-ordinate as temperature is increased but care must be taken to examine the model which best describes the structure at these length scales. In all models the Ti co-ordinate trends towards (0.5,0.5,0.5) as temperature is increased between 300 and 400K. Three standard deviations on a tetragonal Ti co-ordinate on this length scale at 420K was 0.0025 (Table 2.4) so these variations may not be within errors in the tetragonal and disordered-tetragonal models. As *Rw* values converge again at 400K, above this temperature we again have to conclude that the Ti atom is sat in the centre of the unit cell.

3.2.4 Summary of xPDF Refinements

xPDF refinements show the expected phase transitions at long range at the expected temperatures, with the exception of the R-O transition. The difference between O and R fits below 183K at all length scales is interesting because even though it has more variables the orthorhombic model does not always provide the best fit to the experimental data in the expected “tetragonal” and “cubic” region. There is no evidence of an eight site disordered-cubic model from the xPDF refinements or that the Ti atom is still displaced above 400K (given the assumption that when *Rw* values are comparable, the model with the least number of parameters must be chosen to best describe the experimental data). There is also no difference between tetragonal and disordered-tetragonal models at short range, which does not preclude an eight-site model, it just does not give evidence to support it. An attempt at modelling the first Ba-Ti peak with the Ti atom displaced in the [111] direction did provide a better fit than a cubic model but there are problems with this modelling that needs to resolved (Section 3.2.3.2).

3.3 nPDF

3.3.1 Experimental Set Up

The sample of $BaTiO_3$ used in the nPDF study was provided by Antonio Feteira, a senior research fellow at the University of Birmingham. BTO was dried and then sealed in a vanadium can using an indium seal to ensure no moisture could enter the can. The neutron diffraction data were collected at the GEM beamline at ISIS and PDFs were produced from a $S(Q)$ with a Q_{max} of 40Å^{-1}. Data was collected out to Q_{max} = 50Å^{-1} but PDFs were noisy when Fourier transformed using this value of Q_{max}. Eight data sets were collected between 15 and 500K with two diffraction patterns collected at each suggested phase of BTO. Data were

collected in a CCR from 15 to 250K and a furnace between 293 and 500K and six data sets were collected for each temperature and then averaged together in Gudrun, with each data set collected for 150uAHr. Before each data collection the sample was allowed to equilibrate to each temperature by collecting six junk collections for 15uAHr.

3.3.2 Refinement Approach

As previously mentioned (Section 1.6) neutrons interact with matter in a different fashion to x-rays resulting in different scattering powers for atoms. Partial PDFs calculated in PDFGui for a tetragonal model refined against a PDF produced from diffraction data collected at 293K can be seen in Figure 3.26.

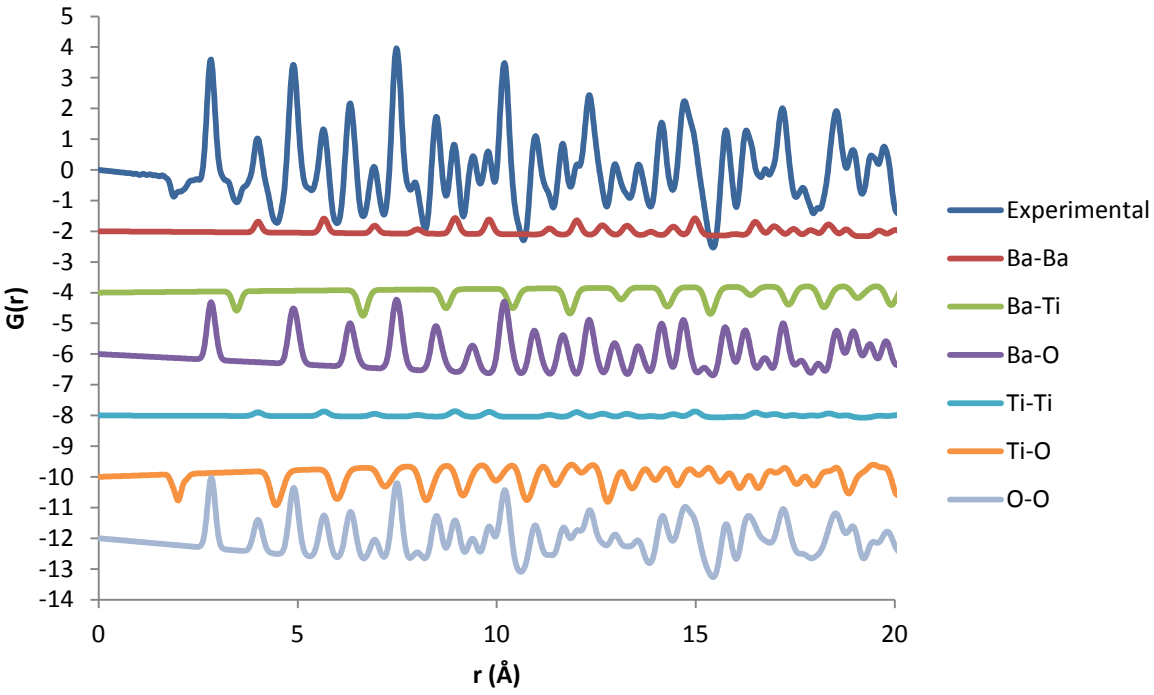

Figure 3.26: Calculated Partial PDFs of BTO at 293K.

In nPDF the oxygen-atom distances contribute a significant amount of the PDF pattern. As a result it was decided it was viable to refine oxygen positions that were previously fixed in

xPDF refinements (Table 3.1). As ringing at low *r* was negligible and the first Ti-O peak was observed it was decided to refine to an r_{min} of 0Å. With previous studies examining the first Ti-O peak to justify local structure, refinements were conducted from 0 to 4.2Å which would model most of the atom-atom distances within one unit cell. This would enable a fit of the first Ti-O peak not to be biased by any atom-atom distances outside of one unit cell, truly modelling local structure. This increased errors in the values for refined parameters but the main focus of the investigation was to model the shape of the first Ti-O peak.

Atomic displacement parameters were again fixed for short and long range refinements from values obtained from refinements run from $r = 0$ to 50Å and *qdamp* was obtained from refining a rhombohedral model between 0 and 50Å at 15K. This value was then fixed for all temperatures, models and length scales. The refined parameters and models were used as seen in Table 3.1).

3.3.3 nPDF Refinements

3.3.3.1 Full Range Refinements (0 to 50Å)

In order to produce high quality PDFs it is important to use a suitably high value of Q_{max} to reduce or negate these termination errors and produce the high resolutions required. The value of Q_{max} obtained (Section 3.3.1) means in this study represents the highest resolution PDFs produced for BTO. Thus assuming that no other errors have been introduced through the normalising of the $S(Q)$, represents the most accurate description of the shape of the first Ti-O peak. In order to investigate the effect of the normalisation on the peak shape, a normalisation was completed with the incorrect density for the vanadium can and the wrong detector calibration file. The peak shape remained constant and there was no effect on the fitting, hopefully showing reliability to the results discussed in this study.

The six models of BTO outlined in Table 3.1 were fit to nPDFs produced and the fitting of a disordered-cubic model was successful. All refined parameters for each model at this length scale can be seen in Appendix 6. The *Rw* values for each of the models fit between 0 and 50Å are presented in Figure 3.27.

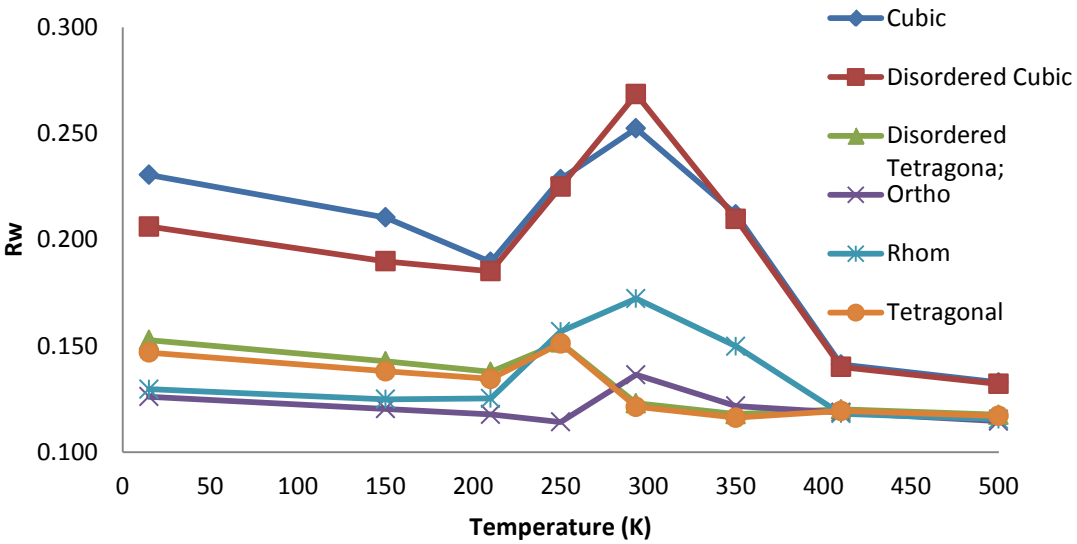

Figure 3.27: *Rw* values from nPDF refinements of BTO from 0 to 50Å for each theoretical model.

In terms of relative *Rw* values, Figure 3.27 is comparable to Figure 3.9 (xPDF), with the orthorhombic model fitting best below ~300K, the tetragonal and dis-ordered tetragonal providing equally as good a fit between 300 and 400K, with *Rw* values appearing to converge above 400K. Interesting the cubic and disordered-cubic model are the worst fit to the experimental data above 400K.

For data collected at 293K and 350K the tetragonal and disordered-tetragonal models provide equally as good a fit to the experimental data. As can be seen below the disordered tetragonal model provides a much better fit to the first Ti-O peak than the standard tetragonal model (Figures 3.28 and 3.29).

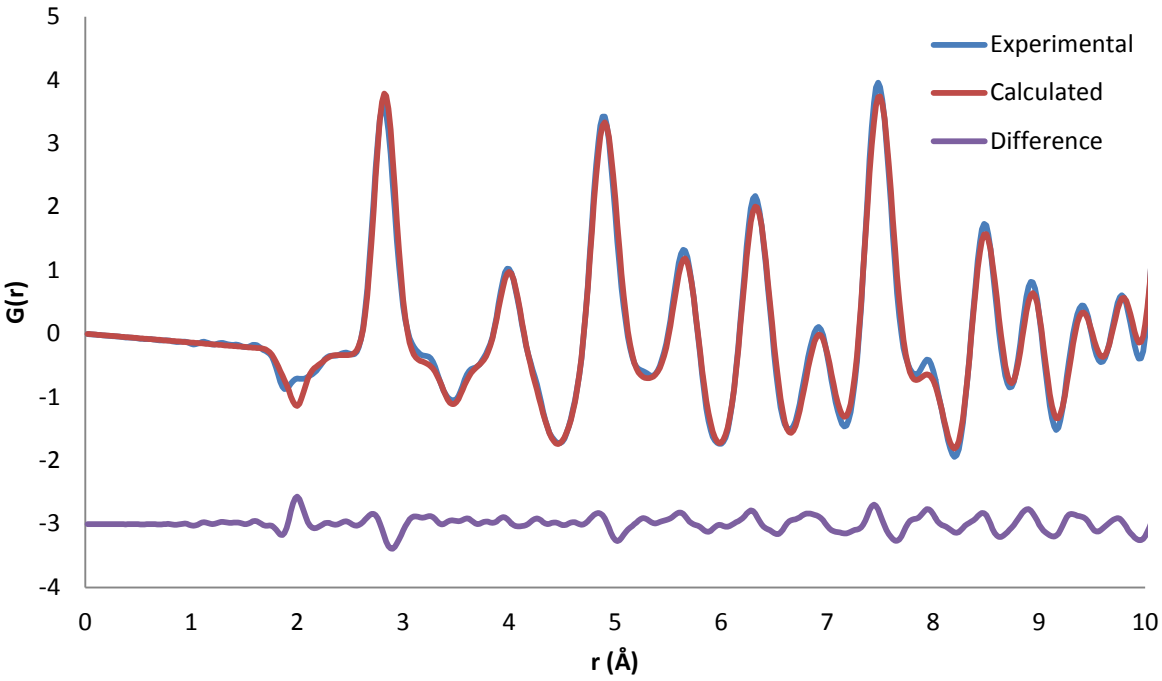

Figure 3.28: Tetragonal model fit to nPDF data of BTO between 0 and 50A at 293K.

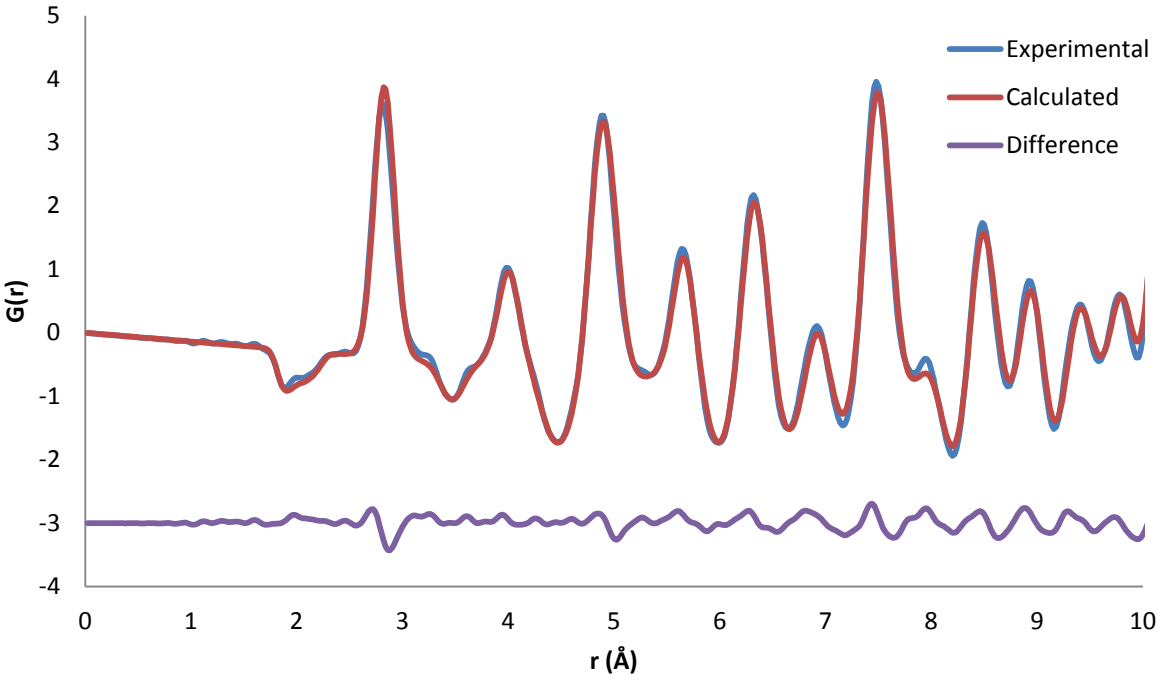

Figure 3.29: Disordered-tetragonal model fit to nPDF data of BTO between 0 and 50A at 293K.

The shape of the first Ti-O peak gives an insight into the nature of the Ti-displacement and the fits presented in Figure 3.28 and 3.29 suggest that the Ti atom is not locally displaced in the [001] direction.

3.3.3.2 Short Range Refinements (0 to 4.2Å)

The first Ti-O peak from the PDFs for each temperature can be seen in Figure 3.30.

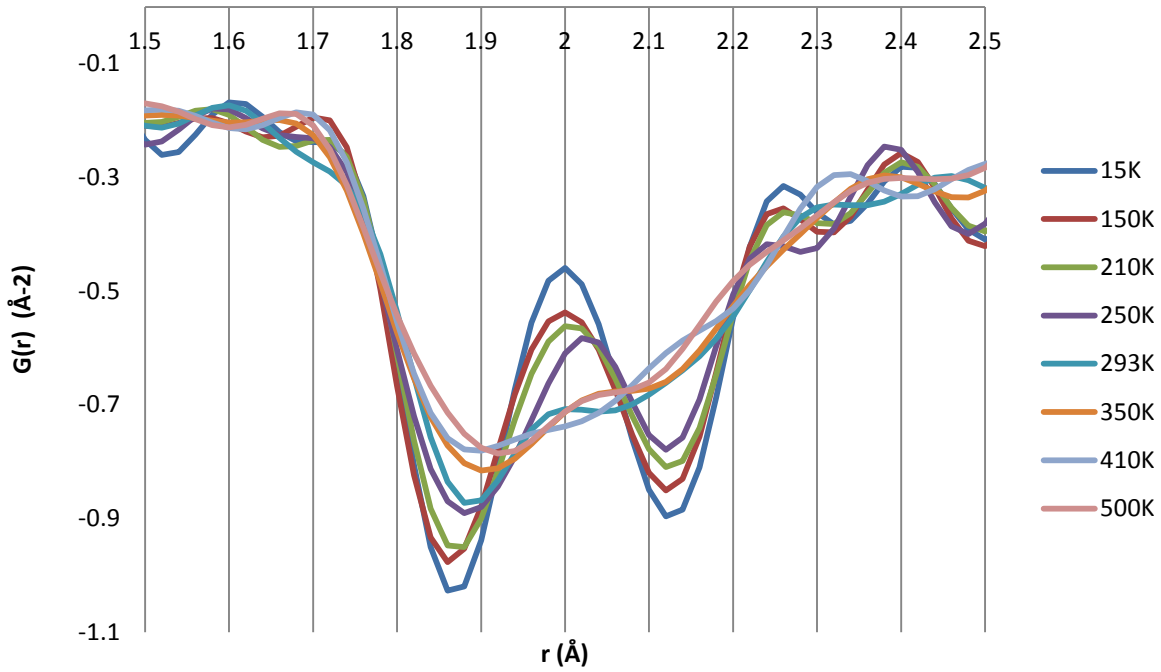

Figure 3.30: The first Ti-O peak between 15 and 500K.

Between 15 and 250K the first peak appears to remain rhombohedral in nature (3:3 distribution of atom-atom distances). The first peak at ~1.8Å appears to shift to longer distances, meaning the Ti-atom is becoming less displaced as temperature is increased. The shape of the peak(s) appears to change at 293K, but it is still does not become either tetragonal (1:4:1 distribution) or cubic (one peak) in nature at any point.

In order to model this first peak, refinements from 0 to 4.2Å were conducted for each theoretical model (refined parameters presented in Appendix 7). *Rw* values from these refinements can be seen below (Figure 3.31).

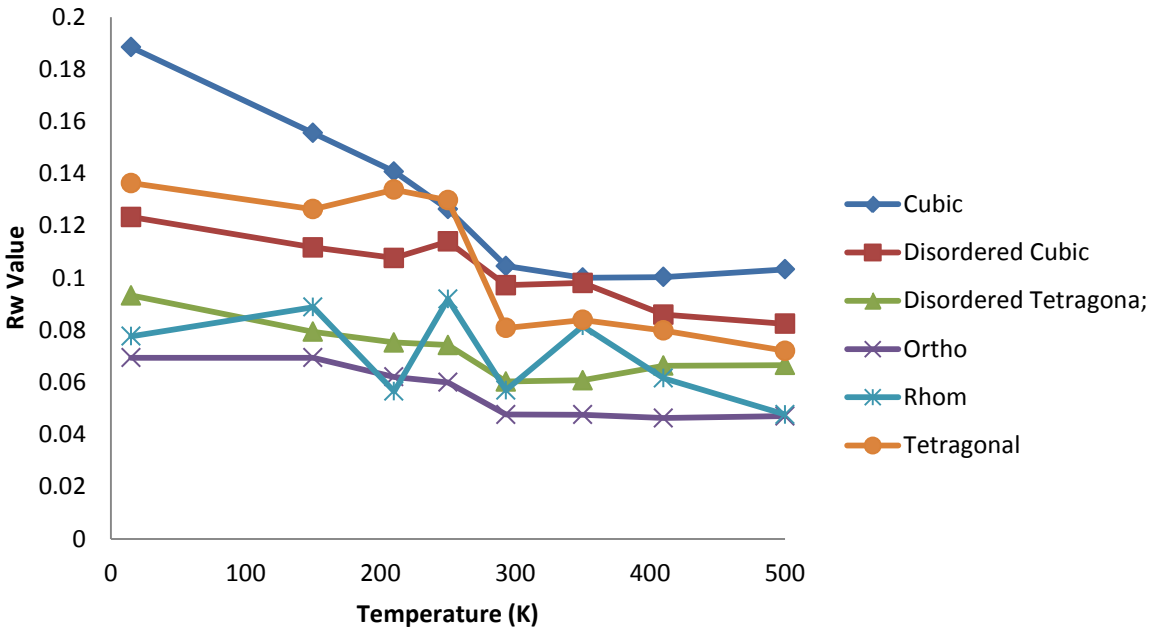

Figure 3.31: *Rw* values from refinements from 0 to 4.2Å.

It is difficult to draw conclusions but there are no spikes in *Rw* values for other models as temperature increases. The orthorhombic model appears to provide the best fit to data at this length scale but it is important to investigate the fit to the first Ti-O peak. For the lowest four data sets (15, 150, 210 and 250K) it is clear that there is no evidence for the Ti displacement to be orthorhombic in nature. The first peak is best fitted by a rhombohedral model, with two peaks of equal area representing 3 short and 3 long Ba-Ti distances (Figures 3.32 to 3.35).

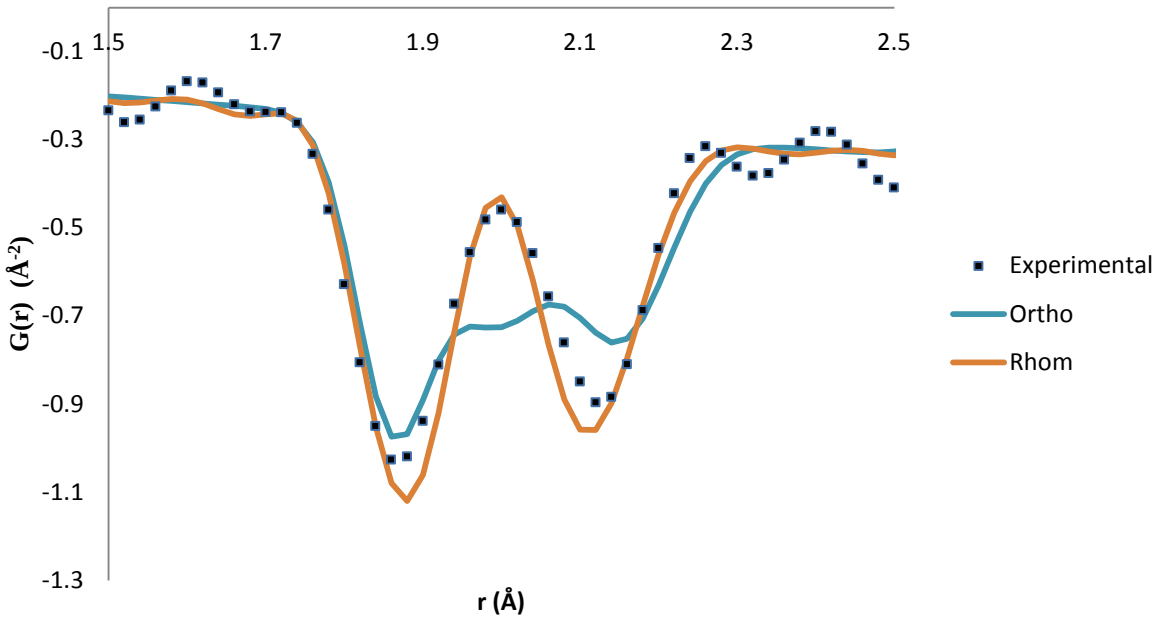

Figure 3.32: Fits to the first Ti-O peak at 15K taken from refinements between 0 to 4.2Å.

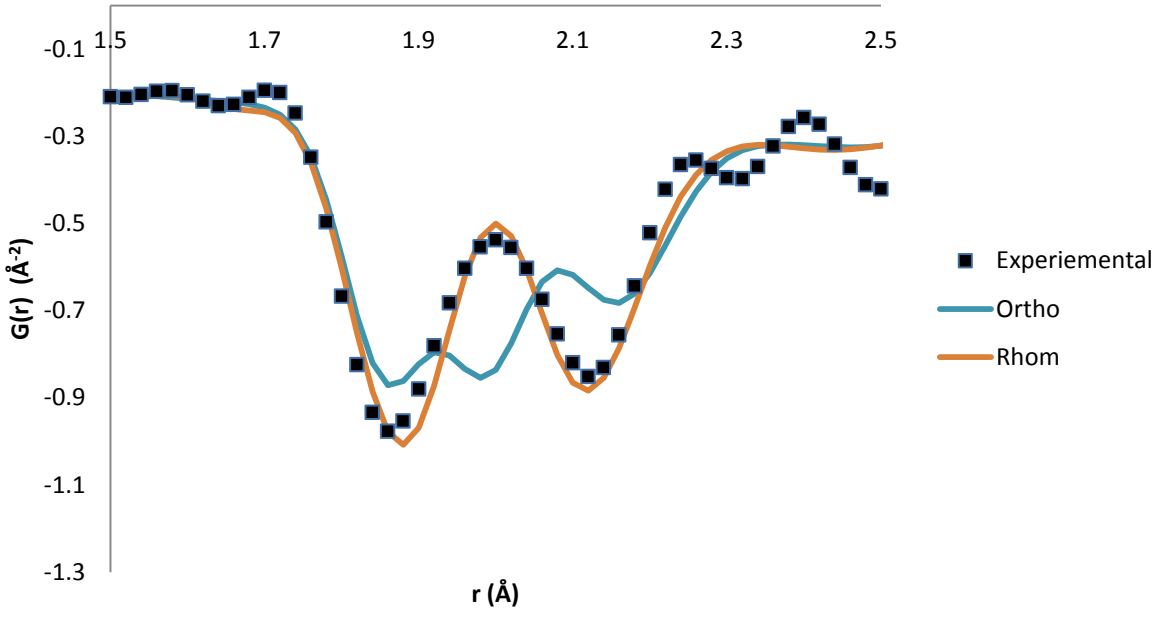

Figure 3.33: Fits to the first Ti-O peak at 150K taken from refinements between 0 to 4.2Å.

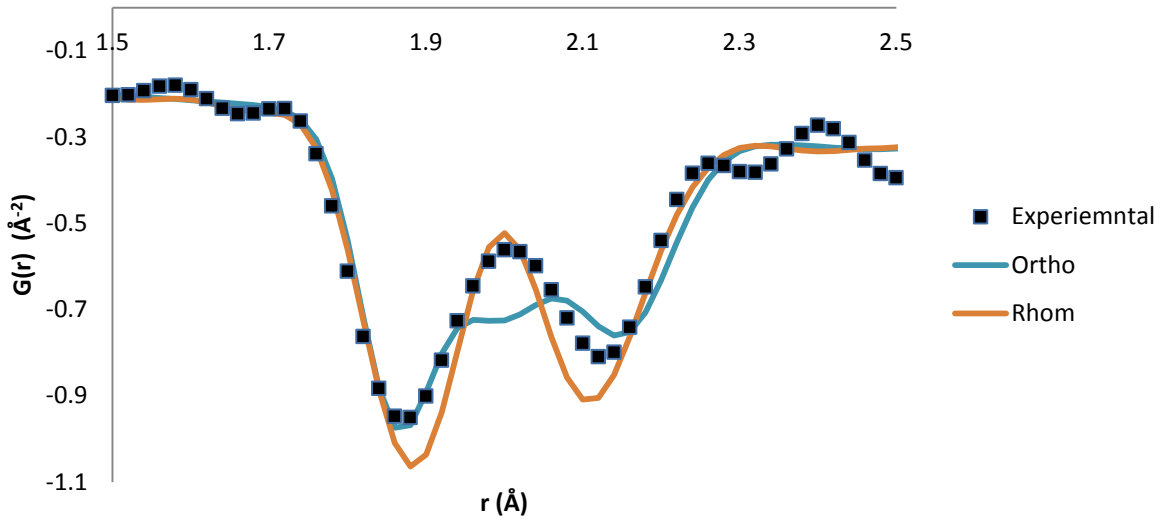

Figure 3.34: Fits to experimental data at 210K taken from refinements between 0 to 4.2Å.

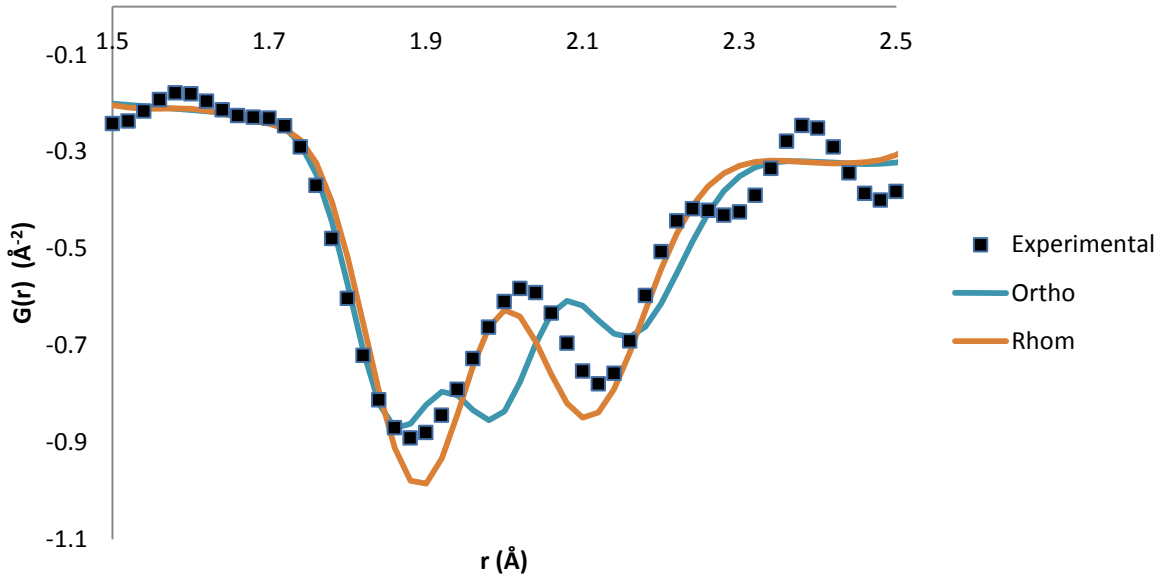

Figure 3.35: Fits to experimental data at 250K taken from refinements between 0 to 4.2Å.

These results appear to be in agreement with the eight-site model of BTO, with the Ti displacement remaining rhombohedral in nature above the R-O transition point. The peak does change shape between the data set collected at 250 and 293K however, which may indicate some form of phase transition. As shown in Section 3.3.3.1 the first Ti-O peak does

not appear to be tetragonal in nature (1:4:1 distribution of Ti-O distances) and it does also not appear to be purely rhombohedral in nature (3:3 distribution of Ti-O distances). Figures 3.36 and 3.37 show that the disordered tetragonal model provides the best fit to this peak (1:2:2:1 distribution of Ti-O distances).

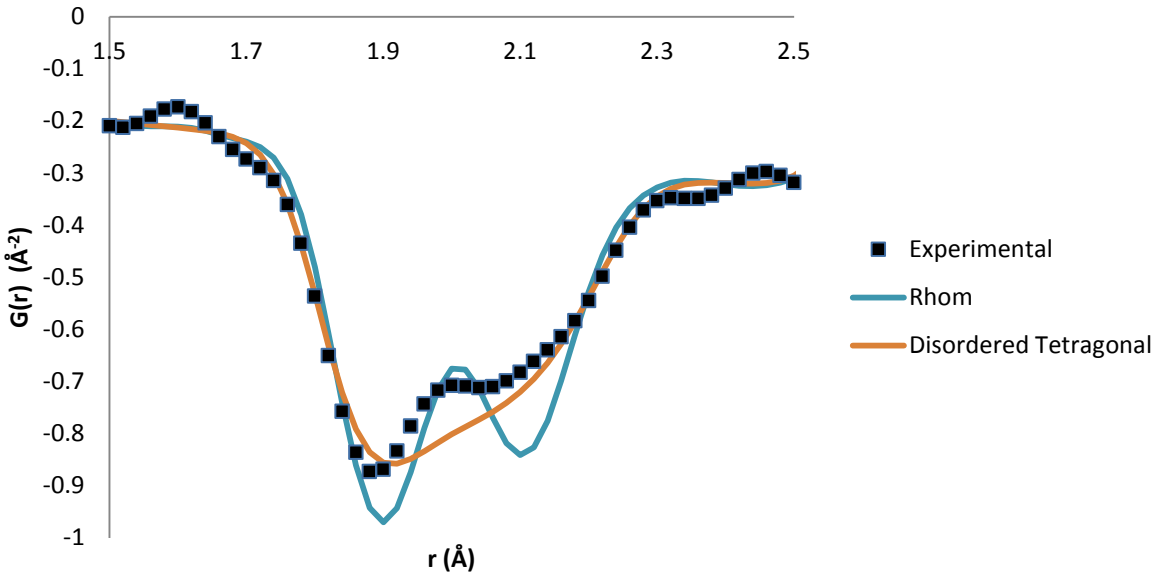

Figure 3.36: Fits to the experimental data at 293K taken from refinements between 0 to 4.2Å.

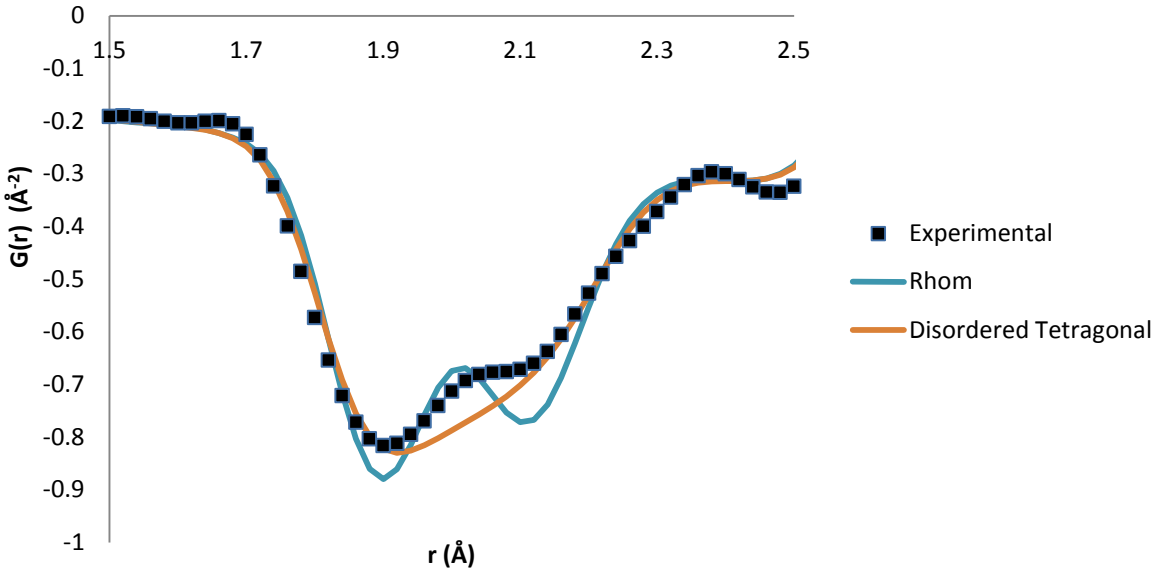

Figure 3.37: Fits to the experimental data at 350K taken from refinements between 0 to 4.2Å.

The fit is not perfect however, suggesting that the disordered-tetragonal model may be too simplistic. This less than perfect fit cannot be explained by artificial ringing as ringing is very small in comparison with the first peak. Ravel *et al* (1998) presented evidence that the Ti atom in the tetragonal phase was displaced from the [111] direction by 12^{o} towards the *c*-axis (Section 3.1.2). In an attempt to model this the disordered tetragonal model was altered so that the Ti co-ordinates were refined as (*x*,*x*,*z*). While the fit to the first peak was slightly improved (Figure 3.38) the *z* co-ordinate (0.5156) refined to be less than *x* (0.5170) which would result in the Ti atom being displaced away from, not towards, the c-axis.

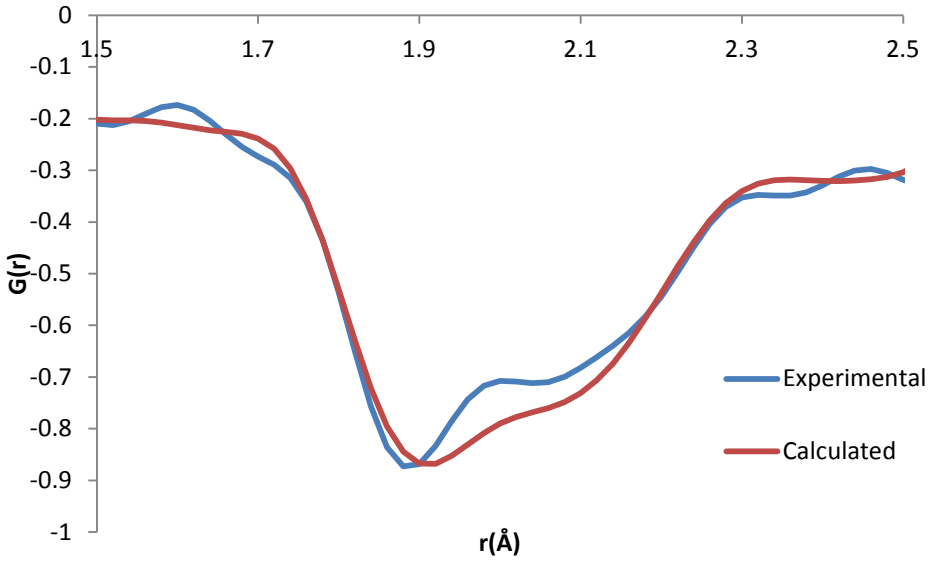

Figure 3.38: Disordered-tetragonal model with Ti position refined as (*x*,*x*,*z*) taken from refinements between 0 to 4.2Å.

There is not a dramatic change in the shape of the peak in the data collected above 400K but it is clear from Figures 3.39 and Figures 3.40 that the first peak does not become cubic in nature (one single peak). A purely disordered cubic model does not provide a very good fit to this peak however, once again suggesting that the Comes model is too simplistic.

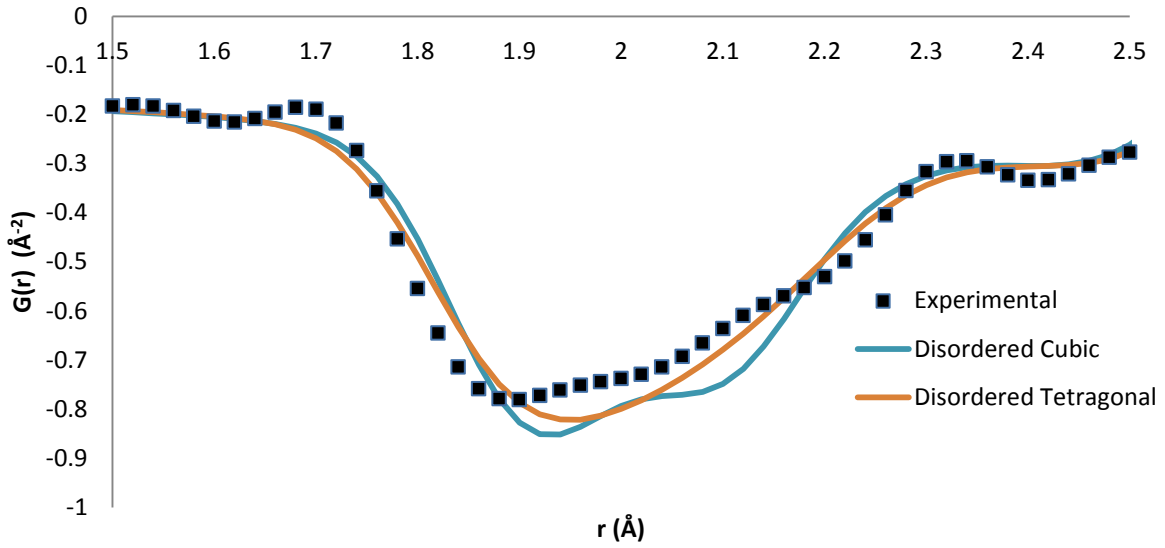

Figure 3.39: Fits to experimental data at 410K taken from refinements between 0 to 4.2Å.

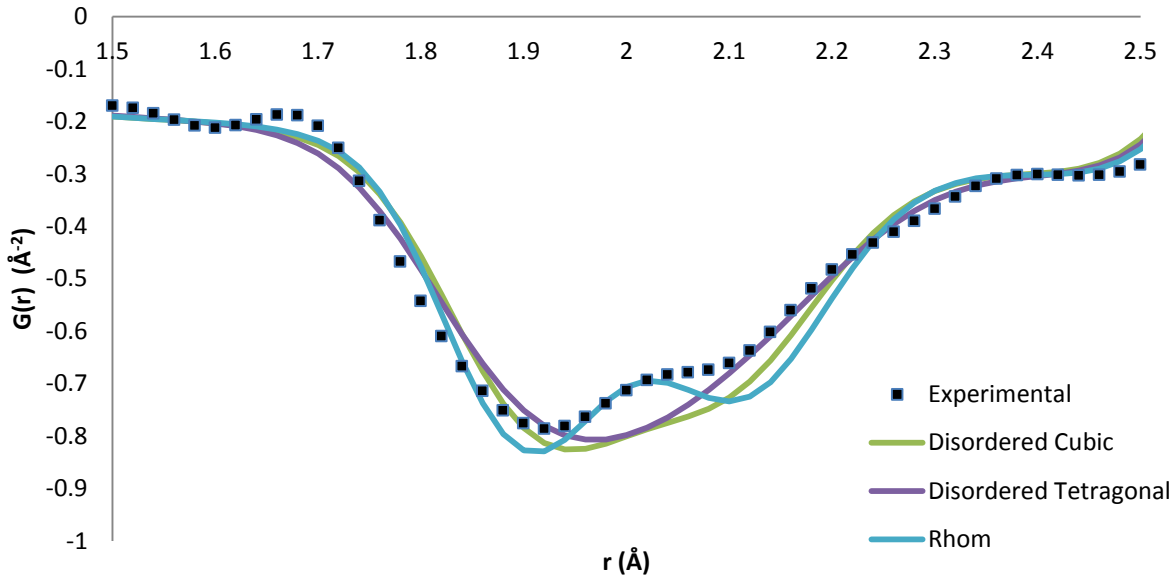

Figure 3.40: Fits to experimental data at 500K taken from refinements between 0 to 4.2Å.

Based on examination of this peak, there is no evidence of a purely displacive tetragonal distortion (1:4:1 distribution of distances) in the cubic phase disagreeing with the findings of Zalar *et al* (2003) but agreeing with Stern (2004) and Pirc (2004).

With Figure 3.29 showing that the Ti becomes less off centre as temperature is increased, the refined Ti position from the models refined between 0 and 4.2A were examined (Figure 3.41)

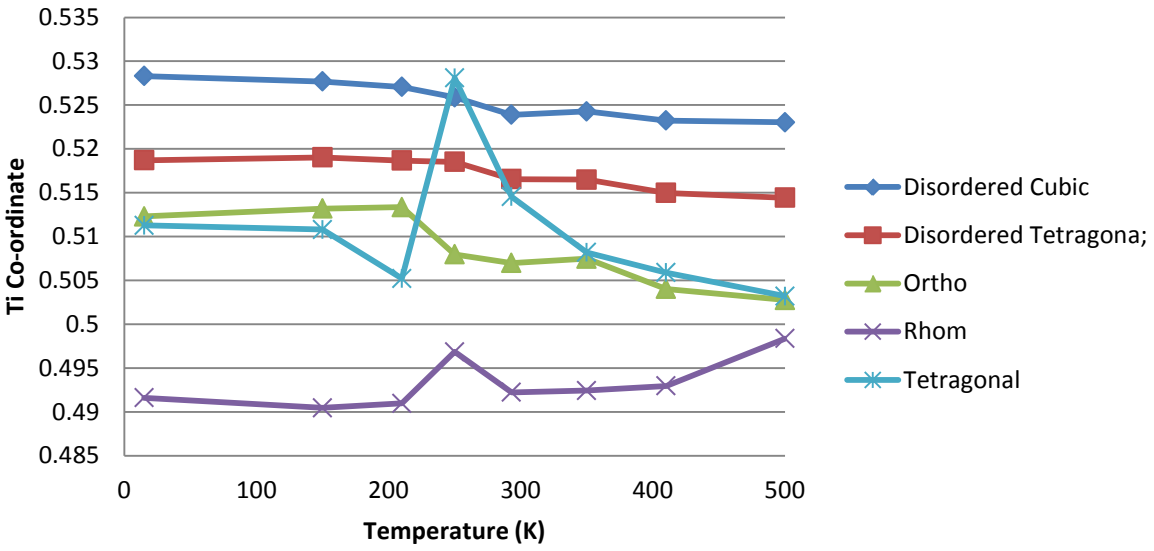

Figure 3.41: Ti-coordinates for each model refined on nPDF data between 0 and 4.2 Å.

While at first glance it appears that the models show that the Ti atom moves towards the centre of the unit cell as temperature is increased we must consider the models themselves and errors. In the "tetragonal" and "cubic" phases there is not a "perfect" fit to the first Ti-O peak so none of these models accurately describe the exact local structure of BTO, so using any of the models presented in Figure 3.41 would not be a valid methodology for accurately describing the position of the Ti atom. Also there are no ESDs presented so all the trends presented here could simple be "within errors", we cannot be certain based on these refinement results. The measured PDF does however show that the Ti atom is becoming less off-centre as temperature is increased. At 500K BTO still does not adopt a local cubic symmetry and it is not certain at what temperature the local structure of BTO would be truly cubic, with no other distortions.

3.3.3.3 Summary of nPDF Refinements

The data presented here represents the highest quality nPDF data that has been recorded of BTO at ambient conditions and at variable temperature. It is clear that with the exception of the rhombohedral phase, that the average structure of BTO is different to the local structure. This is in agreement with almost all previous studies (Section 3.1). From modelling in PDFGui is the clear that the Comes model is too simplistic when describing the local structure of BTO in the "tetragonal" and "cubic" phases. This study does exclude the possibility of some dynamic tetragonal displacements in either the "tetragonal" or "cubic" phase, as these would potentially have weak contributions to the first Ti-O peak.

With ADPs increasing with temperature the peaks become broader and overlap more, which makes visual inspection of the Ti-O peak more complicated at higher temperatures. It is clear from a simple observation of this peak however that the Ti atom appears to become less off-centre as temperature is increased.

3.4 Conclusions

Due to the rapid data collection associated with xPDF this study includes the largest number of data sets utilised for xPDF analysis. This large number of data sets made it possible to use the *Rw* values to examine the phase transitions of BTO at varying temperature and length scales. This type of analysis has not been observed in literature previously. The xPDF refinements show evidence of the expected phase transitions in the average structure of BTO but they do not provide any conclusive evidence for the local structure of BTO. For example, the orthorhombic model provides the best fit to the local structure of BTO below 183K, but this model is disproved in the nPDF refinements. The xPDF does show that the Ti atom is moving towards the centre of the unit cell in the "tetragonal" phase and there is evidence in the first Ba-Ti peak that the local structure is not cubic above 400K.

The nPDF provides more insight to the local structure of BTO with a higher useable Q_{max} from the $S(Q)$ and being able to observe the first Ti-O peak. Unfortunately there is no definitive model presented to explain the "tetragonal" and "cubic" phases but the eight site model appears to describe the "orthorhombic" phase to an acceptable degree.

3.5 Future Work

It is clear the Comes model provides a better description of the local structure of BTO but there are clearly further complexities that this model does not consider. RMC modelling, which is not constrained by the concept of a unit cell uses a large box of atoms to model PDF data. RMCProfile[30] could be used to model both the variable temperature x- and nPDF data and then compare to results from modelling in PDFGui. This would hopefully give more insight into the local structure of BTO at the various temperatures, it would be useful to compare results between the neutron and x-ray refinements. Is the first Ba-Ti peak actually enough to provide information on local structure when modelling in PDFGui or is the first Ti-O peak essential (as suggested by Laulhe 2009)? Modelling the first Ba-Ti peak using peak fitting with correct constraints may also provide further insight.

It is clear that the Ti atom moves towards the centre of the unit cell as temperature is increased but at what temperature the Ti atom sits in the centre of the unit is unclear. It may be useful to conduct a higher temperature study of BTO once RMC modelling is complete. With more insight into the local structure it may be possible to say at what temperature BTO becomes locally cubic. Potentially four data collections at 550K, 600K, 650K and 700K would be sufficient.

Another approach that could be taken would be move the detector "off-centre" to access higher values of Q_{max} when using x-ray diffraction (Figure 3.42a and b). The detector at I15

and 11-ID-B can move away and towards the sample but it is not set up to move off axis relative to the beam centre in this way.

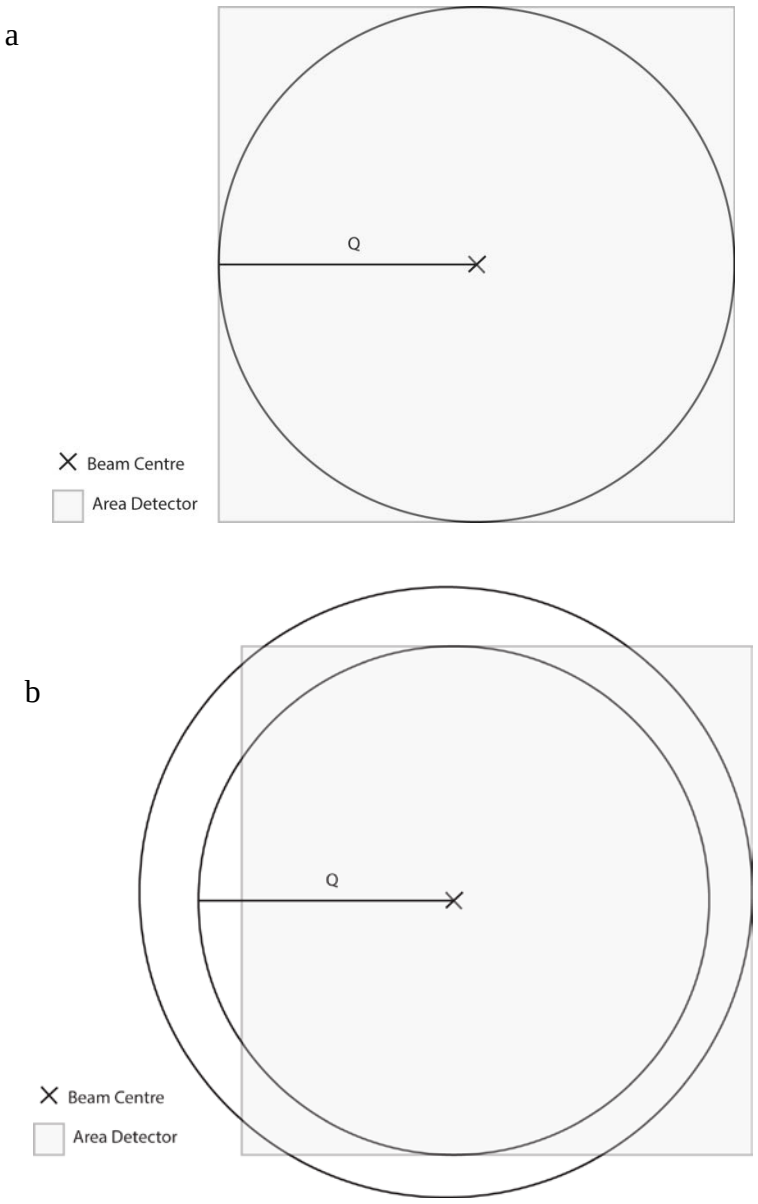

Figure 3.42a: Detector *"on-centre"* with respect to the beam centre, b: Detector moved *"off-centre"*.

Fit2d is capable of calibrating the beam centre and thus can integrate patterns even if a full radial pattern is not available for every accessible value of *Q*. This approach would lead to a larger value of Q_{max} in the $S(Q)$ and thus a higher resolution PDF. This would result in reduced termination errors in the PDF at low *r* (Figure 1.4) and then potentially allow the first

Ti-O peak to be observed in xPDFs. It is unclear if the reduced number of data points at the higher Q values would have any effect on the quality of the PDF but this approach has been successfully utilised at the I-12 beam line at DLS.

References

1. B. Wul and J. Goldman, *Comptes Rendus de l'Académie des Sciences*, 1945, **49**.
2. V. M. Goldschmidt, *Geochemisce Verterlungsgesetze der Elemente.*, 1927, **8**.
3. H. D. Megaw, *Nature*, 1945, **155**, 484-485.
4. W. P. Mason, *Piezoelectric Crystals and Their Application to Ultrasonics*, Van Nostrand, New York, 1950.
5. G. H. Kwei, A. C. Lawson and S. J. L. Billinge, *The Journal of Physical Chemistry*, 1993, **97**, 2368-2377.
6. M. Lambert, M. Quittet and C. Taupin, *Acta Crystallographica*, 1963, **16**, S2-31.
7. G. Honjo, S. Kodera and N. Kitamura, *Journal of the Physical Society of Japan*, 1964, **19**, 351.
8. R. L. Comes, M and A. Guinier, *Solid State Comminications*, 1968, **6**, 715-719.
9. A. S. Chaves, F. C. S. Barreto, R. A. Nogueira and B. ZEKS, *Physical Review B*, 1976, **13**, 207-212.
10. J. Harada and G. Honjo, *Journal of the Physical Society of Japan*, 1967, **22**, 45-57.
11. G. Shirane, J. D. Axe and J. Harada, *Physical Review B*, 1970, **2**, 3651-3657.
12. D. Heiman and S. Ushioda, *Physical Review B*, 1974, **9**.
13. C. E. H. Forbes, W. B., N. E. Cipollini and J. F. Lynch, *Journal of the Chemical Society, Chemical Communications*, 1987, 433-436.
14. O. Kanert and H. Schulz, *Solid State Communications*, 1994, **91**, 465-469.
15. E. A. Stern, *Physical Review Letters*, 2004, **93**, 37601-37604.
16. B. Zalar, A. Lebar, J. Seliger, R. Blinc, V. V. Laguta and M. Itoh, *Physical Review Letters*, 2005, **71**, 64107(64112).
17. R. B. Pirc, R, *Physical Review B*, 2004, **70**, 134107(134108).
18. B. Zalar, V. Laguta and R. Blinc, *Physical Review Letters*, 2003, **90**, 37601.
19. B. Ravel, E. A. Stern, R. I. Vedrinskii and V. Kraizman, *Ferroelectrics*, 1998, **206**, 407-430.
20. A. Scalabrin, A. S. Chaves, D. S. Shim and S. P. S. Porto, *Physica Status Solidi (b)*, 1977, **79**, 731-742.
21. C. Perry and D. Hall, *Physical Review Letters*, 1965, **15**, 700-702.
22. G. H. Kwei, S. J. L. Billinge, S.-W. Cheong and J. G. Saxton, *Ferroelectrics*, 1995, **164**, 57-73.
23. V. Petkov, M. Gateshki, N. Neiderberger and Y. Ren, *Chemistry of Materials*, 2006, **18**, 814-821.
24. A. V. Belushkin, D. P. Kozlenko, N. O. Golosova, P. Zetterstrom and B. N. Savenko, *Physica B*, 2006, **385-386**, 85-87.
25. M. B. Smith, K. Page, T. Siegrist, P. L. Redmond, E. C. Walter, R. Seshadri, L. E. Brus and M. L. Steigerwald, *Journal of the American Chemical Society*, 2008, **130**, 6955-6963.

26. C. Laulhe, F. Hippert, R. Bellissent, A. Simon and G. J. Cuello, *Physical Review B*, 2009, 64104(64110).
27. Y. Yoneda and S. Kohara, *Journal of the Korea Physical Society*, 2009, **55**, 741-745.
28. I. Jeong, C. Y. Park, J. S. Ahm, S. Park and D. J. Kim, *Physical Review B*, 2010, **81**, 214119(214115).
29. K. Page, T. Proffen, N. Neiderberger and R. Seshadri, *Chemistry of Materials*, 2010, **22**, 4386-4391.
30. M. G. Tucker, D. A. Keen, M. T. Dove, A. L. Goodwin and Q. Hui, *Journal of Physics: Condensed Matter*, 2007, **19**, 1-16.

4. LOCAL STRUCTURE AND PHASE TRASITIONS OF $BaTiO_3$ AT HIGH PRESSURE

4.1 Introduction

4.1.1 Overview

There are significantly fewer studies of BTO at high pressures in comparison to at variable temperatures. An attempt will be made to discuss findings of high pressure studies and how they relate to the findings of variable temperature studies that have already been presented in Section 3.1.

The application of pressure results in the lowering of phase transition temperatures so that it is possible to observe the cubic phase at ambient temperature.[1] At ambient temperature it is reported that the average structure of BTO will undergo a tetragonal-to-cubic (T-C) phase transition at roughly 2GPa. [1] A neutron diffraction study also showed an averaged T-C phase transition at slightly higher pressure (3.2GPa), with the Ti displacement in the tetragonal phase smaller at high pressures.[2] X-ray diffraction studies up to 30GPa have shown that the average structure of BTO remains cubic, with no signs of any further phase transitions past this point. [3] It is not clear from this study when diffuse scatter is no longer observed in the diffraction pattern.

The first Raman spectra for single crystal BTO at high pressure (up to 2.2 GPa) was presented by Jayaraman *et al* (1984).[4] This was just a preliminary report however and a more detailed study up to 3.5GPa was presented by Sood *et al* (1995).[5] As with the high-temperature paraelectric phase, the high pressure cubic phase displays Raman activity that is forbidden in a cubic model of BTO, indicating a degree of disorder. Sood *et al* reported "there are similarities and significant differences between the pressure dependence of the line shape

parameters in the coupled-phonon model with the corresponding temperature dependence".[5] This was attributed to the differences between the effects of increasing temperature and pressure. A later study of polycrystalline BTO presented Raman spectra up to much higher pressure (8.5GPa).[6] Strong Raman spectra were still observed up to 8.5GPa and it was suggested that there were two structural changes occurring at roughly 2 and 5 GPa but they did not attempt to explain what the structures of these differing phases would be.

With the application of pressure, bond lengths are reduced and the unit cell volume is decreased. Longer bonds are more compressible than shorter bonds so there is more reduction in the length of the longer Ti-O bonds. The application of pressure leads to a reduction of distortions in the local structure, so it is expected that the ferroelectric distortion in $BaTiO_3$ would decrease, and eventually disappear.

X-ray absorption spectroscopy has been used to investigate the Ti position in the *"cubic phase"* under pressure and has shown that, as with the high-temperature cubic phase, the Ti atom is not in the centre of the oxygen octahedra.[7] This study suggested that the loss of ferroelectricity is due to a lack of long range order of the Ti displacements, which remain of a rhombohedral nature until the Ti atom moves to the (0.5,0.5,0.5) position above 10GPa.[7] This would appear to match the findings from the high-temperature cubic phase (Section 3.3) but, as has already been mentioned, the application of pressure leads to a reduction of distortions in the local structure. These conclusions are also supported by diffuse scattering of x-rays.[8]

4.1.2 Previous PDF Studies of BTO at High Pressure.

With diffuse scatter of x-rays present in the high-pressure paraelectric phase, analysis of PDFs of BTO could be a good experimental technique to investigate this phenomenon. The first high pressure PDF of BTO was presented by Chapman *et al* (2010) when discussing the methodology behind producing high quality x-ray PDFs in diamond anvil cells at high pressure. [9] Although no analysis was presented, a PDF Fourier transformed from a $S(Q)$ up to a Q of 30 $Å^{-1}$ was presented. As with other x-ray PDF studies the first Ti-O peak is not observed, even with the relatively high value of Q_{max}. A more detailed study was later presented by *Ehm et al* (2010), unfortunately it is unclear what Q_{max} they accessed.[10] They suggested that there are tetragonal nano-domains in the high pressure paraelectric phase and the domain size decreases as pressure increases with the Ti atom potentially sitting in the centre of the unit cell above 10GPa (in agreement with XAS studies). An attempt is made to explain their approach to refinements, but it is unclear how they have arrived at their conclusions and how they obtained their values for domain size. At 2.8GPa their disordered-tetragonal model essentially has Ti atoms displaced along the [001], which represents the average tetragonal structure. The conclusions made in the study by Ehm *et al* (2010) do not appear to be supported by any of the data presented.

4.1.3 Summary

The application of pressure allows us to access the average T-C phase transition at ambient temperature. The Ti atom is still displaced from the centre of the oxygen octahedra but appears to move more on centre as pressure is increased (up to 10GPa). This is similar to the effect of increasing temperature, although the unit cell will decrease with increasing pressure and Raman spectra indicate differences between the high pressure and high temperature "cubic" phases. With a previous PDF study showing evidence of local Ti distortions in the

[001] direction up to 6.8GPa, this should be reinvestigated as a 4-site model with Ti atoms displaced along the [111] direction as is more commonly accepted and a study to higher pressure may provide further evidence for the Ti atom sitting in the centre of the unit cell above 10GPa.

4.2 Experimental and Methodology

4.2.1 Experimental Set Up

To obtain high pressures, a Diacell Bragg DAC with a 90° scattering aperture was used, with a upstream diamond that had been drilled to reduce the beam path though the diamond. The sample was loaded into a tungsten gasket which was pre-indented to roughly 100μm and then spark eroded with a hole of 200μm in diameter. In order to collected diffraction data for use in PDF analysis, a sample to detector distance of 200.8mm was used which allowed for Q_{max} = 23Å^{-1}. For each pressure the detector was moved away from the sample so that the detector distance was then 210.78mm. This allowed for the collection higher quality diffraction data for use in Rietveld analysis (which does not require high values of Q to be accessed). At each pressure 6 sets of 60 x 5 second exposures were averaged together to produce the final diffraction pattern. A 4:1 mixture of methanol:ethanol was used as a pressure transmitting fluid to obtain hydrostatic condictions in the sample and a 100μm x 100μm.

4.2.2 Refinement Approach in PDFGui

Sequential fitting was used to refine the PDFs collected at increasing pressure and the same models that were outlined in Table 3.1 were used. Thermal parameters were obtained from a tetragonal model fit to ambient pressure data between 20 and 50Å and then these values were used for all models at all pressures and length scales. This was done as the thermal parameters would not be expected to change significantly as pressure is increased and it meant that each

model had fewer refined parameters, which as discussed in Section 3.2.2 can lead to fewer unrealistic models being produced from refinements. The model and length scale were chosen as it is accepted that the long range structure of ambient BTO is tetragonal (the shorter range data was excluded from the refinement).

Other approaches that could be used to model the PDF data are presented, with results in Appendix 8. Oxygen positions for the tetragonal and disordered-tetragonal models were again fixed using the same values as used for the variable temperature refinements and the same length scales were also used to investigate local and long range structure (Section 3.2.2). Oxygens in the rhombohedral model were fixed to sit in ideal cubic positions.

As with the high temperature data (Figure 3.21) peak fitting was conducted on the first Ba-Ti peak was conducted in order to investigate the shape of this peak but results were inconclusive. A single peak was fit to this Ba-Ti peak and the peak centres and FWHMs are presented in Appendix 9.

4.3 Results and Discussion

4.3.1 Rietveld Structure Refinements

High values of Q (and thus two theta) are not required for Rietveld analysis of x-ray diffraction data. With the detector moved further away from the sample this provided a better resolution on Bragg peaks observed at smaller values of Q. Rietveld analysis of the data collected with the detector further away from the sample was conducted for each pressure collected. As can be seen in Figure 4.1 a good fit was produced when a tetragonal model was fit to the diffraction pattern at ambient pressure.

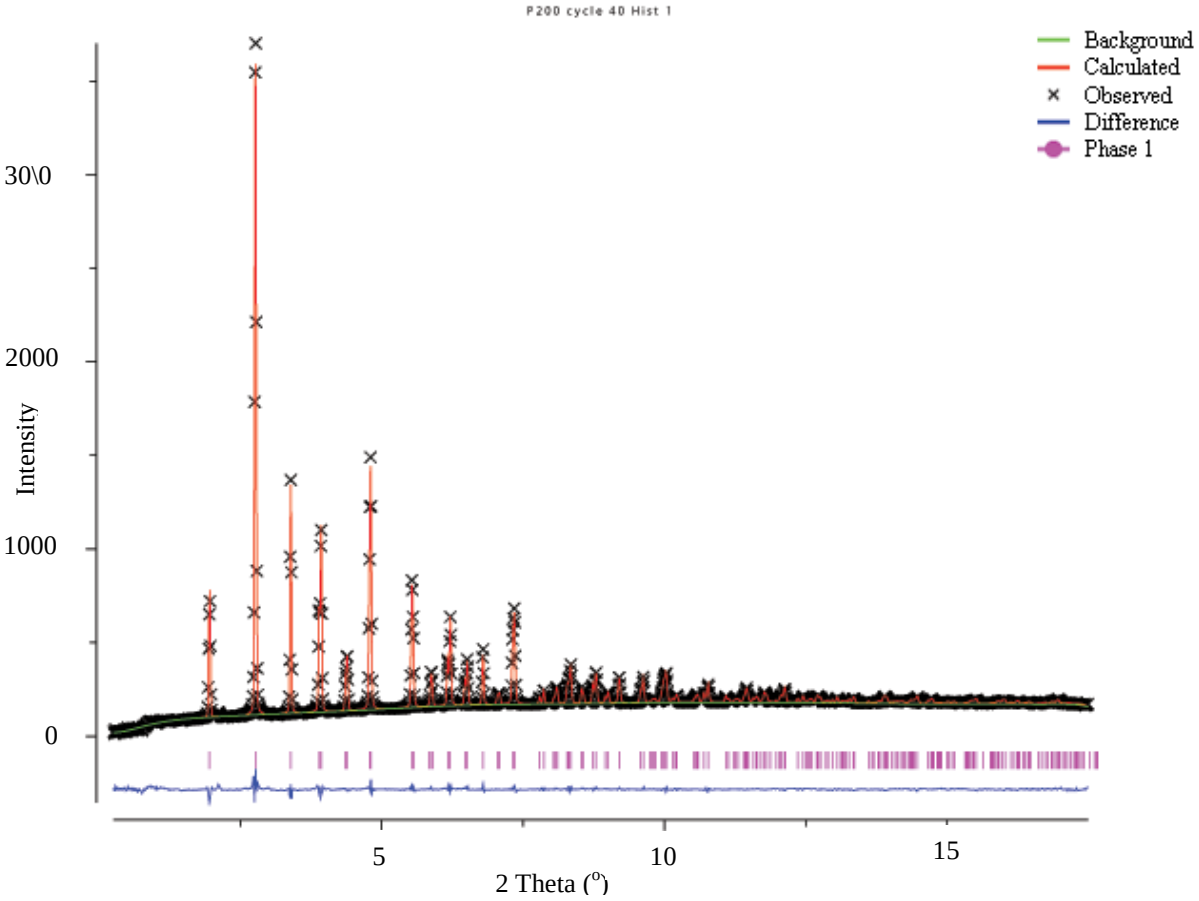

Figure 4.1: Rietveld fit to experimental diffraction data of ambient BTO in a DAC.

Rietveld analysis was also conducted on all the diffraction patterns collected below the expected T-C transition pressure (~2GPa). The results of this analysis can be seen in Table 4.1.

Table 4.1: Parameters from Rietveld refinements of a tetragonal BTO model to diffraction data.

Pressure (GPa)	*wRp*	*a* (Å)	*c* (Å)	Ti *z*	Ba U_{iso} (Å^2)	Ti U_{iso} (Å^2)	O U_{iso} (Å^2)
0	0.0325	3.9945(1)	4.0304(2)	0.507(6)	0.0034(2)	0.0045(6)	0.0069(9)
0.05	0.0394	3.9938(1)	4.0301(2)	0.50(2)	0.0037(2)	0.0046(6)	0.007(1)
0.38	0.0434	3.9906(2)	4.0271(2)	0.50(4)	0.0041(2)	0.0044(9)	0.007(1)
0.77	0.0522	3.9872(2)	4.0226(2)	0.52(2)	0.0039(3)	0.004(1)	0.006(1)
1.25	0.0237	3.9836(1)	4.0161(3)	0.50(3)	0.0040(4)	0.004(1)	0.006(1)
1.87	0.0491	3.9789(2)	4.0086(3)	0.50(2)	0.0044(3)	0.004(1)	0.007)(1)

While lattice parameters and the resulting volume decreases with increasing pressure there are no discernable trends in Ti *z* co-ordinate or any of the U_{iso} values. A simple inspection of the diffraction pattern shows that the peak corresponding to (103)/(310) is not split at 2.62GPa (Figure 4.2) indicating $a = b = c$. A Rietveld fit of the diffraction pattern collected at 3.88GPa using a cubic model can be seen in Figure 4.3.

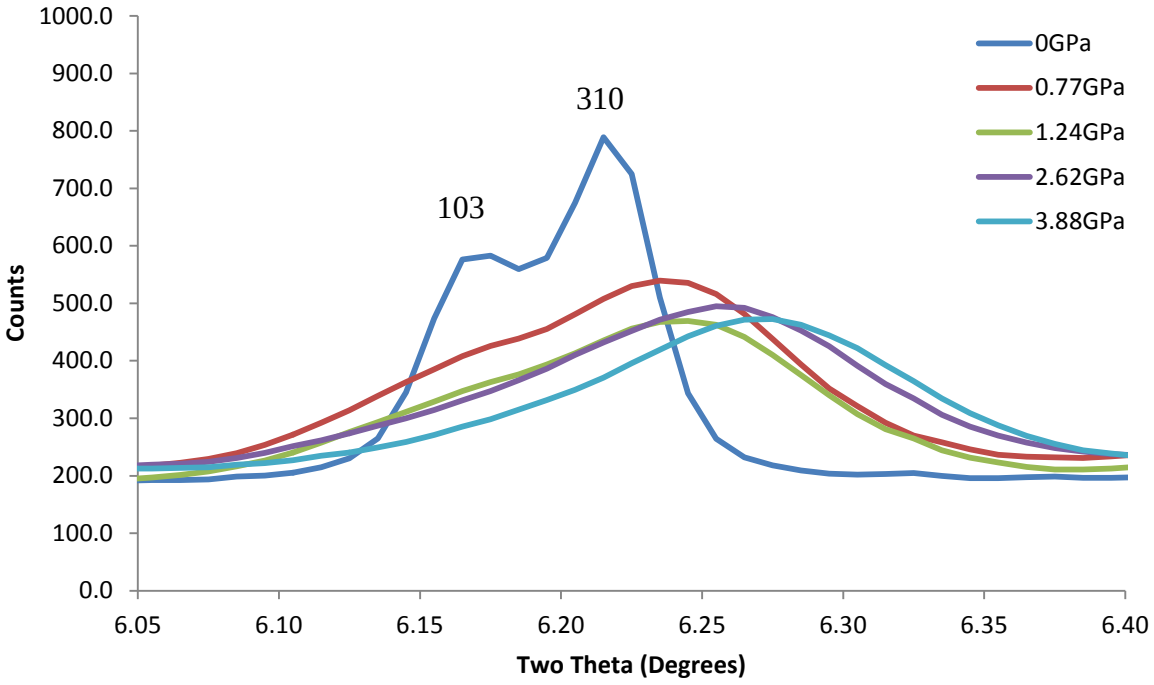

Figure 4.2: Diffraction pattern of BTO collected at various pressures.

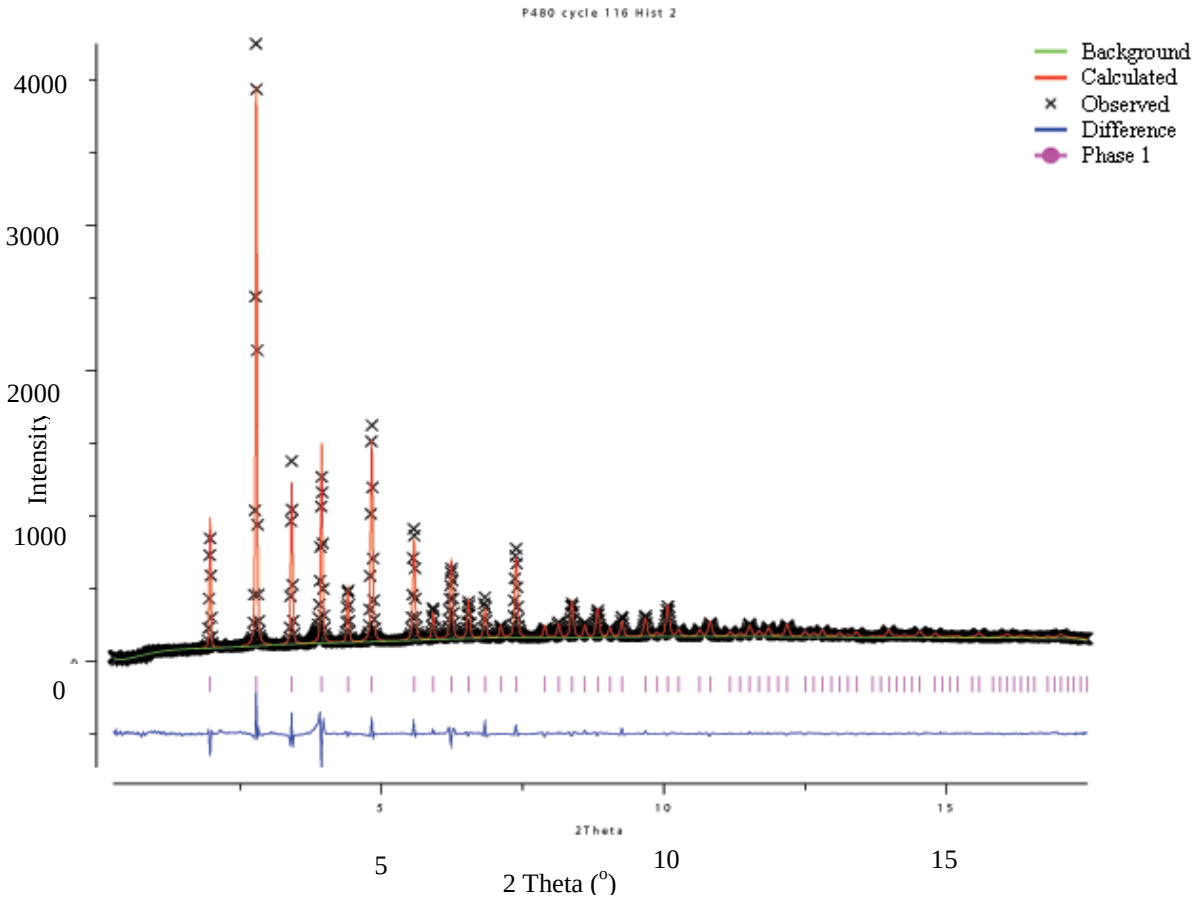

Figure 4.3: Rietveld fit of a cubic model to a diffraction pattern of BTO at 3.88 GPa.

As pressure is increased above 2.63 GPa, BTO remains cubic on average and volume decreases (Table 4.2). This is as expected and fits into previous studies that indicate that the average structure of BTO is cubic above ~2GPa (Section 4.1)

Table 4.2: Parameters from Rietveld refinements of a cubic BTO model to diffraction data.

Pressure (GPa)	*wRp*	*a* (Å)	Ba U_{iso} (Å^2)	Ti U_{iso} (Å^2)	O U_{iso} (Å^2)
2.63	0.0570	3.9814(2)	0.0034(4)	0.0037(6)	0.005(1)
3.88	0.0506	3.9712(2)	0.0028(4)	0.0032(5)	0.003(1)
5.37	0.0444	3.9639(2)	0.0034(3)	0.0036(5)	0.004(1)
6.85	0.0526	3.9482(2)	0.0047(3)	0.0035(5)	0.006(1)
7.38	0.0532	3.9444(2)	0.0047(3)	0.0035(5)	0.007(1)
8.20	0.0487	3.9385(2)	0.0047(3)	0.0033(5)	0.006(1)
8.38	0.0496	3.9371(2)	0.0048(3)	0.0031(5)	0.006(1)
8.58	0.0508	3.9355(2)	0.0047(3)	0.0033(5)	0.006(1)
8.78	0.0426	3.9344(2)	0.0048(3)	0.0031(5)	0.006(1)

4.3.2 xPDF

4.3.2.1 Refinements on data from 2.5 to 50Å

With the disordered tetragonal model providing the best description of the ambient structure of BTO (Section 3.3.3.2) and an uncertain structure at high temperature, a study was conducted to investigate the local structure of BTO at high pressures. At ambient pressure the PDF collected from BTO loaded in a DAC with pressure transmitting fluid is comparable to that collected in a kapton capillary (Figure 4.4).

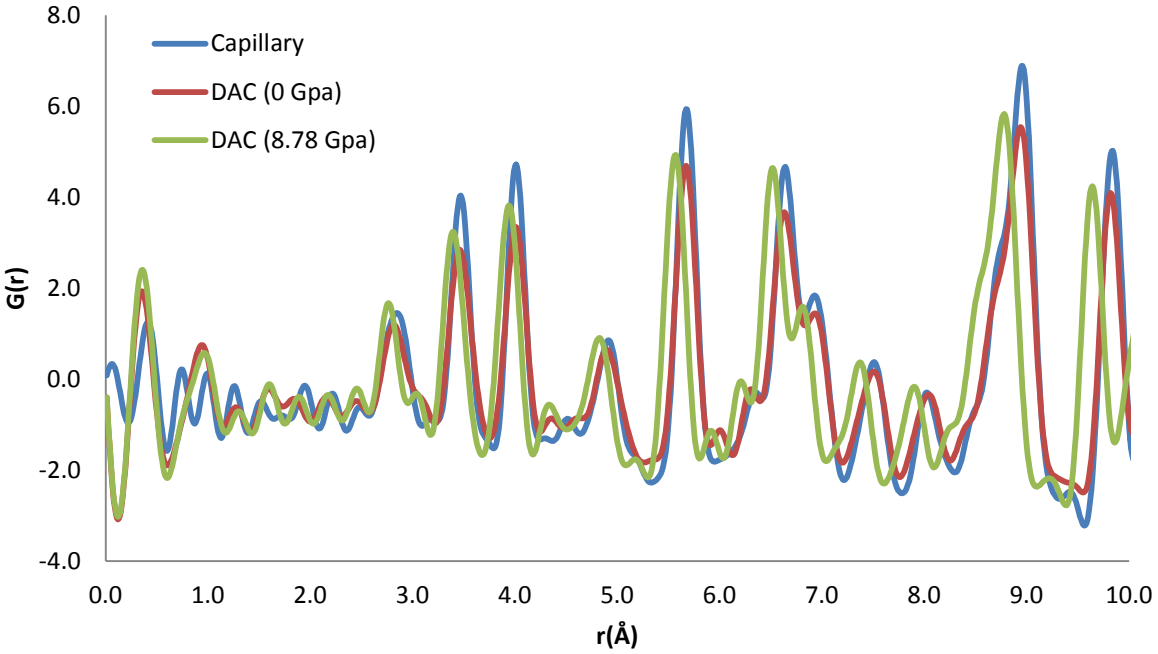

Figure 4.4: Comparison of PDFs of BTO.

As expected atom-atom distances are reduced with the application of pressure as the volume of the unit cell decreases. Resolution on the peaks in the PDF patterns produced from BTO loaded in a DAC is poorer that the data collected in a capillary due to the lower Q_{max} (23 *vs.* 27Å $^{-1}$) which is due to the DAC body limiting the scattering angle.

Refinements of the structural models to experimental data in PDFGui using PDF data between 2.5 and 50Å^{-1} are presented in Figure 4.5. All the refined parameters from are presented in Appendix 10.

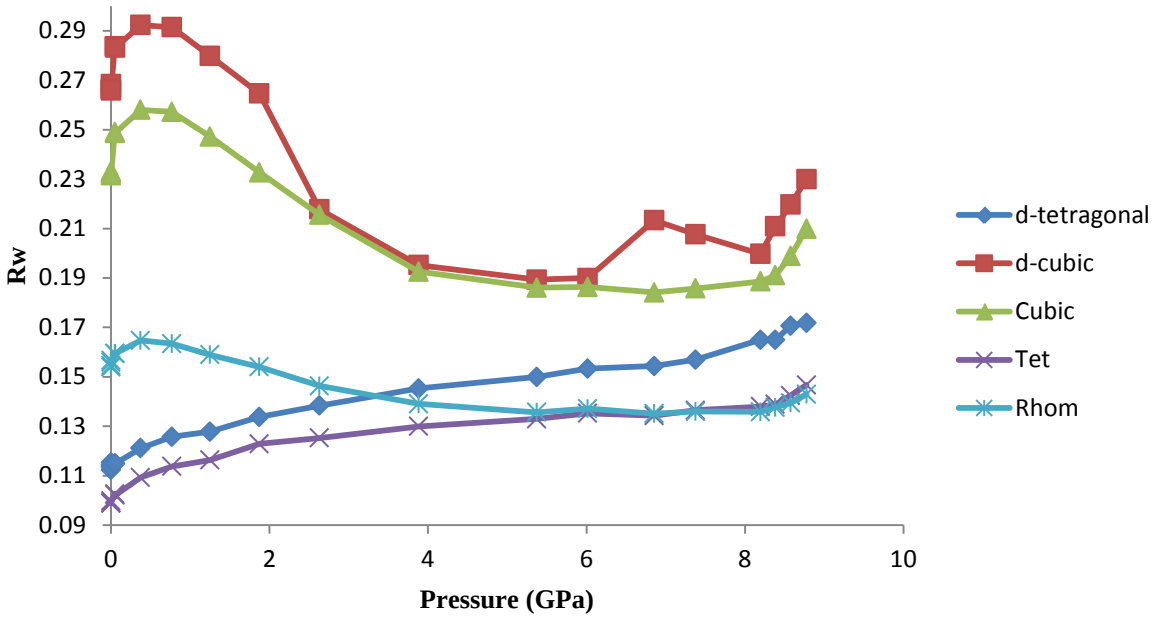

Figure 4.5: Refined *Rw* values for different models of BTO between 2.5 and 50**Å** as pressure is increased.

As can be seen from Figure 4.5, the tetragonal model provides the best fit to data at this length scale at ambient conditions and remains the best fit until higher pressures, when above roughly 6 GPa the rhombohedral model provides an equally good fit to the experimental data. Relative *Rw* values between models have been shown to indicate phase transitions at variable temperatures (Section 3.2.3.1) but with the exception of reductions in *Rw* values for the cubic and disordered cubic models there are no indications of any phase transition at 2.5GPa and the cubic and disordered cubic model provide the worst fits to the experimental data at all pressures. Fits of tetragonal and disordered-tetragonal models are presented in Figures 4.6 and 4.7.

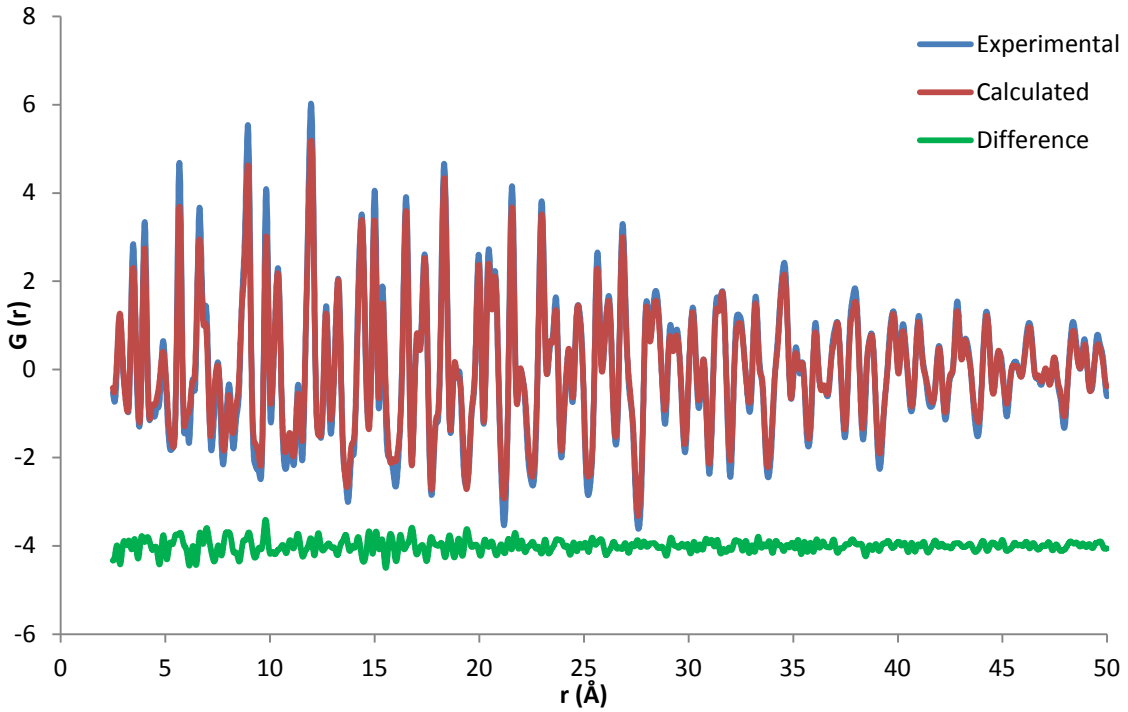

Figure 4.6: Tetragonal model fit to xPDF data of BTO in a DAC at ambient pressure.

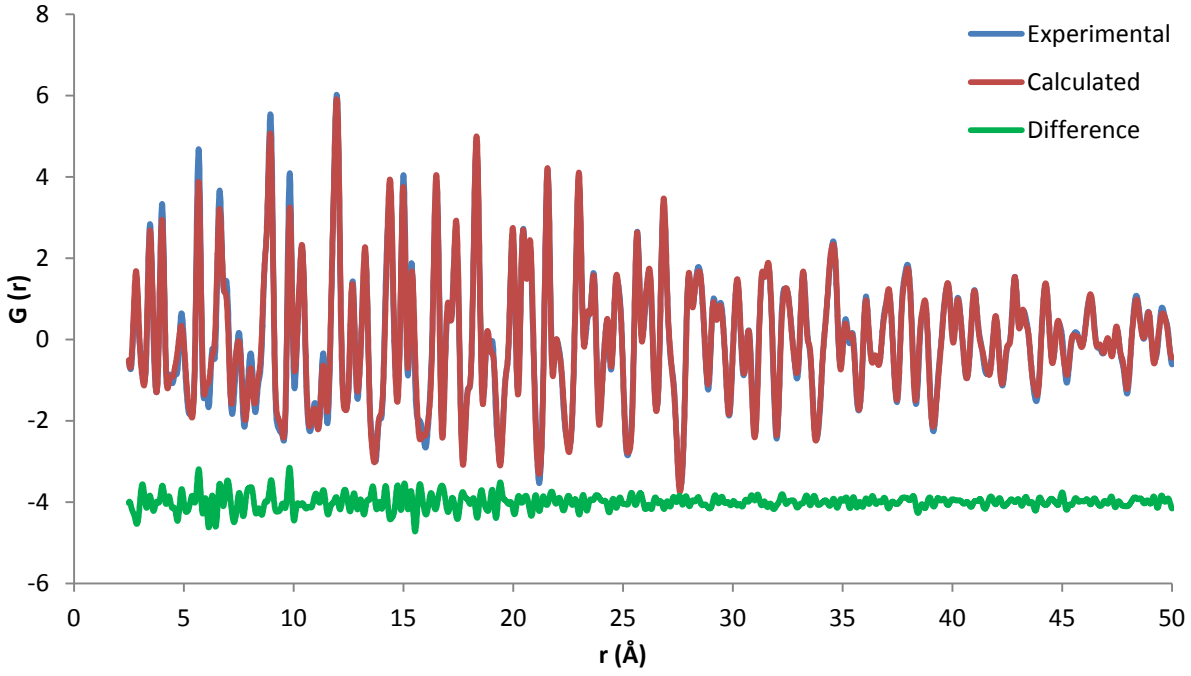

Figure 4.7: Disordered-tetragonal model fit to xPDF data of BTO in a DAC at ambient pressure.

The tetragonal model (*Rw* = 0.010) provides equally as good a fit to ambient data than the dis-ordered tetragonal model (*Rw* = 0.011) but it has already been shown in Section 3.3.3.2 that the disordered model provides a better description to the local structure of BTO (based on the first Ti-O peak) with nPDF data.

With each model having the ability to adopt a cubic structure, it is important to also consider other refinement parameters. Previous studies have suggested that the Ti atom becomes less displaced away from the centre of the oxygen octahedra as pressure is increased, with it eventually sitting in the centre of the unit cell above 10GPa.[10, 11] In the disordered cubic model the Ti atom does not move away from the centre of the unit cell in refinements at any pressures, which was also observed in previous x-ray PDF studies[10](Figure 4.8) and high temperature refinements presented in Section 3.2. The refined titanium positions from all models can be seen in Figure 4.8.

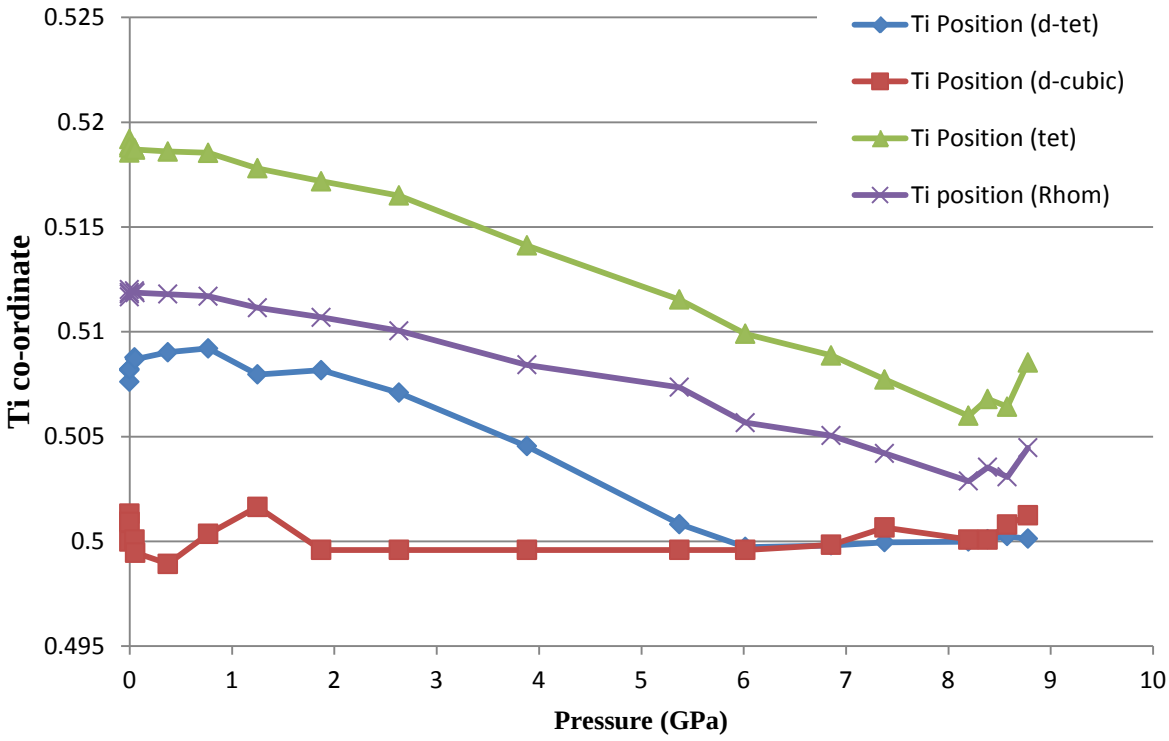

Figure 4.8: Refined titanium co-ordinates over pressure using data from 2.5 to 50A.

At the length scales 2.5 to 50Å, all models agree that the Ti displacement is reduced as pressure increases which agrees with previous studies.[2, 11] Where they differ, however, is at what pressure the Ti atom is no longer displaced from the centre of the oxygen octahedra. Rietveld analysis of x-ray diffraction patterns at high pressures show cubic lattice parameters above 2.5 GPa but $a \neq c$ at all pressure for the refined tetragonal and disordered tetragonal models (Figure 4.9). Ideally we would have an accurate model of the high temperature cubic phase and model that to the high pressure cubic phase, but in the absence of an acceptable model it is only possible to attempt to draw conclusions from other structural models. In this instance all models indicate the Ti atom is becoming less displaced with increasing pressure, it is not possible to draw firm conclusions on the displacement of the Ti atom without an acceptable model for the "*cubic*" phase however. With the refinements showing no evidence of the disordered cubic phase (analogous to the high temperature phase) it is difficult to comment on any proposed phase transition at these length scales.

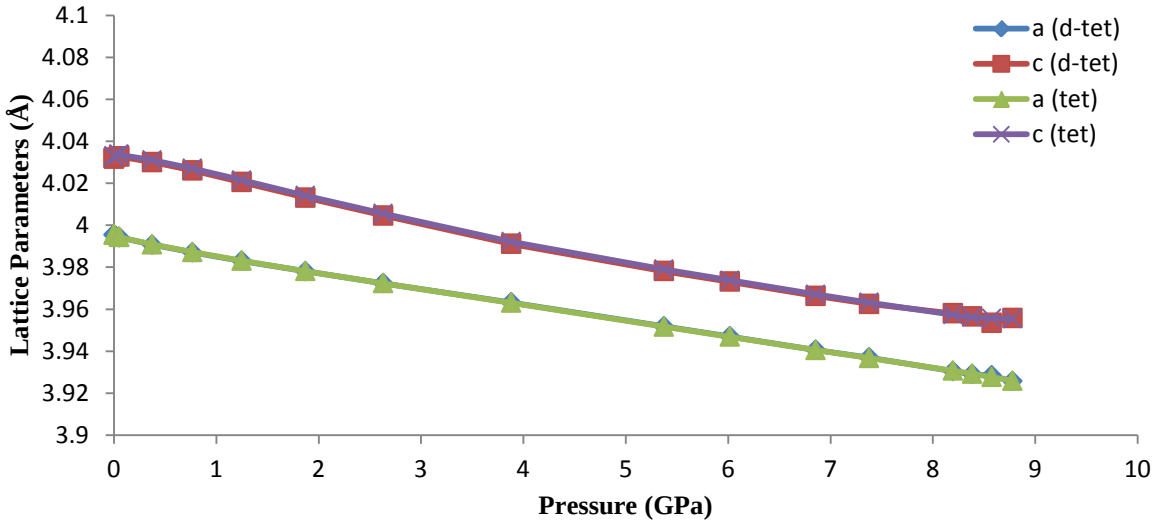

Figure 4.9: Lattice parameters as pressure is increased in the tetragonal models refined between 2.5 and 50Å.

In order to “bump” lattice parameters for the disordered-tetragonal model at ~4GPa, values were altered slightly and re-refined but returned to the values observed in Figure 4.9.

Attempts were made to model tetragonal nano-domains alongside both cubic and disordered-cubic unit cells. A tetragonal phase was included and *spdiameter* was refined to model a tetragonal nano-domain within the two cubic structures. PDFGui refinements did not indicating any nano-domains at any pressure. PDFGui chose to refine the models as mixed phase as opposed to giving meaningful nano-domain sizes using the *spdiameter* variable for refinements.

4.3.2.2 Refinements on data from 2.5 to 13Å

In order to investigate local structure, refinements were conducted from 2.5 to 13Å (Figure 4.10). All refined parameters at this length scale can be found in Appendix 11.

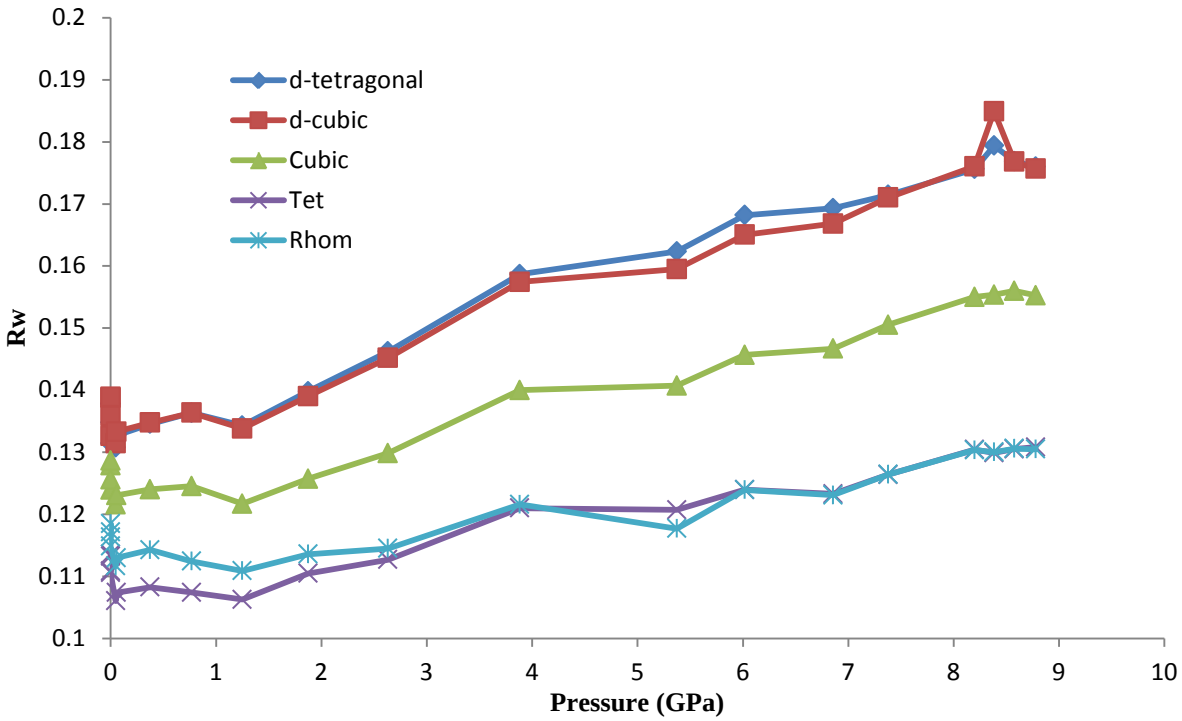

Figure 4.10: Refined *Rw* values for different models of BTO between 2.5 and 13Å as pressure is increased.

At these length scales the tetragonal model provides the best fit to the experimental data up to roughly 3GPa when the rhombohedral model provides an equally good fit. Once again there is no evidence for the disordered cubic structure at any pressure. From the *Rw* values there is also again no sign of any phase transition at 2.5GPa. Tetragonal and disordered-tetragonal fits to PDFs produced at 1.87GPa are presented in Figures 4.11 and 4.12.

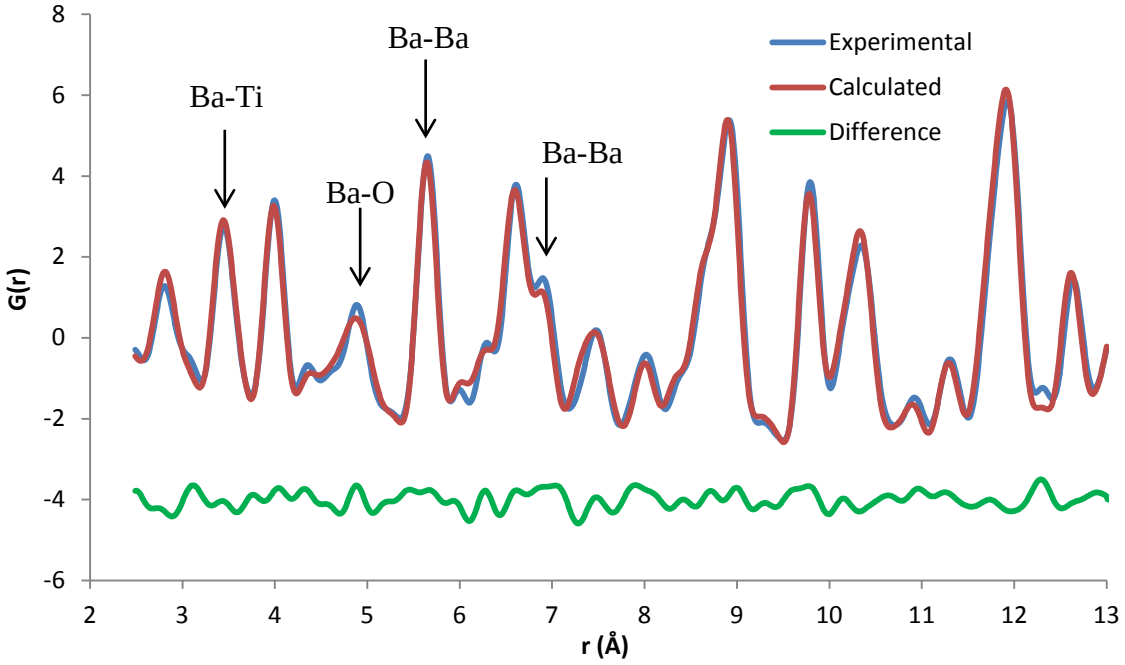

Figure 4.11: Tetragonal model fit to xPDF data between 2.5 and 13Å of BTO in a DAC at 1.87GPa (*Rw* = 0.111).

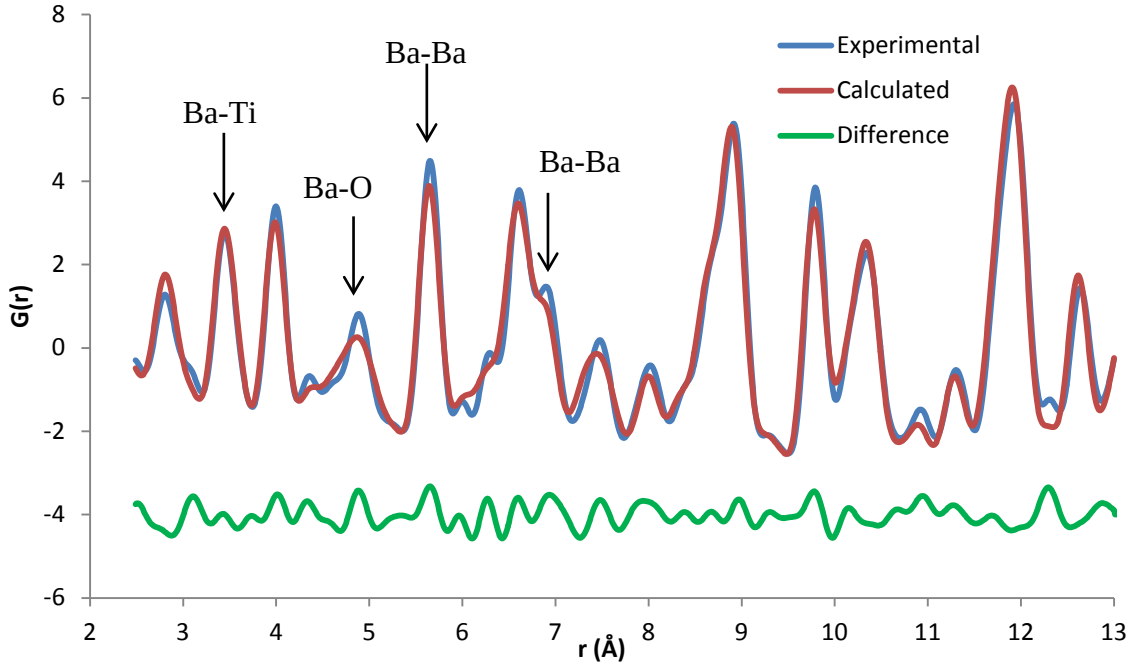

Figure 4.12: Disordered tetragonal model fit to xPDF data between 2.5 and 13Å of BTO in a DAC at 1.87GPa (*Rw* = 0.140).

It is difficult to see where the tetragonal model is providing a substantially better fit to the experimental data over the disordered tetragonal model at 1.87GPa. It can be seen however, that the tetragonal provides a marginally better fit to the Ba-O peak at ~5Å, the Ba-Ba peak at 5.6Å and the Ba-Ba peak at 6.8Å. The Ba-Ti peak at ~3.4Å also shows no variation between the two models. This means that the difference in *Rw* values are likely not down to the difference in titanium displacements between the two models.

Based on the relative *Rw* values of the theoretical models there is no evidence for another structural change at ~5GPa as suggested by Venkateswaran *et al* (1998).

Ti displacements reduce as pressure increases at these length scales with the disordered tetragonal model suggesting the Ti atom is no longer displaced above roughly 5GPa (Figure

4.13). Once again the disordered cubic model again shows essentially no titanium displacement at any pressure.

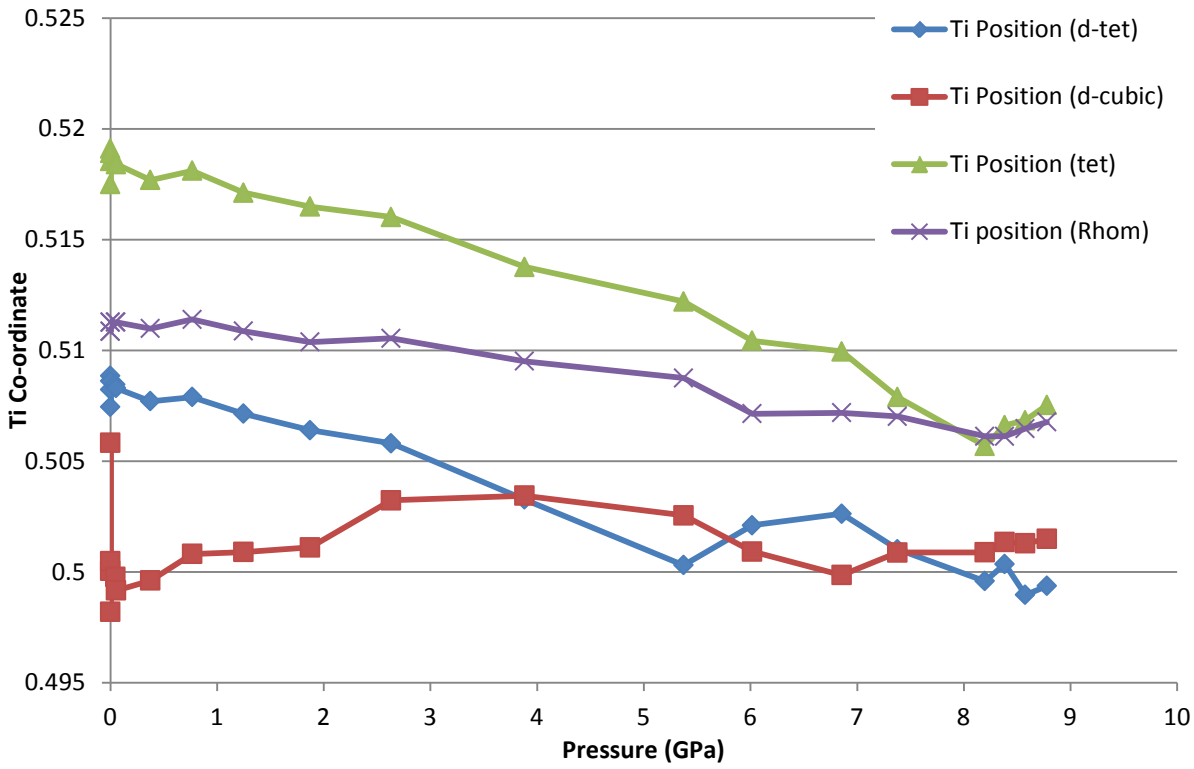

Figure 4.13: Refined titanium co-ordinates over pressure using data from 2.5 to 13Å.

If the disordered tetragonal model provides the best description of the "tetragonal" phase then it appears that the titanium atom moves towards the centre of the unit cell below 2.5GPa. An assumption could be made that this trend continues above 2.5GPa, although no firm conclusions can be made as to what pressure the titanium atom sits in the centre of the unit cell.

The standard deviations of refined Ti positions from data between 2.5 to 13A (Table 2.3) show three standard deviations in Ti co-ordinate of 0.0016 suggesting the trends observed in Figure 4.13 and 4.8 are not simply within errors, although this standard deviation was for data collected at 500K.

At short range lattice parameters do appear to converge to $a = c$ for both tetragonal models (Figure 4.14). As a result the disordered tetragonal model resembles a cubic structure above 5GPa, whereas the tetragonal model possesses cubic lattice parameters but the Ti atom is still displaced from the centre of unit cell.

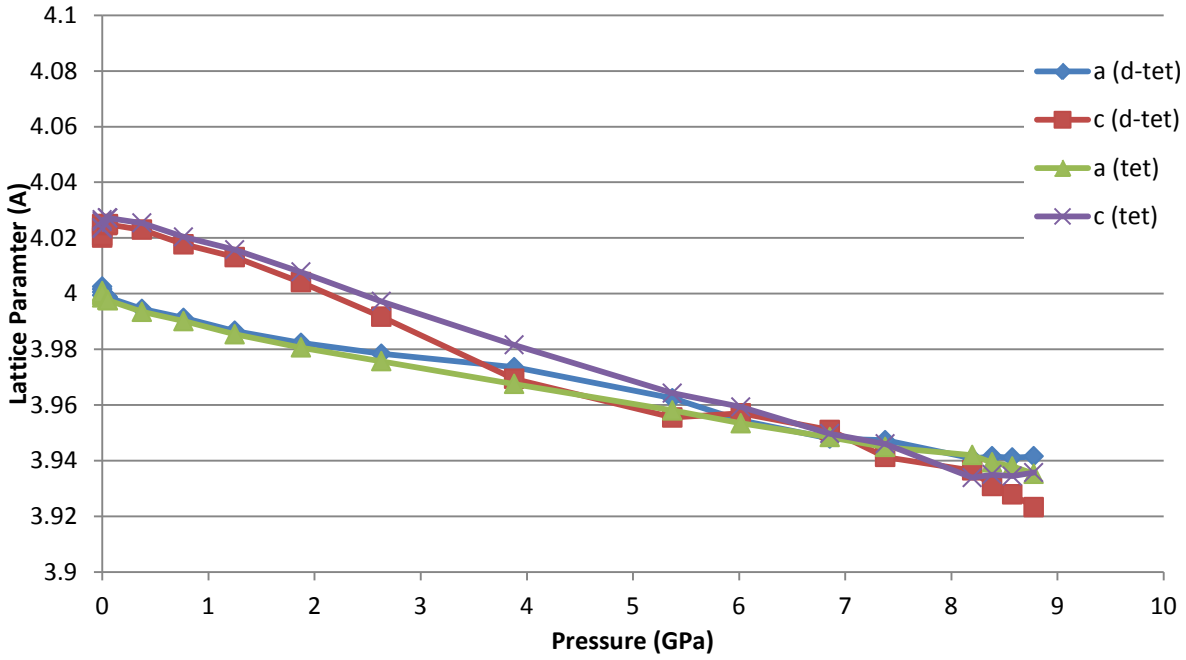

Figure 4.14: Lattice parameters as pressure is increased in the tetragonal models refined between 2.5 and 13Å.

This is not observed in the refinements from 2.5 to 50Å which is interesting as those refinements include much more of the long range data and thus more closely represent an average structure of BTO.

As with the variable temperature refinements conducted on BTO it is difficult to draw any conclusions on local structure without the first Ti-O peak. As very high pressure nPDF studies are not possible, xPDF analysis is currently the only way of investigating the local structure of BTO using PDF. If an acceptable model for the local structure was devised for the high

temperature cubic phase this could be applied to the xPDF data and then, assuming both high temperature and high pressure cubic phases are comparable in terms of Ti displacements, this model could then be used to investigate at what pressure the Ti atom sits in the centre of the unit cell. If the unit cell becomes locally cubic diffuse scatter should also disappear but no study concerning diffuse scattering above 10GPa was found at the time of writing this thesis.

4.3.2.3 Refinements on data from 37 to50Å

In order to investigate the long range PDF data and hopefully show the differences between local and long range structure of BTO at high pressure, refinements were run on data from 37 to 50Å. Problems were encountered when refining the disordered cubic model at these length scales with very poor *Rw* values and the refinements becoming stuck in false minima. As a result the disordered cubic model is not discussed in this section. All refined parameters at this length scale can be found in Appendix 12.

At these length scales the tetragonal (Ti displaced along [001]) and Comes model (4-site along {111}) show equally good fits to the data below 4 GPa (Figure 4.15). Where as the short range refinements showed no clear signs of a phase transition at 2.5 GPa there is a sharp decrease in *Rw* values for cubic and rhombohedral models as pressure increases up to roughly 4 GPa. Above 8GPa the rhombohedral, tetragonal and disordered tetragonal models provide equally good fits to the experimental data.

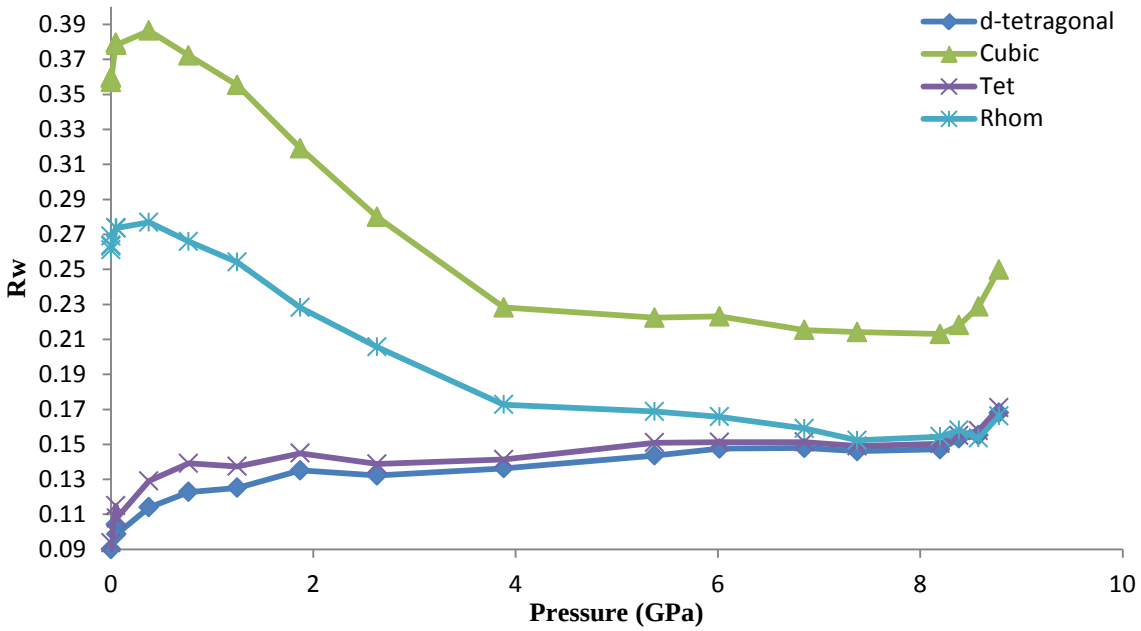

Figure 4.15: Refined *Rw* values for different models of BTO between 37 and 50Å as pressure is increased.

Fits of the cubic (highest *Rw*) and rhombohedral (one of the lowest *Rw*) models to PDFs at 8.78GPa can be seen in Figures 4.16 and 4.17. There is a ~8% difference (*Rw*=0.084) difference between these fits and it is clear that rhombohedral model does provide a better fit to experimental data. There is no evidence in literature for the structure of BTO to be on average rhombohedral above 2.5GPa however but as mentioned previously this rhombohedral model could be adopting a cubic symmetry with the Ti atom sat in the centre of the unit cell and $\alpha=90^{o}$.

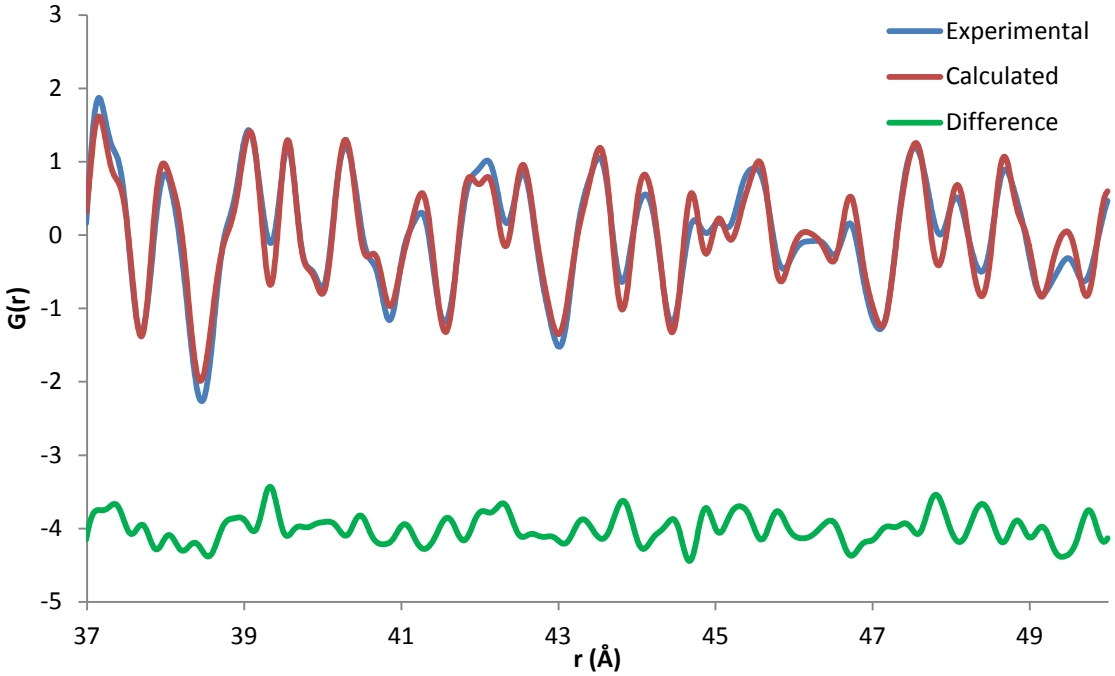

Figure 4.16: Cubic model fit to xPDF data between 37 and 50Å of BTO in a DAC at 8.78GPa (*Rw* = 0.250).

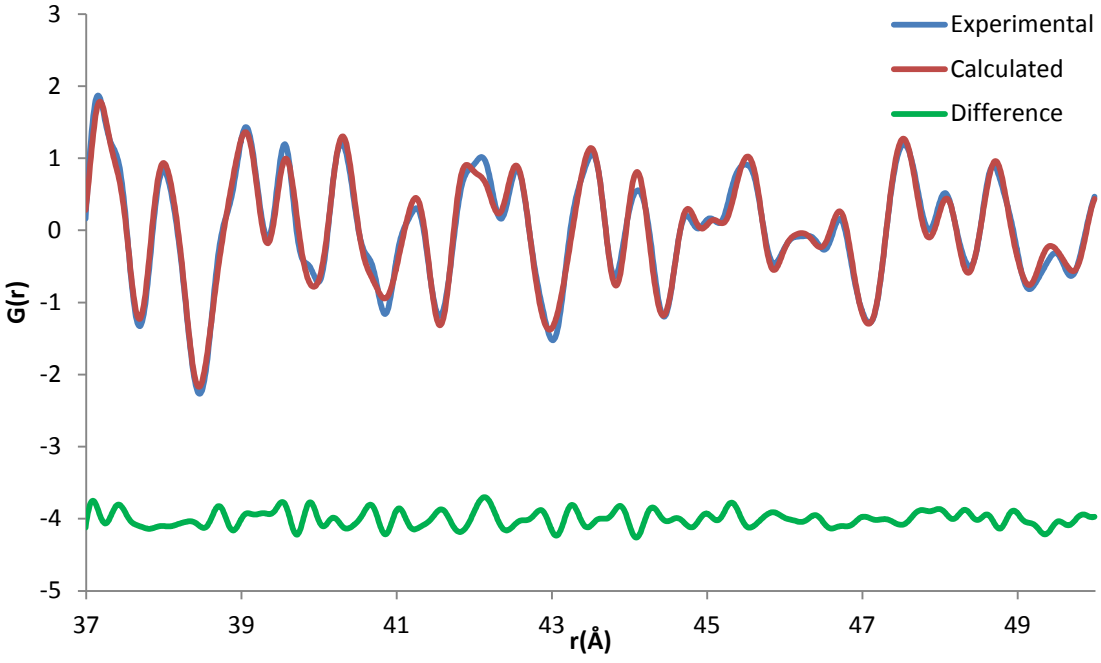

Figure 4.17: Rhombohedral model fit to xPDF data between 37 and 50Å of BTO in a DAC at 8.78GPa (*Rw* = 0.166).

The Ti atom behaves differently for each model with the Ti atom sitting in the centre of the unit cell above ~3 GPa for the tetragonal and rhombohedral refinements and the Ti atom still being off centre up to 7GPa in the disordered tetragonal model (Figure 4.18). Again the lattice parameters do not converge for the tetragonal refinements (Appendix 12) but the rhombohedral model's Ti position appears to sit roughly in the centre of the unit cell and the angles are close to 90^{o} (89.74^{o}) so despite a similar fit to the experimental data as the tetragonal and disordered tetragonal models the rhombohedral model closely resembles a cubic model at 8.78GPa at these length scales.

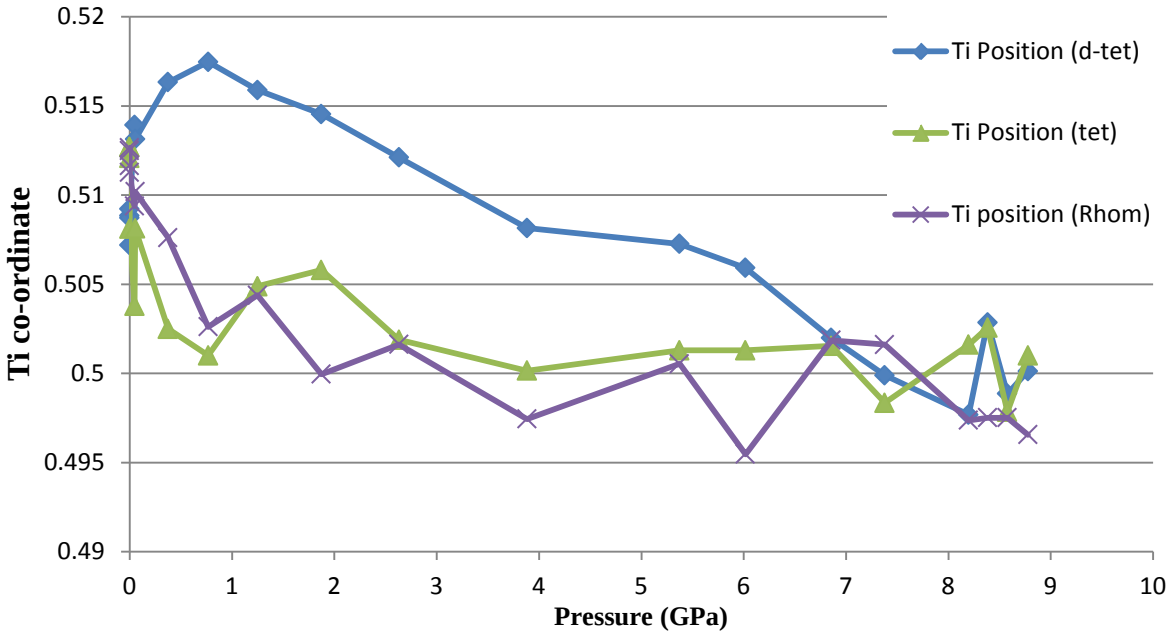

Figure 4.18: Refined titanium co-ordinates over pressure using data from 37 to 50Å.

The long range refinements show that the tetragonal and disordered tetragonal models clearly provide a much better fit to the experimental data below ~6GPa. At longer range the cubic model should provide the best fit above 2.5GPa (which it does not) and ideally all models should adopt a cubic structure above this pressure although the rhombohedral model, which

provides one of the best fits to experimental data at the highest pressure, does adopt something close to a pure cubic structure.

4.4 Conclusions

Refinements at short range do not indicate a phase transition at 2.5GPa (or at 5GPa) and show no evidence for a disordered cubic phase at any pressure or length scale. It is unclear from these results what the local structure of BTO is in the high pressure phase, most likely due to the lack of the first Ti-O peak in the PDFs. The high pressure PDF data clearly indicates that the Ti atom is still off-centre in all the models above the suggested phase transition point, although it is not clear at what pressure the Ti atom truly sits in the centre of the unit cell.

Without a more detailed analysis of the refinement approach adopted by Ehm *et al* (2011) it is not possible to compare refinement results as it is unclear how they arrived at some of their conclusions.

While the refinements do hint at differences between local and long range structure, changes are so subtle that it is not possible to ascertain the local structure of BTO at any pressure by using xPDF data alone but it could be possible to investigate the displacement of the Ti atom when an acceptable model has be devised for the high pressure phase.

4.5 Future Work

Following on from the future work proposed for the variable temperature refinements in Section 3.5, it would be interesting to take a model devised for a high temperature phase produced from RMC refinements and then apply it to the high pressure xPDF data and then use this to investigate Ti displacements. Despite this the Raman spectra of high temperature and high pressure “cubic” phases possess significant differences between them[5] so it is likely this model would still not be a perfect description of the high pressure phase.

It would be interesting to see what model RMCprofile produced when refining a large box of atoms to our high pressure xPDF data. Although it is not clear if the xPDF would contain enough information on local structure (without the first Ti-O peak) for an accurate model to be produced. If modelling of the high pressure cubic phase was successful it would then be useful to collect data above 10GPa to see at what point models adopt a cubic structure (if at all).

If high pressure nPDF experiments became possible it would then an investigation of the first Ti-O peak over pressure would provide a lot of information on the Ti displacements as pressure is increased. If BTO adopted a truly cubic structure then this peak would be a single peak containing six Ti-O distances of equal length.

References

1. L. Liu and W. Basset, *Elements, Oxides and Silicates*, Oxford University Press, New York, 1986.
2. S. A. Hayward, S. A. T. Redfern, H. J. Stone, M. G. Tucker, K. R. Whittle and W. G. Maeshall, *Zeitschrift für Kristallographie*, 2005, **220**, 735-739.
3. P. Pruzan, D. Gourdain, J. C. Chervin, B. Canny, B. Couzinet and M. Hanfland, *Solid State Communications*, 2002, **123**, 21-26.
4. A. Jayaraman, J. Remeoka and R. Katiyar, in *Defect Properties and Processing of High Technology Nonmetallic*, Materials Research Society, 1986.
5. A. K. Sood, N. Chandrabhas, D. V. S. Muthu and A. Jayaraman, *Physical Review B*, 1995, **51**, 8892-8896.
6. U. D. Venkateswaran, V. M. Naik and R. Naik, *Physical Review B*, 1998, **58**, 14256-14260.
7. J. P. Itie, B. Couzinet, A. Polian, A. M. Flank and P. Lagarde, *Europhysics Letters*, 2006, **74**, 706-711.
8. S. Ravy, J. Itie, A. Polian and M. Hanfland, *Physical Review Letters*, 2007, **99**, 117601(117604).
9. K. W. Chapman, P. J. Chupas, G. J. Halder, J. A. Hriljac, C. Kurtz, B. K. Greve, C. J. Ruschman and A. P. Wilkinson, *Journal of Applied Crystallography*, 2010, **43**, 297-307.
10. L. Ehm, L. A. Borkowski, J. B. G. Parise, S and Z. Chen, *Applied Physics Letters*, 2011, **98**, 21901.
11. J. P. Itie, B. Couzinet, A. Flank, P. Lagarde and A. Polian, AIP Conference - 13th International Conference, 2007.

5. LOCAL STRUCTURE OF $Ba_{1-x}Bi_xTi_{1-x}Yb_xO_3$

5.1 Introduction

This study was part of an investigation into the structure of $Ba_{1-x}Bi_xTi_{1-x}Yb_xO_3$ (BBTYb), a new material produced *via* a solid state reaction.[1] While there are very few studies that discuss this system there have been others investigating the effect of individually doping $BaTiO_3$ (BTO) with either Bi^{3+} or Yb^{3+} and also the structure of $BiYbO_3$ is known.[2] X-ray powder diffraction shows that $BiYbO_3$ has a triclinic cell with a *P*-1 space group.[2]

It is possible to substitute a large variety of dopants on both the A and B site of BTO and this doping can affect the physical properties of BTO. The ability to dope ions onto either site is dictated the ionic radii of the dopants, with large ions substituting for Ba and smaller ions substituting for Ti. Depending on the charge of the ion substitution it must be accompanied by charge compensation mechanisms which can lead to vacancies in the BTO lattice.[3]

When doped into the lattice, Bi^{3+} ions will occupy the A sites in BTO creating a charge imbalance that is compensated by electron and barium vacancies.[4] X-ray diffraction and scanning electron microscopy studies show that below 3% doping $Ba_{1-x}Bi_xTiO_3$ is single phase and possess a tetragonal structure but above this level a second phase ($Bi_2Ti_2O_7$) appears.[4, 5] The unit cell volume decreases as more Bi^{3+} doping increases which can be attributed to Bi^{3+} (1.17Å, 8 co-ordinate) possessing a smaller ionic radius than Ba^{2+} (1.61Å 12 co-ordinate, 1.42Å - 8 co-ordinate,).[6] It should also be noted that the Bi^{3+} ions also possess a lone-pair of electrons which can affect local structure.

Yb^{3+} substitution will occur exclusively at the B site and it possesses a larger ionic radus (0.87 Å than Ti^{4+} (0.61Å).[7] This introduces defects into the structure in the form of negatively charged defect centres and oxygen vacancies.[8] When the Yb concentration increases above

2.5 mol% $Ba(Ti_{1-x}Yb_x)O_{3-x/2}$ becomes cubic and the unit cell volume increases with increasing Yb content.[7]

BBTYb, with doping on both sites, possess a tetragonal space group (*P*4*mm*) when $x<0.04$ and at higher values of x can be indexed in the cubic *Pm*3*m* space group.[1] The unit cell volume increases as x is increased most likely due to the relative ionic sizes of Ti^{4+} and Yb^{3+} and this may also be accompanied with large lattice strains which can impact on the local structure of BBTYb. Raman spectroscopy indicates that displacements of the Ti atom may be affected by the lone pair of the Bi^{3+} ion and also still shows forbidden Raman bands in the cubic structure.[1] Strathdee *et al* 2011 also suggested non-tetragonal clusters in the tetragonal unit cell with these clusters increasing with x. It was shown that when $x\geq0.16$ Yb combines with Ti to form a secondary phase which was speculated to be $Yb_2Ti_2O_7$ although it was also shown that this secondary phase was present when $x\leq0.16$ albeit in very small amounts.

Schilleo *et al* (2013) later investigated $Ba_{1-x}Bi_xTi_{1-x}Yb_{x/2}Fe_{x/2}O_3$ and related their findings to BBTYb. In this system there will be a lower concentration of Yb on the B site due to the introduction of Fe^{3+}. Scanning electron microscopy (SEM) was used to examine the grain structure of $Ba_{1-x}Bi_xTi_{1-x}Yb_{x/2}Fe_{x/2}O_3$ at varying values of x and found the average grain size was smaller when Bi, Yb and Fe were doped into the system and it also revealed the presence of a secondary phase that increased in concentration as x was increased. This phase was of higher density than $Ba_{1-x}Bi_xTi_{1-x}Yb_{x/2}Fe_{x/2}O_3$ and elemental analysis showed the presence of Yb rich regions which increased in concentration and size as x increased.

In a different study clustering was also observed in $_{(1-x)}BaTiO_3$-$_xLaYO_3$ systems with electron diffraction suggested the formation of $LaYO_3$ based clusters within the BTO lattice.[3]

The structure and composition of the clusters was not determined but they were observed as low as $x = 0.025$.

While there are no previous pair distribution function studies of BBTYb it may be an ideal method for investigating local structure. There have been a few previous studies looking at doping of BTO on the B site[9-11], no previous study was found with doping on both sites simultaneously.

Laulhe *at al* (2009) observed two distinct oxygen octahedra when Zr was doped onto the B site showing longer Zr-O distances and a Zr-O octahedra related to $BaZrO_3$ which possess a larger unit cell volume that $BaTiO_3$. They also concluded that the Ti^{4+} was still displaced when Zr was doped into the structure so it is possible that this is still the case in BBTYb.

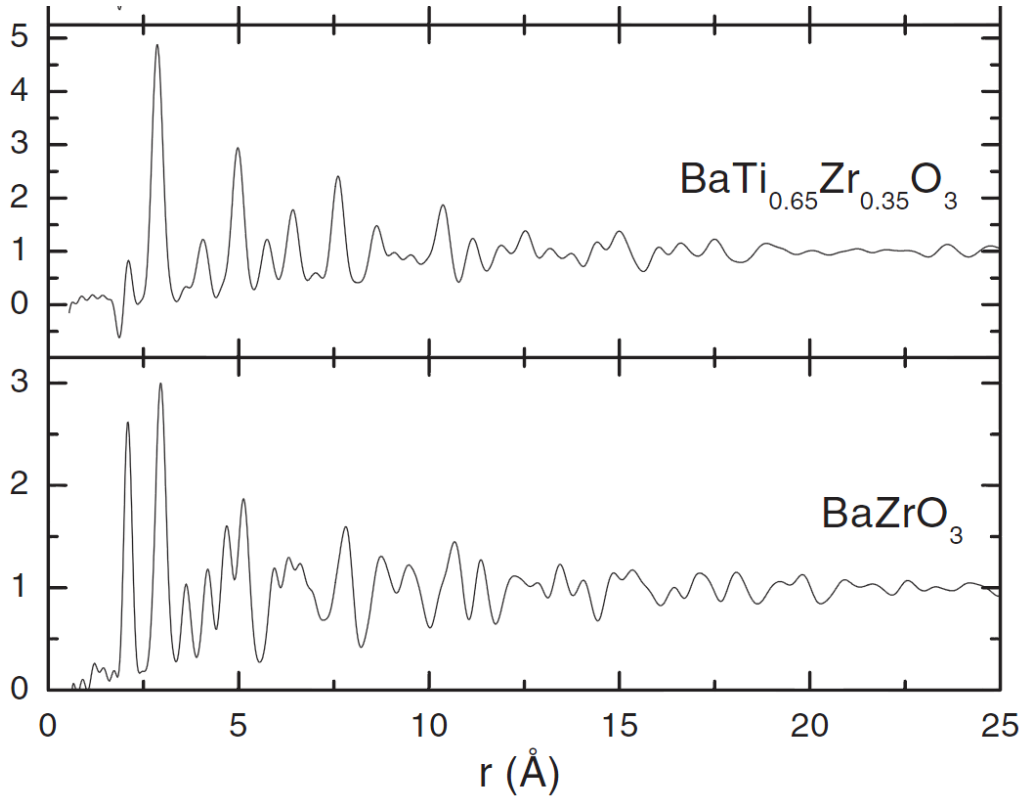

Figure 5.1: Experimental neutron pair distribution functions of $BaTi_{1-x}Zr_xO_3$ collected at 300K. (Taken from Laulhe *et al* 2009).[9]

The BBTYb system clearly possesses some form of local disorder that deviates away from the average structure suggested by X-ray diffraction. Any clustering may show up in PDF analysis and nPDF studies may shed light on the shape and size of the oxygen octahedra in the various systems. The aims of this investigation were to investigate any clustering present, determine local structure and try and ascertain how Bi^{3+} and Yb^{3+} are distributed in the lattice. It will be difficult to relate any structural changes back to pure BTO with the exact local structure of BTO still unknown (Chapter 3).

5.2 Experimental and Methodology

5.2.1 Rietveld Analysis of x-ray and Neutron Diffraction Data

X-ray diffraction patterns were collected at the APS on beamline 11-ID-B. Samples were provided by collaborators and loaded into kapton capillaries 1mm in diameter. The samples provided were $BaTiO_3$ and BBTYb with $x = 0.02$, $x = 0.04$, $x = 0.06$, $x = 0.08$, $x = 0.10$ and $x = 0.15$. The beam energy was set to 58.25KeV ($\lambda = 0.2127$Å) and a CeO_2 calibration was conducted which calibrated the sample to detector distance of 840.538mm. Samples were loaded in an automatic sample changer and one image was collected for each sample which was composed of 20 x 0.1 second exposures summed together. These images were then input into Fit2d, the beam stop was masked out and then they were integrated in two theta using parameters obtained from the CeO_2 calibration.

Rietveld analysis was then conducted on all the x-ray diffraction patterns from each sample. For samples where $x = 0.02$ and 0.04 a structure with a *P*4*mm* space group was used and for samples where $x \geq 0.06$ a *Pm*3*m* space group. Bi and Yb atoms were introduced in samples where $x \neq 0$ using partial occupancies on the A and B site respectively (Figure 5.2).

Add Phase

a	3.999669	b	3.999669	c	4.034833	Edit Cell
α	90.0000	β	90.0000	γ	90.0000	

*	name	type	ref/damp	fractional coordinates			Mult	Occupancy	Uiso
1	Ba1	BA+2	0 U0 0	0.000000	0.000000	0.000000	1	0.9600	0.00624
2	Ti1	TI+4	X0 U0 0	0.500000	0.500000	0.488815	1	0.9600	0.00835
3	O1	O-2	0 0 0	0.500000	0.500000	-0.000251	1	1.0000	0.01751
4	O2	O-2	0 0 0	0.000000	0.500000	0.512997	2	1.0000	0.01751
5	BI5	BI	0 U0 0	0.000000	0.000000	0.000000	1	0.0400	0.00624
6	YB6	YB	0 U0 0	0.500000	0.500000	0.500000	1	0.0400	0.00835

Figure 5.2: Phase set up in GSAS for $Ba_{0.96}Bi_{0.04}Ti_{0.96}Yb_{0.04}O_3$.

For pure BTO all positions and thermal parameters were refined but for samples where $x>0$ GSAS produced both unrealistic U_{iso} values for the O1, O2, Bi and Yb atoms and oxygen positions were moving far away ideal positions when $x = 0$, 0.02 and 0.04 (with no benefit to the goodness of fit). With the sensitivity to the oxygen atoms in x-ray diffraction patterns of BTO already discussed in Section 3.2.2 the oxygen positions and thermal parameters were fixed from the values obtained in BTO for tetragonal samples and the O U_{iso} was fixed in the cubic sample. The Bi U_{iso} values were constrained to be the same as Ba U_{iso} and the Yb U_{iso} values were constrained to be the same as the Ti U_{iso} values. The Yb atom was set to sit in the centre of the unit cell for all samples and the position was not refined. Results are presented and discussed in Section 5.3.1.1.

Neutron diffraction patterns were collected at ISIS on the GEM beam line. Due to the longer collection times association with neutron diffraction it was not possible to run as many samples as using x-ray diffraction. As a results four samples were studied where $x = 0$, $x = 0.02$, $x = 0.10$ and $x = 0.15$. Samples were sealed in vanadium cans in an argon filled glove box and then sealed and transported in a desiccator to ensure no water was present in the sample. Two data collections of 500μAhr each were performed on each sample but for Rietveld analysis only one of these collections is examined for each sample. Diffraction

patterns from banks 4, 5 and 6 were input into GSAS and fit using identical models to those used for x-ray diffraction but thermal parameters for the Bi and Yb atoms were again constrained to be the same as Ba and Ti U_{iso} values, respectively. The oxygen positions (where appropriate) and O U_{iso} values were also refined due to the increased sensitivity to the oxygen atoms in neutron diffraction. Results are presented and discussed in Section 5.3.1.2.

5.2.2 PDF Analysis

For xPDF analysis the same samples as outlined in Section in 5.2.1 were again investigated at the APS, beamline 11-ID-B. The detector was moved toward the samples and another CeO_2 calibration was conducted. The refined sample to detector distance was then 156.912mm and the energy was kept the same for the same set of capillaries as outlined in Section 5.2.1. For each sample one image was collected that consisted of 200 x 0.5 second exposures that were summed together. A diffraction pattern for an empty kapton capillary of identical diameter was also collected to act as the background for all the samples. These images were then masked in Fit2d and integrated using the parameters obtained from the CeO_2 calibration. The integrated patterns were then input into PDFGetX2 and Fourier transformed using a Q_{max} of 24Å^{-1}.

The same nPDF diffraction data from Section 5.2.1 was used to produce PDFs and detector banks 6, 7 and 8 of GEM were used for the Fourier transform in GudrunN using a Q_{max} of 40 Å^{-1}. Both data collections of 500μAhr were conducted for each sample and these were averaged in GudrunN to produced better statistics.

Modelling in PDFGui concentrated on the sample where x=0.15 due to this possessing the clearest changes in the PDF pattern. The aim was to model this sample and then use this as a starting model to investigate the local structure in samples with lower values of x. For clarity

the models used and justifications for their use will be presented in Section 5.3 as the results from one modelling led to the next approach.

A differential PDF was produced to investigate differences in the PDF patterns of BTO and BBTYb with $x = 0.15$. This was simply done by subtracting the experimental PDF of BTO from the BBTYb and then individual peak fitting was conducted using fityk.

5.3 Results and Discussion

5.3.1 Rietveld Analysis of Diffraction Data

5.3.1.1 Analysis of X-ray Diffraction Data

With x-ray and neutron diffraction data available for samples of varying values of x it is possible to run Rietveld analysis on the diffraction patterns before looking at local order/dis-order. The x-ray diffraction patterns for BBTYb with differing values of x can be seen in Figure 5.3.

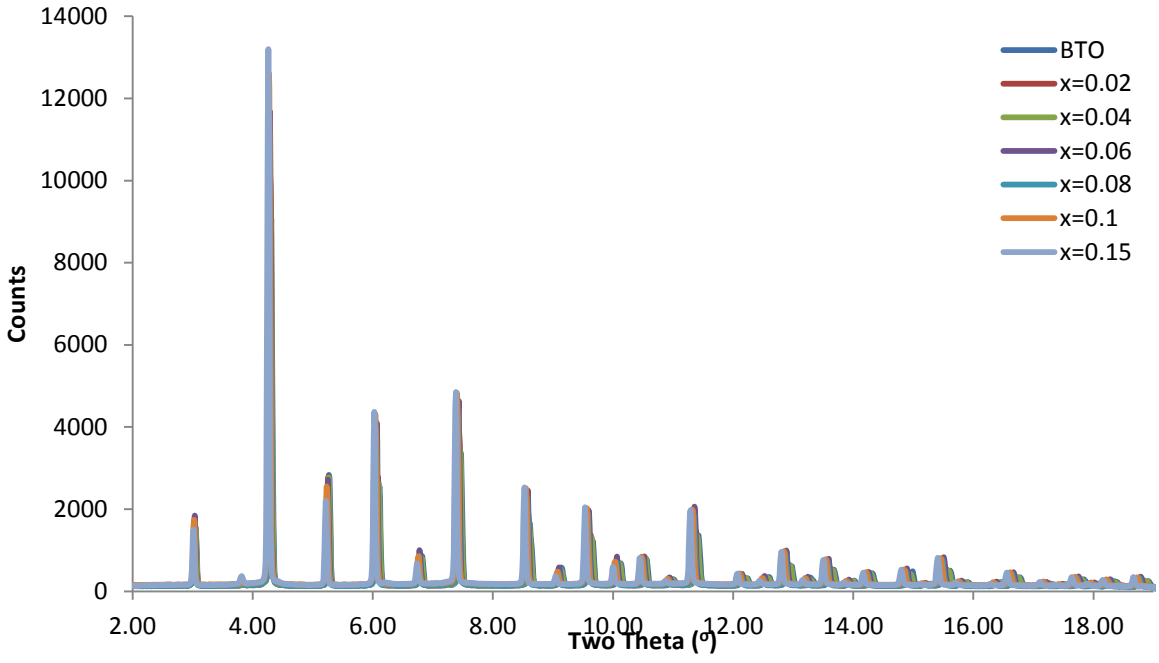

Figure 5.3: X-ray diffraction pattern for BBTYb samples with different values of x.

While it is not very clear in Figure 5.3 it is clear in Figures 5.4 and 5.5 that the unit cell volume appears to be increasing as x increases, consistent with previous studies (Section 5.1). Figure 5.4 shows the {002}/{200} peaks merge into a single reflection {200} when $x \geq 0.06$ with is consistent with the findings of Strathdee *et al* (2011).[1] For values of x higher than 0.06 this peak appears to remain a single peak and shifts to lower values of two theta, consistent with an increase in unit cell volume.

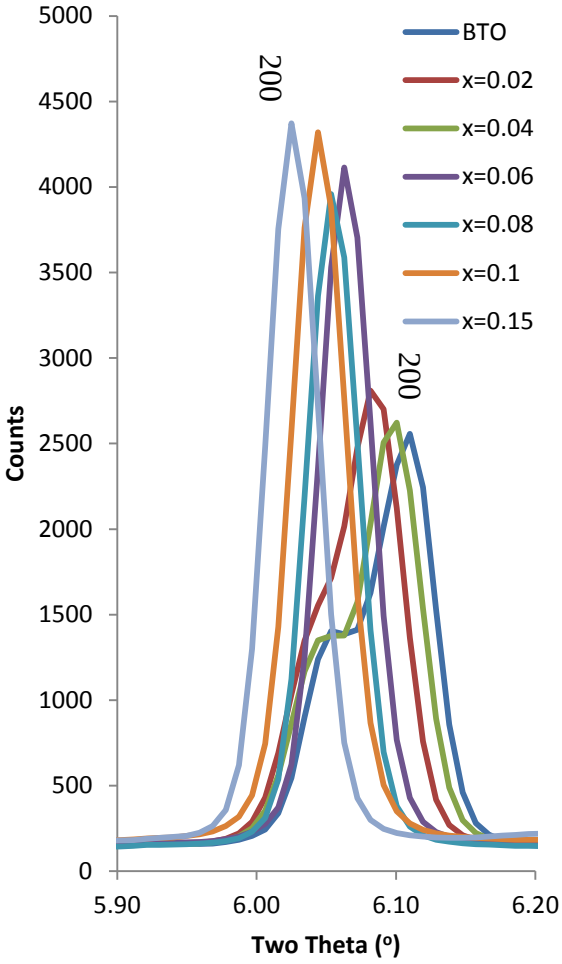

Figure 5.4: {002}/{200}for $x \leq 0.04$.

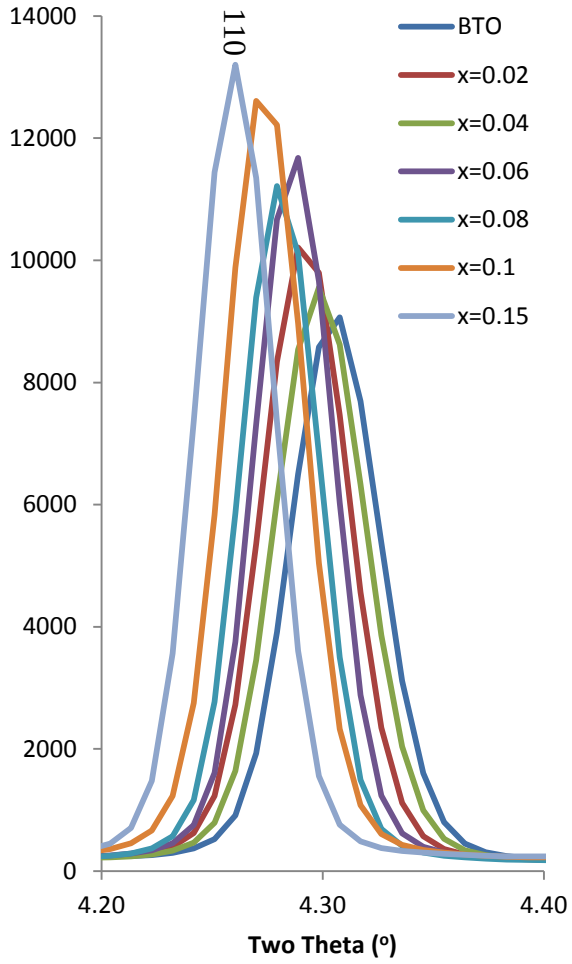

Figure 5.5: {110} reflection with varying x.

Previous Rietveld analysis has shown that the diffraction patterns for $x<0.04$ can be indexed using a *P*4*mm* space group and for x=0.06 to 0.08 can be indexed using a *Pm*3*m* space group.[1] Rietveld analysis was undertaken on the x-ray diffraction patterns collected for samples

between x=0 and x=0.15 and the refined parameters can be seen in Table 5.1 and all the Rietveld fits can be seen in Appendix 13.

Table 5.1: Refined parameters from Rietveld refinements of x-ray diffraction data from BBTYb samples with different values of x.

	BTO	x =0.02	x=0.04	x=0.06	x=0.08	x=0.1	x=0.15
wRp	0.0607	0.0519	0.0435	0.0551	0.0569	0.0480	0.0472
a (Å)	3.9939(2)	4.0077(1)	3.9997(1)	4.0229(1)	4.0290(1)	4.0356(1)	4.0484(1)
c (Å)	4.0286(2)	4.0372(2)	4.0348(2)				
c/*a*	1.0087	1.0074	1.0088				
Volume (Å^3)	64.816	65.319	65.114	65.1074	65.4018	65.7226	66.3504
Ti *z*	0.488(8)	0.490(10)	0.489(5)				
O1 *z*	-0.0003(69)	-0.0003	-0.0003				
O2 *z*	0.513(4)	0.513	0.513				
Ba U_{iso} (Å^2)	0.0053(2)	0.0083(3)	0.0061(2)	0.0104(3)	0.0121(3)	0.0146(3)	0.0183(5)
Ti U_{iso} (Å^2)	0.0042(6)	0.0022(8)	0.0083(7)	0.0068(5)	0.0065(5)	0.0060(4)	0.0057(6)
O1 U_{iso} (Å^2)	0.0175(3)	0.0175	0.0175	0.0175	0.0175	0.0175	0.0175
O2 U_{iso} (Å^2)	0.0175(3)	0.0175	0.0175				
Bi U_{iso} (Å^2)		0.00834	0.0061(2)	0.0104(3)	0.0121(3)	0.0146(3)	0.0183(4)
Yb U_{iso} (Å^2)		0.00222	0.0083(7)	0.0068(5)	0.0068(5)	0.0060(4)	0.0057(6)

It can be seen in Table 5.1 and Figures 5.4 to 5.5 that the samples with x = 0.02 and x = 0.04 appear to have been mixed up. While there is no way to be certain it is likely that these capillaries may have been labelled incorrectly and x = 0.02 is actually the x = 0.04 sample (and *vice versa*). If this was the case then it can be seen that unit cell volume increases as x increases. The Rietveld fits for tetragonal x = 0.04 and cubic x = 0.06 can be seen in Figures 5.6 and 5.7.

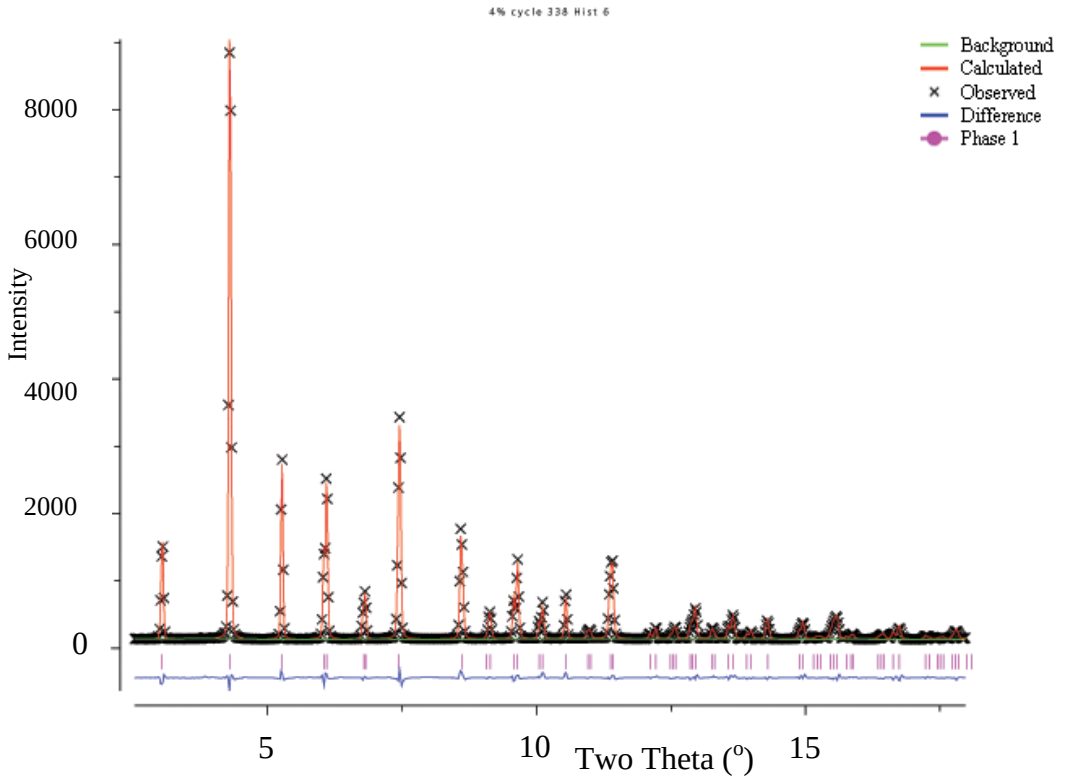

Figure 5.6: Rietveld fit of $Ba_{0.96}Bi_{0.04}Ti_{0.96}Yb_{0.04}O_3$ using a *P*4*mm* space group.

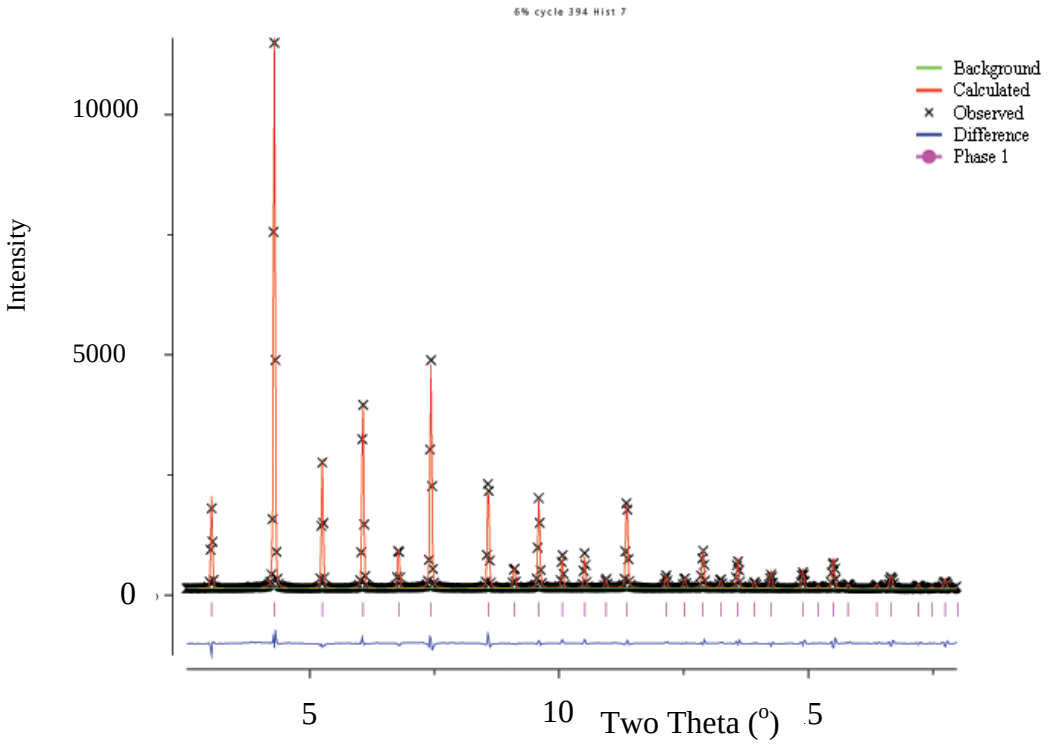

Figure 5.7: Rietveld fit of 5.2 $Ba_{0.94}Bi_{0.06}Ti_{0.94}Yb_{0.06}O_3$ using a *Pm*3*m* space group.

The Ba/Bi U_{iso} value from the refinements increases with increasing substitution which would suggest that the Bi is not sitting perfectly in the (0,0,0) position in the unit cell. If the Bi atom is displaced then the U_{iso} value would be increased to effectively increase the uncertainty in the position of atoms on the A site. The Ti/Yb U_{iso} values do not show any clear trend as Yb concentration is increased, this would suggest that the Yb atom is sat in the centre of the unit cell based on these refinements (on average).

5.3.1.2 Analysis of Neutron Diffraction Data

Diffraction data was taken from banks 4, 5 and 6 of GEM and input into GSAS and refined using the same models as in Section 5.3.1.2. The refined parameters can be seen in Table 5.2.

Table 5.2: Refined parameters from Rietveld refinements of neutron diffraction data from BBTYb samples with different values of *x*.

Parameter	BTO	*x* = 0.02	*x* = 0.10	*x* =0 .15
Total wRp	0.0842	0.1027	0.0742	0.1080
a (Å)	3.99360(5)	4.00220(9)	4.0365(7)	4.04980(9)
c (Å)	4.03490(5)	4.0377(1)		
c/*a*	1.0103	1.0089		
Volume (Å^3)	64.35	64.67	65.77	66.33
Ti *z*	0.510(1)	0.475(1)		
O1 *z*	-0.0301(6)	0.0225(5)		
O2 *z*	-0.5219(9)	0.512(1)		
Ba/Bi U_{iso} (Å^2)	0.0020(2)	0.0425(3)	0.0162(5)	0.017(7)
Ti/Yb U_{iso} (Å^2)	0.0059(3)	0.0039(4)	0.024(1)	0.031(2)
O1 U_{iso} (Å^2)	0.0037(5)	0.0023(6)	0.0085(1)	0.00753(2)
O2 U_{iso} (Å^2)	0.0039(2)	0.0058(2)		

Rietveld refinements of neutron diffraction data also shows that the Ba/Bi U_{iso} value increases as the value of x increases, which is consistent with refinements on x-ray diffraction data (Section 5.3.1.1). As there is more sensitivity to the oxygen atoms in the neutron data it was possible to refine the O U_{iso} values. It can be seen that the oxygen U_{iso} values are higher when x= 0.10 and 0.15 suggesting there is increased disorder on the oxygen sites in comparison to pure BTO. The Rietveld fit to the neutron diffraction data when x = 0.15 is presented in Figure 5.8 (bank 5).

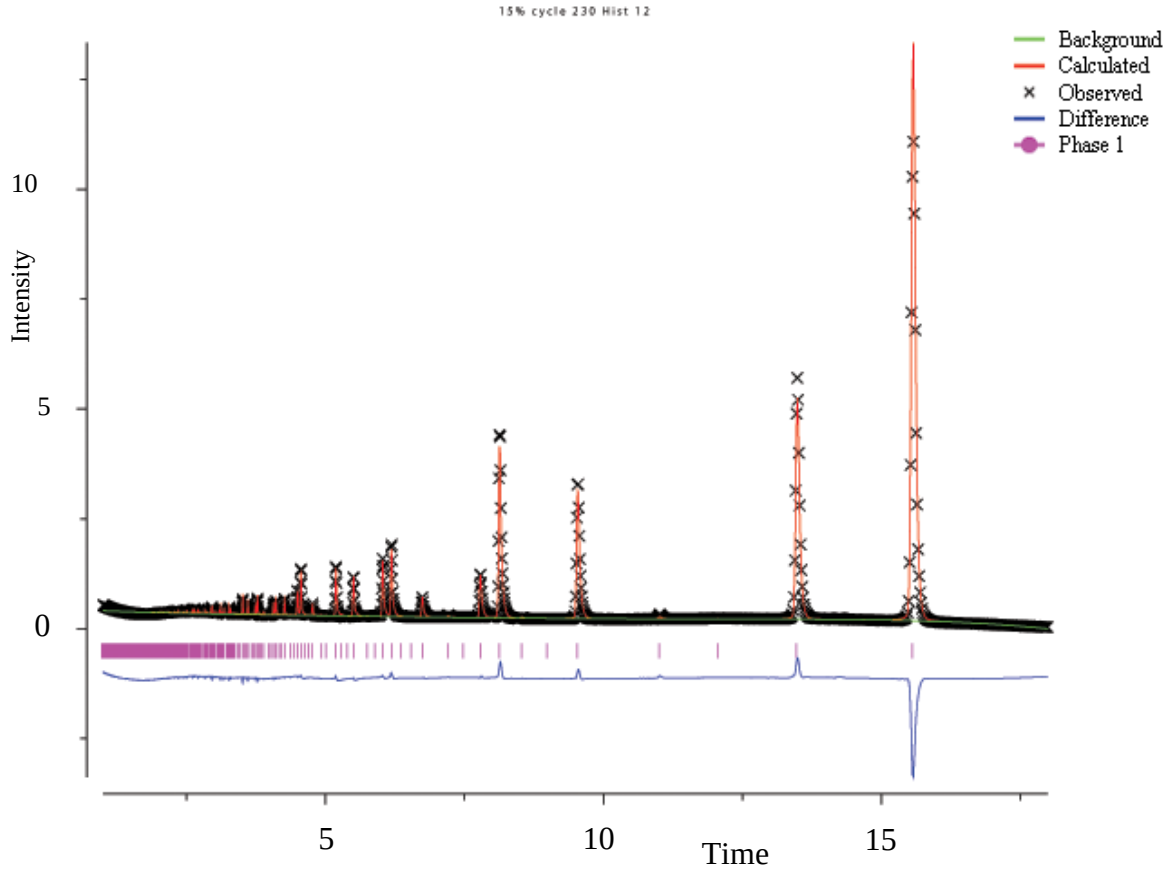

Figure 5.8: Rietveld fit of $Ba_{0.85}Bi_{0.15}Ti_{0.85}Yb_{0.15}O_3$ from bank 5 of GEM.

In contradiction of the results presented in the previous section the Ti/Yb U_{iso} values also increase as x increases which points to disorder on the B site as well as disorder on the A site

and the oxygen sites. The Ba/Bi U_{iso} values and calculated unit cell volumes show similar trends as those seen in Table 5.1.

Rietveld analysis of x-ray and neutron diffraction data suggests that while the diffraction patterns can be indexed using a cubic *Pm*3*m* space group when $x \geq 0.06$, there is evidently further disorder introduced as the value of *x* increases.

5.3.2 nPDF

5.3.2.1 Experimental PDFs

With Rietveld analysis suggesting a high degree of local disorder in the structure of BBTYb at all values of *x*, it was hoped that PDF analysis would shed some light on local structure. It was also not clear if the Bi and Yb dopants cluster together or if they are randomly distributed throughout the lattice. nPDFs of BBTYb with differing values of *x* are shown in Figure 5.9.

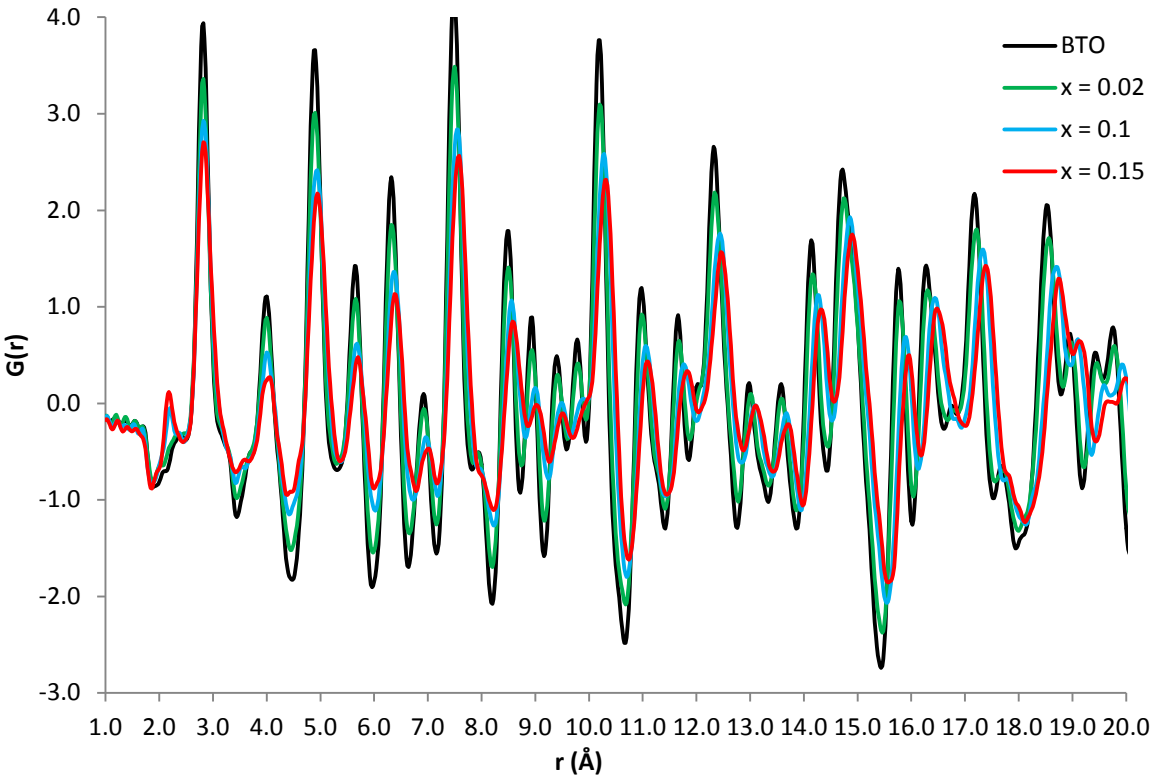

Figure 5.9: Experimental PDFs of BBTYb with differing values of *x*.

It can be seen in Figure 5.9 that the overall shape of the first peak changes as Yb concentration increases. Yb has a positive scattering length (12.43) in neutron diffraction (as opposed to titanium's -3.438 scattering length) which results in clear changes in this first peak (Figure 5.10).

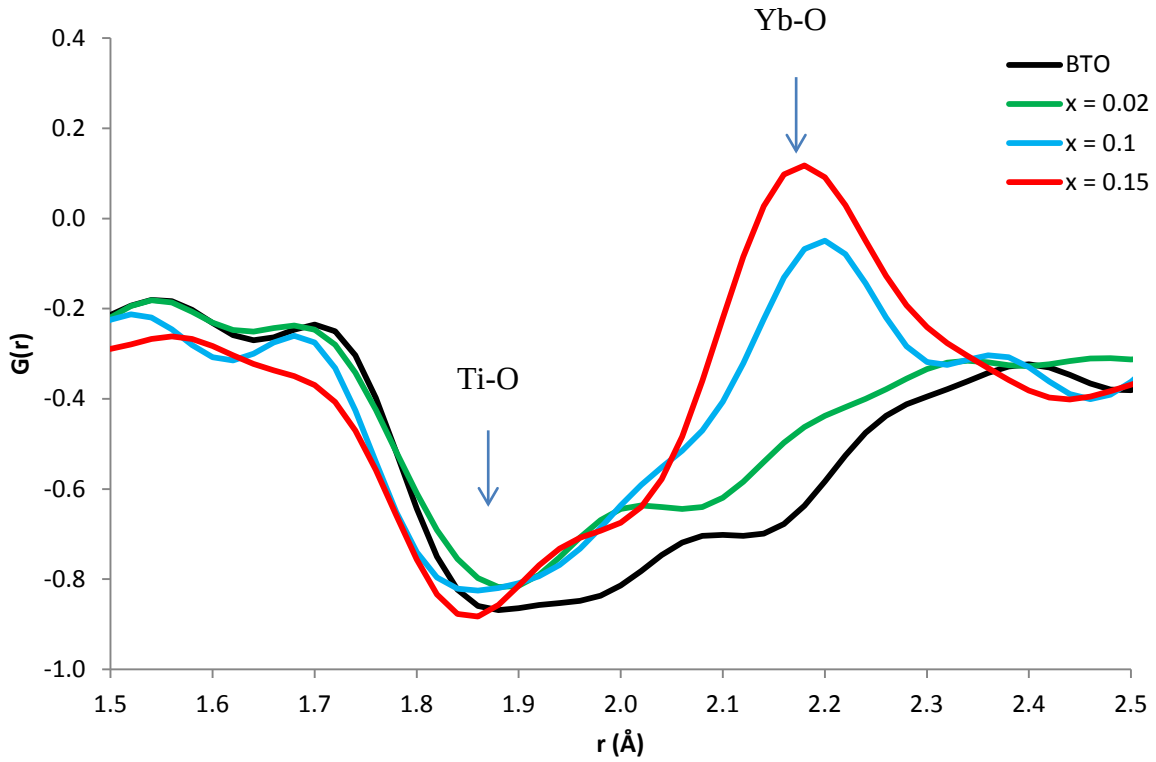

Figure 5.10: First Ti/Zr-O peak in BBTYb with differing values of x.

What is interesting is how intense the Yb-O peak is with only 15% doping, which would suggest little overlap between the negative Ti-O and positive Yb-O peaks as they would begin to cancel each other out if overlapped. It be should noted that Yb has a large neutron scattering length (12.43fm) in comparison to the other atoms present. The Ti-O peak appears to become shifted to lower *r* values for $x = 0.1$ and = 0.15 but to longer *r* distances for x=0.02. The reduction in Ti-O distances in $x = 0.1$ and 0.15 may be a result of a variety of factors such as; oxygen atoms being displaced away from Yb in one unit cell and thus closer to

surrounding Ti atoms in adjacent cells, the Ti atom becoming more displaced leading to shorter Ti-O distances or the oxygen atoms becoming displaced in some manner. It is difficult to draw firm conclusions from the shape of the first Ti-O peak at any value of *x* due to the Yb-O distances being introduced. When *x* = 0.02 the Ti-O peak appears to consist of two peaks, which would represent a Ti displacement in the [111] direction assuming the oxygen positions remain constant. There are no obvious signs of Yb-O distances when *x*=0.02 but when *x*=0.1 there is a peak very similar to the Yb-O peak when *x* = 0.15 but it would appear that the Yb-O distances are marginally longer when *x*=0.10 compared to when *x* = 0.15.

The Yb-O distances are clearly longer than the Ti-O distances when *x*=0.10 and *x*=0.15 and by producing a differential PDF between pure BTO and BBTYb where *x*=0.15 it is possible to observe the differences between the structures (Figure 5.11).

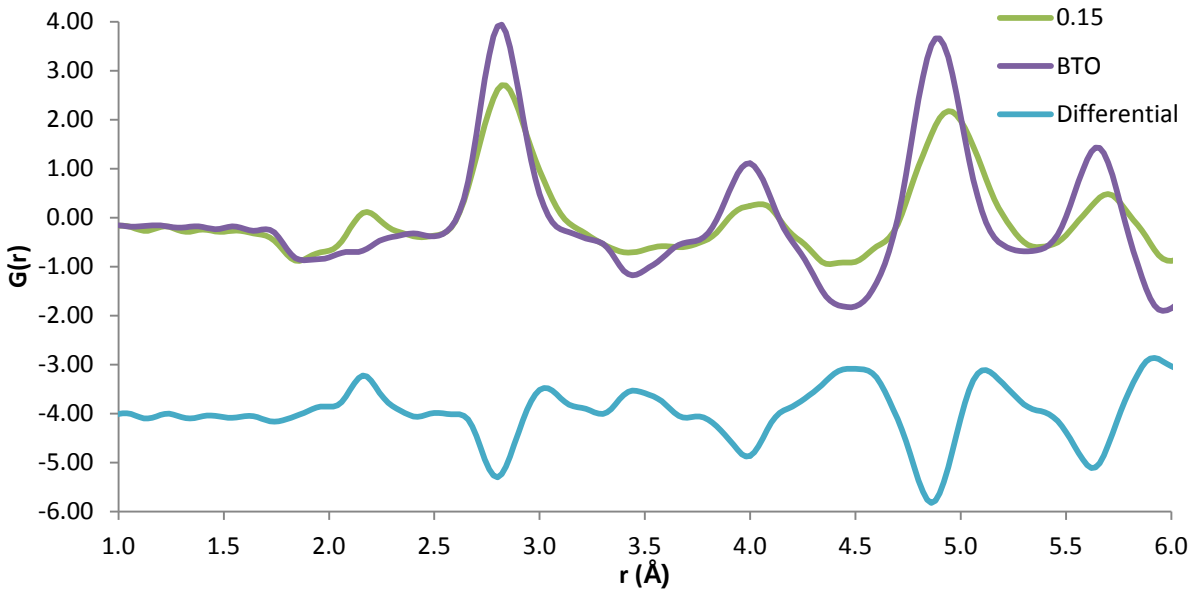

Figure 5.11: Experimental PDFs of BTO and BBTYb (*x*=0.15) and the differential PDF.

There are some fairly substantial differences between the two PDFs. The new Yb-O distances are shown clearly at ~2.1Å and the Ba/Bi-O and O-O peak at ~2.7Å has become broader,

suggesting a greater variety of distances. The first Yb-O peak appears to be a single peak, so to investigate this fityk was used to fit it (Figure 5.12)

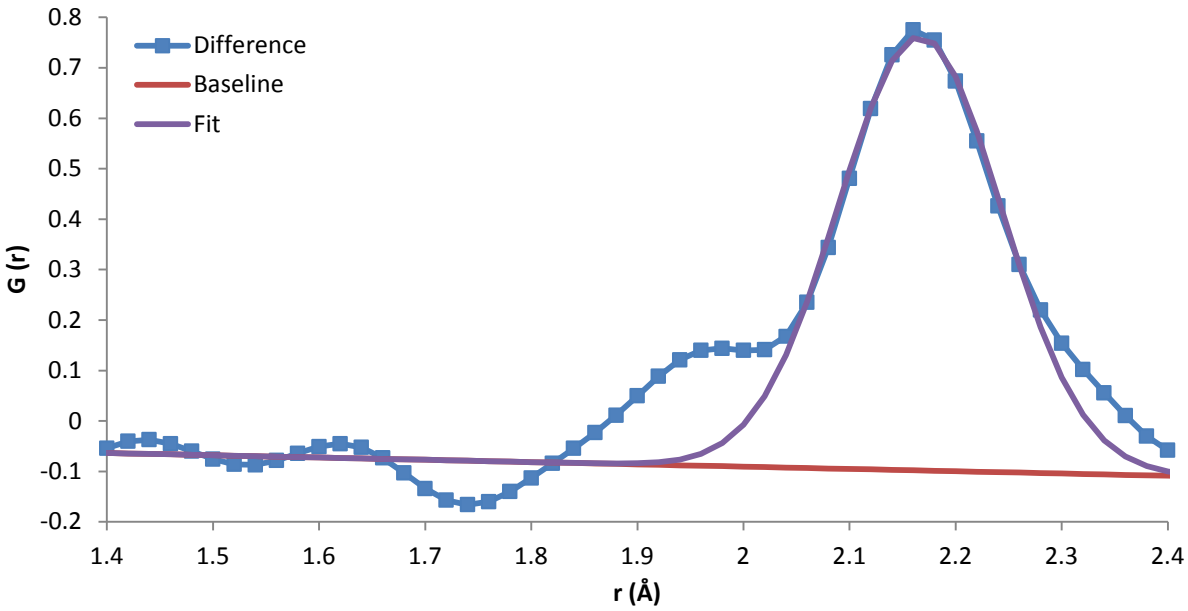

Figure 5.12: A single peak fit to a differential PDF between BTO and BBTYb (x=0.15) at ~2.1Å.

The peak position refines to 2.166Å, but a single peak does not provide a perfect fit to the differential PDF. The shoulder at 1.95Å could be simply due to the Ti-O distances becoming reduced but the negative peak at ~1.75Å does not appear to be significant enough to account for this shoulder. A positive peak in Figure 5.12 may show a loss of Ti-O distances due to Ti possessing a negative scattering length. Modelling the Yb-O distances using the differential PDF in this manner requires that there is no change in the Ti-O distances to ensure the Yb-O peak is represented accurately in the differential PDF. With Rietveld analysis suggesting disorder in the oxygen atoms it is likely that the oxygen octahedra is distorted by the lone pair on the Bi atoms, which would result in an analysis of the Ti/Yb peak becoming difficult as both Ti and O atoms could be displaced relative to the A site cations. It is clear however that

the Yb-O distances are longer than Ti-O distances, which may be a result of a larger unit cell when Yb is occupying the B site (as opposed to Ti). An easy way to investigate the changes in unit cell size is to simply examine the PDFs at long range, where changes are more dramatic (Figure 5.13).

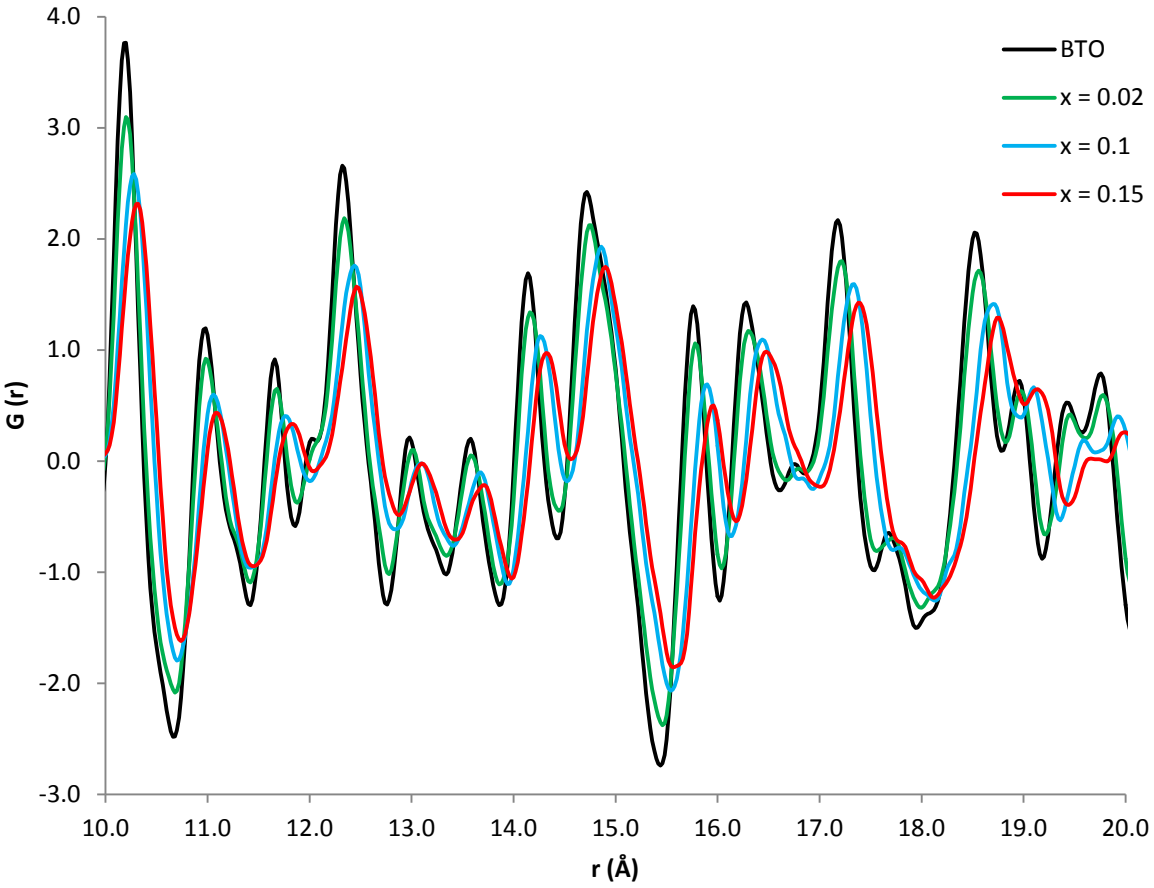

Figure 5.13: Experimental PDFs of BBTYb between 10 and 20Å for varying values of *x*.

Indeed it can be seen that the PDFs show that the unit cell is increasing as *x* increases, which is expected based on previous studies and the Rietveld analysis conducted in Section 5.3.1 and 5.3.2. This would appear to be in conflict with the shorter Ti-O distances observed, unless disorder in the O atoms has been introduced leading in to a greater distribution of Ti-O distances. It is difficult to draw firm conclusions on the Ti displacements however, and this is

made more difficult with no precise information on the exact Ti displacements in pure BTO (Chapter 3). If it is assumed that the Yb atom is sat in the centre of the unit cell, in a non-distorted oxygen octahedra then the observed Yb-O peak would give a cubic lattice parameter of a=4.332Å and a unit cell volume of 81.295Å^3. This would be an extreme departure from the trends in unit cell volumes presented by Strathedee *et al* for lower values of x and from the values of 4.0484 and 4.0498 Å obtained from the Rietveld analysis of x-ray and neutron diffraction data, respectively (Sections 3.2 and 3.3).

While substitution on the B site is clearly observable in the first B-O peak, there will also be new Bi-atom distances present. Bi (8.532 fm) has a larger scattering length than Ba (5.03 fm). The Ba/Bi-O and O-O peaks at 2.9 and 5Å are a lot broader when $x = 0.15$ suggesting more variety in atom-atom distances but it not clear if this is due to oxygen distances or Bi/Ba. It is possible that substitution of Bi on the A site leads to a smaller unit cell if the B site atom is Ti, which would explain the smaller Ti-O distances observed as x increases. To allow for these differing Ti/Yb-O distances the Bi and Yb dopants would not cluster together and would potentially lead to differing cell sizes throughout the lattice.

5.3.2.2 Modelling Experimental PDFs in PDFGui

Clearly a lot of information is available through simply inspecting the experimental PDFs, in contrast with PDF data presented in Chapters 3 and 4, changes are relatively dramatic and clear. Different models can be constructed in PDFGui to try and investigate substitution of Bi and Yb into the crystal structure of BTO.

A model for BBTYb (where $x = 0.15$) was constructed where the Bi occupied the A site at (0,0,0) and Yb occupied the B site in the centre of the unit cell (0.5,0.5,0.5). Lattice parameters were fixed so $a = b = c$ as x-ray diffraction indicated an average cubic model

(section 5.2 and 5.1). The Bi and Yb U_{iso} were allowed to refine and the value of qdamp was obtained from a tetragonal fit to pure BTO from 0 to 50Å and fixed for all refinements. This model represents the same structure fit in the Rietveld analysis of diffraction data. Atom positions and occupancies can be seen in Table 5.3.

Table 5.3: Cubic Model of BBTYb (x = 0.15) constructed in PDFGui.

Atom	*x*	*y*	*z*	Occ	Refined U_{iso} (0 to 50 Å)	Refined U_{iso} (2.5 to 20 Å)	Tetragonal fit to Pure BTO
Ba	0	0	0	0.85	0.0095	0.0072	0.0052
Bi	0	0	0	0.15	0.0403	0.0036	-
Ti	0.5	0.5	0.5	0.85	0.1047	0.0078	0.0082
Yb	0.5	0.5	0.5	0.15	0.6480	0.0024	-
O	0.5	0.5	0	1	0.0403	0.0201	0.0097
O	0	0.5	0.5	1	0.0403	0.0201	0.0097
O	0.5	0	0.5	1	0.0403	0.0201	0.0097

When refinements using this model were conducted in PDFGui a *Rw* value of 0.1562 was obtained, but as seen in Table 5.3 values of U_{iso} were very large for Ti and Yb atoms as well as potentially being too large for Bi (for refinements between 0 and 50Å). PDFgui was struggling to fit the first Ti/Yb-O peak and it was not clear how much the poor fit was affecting the refined parameters. Using thermal parameters from pure BTO leads to peaks being too sharp which again points to increased disorder upon doping. In reality it is unlikely atoms are vibrating more upon doping with Bi and Yb ions. If there is an increased variety in atom-atom distances PDFGui can artificially increase the thermal parameters in order to broaden peaks.

In order to exclude the first peak, refinements were then conducted using the same model between 2.5 and 20Å. Refined thermal parameters appeared more realistic (Table 5.4) so these values were then fixed and used to refine the model between 0 and 50 Å. For comparison the U_{iso} values obtained from refining a tetragonal model of BTO at ambient conditions can also be seen in Table 5.3 for comparison (taken from Appendix 6).

This cubic model of BTO with Yb and Bi substituted into the relevant sites was then fit to the experimental PDF (Figure 5.14 and 5.15).

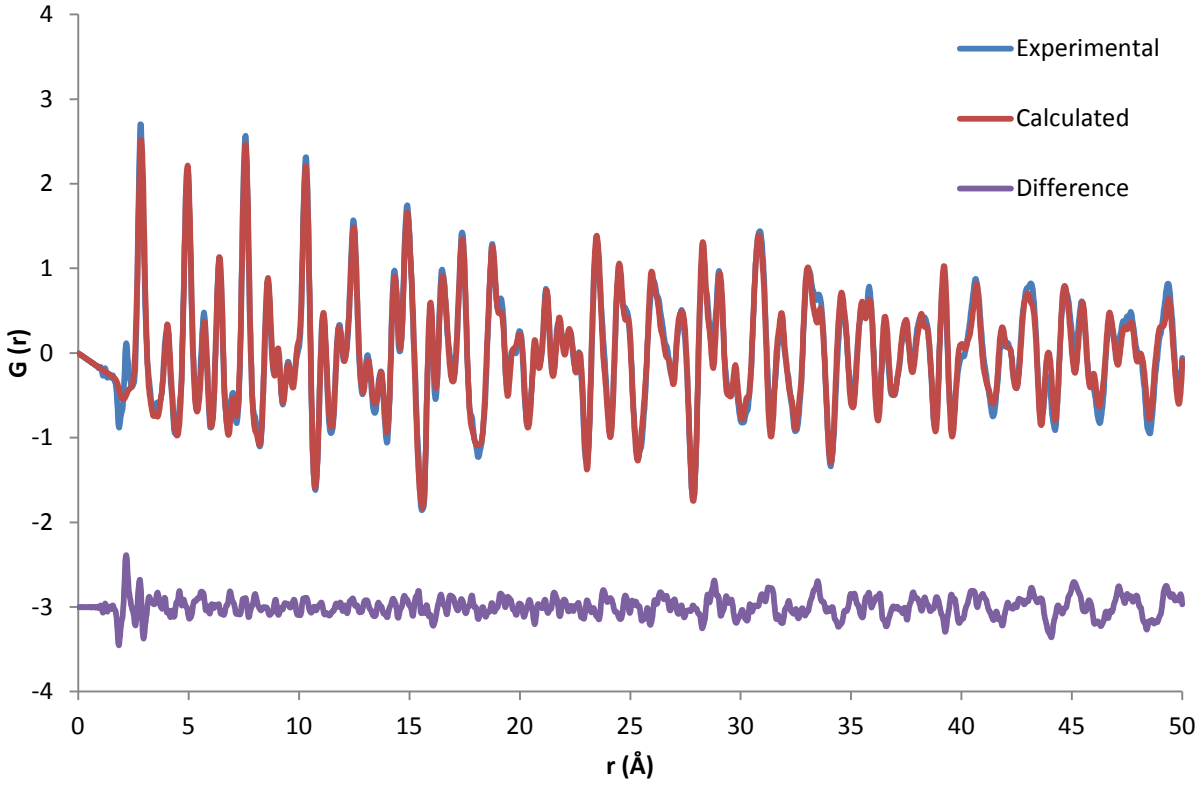

Figure 5.14: Fit of a Cubic Model of BBTYb (x = 0.15) to experimental data from 0 to 50 Å with fixed thermal parameters obtained from a refinement from 2.5 to 20 Å (*Rw* = 0.167).

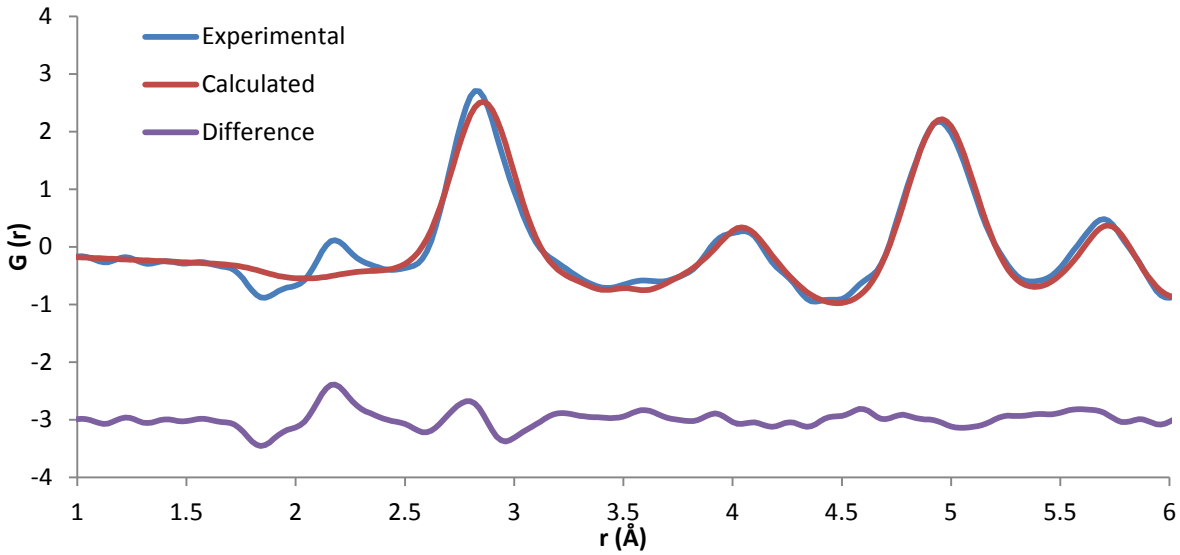

Figure 5.15: Fit of a Cubic Model between 1 and 6Å of BBTYb (x=0.15) to fit experimental data from 0 to 50 Å with fixed thermal parameters obtained from a refinement from 2.5 to 20Å).

It can be seen from Figures 5.14 and 5.15 that the fit to the first Ti/Yb-O peak is very poor. This is due to the model only having freedom to give one value for Ti-O and Yb-O distances due all atoms sitting in the same relative position in each unit cell. This leads to the Ti-O and Yb-O peaks overlapping at the same value of r and cancelling each other out to give the shallow peak seen in the calculated pattern in Figure 5.14. The model gave a=4.5039Å which is comparable to the lattice parameter obtained from Rietveld analysis of diffraction data of the same sample.

Laulhe *et al* (2009) observed a similar shape of the first peak when Zr was substituted onto the B site of BTO with longer Zr-O distances and a Zr-O octahedral related to $BaZrO_3$ which possesses a larger unit cell volume that $BaTiO_3$. They also concluded that the Ti^{4+} was still displaced when Zr was doped into the structure so it is possible that this is still the case in here.

It was shown in Chapters 3 and 4 that even in the *"cubic"* phase the Ti atom does not sit in the centre of the unit cell. An eight site model for the Ti displacement was constructed in attempt to more accurately model the first Ti-O peak. Eight Ti atoms were included in the refinement each with an occupancy of 0.10625 and the Yb atom remained at the centre of the unit cell. PDFGui had problems refining this model so the Ti positions had to be fixed in order to investigate the shape of the first peak in PDFGui.

All refined parameters were fixed from the cubic model outlined in Table 5.3 but the Ti position was allowed to refine. The Ti position would not refine so the Ti co-ordinate was set to a co-ordinate of (0.52, 0.52, 0.52) which represents a larger displacement that is seen in any phase of BTO (Figure 5.16).

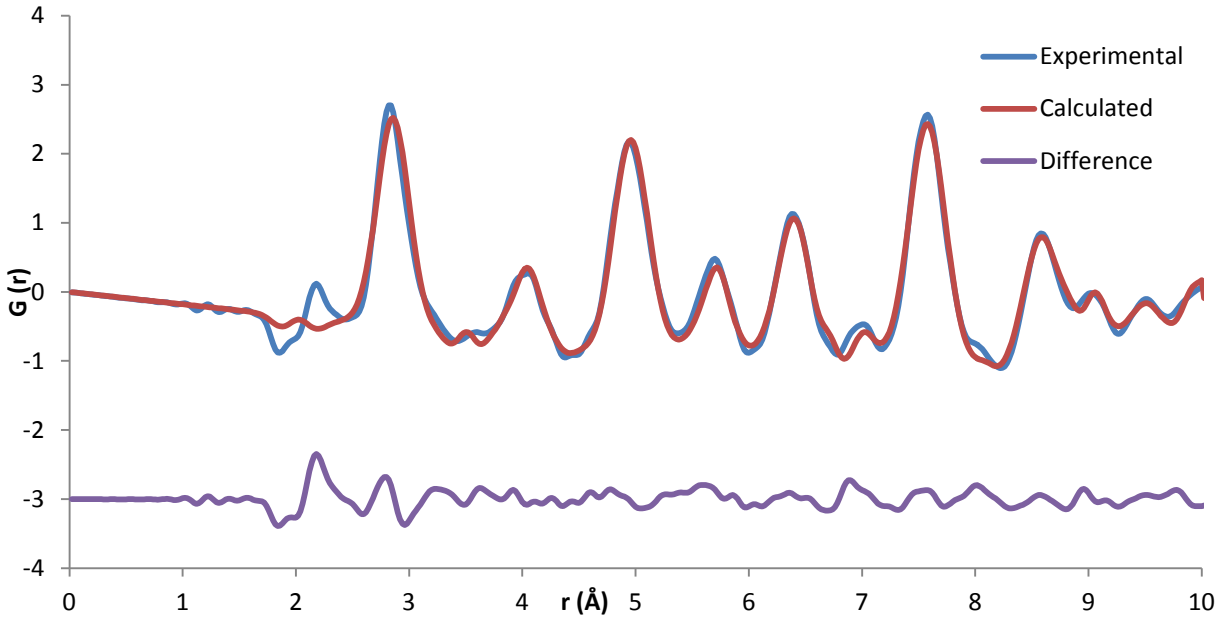

Figure 5.16: Fit between 0 and 10Å from a model of BBTYb (x = 0.15) including an eight-site Ti displacement to fit experimental data from 0 to 50 Å.

It is clear from Figure 5.16 that a Ti atom with a large displacement in the [111] direction

within a large unit cell is not enough to account for the small Ti-O distances observed. The calculated unit cell volume is 66.62Å^3 (a = 4.0539Å), which appears far too small to accommodate 6 equivalent Yb-O distances of 2.166Å without significant disorder in the oxygen octahedra. There is a poor fit to the Ba/Bi-O and O-O peak with the calculated pattern giving values for these distances that are too large for this peak.

The refined thermal parameters (Table 5.3) are higher for each atom in comparison to those obtained via refinements on pure BTO which points towards increased disorder in the structure. It can be seen from Figure 5.11 that there is an increased variation in Ba/Bi-O and O-O distances and without the freedom to move atoms PDFGui can increase the U_{iso} values so that the peaks become broader, the scale factor can then be increased to obtain the correct peak intensity.

In an attempt to model Yb-O octahedra a two phase refinement was set up with one phase consisting of only Ti on the B site and one phase consisting of only Yb on the B site. In order to try and restrain the concentrations of each phase the *scale factor* was fixed for each phase to the correct concentrations (0.85 for $BaTiO_3$ and 0.15 $BiYbO_3$) and then an overall scale factor was used a multiplier for these. This ensured that the correct ratios of atoms were kept consistent during refinements.

To compensate for this, thermal parameters for each atom were fixed from those for a tetragonal fit of pure BTO. As it has already been shown that the Yb-O octahedra are different to the Ti-O octahedra a two phase fit was conducted in an attempt to model this (Table 5.4). To investigate clustering Phase 2 also included only Bi on the A site. This model was then refined against data from 1.5 to 20Å, when investigating different models refinements are

more efficient on smaller *r* ranges but if an acceptable model is found it can then be used on PDF data out to a larger values of *r*.

Table 5.4: Two phase refinement for BBTYb.

Phase 1						**Phase 2**					
	x	*y*	*z*	Occ.	U_{iso} (Å^2)		*x*	*y*	*z*	Occ.	U_{iso} (Å^2)
Ba	0	0	0	1	0.0052	Bi	0	0	0	1	0.0052
Ti	z	z	z	1	0.0082	Yb	0.5	0.5	0.5	1	0.0050
Ti	1-z	z	z	0.125	0.0082	O	0.5	0.5	0	1	0.0097
Ti	z	1-z	z	0.125	0.0082	O	0	0.5	0.5	1	0.0097
Ti	1-z	1-z	z	0.125	0.0082	O	0.5	0	0.5	1	0.0097
Ti	z	z	1-z	0.125	0.0082						
Ti	1-z	z	1-z	0.125	0.0082						
Ti	z	1-z	1-z	0.125	0.0082						
Ti	1-z	1-z	1-z	0.125	0.0082						
O	0.5	0.5	0	1	0.0097						
O	0	0.5	0.5	1	0.0097						
O	0.5	0	0.5	1	0.0097						

Cubic lattice parameters were refined for each model and the scale factors of the relative phases were kept to 0.85 for the $BaTiO_3$ phase and 0.15 for the $BiYbO_3$ phase. *sratio* was refined (using an *rcut* of 2.5Å) for each phase and the only other parameter that was allowed to refine was the Ti position in phase one, this was due to there being evidence of the Ti atom still being displaced when *x*=0.15 and the structure appears cubic. The fit using these models using an *r* range of 1.5 to 20Å can be seen in Figure 5.17.

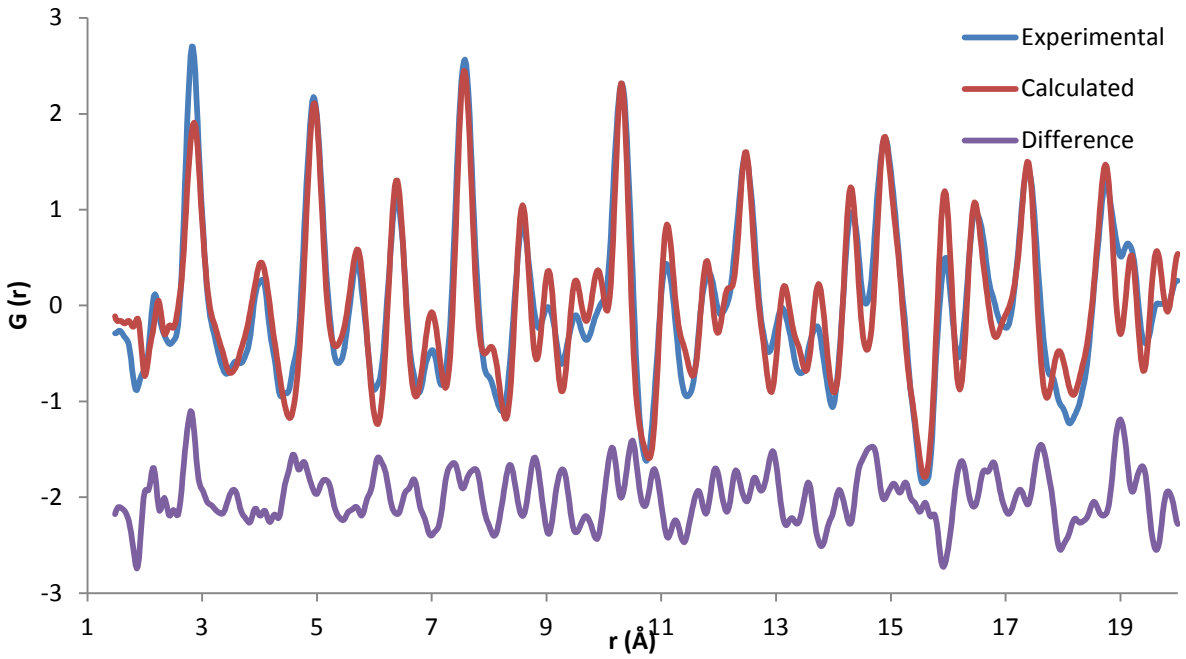

Figure 5.17: A two phase refinement on data from 1.5 to 20Å for a $0.85BaTiO_3$-$0.15BiYbO_3$ model on PDF data of BBTYb (x = 0.15).

The fit is very poor, with Rw = 0.329, although the fit to the first Ti/Yb-O appears to be slightly improved. The refined a values were 4.0450Å and 4.4702Å for the BTO and $BiYbO_3$ phases respectively and the Ti position was (0.5099,0.5099,0.5099). It should be noted that *sratio* was used to simulate correlated motion only in the first peak and it is not clear if this led to a accurate description of correlated motion for these peaks. PDFGui clearly needed to use sratio to sharpen up the Ti-O and Yb-O peaks for both these models.

The fit using these models is clearly rather poor and PDFGui would not have calculated inter-phase atomic distances but even without these distances it is clear that this two phase modelling doesn't accurately describe local structure in BBTYb (x = 0.15) without introducing disorder in the oxygen positions. The Ti-O distances are still not short enough using this model. The Ti-O distance when x = 0.15 is ~1.85Å which would result in a unit cell size of 3.7Å if there was no oxygen or Ti disorder in a cubic unit cell. This unit cell size can

be discounted due to the Ba/O-O distances at ~3Å not showing a significant shoulder at shorter distances. Attempts were made to build a super cell in PDF Gui in which oxygen atoms could be displaced away from the Yb atom and thus intrude upon surrounding cells that contained Ti atoms but this modelling was unsuccessful and provided no better fit to the experimental data. It is likely that this model was far too simplistic with no information regarding the effect of the Bi lone pair on local structure.

As Rietveld refinements suggest an average cubic structure for $Ba_{0.85}Bi_{0.15}Ti_{0.85}Yb_{0.15}O_3$ it is also useful to investigate the long range structure in the PDF. The long range data, again defined as 37 to 50Å should more closely represent the average structure. The same model that was used for Rietveld refinement (Figure 5.2) was used with the Bi Uiso set to be the same value as Ba U_{iso} but allowed to refine and Yb was allowed to refine independently. Deta 1/2 or sratio were not refined as at these distances the effect of correlated motion is not relevant. The Fit of this model can be seen in Figure 5.18 and the relevant refined parameters can be seen in Table 5.5.

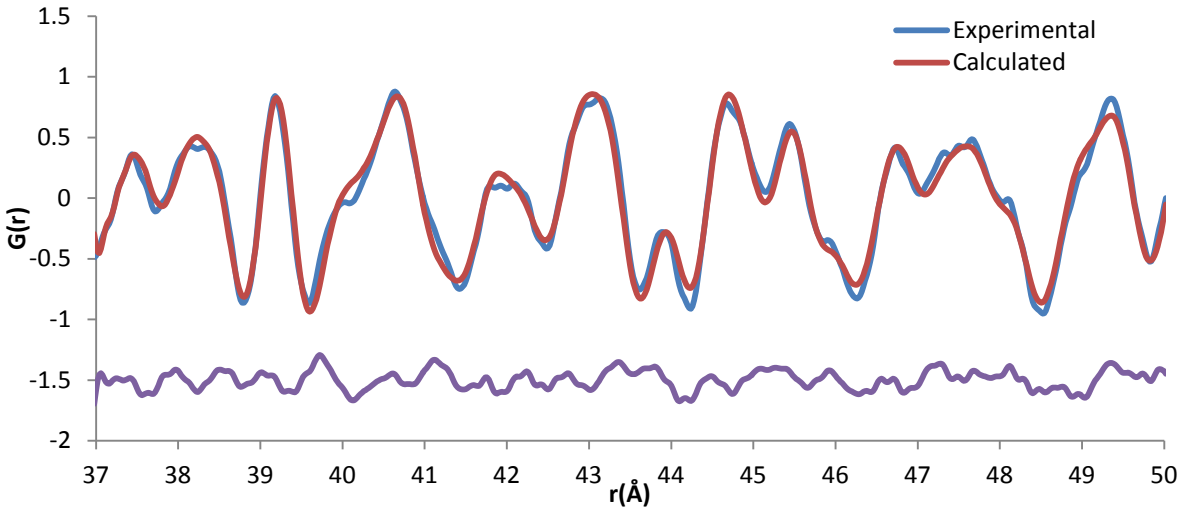

Figure 5.18: Refinement of a cubic model of $Ba_{0.85}Bi_{0.15}Ti_{0.85}Yb_{0.15}O_3$ between 37 and 50Å.

Table 5.5: Refined parameters using a cubic model of $Ba_{0.85}Bi_{0.15}Ti_{0.85}Yb_{0.15}O_3$ to PDF data between 37 and 50Å.

Parameter	Refined Value
a	4.051Å
Volume	66.48Å^3
Ba U_{iso}	0.0571Å^2
Bi U_{iso}	0.0571Å^2
Ti U_{iso}	0.0214Å^2
Yb U_{iso}	0.0215Å^2
O U_{iso}	0.0174Å^2

While the fit appears reasonable with an *Rw* value of 0.163 it can be seen from Table 5.5 that all the thermal parameters are fairly large for all atoms. This means that PDFGui is having to broaden out peaks in attempt to get a better fit, which once again points at disorder in the structure, even with the exclusion of short range data.

X-PDFs were also produced of several samples containing varying values of *x* up to 0.15 (Figure 5.19). As with pure-BTO the first Ti/Yb-O peak was not observed in the x-ray PDFs.

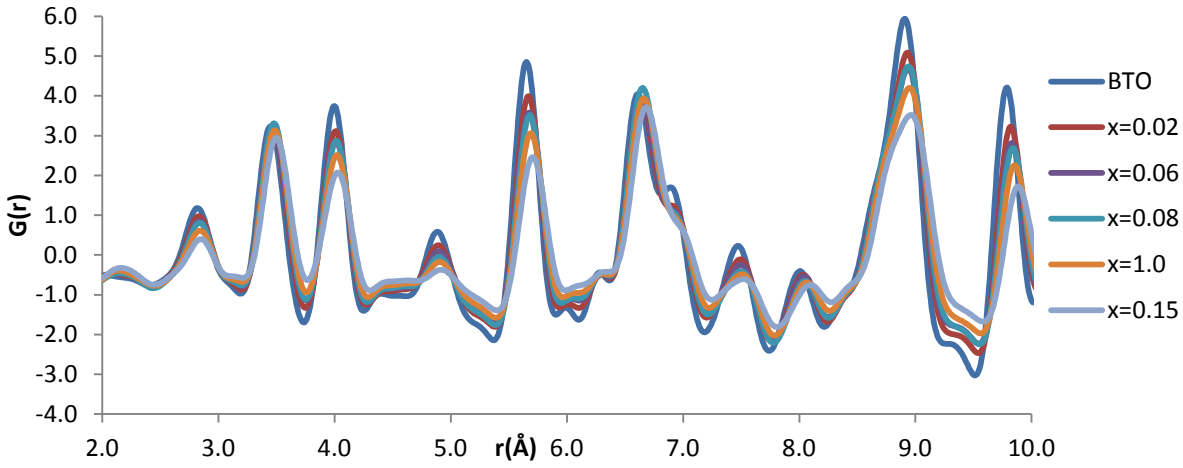

Figure 5.19: X-PDFs of BBTYb between 2 and 10Å with varying values of *x*.

The xPDFs show a lengthening of the Ba-atom distances as *x* increases, which is to be expected with the increase in unit cell volume but the Ba/Bi-O peak at ~2.7Å appears broader along with the Ba/Bi-Bi/Ba distances at 4.0Å (Figure 5.20).

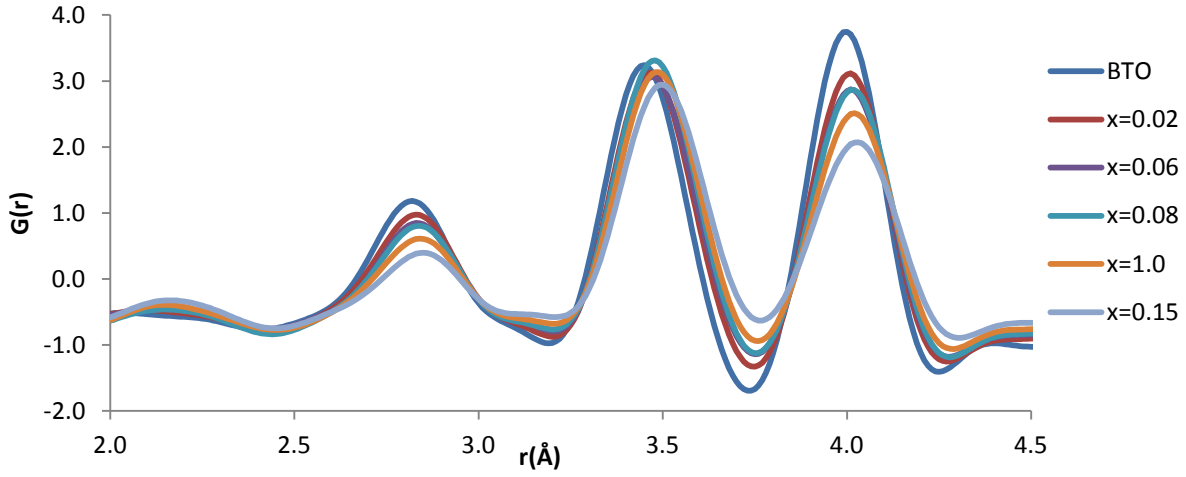

Figure 5.20: The first three observable atom-atom distances from Figure 5.19.

The shift in peak position is expected but the broadening of these peaks points towards disorder in the oxygen octahedral and also that the Bi atom is displaced away from the (0,0,0) position.

5.4 Summary and Future Work

The PDFs show clear trends such as increases in the unit cell volume and the apparent increase in disorder as the doping levels are increased up to $x = 0.15$. Based on Rietveld and x-ray refinements it is apparent that the oxygen octahedra becomes distorted most likely due to the lone pair effect from the Bi atoms, which themselves are likely displaced from the (0,0,0) position. The effect of this disorder is that the Ti-O distances decrease slightly, despite the increase in unit cell volume. This is coupled with new longer Yb-O bonds being introduced. There is evidence that the Yb-O distances are all equivalent but distortions of the oxygen octahedra have not been modelled.

Unfortunately no information was obtained about any clustering of dopants in the BTO lattice. This system appears to be far too complex to be analysed by PDFGui alone, with the lattice becoming distorted in several ways as dopant levels are increased. In order to model local structure a super cell would need to be created in which the structure of one unit cell has a impact on all the surrounding cells. While this study has given some insight into relative atom-atom distances in the $x = 0.15$ structure it has shown that there is clearly disorder in the oxygen octahedra, which is giving rise to the apparently anomalous Ti/Yb-O distances. With modelling unsuccessful on the neutron data, no modelling was attempted on the x-ray data. The best approach would be to use the neutron data to devise an accurate model (due to the appearance of the Ti/Yb-O) peak and then apply this model to the x-ray PDF data.

It would be interesting to see how RMCprofile would handle refinements on this data which possess such a large amount of local disorder present in the structure. As with all studies the model produced would have to be thoroughly scrutinised to ensure it makes "physical sense". It is expected based on the analysis presented in this chapter that the model produced would be very complex.

While even Rietveld analysis shows clear signs of disorder in all the doped samples, it is clear that while peaks can be indexed to a *Pm*3*m* space group, the local structure is very different to the apparent average structure for all dopant levels.

References

1. T. Strathdee, L. Luisman, A. Feteira and K. Reichmann, *Journal of American Ceramic Society*, 2011, **98**, 2292-2295.
2. M. Drache, P. Roussel, J. P. Wignacourt and P. Conflant, *Materials Research Bulletin*, 2004, **39**, 1393-1405.
3. A. Feteira, D. Sinclair and J. Kreisel, *Journal of American Ceramic Society*, 2010, **93**.
4. L. Zhou, P. Vilainho and J. Baptista, *Journal of the American Cermaic Society* 1999, **82**, 1064-1066.

5. A. Nath and N. Medhi, *Materials letters*, 2012, **73**, 75-77.
6. R. Shannon, *Acta Crystallogr A.*, 1976, **32**, 751-767.
7. D. W. Hahn and Y. H. Han, *Japanese Journal of Applied Physics*, 2009, **48**, 111406(111405).
8. C. L. Freeman, J. A. Dawson, H. Chen, J. H. Harding, B. L and D. C. Sinclair, *Journal of Materials Chemistry*, 2011, **21**, 4861-4868.
9. C. Laulhe, F. Hippert, R. Bellissent, A. Simon and G. J. Cuello, *Physical Review B*, 2009, 64104(64110).
10. V. Petkov, M. Gateshki, N. Neiderberger and Y. Ren, *Chemistry of Materials*, 2006, **18**, 814-821.
11. I. Jeong, C. Y. Park, J. S. Ahm, S. Park and D. J. Kim, *Physical Review B*, 2010, **81**, 214119(214115).

6. THE PRESSURE INDUCED AMORPHISATION OF CUBIC $ZrMo_2O_8$

6.1 Introduction

Pressure-induced amorphisation (PIA) occurs when a solid is taken above a phase transition pressure but is unable, due to slow kinetics, to transform into the thermodynamically more stable and dense crystalline high pressure phase.[1] It is common in many solids composed of what are essentially rigid structural units joined together by "weak" links that can distort much more readily, the links are usually metal-oxygen-metal bonds. PIA is increasing being used to access amorphous phases of materials that may possess different physical properties than the original structures. PIA of materials that possess negative thermal expansion (NTE) have been investigated due to the relatively low amorphisation pressures and there is speculation that NTE and PIA mechanisms are linked.[2]

The most widely studied NTE material of its type is cubic α-ZrW_2O_8, it shows NTE behaviour from 0 to 1050K[3] as well as PIA at low pressure. The crystal structure is made up from a framework of corner sharing ZrO_6 octahedra and WO_4 tetrahedra and each ZrO_6 octahedron shares a corner with six WO_4 tetrahedra but each WO_4 tetrahedron is only linked to three ZrO_6 octahedra (Figure 6.1a).

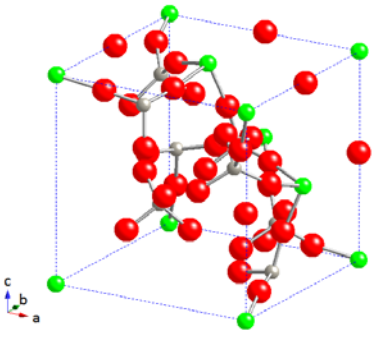

Figure 6.1a. Structure of α-ZrW_2O_8.

(Red=Oxygen, Green=Zr, Grey=W)

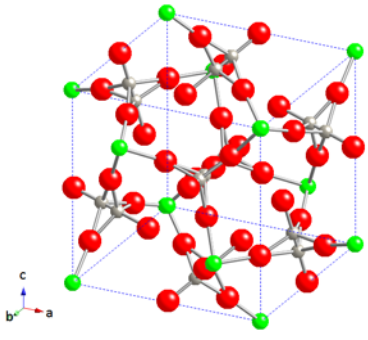

Figure 6.1b. Structure of β-ZrW_2O_8.

(Red=Oxygen, Green=Zr, Grey=W)

This results in one oxygen in the WO_4 tetrahedra only being bonded to W, resulting in a shorter W-O bond (1.705Å *vs.* 1.801Å) and a high degree of flexibility in the structure.[4] It is this flexibility that gives rise to NTE and at 450K there is discontinuity in the NTE as the structure changes to β-ZrW_2O_8 which is a cubic structure with a *Pa*-3 space group (Figure 6.1b).[5] In this structure O4 (a non-bridging oxygen atom) becomes disordered over eight sites and the WO_4 groups become disordered.[5] This leads to W sites in close proximity that are half occupied and O2 and O3 sites that are also half occupied.

An ex-situ RMC analysis of PDFs produced from recovered samples suggested that upon PIA at ambient temperature (~2.5GPa) the W co-ordination of α-ZrW_2O_8 changes from 4 to 5 due to pairs of WO_4 tetrahedra joining together to form W_2O_8 units via the oxygen atom not linked to a ZrO_6 octahedra.[6] An EXAFS and XANES study investigating the PIA of $ZrWO_2O_8$ also indicated the Zr co-ordination increases from 6 to 7.[7] A later total scattering study utilising RMC analysis however disagreed, instead suggesting an increase in Zr co-ordination with additional W-O-W linkages being preferred over additional Zr-O-W linkages.[8]

6.2 PIA of Cubic $ZrMo_2O_8$

The PIA of cubic $ZrMo_2O_8$ has not been as widely studied as the tungsten analogue. $ZrMo_2O_8$ possesses several polymorphs but cubic $ZrMo_2O_8$ is the only one to show NTE behaviour. It has been suggested that it adopts a structure at room temperature that is directly related to β-ZrW_2O_8 (Figure 1b), with a model for $ZrMo_2O_8$ based on this structure providing a better Rietveld fit to pXRD data than the model based on α-ZrW_2O_8.[9] A PDF study has reported a "good fit" to experimental data using the ordered α-ZrW_2O_8 but there are no quality indicators, such as an *Rw* value, presented.[3]

Cubic $ZrMo_2O_8$ exists over a smaller temperature range (0 to 660K) than α-ZrW_2O_8 but it does not possess a phase transition in this range and as a result no discontinuity in NTE, making it potentially useful for some applications.[9] Under quasi-hydrostatic conditions cubic $ZrMo_2O_8$ undergoes a reversible first order phase transition from 0.7 to 2.0GPa and this is accompanied by a volume decrease.[10] Under non-hydrostatic conditions PIA starts to occur at roughly 0.3GPa but the exact pressure is dependent on the stress state of the sample,[10] these amorphous samples can be re-crystallised by heating.[7]

Interpretation of XANES and EXAFS data has suggested that the amorphous glass still contains four co-ordinate Mo but that this co-ordination number could increase with pressure (above 5GPa).[7] There is also evidence from XANES data that the average co-ordination number of Zr increases from 6 to 7 in the amorphous phase indicating that the non-bridging oxygen atoms bonded to Mo atoms are forming bonds with Zr atoms.[7] This assertion was made assuming the structure of $ZrMo_2O_8$ was related to α-ZrW_2O_8. EXAFS shows that metal-metal distances become more distributed in the amorphous phase but the metal oxygen distance distribution remains fairly constant.[7]

An *in situ* total scattering study showed that there was an increase in Mo co-ordination, but was unable to draw firm conclusions on the Zr co-ordination in the amorphous phase.[3] The study indicated the formation of new Mo-O-M linkages in the amorphous sample as pressure is increased up to 7.2GPa. The position of the Mo-O peak (~1.75Å) did not noticeably change upon compression and this has been explained by the amorphous phase containing irregular Mo co-ordination environments which contain varying Mo-O bond lengths. Figure 6.2 shows the PDFs they produced in their study which were treated with a "Lorch" function[11] which was used to damp the termination ripples in the PDFs. The function artificially dampens the $F(Q)$ with a Gaussian function to reduce termination ripples in the PDFs.

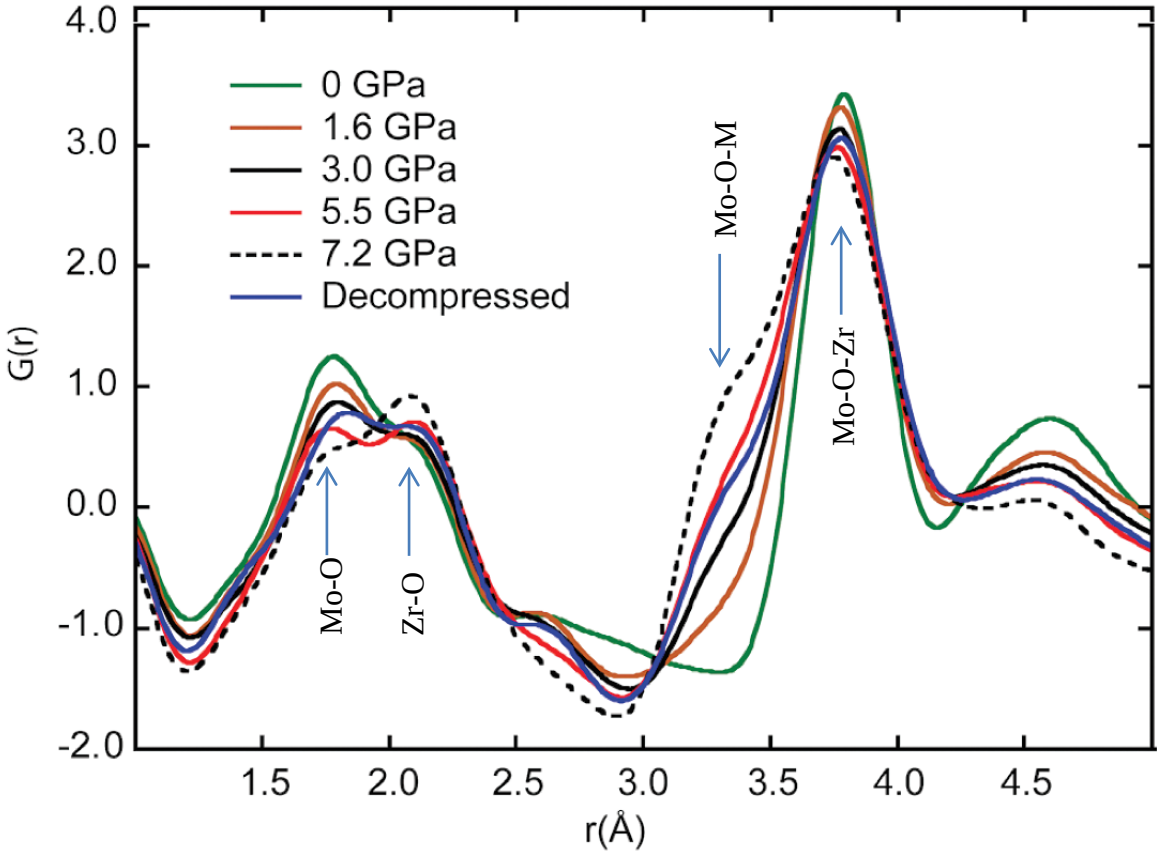

Figure 6.2: Experimental PDFs presented by Wilkinson *et al*.[3] Taken from ref 3.

There is still debate on the exact nature of PIA in the more widely studied ZrW_2O_8. The exact mechanism of PIA of cubic $ZrMo_2O_8$ is also still unclear, particularly when considering the suggested formation of new Mo-O-M linkages and increasing Zr and Mo co-ordination numbers. PDF data collected to higher values of Q_{max} and higher pressure may be able to shed further light on the exact PIA mechanism in $ZrMo_2O_8$. The high pressure PDF study by Wilkinson *et al* (2012) was published during the data analysis presented in Section 6.5. It will be important to refer to this study when drawing conclusions.

6.3 Experimental

6.3.1 Production of PDFs

Data were collected at DLS beamline I15 with a monochromatic 72 keV (0.1722Å) beam and a PE area detector. The sample distance was set to ~223 mm allowing the collection of diffraction data to a Q_{max} of 21Å^{-1}. Calibration of the exact distance was done using CeO_2. The sample was then dry loaded in a spark eroded hole of ~250μm diameter in a W gasket of a DAC along with a few small ruby crystals. Pressure was measured using laser-induced fluorescence and data were collected prior to pressurisation, then at 0.85, 1.72, 2.84, 4.28, 8.40 and 11 GPa and pressure release. Images were integrated in *Q* using Fit2D and a data set of scattering from the empty DAC was also collected for normalisation to produce PDF patterns using the programme PDFGeX2.

Data were also collected for a pristine sample in a kapton tube and an empty kapton tube to produce a PDF in similar fashion for direct comparison to the starting material. Data out to a Q_{max} = 25Å^{-1} was normalised to produce a PDF.

6.3.2 Refinements in PDF GUI

The value of Q_{damp} (0.034) was obtained via a refinement of a standard Ni sample with PDF data collected in a capillary up to a Q_{max} of 25Å^{-1}. This value was then used in the refinements of PDF data of $ZrMo_2O_8$. Using *delta1* or *delta2* (Section 2.3.1) to model correlated motion provided poor fits to the data and eventually a *rcut* value of 4.1Å was used and *sratio* was refined for all refinements presented in Section 6.5.

6.4 Results and Discussion

6.4.1 Capillary xPDF at Ambient Conditions

With PIA, long range structure will be lost and thus it will not be possible to effectively model long-range structure at high pressure using PDFGui. For this reason it is important to provide an accurate description of the local structure at ambient pressure and temperature in order to investigate changes to this as pressure is increased. The normalised *S*(*Q*) obtained for cubic $ZrMo_2O_8$ in a capillary at ambient condition is presented in Figure 6.3 and an experimental PDF from 1-50 Å fitted with a model based on the α-ZrW_2O_8 structure can be seen in Figure 6.4.

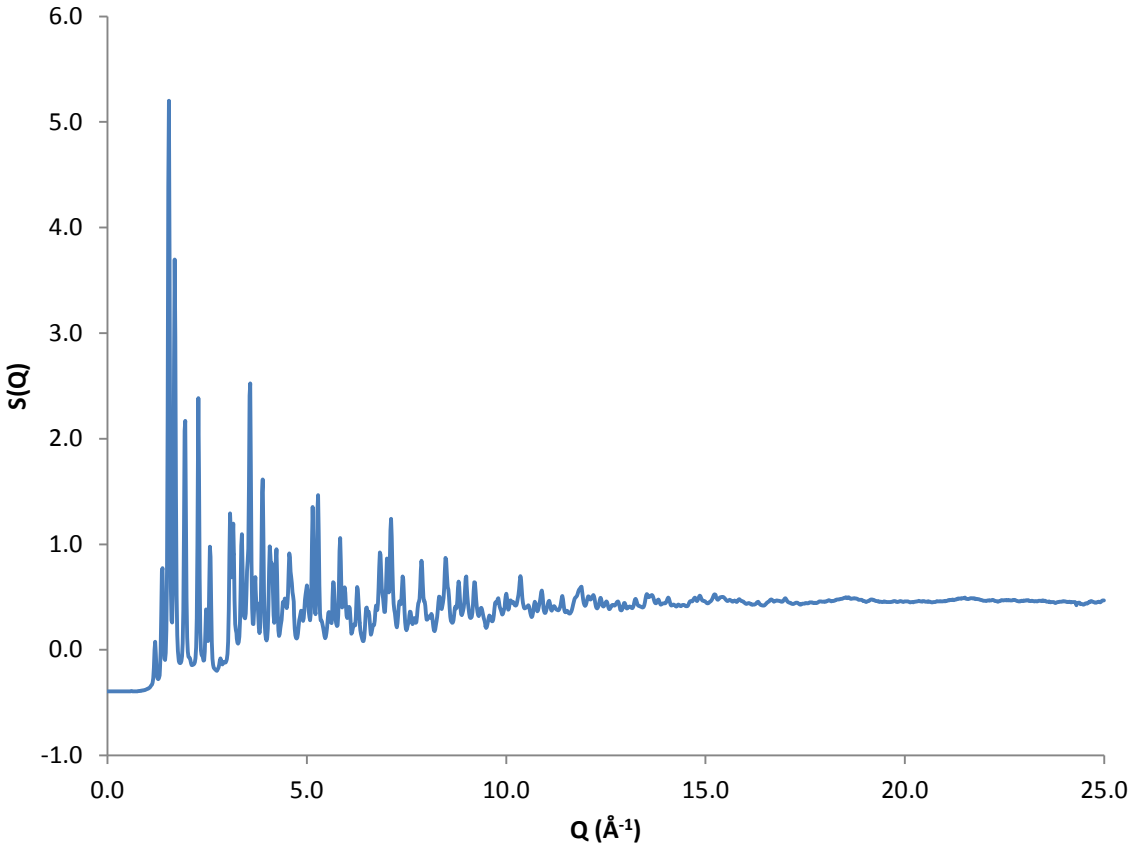

Figure 6.3: *S*(*Q*) for $ZrMo_2O_8$ in a capillary at ambient conditions.

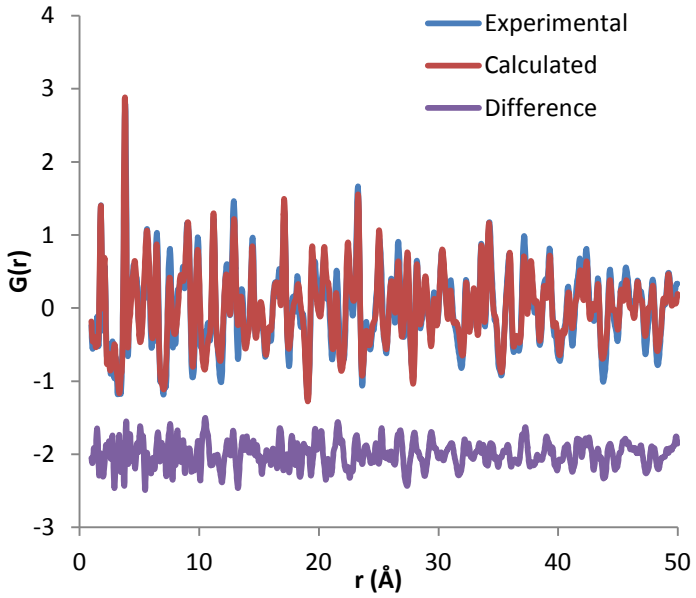

	Mary *et al* (1996) (α-ZrW_2O_8)	This Study
a	9.15993 Å	9.1414 Å
Zr *x*	0.0003	0.0 (fixed)
Zr U_{iso}	0.01 Å^2	0.0070 Å^2
Mo1 *x*	0.3412	0.3414
Mo1 U_{iso}	0.012 Å^2	0.0206 Å^2
Mo2 *x*	0.6008	0.6086
Mo2 U_{iso}	0.01 Å^2	0.0206 Å^2
O1 *x*	0.207	0.2104
O1 *y*	0.4378	0.4281
O1 *z*	0.447	0.4592
O1 U_{iso}	0.022 Å^2	0.0347 Å^2
O2 *x*	0.7876	0.7902
O2 *y*	0.5694	0.5696
O2 *z*	0.5565	0.5661
O2 U_{iso}	0.02 Å^2	0.0347 Å^2
O3 *x*	0.4916	0.5067
O3 U_{iso}	0.023 Å^2	0.0347Å^2
O4 *x*	0.2336	0.2263
O4 U_{iso}	0.037 Å^2	0.0469 Å^2

Figure 6.4: Experimental PDF between 1 and 50 Å of $ZrMo_2O_8$ in a capillary at ambient conditions (*Rw* = 0.313) fit to an α-ZrW_2O_8 type structure.

The fit based on an α-ZrW_2O_8 structure gives a poor fit to the experimental data at this length scale, this is particularly noticeable for the 1-10 Å region as shown in Figure 6.5. Despite this the results from refinements from our PDF analysis are comparable but not identical to literature values of α-ZrW_2O_8 from Rietveld refinements on x-ray diffraction data (Figure 6.4).[12] It is difficult to directly compare this modelling to that presented by Wilkinson *et al* (2012) due to the *Rw* value not being presented in that work and the higher Q_{max} used to produce the PDF in this study (25 Å^{-1} vs 19 Å^{-1}).

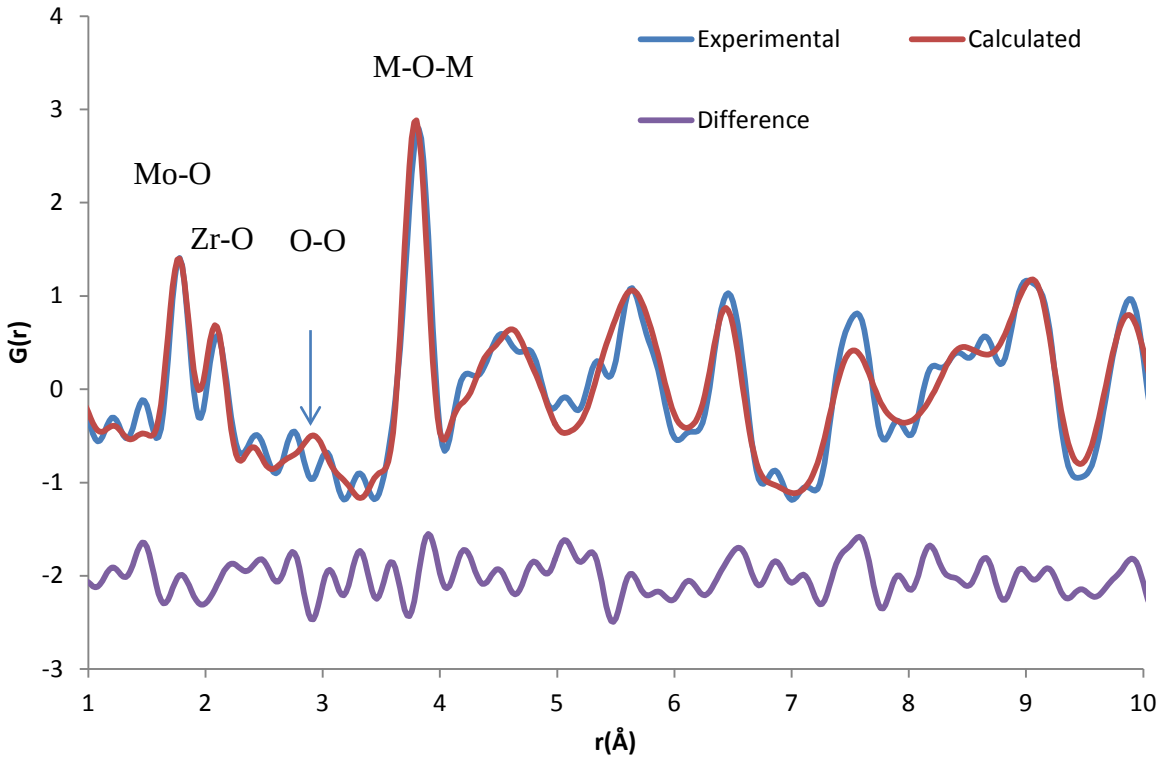

Figure 6.5: Experimental PDF between 1 and 10 Å with a theoretical model of $ZrMo_2O_8$ based on in a capillary at ambient conditions (*Rw* = 0.313).

The higher value of Q_{max} used here means that the PDFs have increased peak resolution and thus data quality is theoretically higher. While there is a relatively good fit to the first three peaks, above 4 Å the fit becomes poor (Figure 6.5). It can also be observed in Figure 6.5 that the O-O region at ~3 Å is not clearly observed but PDFGui is still attempting to fit the ringing as this peak. Without cutting all the data below 3 Å it is not possible to exclude this region from the refinements but on the whole it is clear that the model fits the data poorly above 4 Å.

There are 5 separate Mo-O distances and 2 distinct Zr-O distances in this model of cubic $ZrMo_2O_8$ (Figure 6.6) and refined values are listed in Table 6.1.

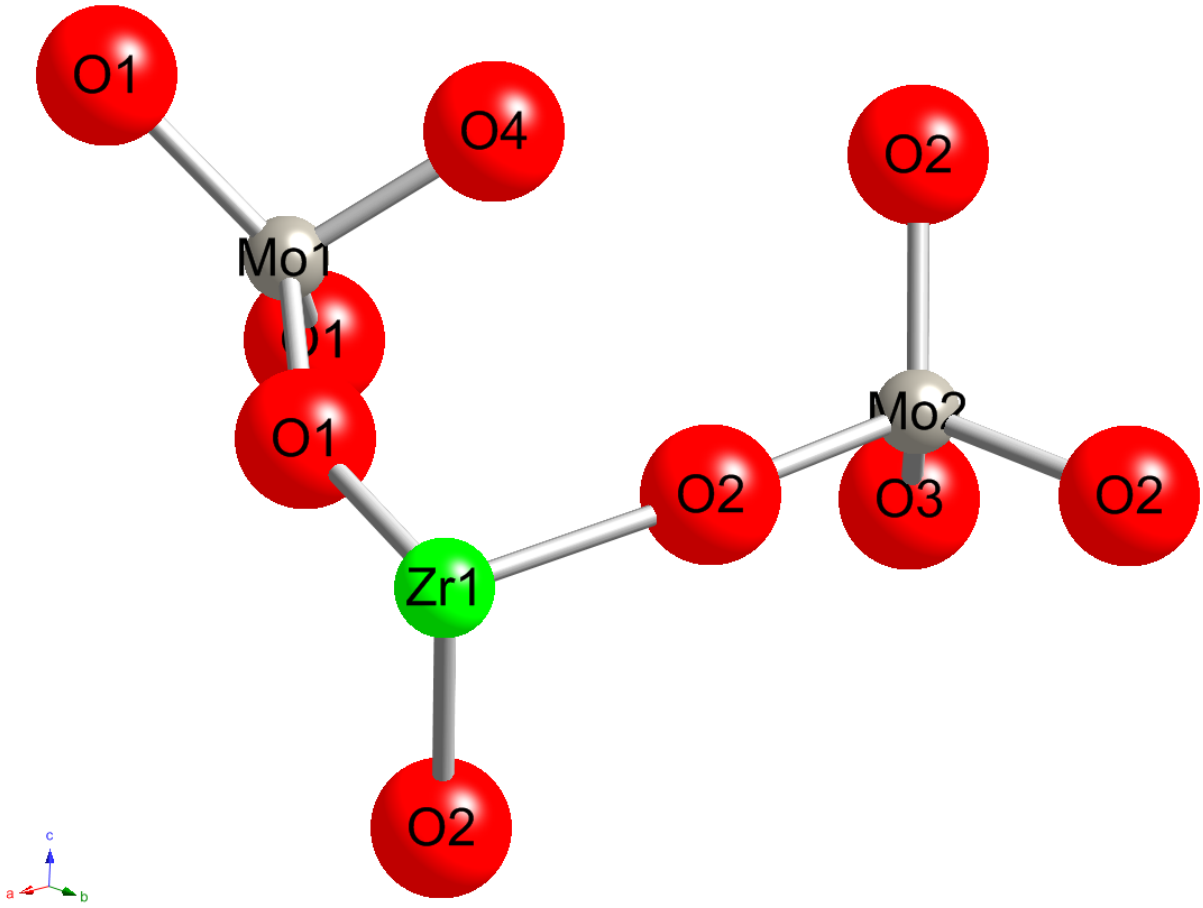

Figure 6.6: Model of $ZrMo_2O_8$ based on a α-ZrW_2O_8 type structure with atoms removed for clarity (Only three of six oxygens surrounding the Zr atom are shown).

Table 6.1: Refined atom-atom distances from the fit presented in Figure 6.4.

	No. of bonds	Distance (Å)		No. of bonds	Distance (Å)
Mo1 – O1	3	1.795	Zr – O1	3	2.067
Mo1 – O4	1	1.822	Zr – O2	3	2.110
Mo2 – O2	3	1.741			
Mo2 – O3	1	1.825			

The non-bridging oxygen atoms refined to have longer bonds with the Mo than the bridging oxygens (rather than shorter as suggested in Section 6.1 for ZrW_2O_8) but this may simply due to the overall fit being poor.

It was suggested by Lind *et al* (1998) that a model for $ZrMo_2O_8$ based on the disordered high temperature structure of β-ZrW_2O_8 (see Section 6.1) provided a better Rietveld fit to pXRD data. This model was also fit to the experimental PDF data to investigate if there was any improvement in *Rw* value and the fit is presented in Figure 6.7. The starting model was based on the structure for β-ZrW_2O_8 reported by Evans *et al* 1996.[4]

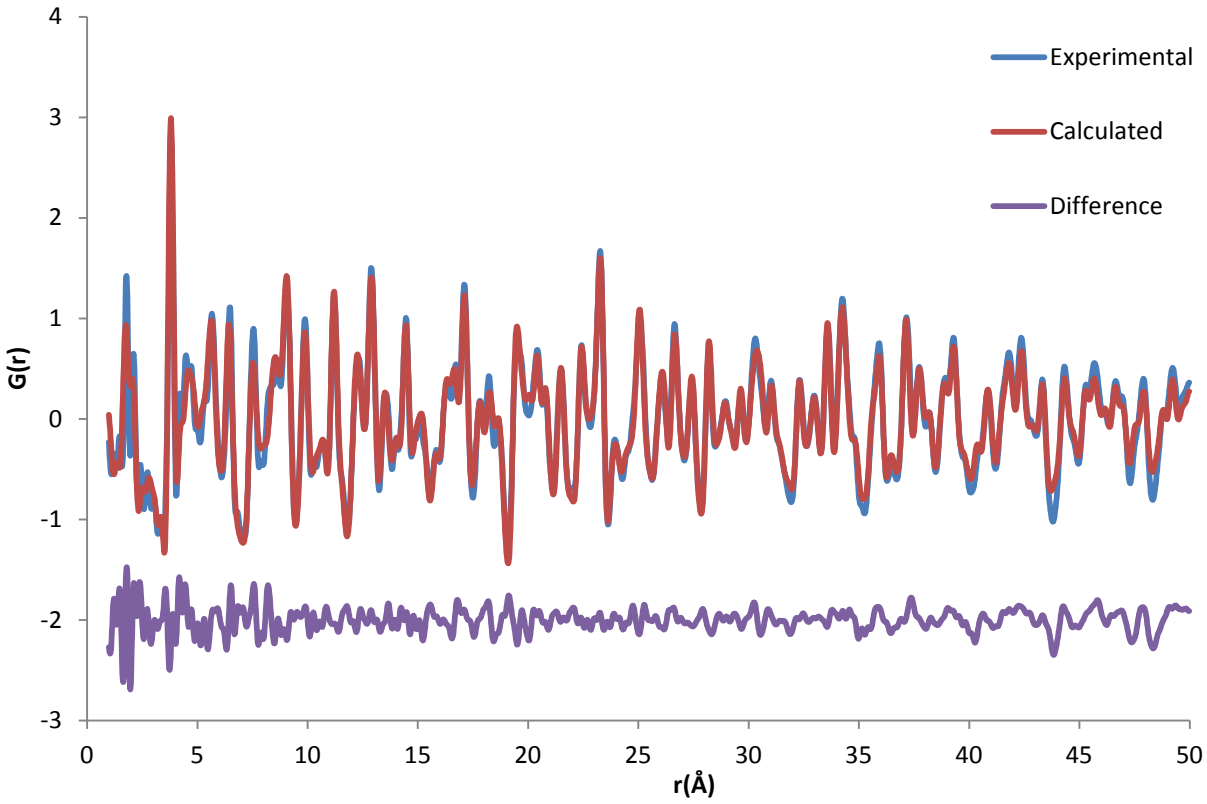

Figure 6.7a: Experimental PDF between 1 and 50 Å with a theoretical model based on β-ZrW_2O_8 for $ZrMo_2O_8$ in a capillary at ambient conditions (*Rw* = 0.219).

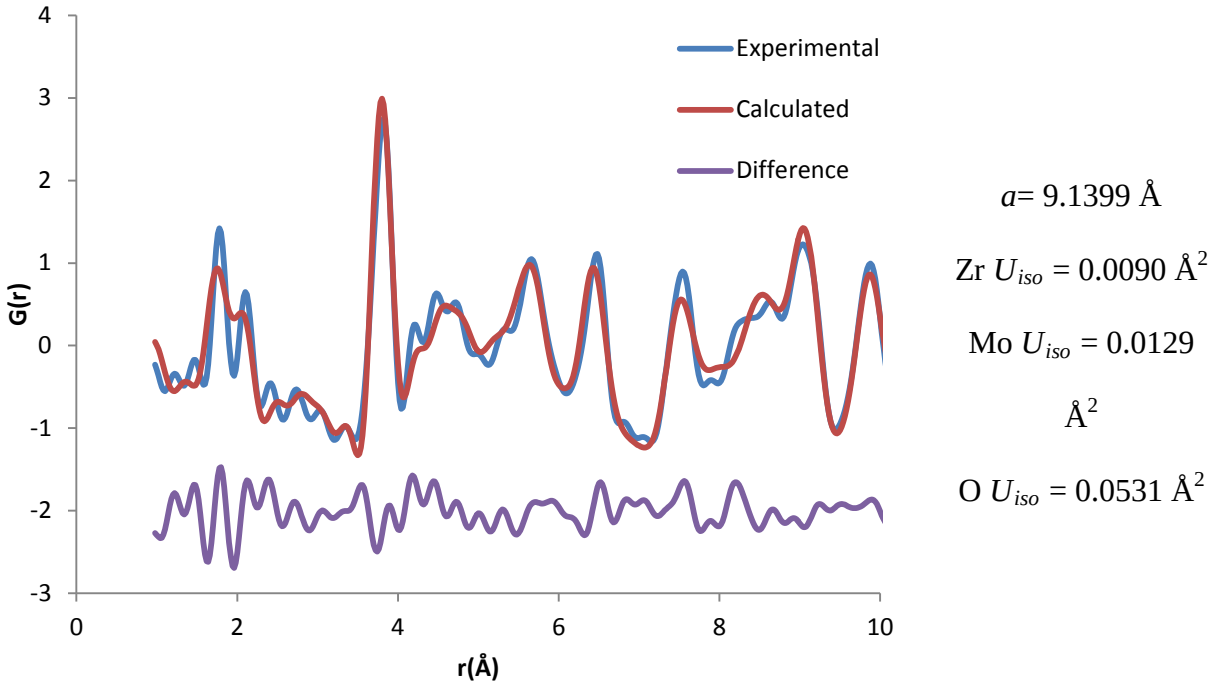

Figure 6.7b: Experimental PDF between 1 and 10 Å for $ZrMo_2O_8$ in a capillary at ambient conditions using a model based on β-ZrW_2O_8.

Initially the only parameters that were allowed to refine were lattice parameters, scale factor, *sratio* and the temperature factors for all atoms. It can be seen from Figure 6.7a that even without refining atom positions the fit is much improved compared to the model based on α-ZrW_2O_8 and the refined unit cell volume for $ZrMo_2O_8$ (763.5Å^3) is comparable to that of β-ZrW_2O_8 at 483K (762.8Å^3). The model of $ZrMo_2O_8$ based on β-ZrW_2O_8 provides a better fit at all length scales with the exception of the first M-O peaks (Figure 6.7b). In order to investigate this further the atom-atom distances were investigated. A representation of the MoO_4 groups is shown in Figure 6.8 and the distances from this given in Table 6.2.

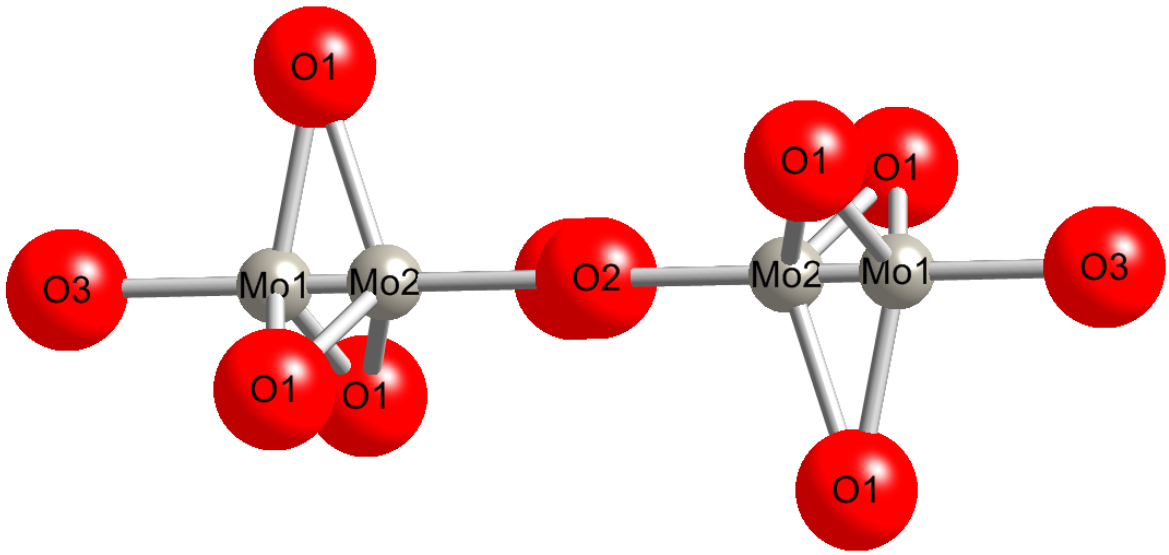

Figure 6.8: MoO_4 tetrahedra (with partial occupancies) in $ZrMo_2O_8$ based on a β-ZrW_2O_8 structure.

Table 6.2: Refined atom-atom distances from the fit presented in Figures 6.5a and b.

	No. of atom-atom distances	Distance (Å)		Distance (Å)
Mo2 – O2	1	1.55	Zr1 – O1	2.067
Mo1 – O3	1	1.697		
Mo2 – O2	1	1.726		
Mo1 – O1	3	1.757		
Mo2 – O1	3	1.802		
Mo1 – O2	1	2.455		
Mo2 – O3	1	2.601		
Mo1 – O2	1	2.629		

In the β-ZrW_2O_8 structure Mo1, Mo2, O2 and O3 are half occupied; O3 is connected with Mo1 and O2 connected with Mo2. Clearly the adjacent Mo1 and Mo2 sites (and O3 and O2

sites) cannot be simultaneously occupied and this has produced an unrealistic PDF in the M-O region

In an attempt to try and solve this problem a model was built where one of the Mo was removed in each of the eight tetrahedra in the unit cell and the corresponding oxygen was kept (Figure 6.9). O2 was never allowed to sit in close proximity to another O2 atom which also resulted in no short Mo2-Mo2 distances with Mo1-Mo2 distances calculated as 4.18Å.

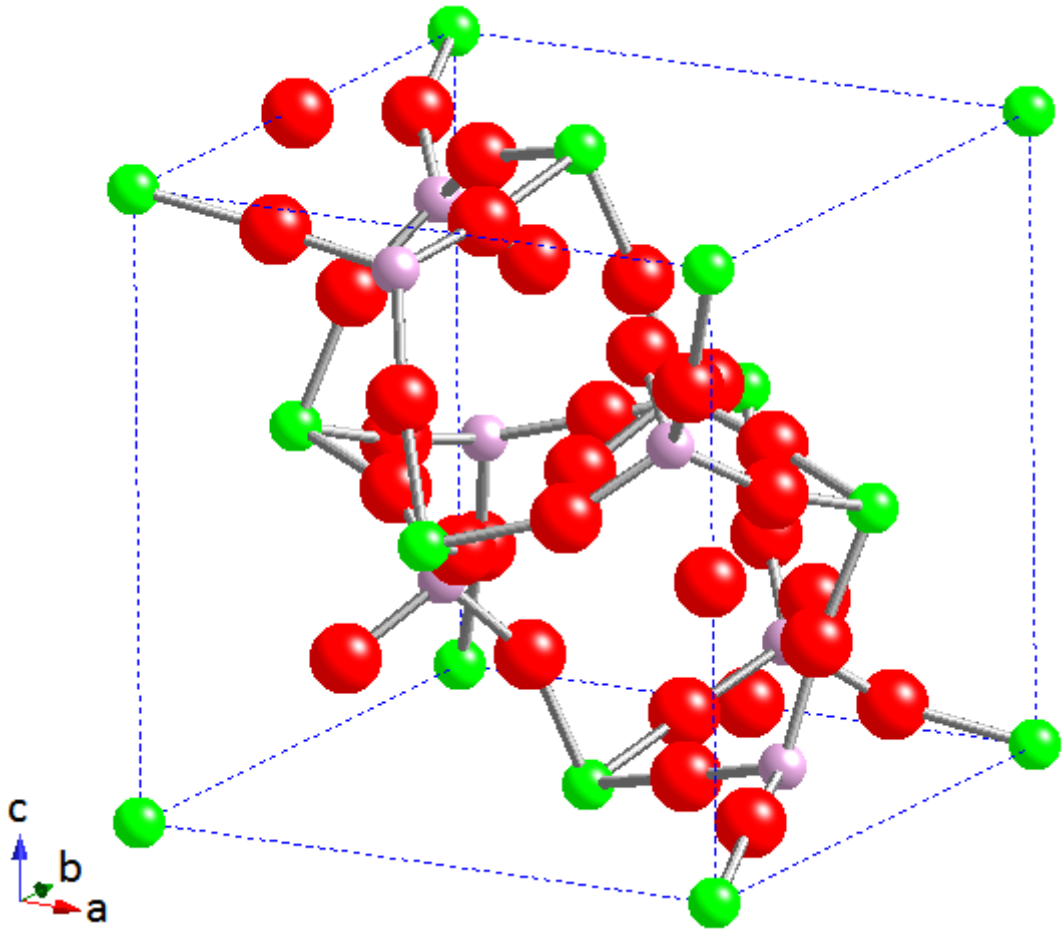

Figure 6.9: Adapted model of $ZrMo_2O_8$ based on the β-ZrW_2O_8 structure (Green=Zr, Red=Oxygen, Purple=Mo).

Table 6.3: Atomic Co-ordinates for the model presented in Figure 6.9.

	x	*y*	*z*	Occ.
Zr1	0.5	0.5	0	1
Zr2	0.5	0	0.5	1
Zr3	0	0.5	0.5	1
Zr4	0	0	0	1
Mo1	0.8394	0.1606	0.6606	1
Mo2	0.1606	0.6606	0.8394	1
Mo3	0.6606	0.8394	0.1606	1
Mo4	0.3394	0.3394	0.3394	1
Mo5	0.1035	0.8965	0.3965	1
Mo6	0.8965	0.3965	0.1035	1
Mo7	0.3965	0.1035	0.8965	1
Mo8	0.6035	0.6035	0.6035	1
O1	0.5671	0.5549	0.7911	1
O2	0.4329	0.0549	0.7089	1
O3	0.9329	0.4451	0.2911	1
O4	0.0671	0.9451	0.2089	1
O5	0.7911	0.5671	0.5549	1
O6	0.7089	0.4329	0.0549	1
O7	0.2911	0.9329	0.4451	1
O8	0.2089	0.0671	0.9451	1
O9	0.5549	0.7911	0.5671	1
O10	0.0549	0.7089	0.4329	1
O11	0.4451	0.2911	0.9329	1
O12	0.9451	0.2089	0.0671	1
O13	0.4329	0.4451	0.2089	1
O14	0.5671	0.9451	0.2911	1
O15	0.0671	0.5549	0.7089	1
O16	0.9329	0.0549	0.7911	1
O17	0.2089	0.4329	0.4451	1
O18	0.2911	0.5671	0.9451	1
O19	0.7089	0.0671	0.5549	1
O20	0.7911	0.9329	0.0549	1
O21	0.4451	0.2089	0.4329	1
O22	0.9451	0.2911	0.5671	1
O23	0.5549	0.7089	0.0671	1
O24	0.0549	0.7911	0.9329	1
O25	0.9945	0.0055	0.5055	1
O26	0.0055	0.5055	0.9945	1
O27	0.5055	0.9945	0.0055	1
O28	0.4945	0.4945	0.4945	1
O29	0.7322	0.2678	0.7678	1
O30	0.2678	0.7678	0.7322	1
O31	0.7678	0.7322	0.2678	1
O32	0.2322	0.2322	0.2322	1

This model with fixed atom positions was then used to fit the data between 0 and 10 Å. Lattice parameters and *U*'s were refined (values presented in Figure 6.10). The calculated pattern based on the new model can be seen in Figure 6.10.

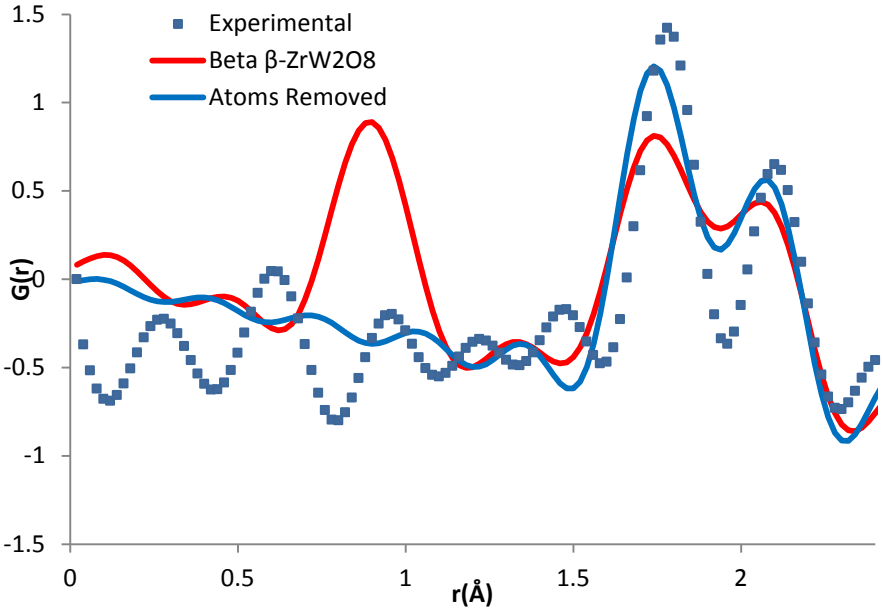

New Model

a= 9.1389 Å

Zr U_{iso} = 0.00452 Å^2

Mo U_{iso} = 0.02470 Å^2

O U_{iso} = 0.03871 Å^2

Figure 6.10: Fit to the PDF data between 0 to 2.5 Å using the new model of $ZrMo_2O_8$.

It can be seen in Figure 6.10 that as expected this new model has no unrealistic atom-atom distances below ~1.5Å and the fit to the first M-O peaks is improved. The short Mo-O2 distance shown in Table 6.2 has been removed but the first Mo-O peak is still not fit acceptably. The rest of the Mo-O distances are the same as in Table 6.2 and it is clear that some of the Mo-O distances are still too short. With the peak having several different Mo-O contributions it is difficult to pinpoint exactly which distances are too short but the Mo-O1 distances appear to be roughly correct based on the experimental data.

The first Zr-O peak also provides a relatively better fit with this new model but the peak is still fit poorly. The Zr-O distances are refining to be smaller than is shown in the experimental PDF.

One thing that has not been done thus far is allowing the atom positions to refine away from the positions provided by Evans *et al* (1996). Atom positions were thus allowed to refine and the new fit to data between 1 and 10Å can be seen in Figure 6.11.

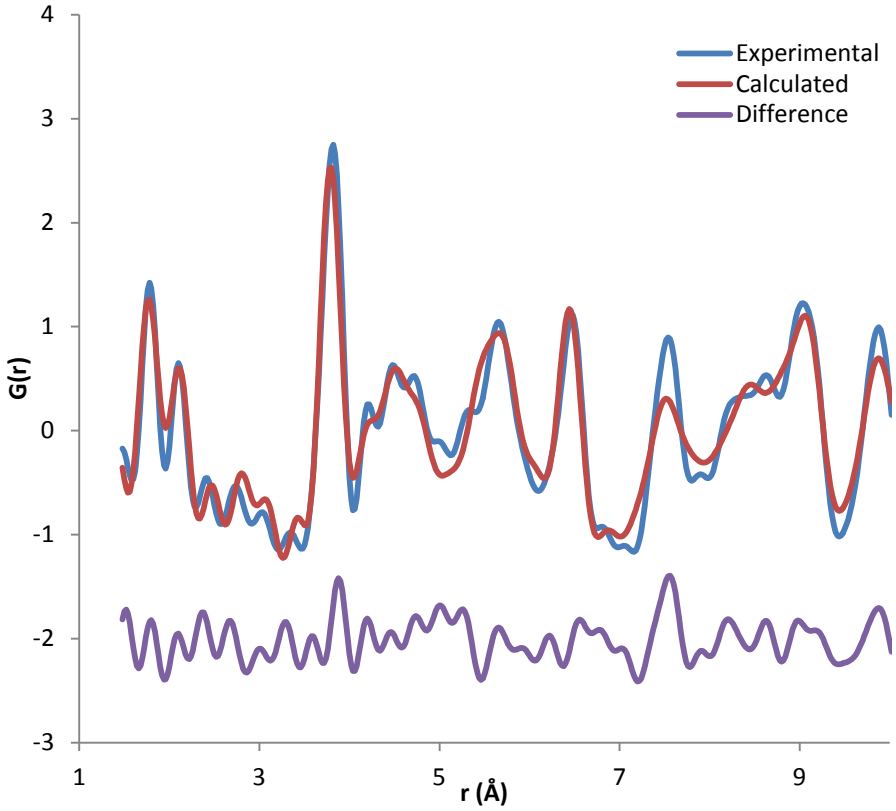

a= 9.15712 Å

Zr U_{iso} = 0.0047 Å^2

Mo U_{iso} = 0.0185 Å^2

O U_{iso} = 0.04737 Å^2

Figure 6.11: The fit to the experimental PDF between 0 and 10 Å (Rw = 0.259) after the refinement of atom positions.

The fit for both the first Mo-O and Zr-O peak is improved and the atoms do not move too far away from the starting positions obtained from the β-ZrW_2O_8 model provided by Evans *et al* 1996. The refined Mo-O distances are presented in Table 6.4 and now show the non-bridging oxygen atoms are forming longer bonds than the Mo-O1 distances, which is not expected (Section 6.1). The Zr-O distances refine to 2.1 Å which would appear to be correct based on a simple visual inspection of the experimental Zr-O peak.

Table 6.4: M-O distances obtained when atom positions were refined using experimental data between 1 and 10 Å.

	No. of atom-atom distances	Distance (Å)		Distance (Å)
Mo1 – O3	1	1.789	Zr1 – O1	2.101
Mo2 – O2	1	1.889		
Mo1 – O1	3	1.776		
Mo2 – O1	3	1.767		

The model with atoms removed was then fit to the experimental data between 1.5 and 50 Å with the atom positions again refined (Figure 6.12a and b).

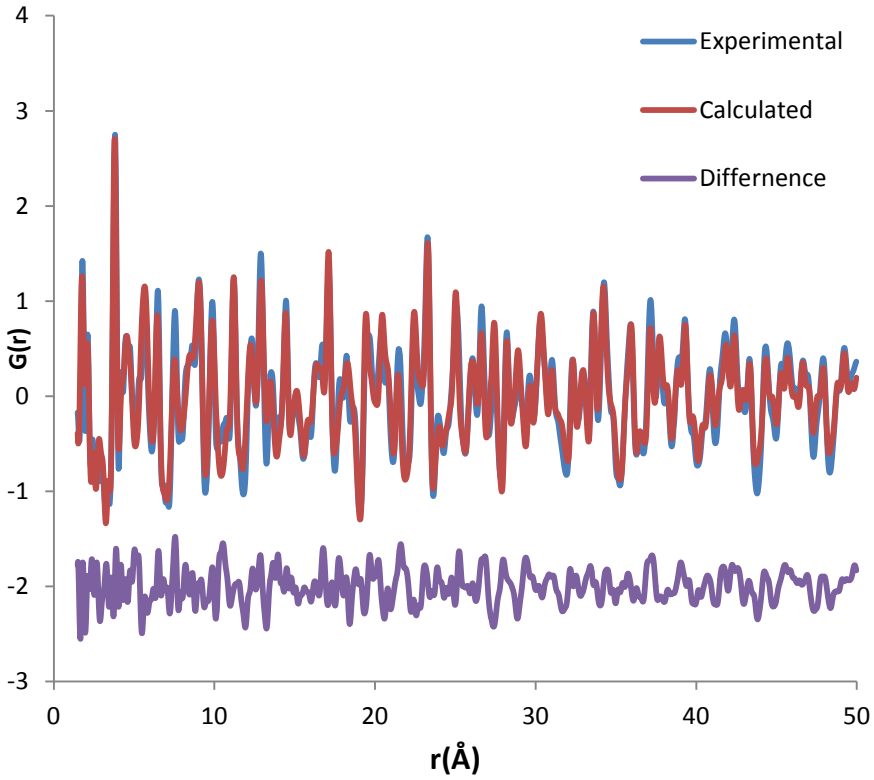

a= 9.14141 Å

Zr U_{iso} = 0.007 Å^2

Mo U_{iso} = 0.02245 Å^2

O U_{iso} = 0.04347 Å^2

Figure 6.12a: Experimental PDF between 1.5 and 50 Å with the new model for $ZrMo_2O_8$ (*Rw* = 0.312).

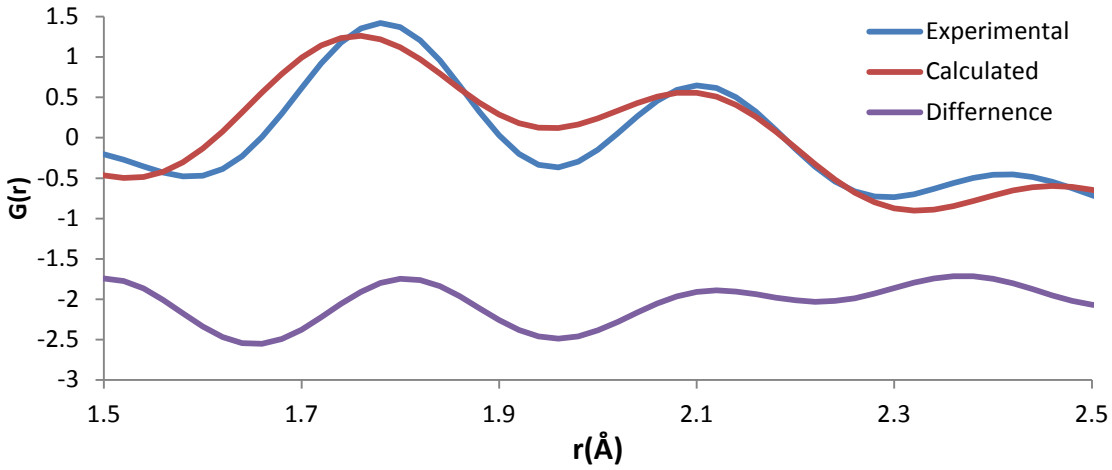

Figure 6.12b: Expanded region showing the first M-O peaks using the new model and data from 1.5 to 50 Å.

The overall fit is worse than using the model based on β-ZrW_2O_8 with all the atoms included (Figure 6.7a). The lattice parameter is now comparable to previous refinements as well which appears to have the knock on effect of providing a worse fit to the Mo-O and Zr-O peaks. With a larger refined unit cell volume the atoms will inherently be further away from each other if the atoms positions are relatively constant in the refinement.

Table 6.5: Refined M-O distances using the altered model against experimental data between 1 and 50 Å.

	No. of atom-atom distances	Distance (Å)		Distance (Å)
Mo1 – O3	1	1.816	Zr1 – O1	2.084
Mo2 – O2	1	1.850		
Mo1 – O1	3	1.740		
Mo2 – O1	3	1.768		

Table 6.5 shows the Mo-$O_{non\text{-}bridging}$ distances are still longer than the Mo-O1 distances but it is clear that the Mo-O1 distances are refining to be too short and thus a poor fit is given for the first Mo-O peak. The peak centre for the Mo-O peak is roughly 1.78 Å so a correct model will have Mo-O distances around this distance which will be relatively similar. Without a model that truly represents cubic $ZrMo_2O_8$ PDFGui it is difficult to make a firm conclusion that this proposed structure is accurate at all length scales using analysis of PDFs.

There are eight WO_4 tetrahedra in the expanded β-ZrW_2O_8 unit cell (Figure 1.b) but they are linked in pairs when considering occupancies of Mo and O2 and O3 sites (Figure 6.6). This gives four pairs of Mo tetrahedra (Figure 6.13) that can have two different configurations depending on occupancy. As a result a more accurate model would be to create a 4x4 super cell and have the sixteen different configurations of these occupancies in each unit cell. This should provide a better fit overall in PDFGui although the model assumes that occupancies in one tetrahedral pair is not affected by the surrounding tetrahedral pair.

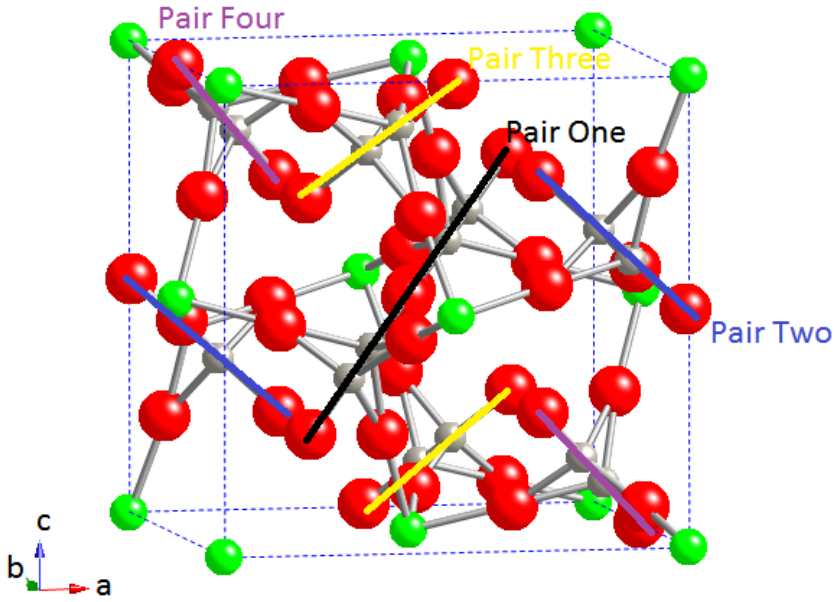

Figure 6.13: Pairs of MoO_4 tetrahedra in the ambient structure of $ZrMo_2O_8$.

This box of atoms is similar to the type of modelling that is used in RMCProfile but crystallographic constraints will still be imposed on the structure by PDFGui. RMCProfile may be useful to model cubic $ZrMo_2O_8$ although it is not clear if RMCProfile would take into account the occupancies of the sites being linked or if it would also have unrealistic atom positions.

6.4.2 Summary of Ambient Structure

It is clear from the refinements presented in Section 6.5.1 that the structure of $ZrMo_2O_8$ is best described by a model based on β-ZrW_2O_8. Unfortunately it was discovered that there were problems with the way PDFGui was calculating the PDF from a model with half occupied sites, so although the fit was much improved the model was not fully correct. When one unit cell was constructed with some sites fully occupied sites and others unoccupied (depending on Mo site occupancy) the fit to the first M-O peaks was improved, with the unrealistic atom-atom distances being removed. A super cell could be constructed and attempts made to refine this in PDFGui but removing the correct atoms from the unit cell would be a time consuming and a complex task and it is unknown if PDFGui would be able to model such a super cell to experimental data.

Despite this poor modelling it is likely that $ZrMo_2O_8$ possesses a structure similar to β-ZrW_2O_8 with a *Pa*-3 space group, consistent with previous studies (Section 6.2). Although the introduction to Wilkinson *et al*'s 2012 paper made this same assertion they go on to only produce an acceptable fit to $ZrMo_2O_8$ data from a model based on the α-ZrW_2O_8 structure. This refinement was apparently only conducted between 0 and 10 Å on data with a lower Q_{max} used to produce the PDF than that presented in this work. Both these factors may contribute to an acceptable fit to their data and no mention is made of having fit any other model of $ZrMo_2O_8$.

The discussion presented in the next section will assume that the local structure of $ZrMo_2O_8$ is adequately described using the modified β-ZrW_2O_8 structure with atoms selectively removed.

6.4.3 Cubic $ZrMo_2O_8$ at High Pressures

6.4.3.1 Comparison of Capillary and DAC PDFs

High quality PDFs were produced up a Q_{max} of 20Å^{-1} and the PDF for the sample loaded in a DAC at ambient pressure and temperature can be compared with the PDF produced from a sample in a kapton capillary in Figure 6.14.

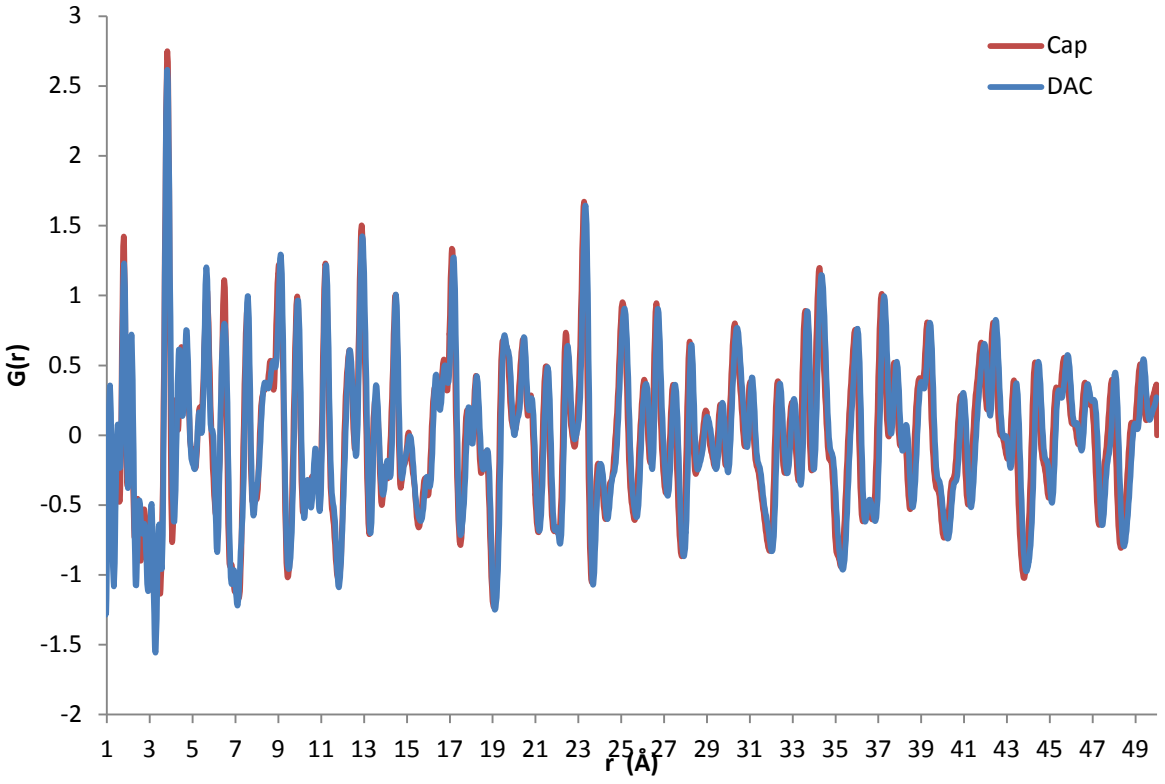

Figure 6.14: Comparison of PDFs of $ZrMo_2O_8$ at ambient conditions in two different sample containers.

Some variation between the PDFs was expected due to the different Q_{max} used for the Fourier transform from the $S(Q)$ and poorer sample to background ratios in the DAC sample, but it can be seen in Figure 6.14 the PDFs do not track absolutely perfectly on top of each other. Figures 6.15a and b show that the peaks are not in the same position in both PDFs. The position of the Zr-O peak is ~2.10Å in the capillary PDF and 2.12Å so only represents roughly a 1% variation, which is likely attributed to small experimental errors. This can be a result of incorrect values for x-ray wavelength (due to, e.g. monochromator drift), an incorrect sample-to-detector distance or a temperature variation in the sample. There is, however, no evidence of variation of the data collected at different pressures with the sample in the DAC and so observed trends are real.

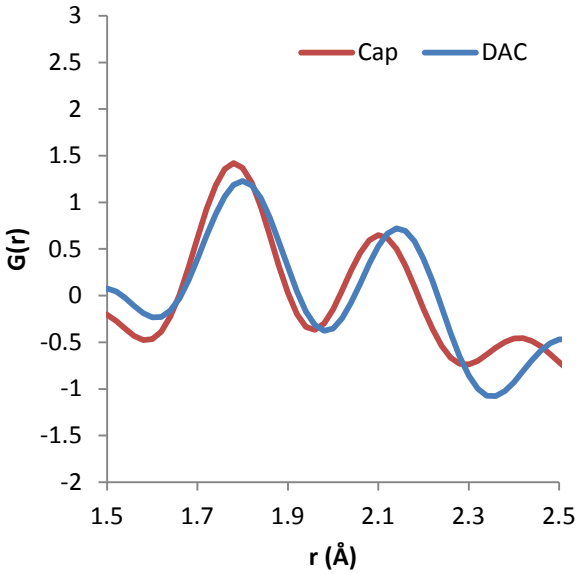

6.15a: Capillary vs. DAC PDF between 1.5 and 2.5Å.

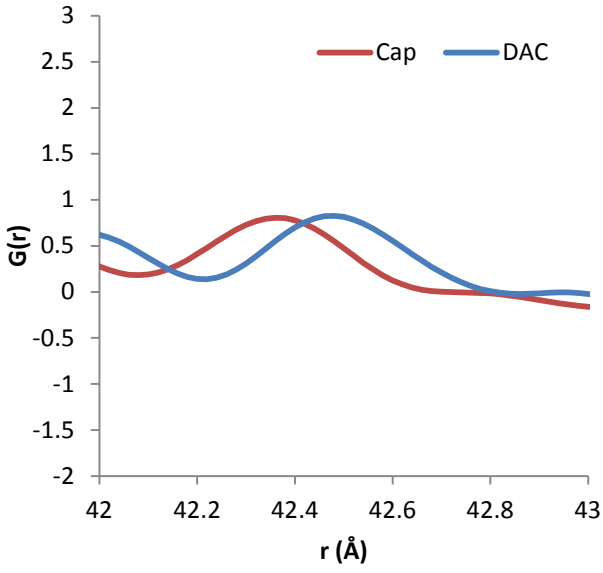

6.15b: Capillary vs. DAC PDF between 42 and 43Å.

6.4.3.2 PIA of $ZrMo_2O_8$

As pressure was increased $ZrMo_2O_8$ began to amorphise and all Bragg peaks had disappeared by 2.84 GPa (Figure 6.16). After this point only diffuse scatter was observed in the diffraction pattern.

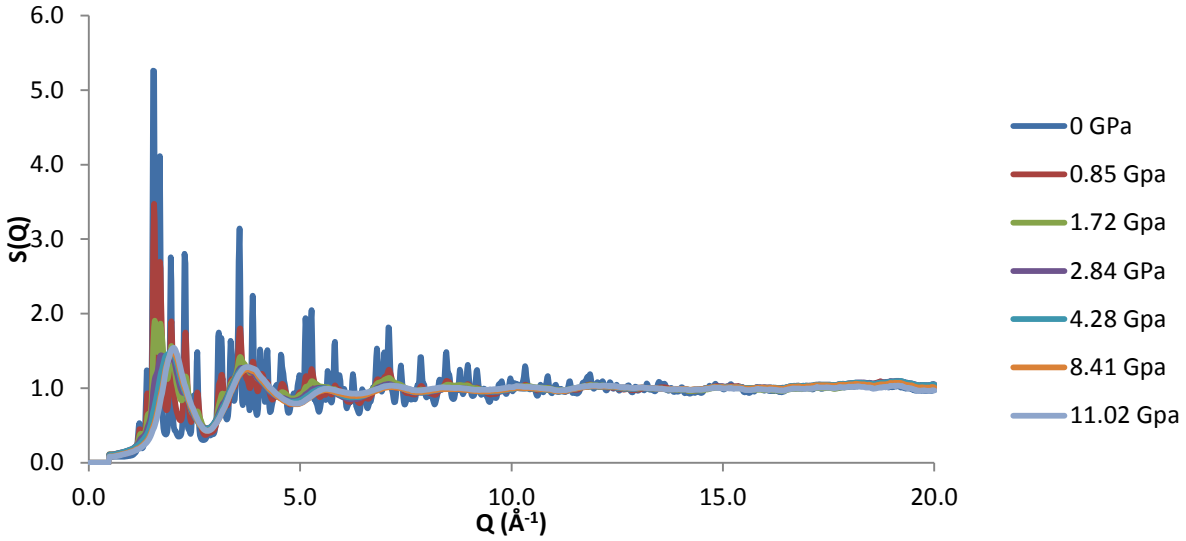

Figure 6.16: $S(Q)$ for $ZrMo_2O_8$ in a DAC with increasing pressure.

This loss of long range order is also reflected in the experimental PDFs, with peaks above 5 $Å^{-1}$ disappearing by 2.84 GPa (Figure 6.17). As pressure is increased there are very clear changes in the PDF pattern as local structure changes which is in stark contrast to the relatively subtle changes in PDF patterns seen in BTO (Figure 4.4). While there is the expected loss of long range order, there are still peaks present below 5 $Å^{-1}$ even at 11 GPa.

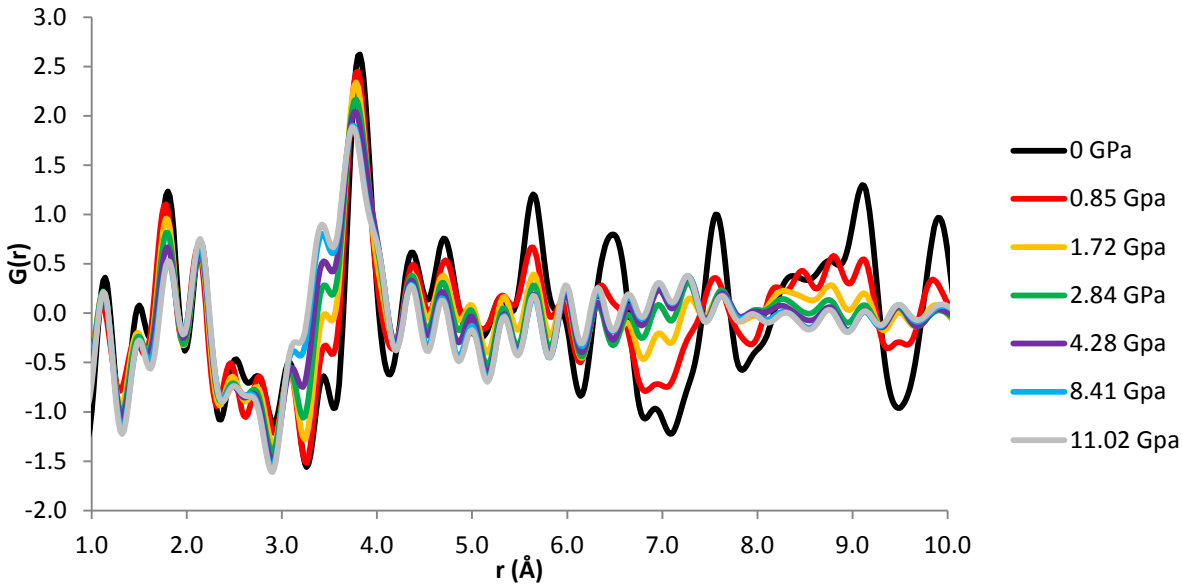

Figure 6.17: Experimental PDFs of $ZrMo_2O_8$ in a DAC with increasing pressure.

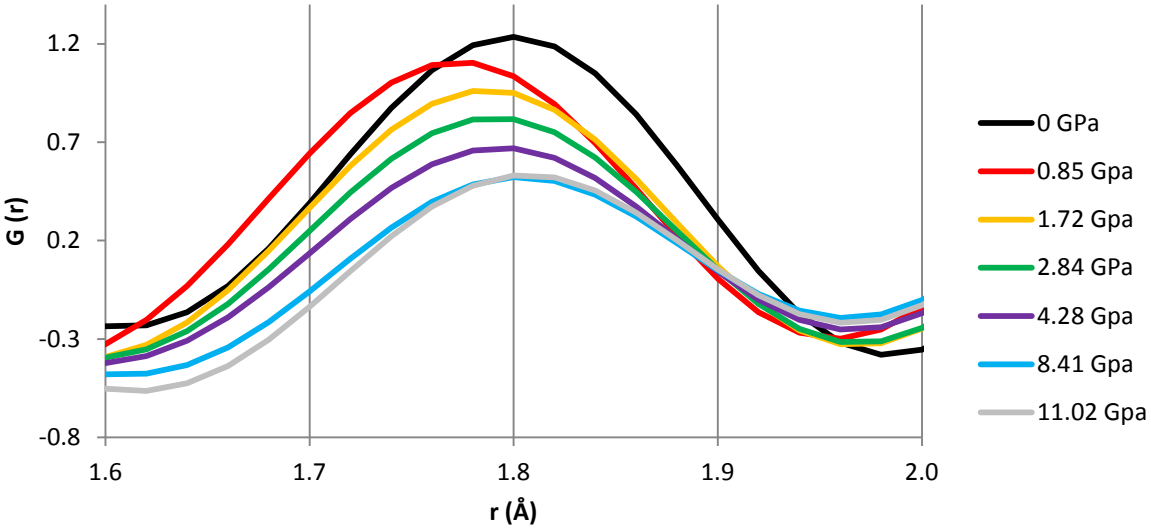

Figure 6.18: First Mo-O peak as pressure was increased up to 11.02GPa.

The first peak, which contains the Mo-O distances, shows a definite change as pressure is increased (Figure 6.18). Upon the initial application of pressure the Mo-O bonds are compressed. The trend then reverses and the centre shifts to higher distance whilst it also

appears to reduce in intensity as pressure is increased up to 8.41 GPa and then remains relatively constant to 11.02GPa. The density of $ZrMo_2O_8$ is increasing with pressure and this will affect the baseline ($-4\pi\rho_0 r$) in the PDF but it is clear its area is being reduced as pressure is increased. In agreement with Wilkinson *et al* (2012) there is a reduction in the number of Mo-O bonds at ~1.8 Å. With this peak comprising four different Mo-O distances at ambient pressure, it is not possible to ascertain exactly which Mo-O bonds are lengthening however we can fit the peak to get a rough idea of relative areas between 0 GPa and 11 GPa PDFs. Fitting as a single Gaussian peak suggests that roughly half of the area of the peak has been lost by 11 GPa. Fitting with a single Gaussian was done in order to obtain a rough estimate of peak area, however as this peak is not made up of a single Gaussian guesses had to be made about the baseline due to not knowing ρ_0 for either pressure. It is clear that between 8.41 GPa and 11.02 GPa there is a loss of the shorter Mo-O bonds in the structure.

The first Zr-O peak also shows changes as pressure is increased with these distances reducing upon initial compression (Figure 6.19)

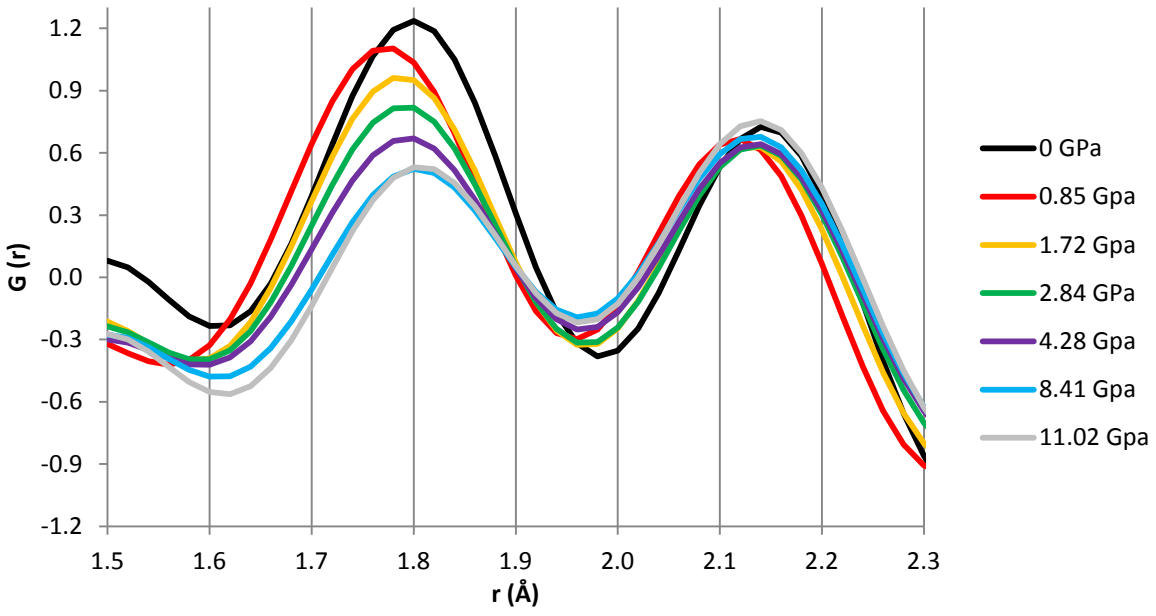

Figure 6.19: First two peaks in the PDF pattern of $ZrMo_2O_8$ as pressure is increased.

Due to the less dramatic changes observed in this peak over pressure it is difficult to extract any definitive trends. While there is a clear compression of the Zr-O bonds between 0 and 0.85 GPa the trends past this point are unclear. To investigate the changes in this peak as pressure increased between 0.85 and 1.72 GPa the PDFs corresponding to these pressures are presented in Figure 6.20.

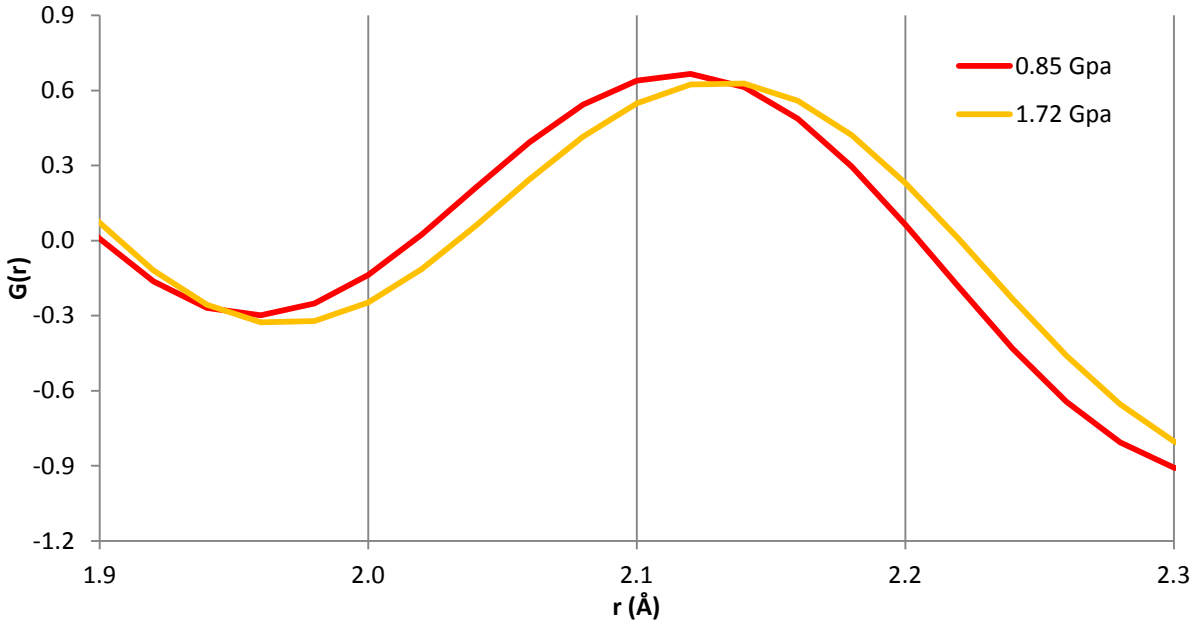

Figure 6.20: Zr-O peak at 0.85 and 1.72GPa.

Between 0.85 GPa and 1.72 GPa there is an apparent increase in Zr-O bond length with the peak centre shifting to larger *r*. After 1.72 GPa the peak centre appears to stay consistent (Figure 6.19) but the peak broadens as pressure is increased.

In order to investigate the evolution of this peak with pressure the best way of representing the changes is by producing differential PDFs where each pressure is subtracted from the previous. This will give indications of how the structure has changed between any given

pressure points. For example the differential PDF that represents the change from 1.72 to 2.84 GPa is simply the PDF for 1.72 GPa subtracted from the PDF collected at 2.84 GPa. Positive peaks in Figure 6.21 represent an increase in the G(r) and thus an increase is atom-atom distances at the given length scale, the opposite is true with negative peaks. A differential PDF of 0 to 0.85 GPa and 0.85 GPa to 1.72 GPa are difficult to analyse due to the peak position shifting. It is clear from Figure 6.15 that there is loss of the shorter Mo-O distances between 0.85 and 1.72 GPa but visual inspection of the distances at ~2.1 Å presented in Figure 6.17 is not conclusive on how these bonds are lengthened.

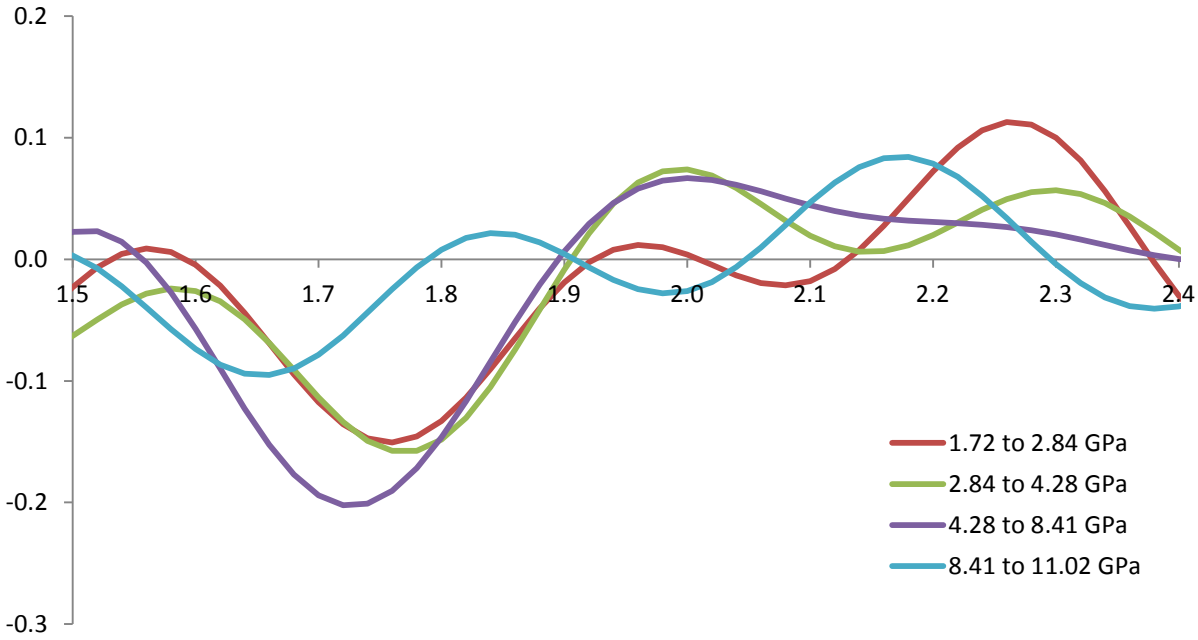

Figure 6.21: Differential PDFs of $ZrMo_2O_8$ between 1.5 and 2.4 Å from 1.72 to 11.02 GPa.

Figure 6.21 shows that new atom-atom distances are introduced above 1.9 Å as pressure is increased but the exact distance these are introduced is pressure dependant. Between 1.72 and 2.84 GPa there is an introduction of atom-atom distances at roughly 2.25 Å which corresponds to a loss of Mo-O distances at ~1.75 Å. The areas of these peaks appears to be

roughly equal so it can be deduced that some Mo-O bond lengths are increasing from ~1.75 Å to 2.25 Å.

Between 2.84 GPa and 4.28 GPa there are two distinct atom-atom distances that are introduced at ~2.0 and 2.3 Å and there is also a loss of Mo-O distances similar to the loss between 1.72 and 2.84 GPa. This shows that between 2.84 and 4.28 GPa the Mo-O bonds at ~1.8GPa become lengthened to two separate distances.

Between 4.28 GPa and 8.41 GPa shorter Mo-O distances are lost in comparison to those lost between 1.72 and 4.28 GPa. These bonds are lengthened to a range of distances between 1.9 and 2.4 Å. It is not possible to ascertain the different Mo-O distances introduced based on Figure 6.18. Between 8.41 and 11.02 there are still changes in the PDF pattern as even shorter Mo-O bonds are lengthened to ~2.15 Å.

The differential PDFs show that as pressure is increased the amorphisation proceeds in stages with different Mo-O bond lengths being affected. It is clear that different Mo-O distances are being lengthened to roughly three unique new lengths and it appears that each new Mo-O distance may correspond to a lengthening of specific Mo-O bonds.

With the changes in the peak at ~2.1 Å appearing to be precisely related to the changes in the Mo-O peak at ~1.8 Å it is apparent that the Zr-O distances are remaining fairly consistent after 1.72GPa. It is clear that the Zr-O bond length decreases upon compression up to 0.85 GPa then there is an increase in Zr-O distances between 0.85 and 1.72 GPa. It is possible that this lengthening of the Zr-O bonds could be attributed to higher co-ordinate Zr atoms. It appears that processes above this pressure do not involve a change in co-ordination number of Zr however with these distances remaining constant up to 11.02 GPa.

XANES and EXAFS data suggest an increase in Zr co-ordination from 6 to 7 (along with a increase in Mo co-ordination.[7] There is no evidence of any new metal-oxygen distances below 2.4 Å so any weakly bonded oxygen atoms forming higher co-ordinate Mo or Zr atoms have bonds longer than 2.4 Å. That is to say the 5th bonded oxygen would be further than 2.4Å away from the Mo or Zr atoms in the amorphous structure.

As well as changes in the first M-O peaks there are remarkably clear trends in the Mo-Zr peak at ~3.8 GPa (Figure 6.22). There is an apparent reduction of the Zr-Mo distances as pressure is increased which is also accompanied with the introduction of a new atom-atom distance at roughly 3.4 Å and there are clear signs of another atom-atom distance introduced at 4.0 Å.

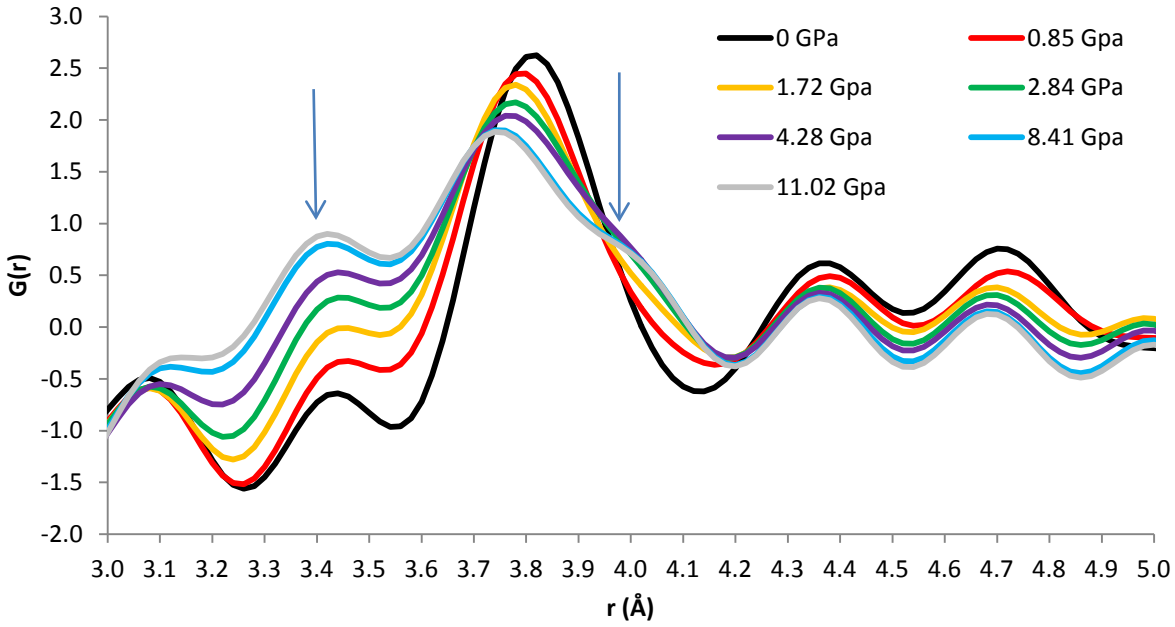

Figure 6.22: The M-O-M peaks in the PDF pattern of $ZrMo_2O_8$ as pressure is increased.

Analysis of EXAFS data has shown that the Zr-Mo distances become more distributed upon PIA[7] and the PDFs appear to be agreement with this. On first glance the introduction of peaks at 3.4 and 4.0 Å do not appear to correspond with a sharp enough decrease in Zr-Mo distances at 3.8 Å to be purely explained by the Mo-Zr distances becoming more distributed as pressure

increases however. Again differential PDFs can be used to investigate changes in the PDFs as pressure is increased and Figure 6.23 presents these where the higher pressure has been subtracted from the lower pressure so that anything above the zero line represents an increase in atom-atom distances.

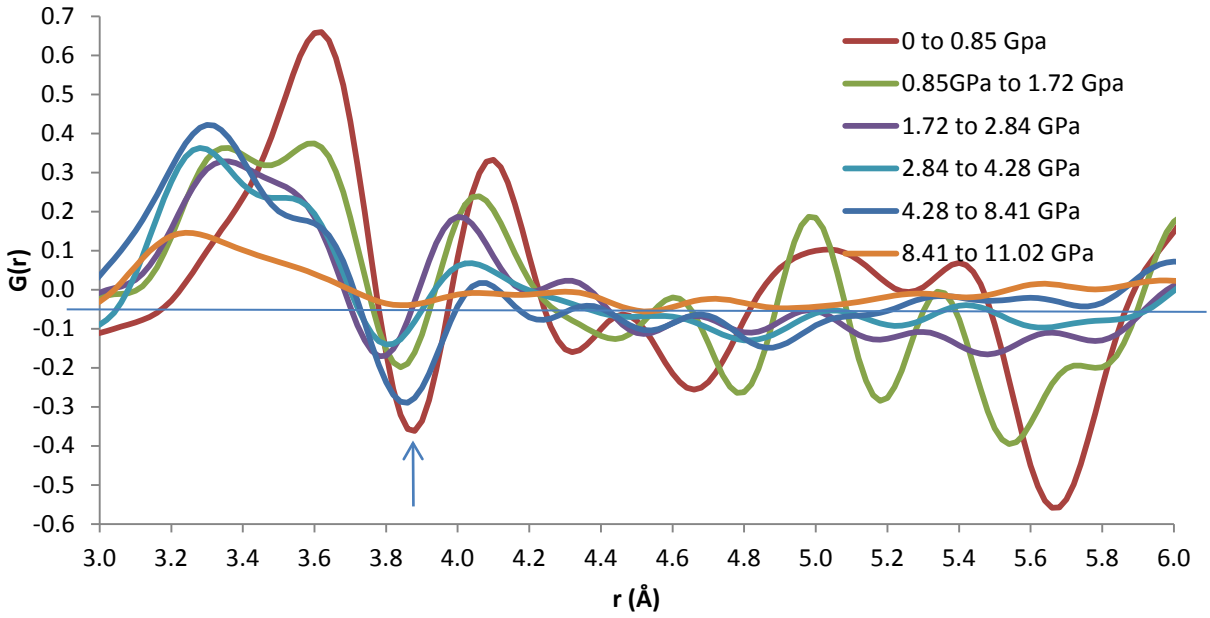

Figure 6.23: Differential PDFs of $ZrMo_2O_8$ between 3 and 6Å as pressure is increased.

Between 0 and 0.85 GPa Figure 6.20 shows the loss of Mo-Zr distances at roughly 3.85 Å with new distances appearing at 4.1 Å, 3.6 Å and 3.3 Å. It is likely that some of these changes are due to compression of the Zr/Mo-O bond length which is observed in Figures 6.15 and 6.16. It is apparent that more atom-atom distances are formed between 3.0 and 4.3 Å than are lost and thus there is a net gain of atom-atom distances in this region. As a result it is likely there is a contribution from other atom-atom distances than just Zr-Mo distances.

Between 0.85 and 1.72 GPa there is an increase of atom-atom distances at 4.0, 3.6 and 3.3 Å with a loss of Zr-Mo distances at 3.86 Å. Between 2.84 and 11.02 GPa there is little increase in the number of atom-atom distances at 4.1 Å but the other increases and decreases persist at

roughly the same lengths up to 8.41 GPa. Between 8.41 and 11 GPa there is no major decrease in Zr-Mo distances at ~3.8 A but there are still an increase in atom-atom distances at ~3.2 Å which again is an indication that the changes in the PDF pattern presented in Figure 6.23 cannot be attributed simply to a larger distribution of Zr-Mo distances.

The peak at 3.8 Å is made up of two Zr-Mo distances, a shorter Zr1-Mo1 distance and a longer Zr1-Mo2 distance. A unit cell with certain atoms removed for clarity is presented in Figure 6.24.

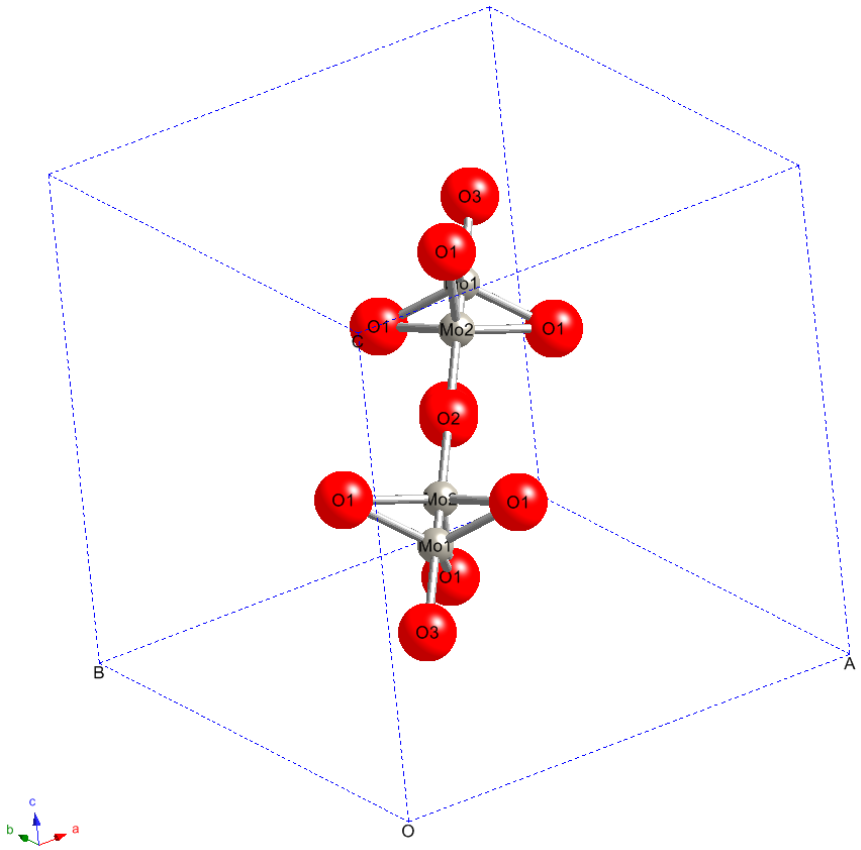

Figure 6.24: Closest Mo-Zr distances in cubic $ZrMo_2O_8$.

It was shown in Figure 6.21 that with the exception of a compression in Zr-O bonds between 0 and 0.85 GPa and a lengthening of these distances between 0.85 and 1.72 GPa the changes in the 1.9 to 2.4 Å region with pressure can be attributed to the addition of longer Mo-O

bonds. This means that the Zr-O distances are remaining fairly stable at high pressures and the main changes are in the Mo-O distances. If it is assumed that the Zr-O octahedra are stable as pressure is increased then the Mo atom moves relative to the zirconium atoms. Given the close proximity of O2 and Mo1 when these sites are occupied it would be surprising if the O2 atoms did not co-ordinate with the Mo2 atoms, this formation of a bridge between the tetrahedra would be similar to what is observed in the PIA of α-ZrW_2O_8.[6] The distance between Mo1 and O2 at ambient pressure is ~2.5 Å which is much shorter than the distance to the closest Zr atoms (~4.6 Å). If the Mo1 atom moved toward the O2 atom then this would lead to a reduction in Zr-Mo distances but not by enough to create Mo-Zr distances of ~3.4 Å if it is assumed the Mo moves in the (*z*,*z*,*z*) direction. The Mo1-Mo2 distance is around 4.2 Å in the ambient structure and the partial PDF does show a loss of atom-atom distances at 4.2 Å. It may be possible that the Mo1 and Mo2 are forming a weak bridge through O2 atoms in the unit cells where this configuration exists, this would have the effect of reducing Mo-Mo distances but there could be no Mo1 – O2 distances below 2.4 Å.

The O3 atom must also be considered as this atom may also form weak bonds with other metal atoms in the structure. It is sensible to assume that this would happen with a nearby atom, so consideration must be given to the structure surrounding each O3 atom (Figure 6.25).

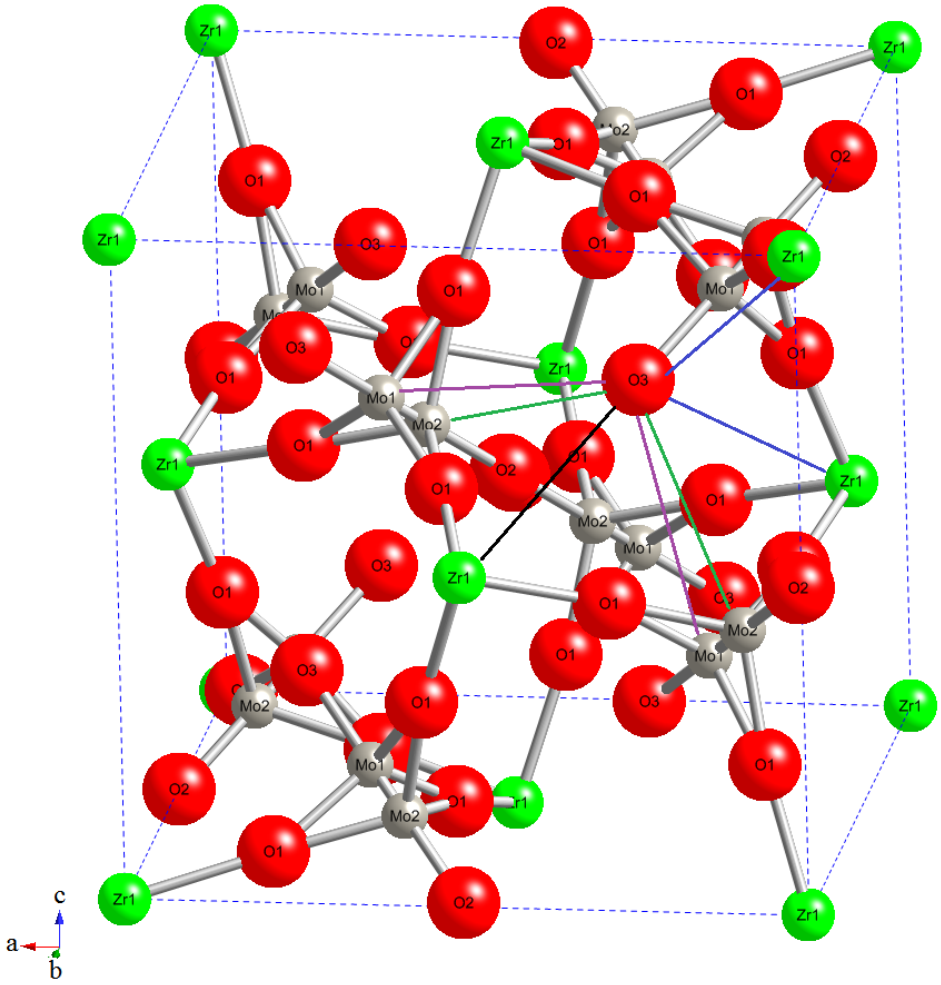

Figure 6.25: Closest O-atom distances in cubic $ZrMo_2O_8$.

In the proposed structure of $ZrMo_2O_8$ at ambient conditions Mo1 and Mo2 are half occupied so we must consider both of these potential occupancies when considering O3 – M distances. The closest Zr-O3 and Mo-O3 non-bonding distances can be seen in Table 6.6. These distances are calculated from a model of $ZrMo_2O_8$ without the atom positions being allowed to refine away from the initial starting values.

Table 6.6: O-atom distances in cubic $ZrMo_2O_8$ corresponding to Figure 6.25.

Atom-Atom	Distance
O3- Zr (black line)	3.619 Å
O3 – Zr (blue lines)	4.059 Å
O3 – Mo2 (green lines)	3.612 Å
O3-Mo1 (purple lines)	3.777 Å

The closest atom O3 could potentially co-ordinate with is the Mo2 atom, assuming this position is occupied. This would require the O3 atom to be displaced away from the [111] diagonal to bring into closer proximity with Mo2 atoms which would result in a rotation of the oxygen tetrahedra although it is unclear how this potential rotation would fit with the lack of change in the Zr-O distances above 1.72 GPa

It is very difficult to investigate how this oxygen atom moves in relation to the Zr and Mo atoms due to the domination of the pattern by metal-metal distances around 3.7 Å (Figure 6.8). It can be seen in Figure 6.26 that there is little/no information in the PDFs regarding metal-oxygen distances above 2.4 Å so it is difficult to say how the oxygen atoms are moving relative to their surrounding metal atoms.

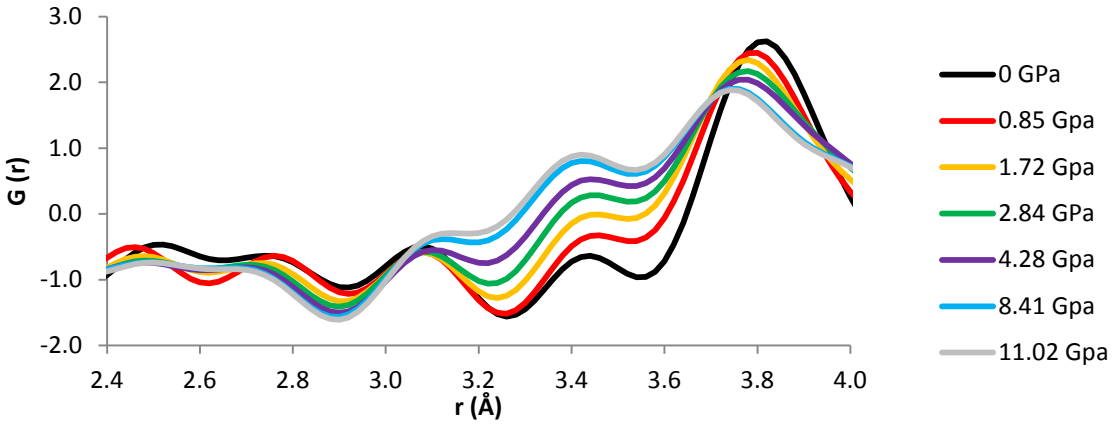

Figure 6.26: PDFs between 2.4 and 4.0 Å for cubic $ZrMo_2O_8$ as pressure is increased.

It would be useful to investigate neutron PDFs, which would be more sensitive to the oxygen atoms but as mentioned in Section 1.6 it is not currently possible to carry out high pressure neutron PDF studies.

In an attempt to model the Zr-Mo distances in PDFGui, an ambient structure from Section 6.4.1 was taken and the Mo1 position was allowed to refine against the highest pressure data between 3 and 4.2 Å. Unfortunately the Mo position moved unrealistically off its starting position and the fit was still poor. It was thus deemed impractical to model the atom movements using PDFGui. As a result it is difficult to deduce the amorphisation mechanism from purely visually examining the data alone and once again it would be interesting to see what results could be produced by RMCProfile. If the modelling was successful then this approach may be able to justify the changes that are occurring between each pressure and why some processes appear to stop/complete and then others begin as pressure is increased.

6.4.3.3 "Lorched" PDFs of Cubic $ZrMo_2O_8$ at High Pressure

Wilkinson *et al.*[3] concentrated their analysis of their high pressure data on PDFs produced with the "Lorch" function in PDFGetX2 and it is not clear how this may have affected their data analysis. They did present two high pressure PDFs of $ZrMo_2O_8$ that had not been produced using the Lorch function however (Figure 6.27) and these can be compared to non-Lorched PDFs from this study (Figure 6.28).

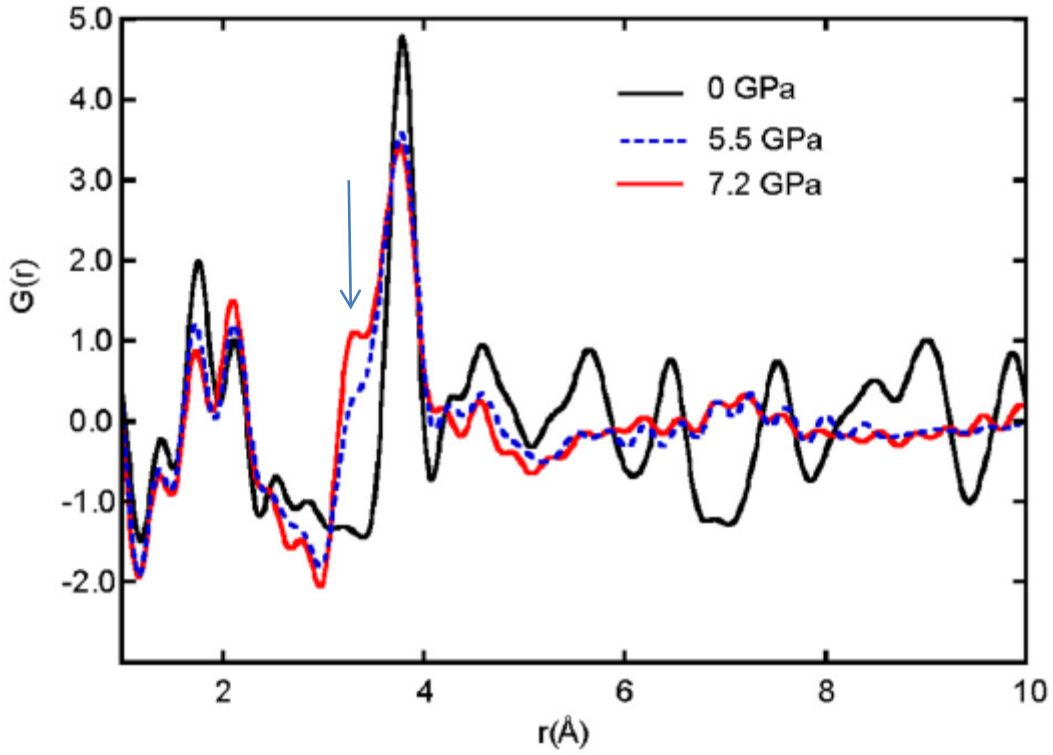

Figure 6.27: Non-Lorched PDFs of $ZrMo_2O_8$ taken from Wilkinson *et al.*[3]

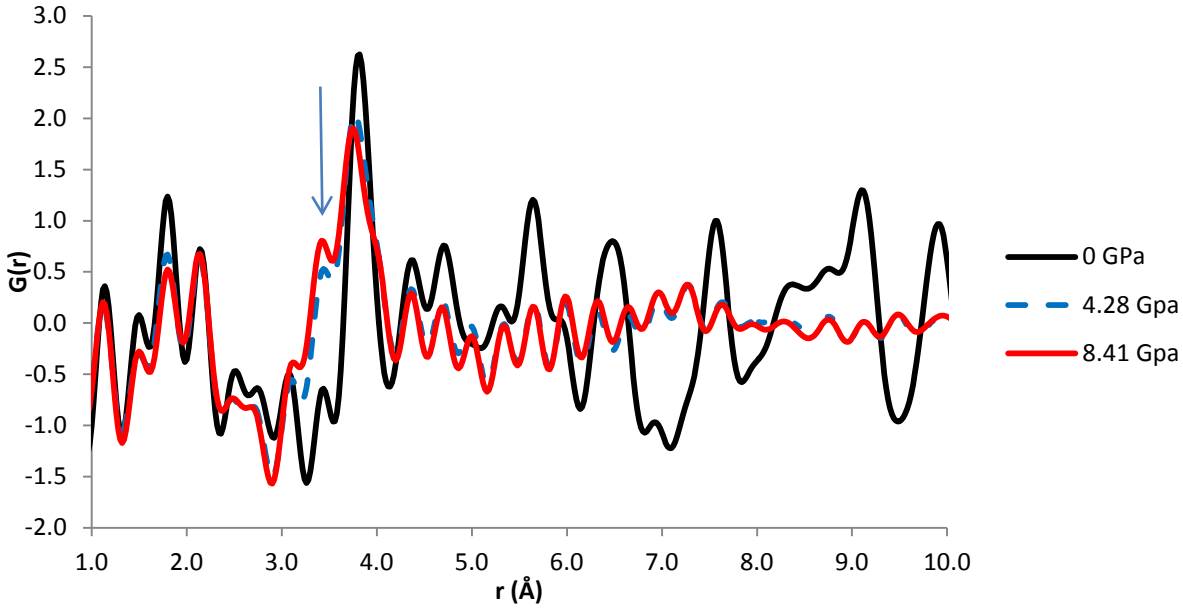

Figure 6.28: PDFs of $ZrMo_2O_8$ at comparable pressures to those presented in Figure 6.27.

The non-Lorched PDFs from this study and those presented by Wilkinson *et al.*[3] are comparable but there are subtle differences. There is no increase in the peak intensity at 2.2Å for the highest pressure PDF from this study presented in Figure 6.28. Also if the PDF at 4.28GPa from Figure 6.28 is compared with the PDF at 5.5 GPa from Figure 6.27 it is apparent that there is an improved peak resolution with the PDFs produced in the Figure 6.28. This can most clearly be seen in the comparing the new atom-atom distances at ~3.8GPa (Marked). The improved resolution can be attributed to the higher value of Q_{max} (21Å^{-1}) used for the PDFs presented in Section 6.4.3.2 in comparison to Wilkinson *et al.*[3] (Q_{max} = 19Å^{-1}). With Wilkinson *et al.*[3] making their conclusions from their lorched PDFs (Figure 6.29) however it is possible to produced PDFs from this study in a similar fashion (Figure 6.30) for comparison.

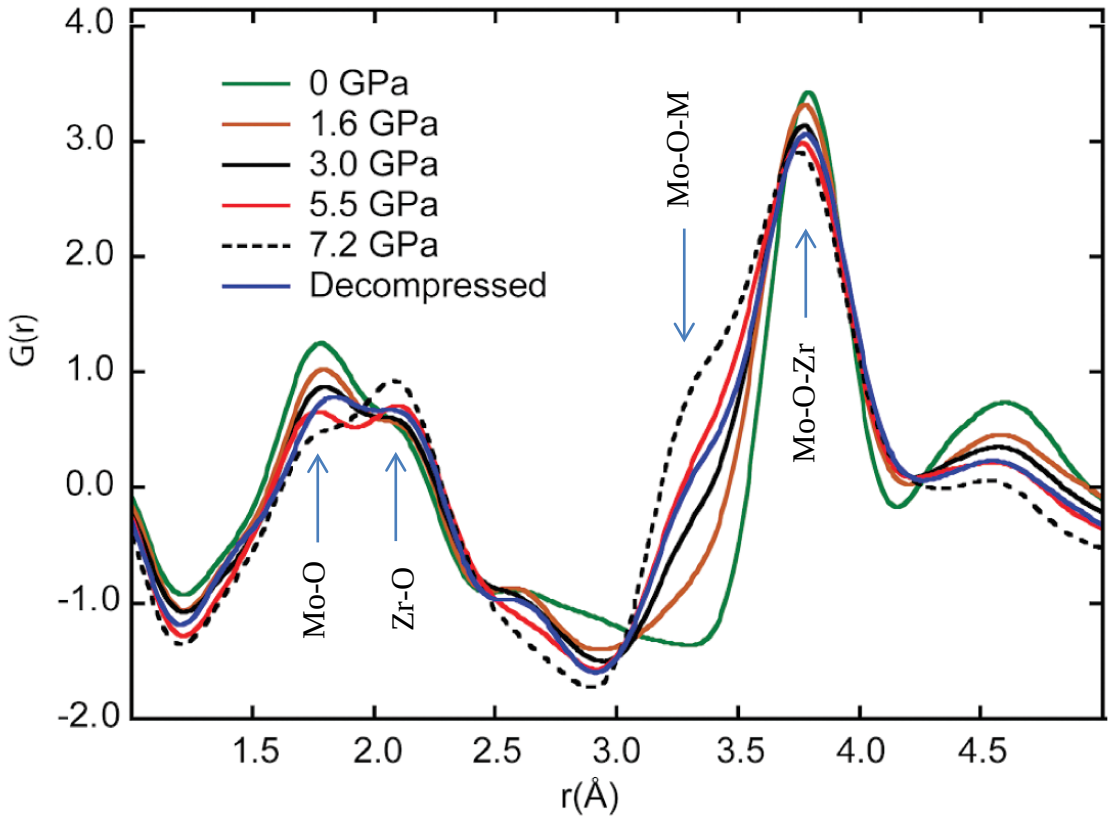

Figure 6.29: Lorched PDFs presented by Wilkinson *et al* (2012). Taken from ref 3.

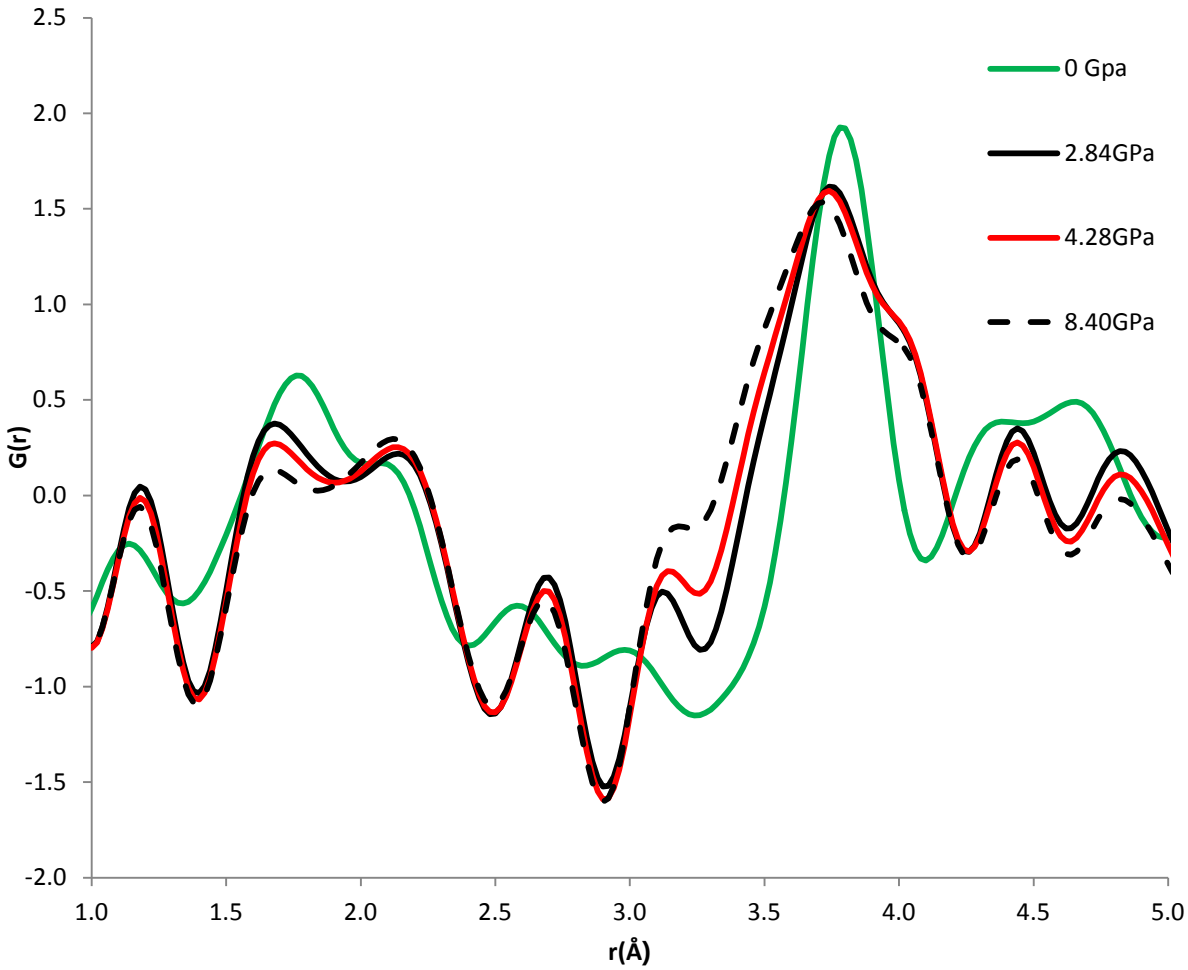

Figure 6.30: PDFs produced using the Lorch function on data from this study.

For comparison, only PDFs from roughly corresponding pressures to the study by Wilkinson *et al.*[3] are presented in Figure 6.30. The same trends are observed in the Mo-O peak and the new Mo-O-M distances are also seen at ~3.2Å. The new M-O-M distances at ~4.2Å are still clearly shown in the Lorched PDFs from this study while they are not clearly shown in the PDFs by Wilkinson *et al.*[3], most likely due to the poorer peak resolution. As with the comparison with the non-Lorched PDFs the changes in the peak at 2.2Å are not as dramatic in this study. Our data shows a similar change occurring in the peak at 2.2Å between 8.40 and

11.02 GPa as is seen in the study Wilkinson *et al*.[3] between 5.5 and 7.2GPa however. This is clearly a discrepancy between the two data sets that cannot be attributed to peak resolution. The cause of this difference is unclear, particularly as the rest of the PDFs presented in Figures 6.30 and 6.31 are comparable.

The analysis presented in Section 6.4.3.2 are largely in agreement with the work of Wilkinson *et al* although they did not observe the new atom-atom distances at 4.2Å, probably due to their data quality. This study has also provided evidence that the changes in the peak at 2.2Å are due to the Mo-O bonds lengthening and not the introduction of Zr-O bonds at this distance. Wikinson *et al* did not consider their differential PDFs so it is unclear if the same conclusions could be drawn from their data.

6.4.4 Conclusions and Further Work

Clearly a lot of information can be extracted from PDF analysis even if the structure of the material is not known. For $ZrMo_2O_8$ there is clearly a conflict in the literature studies where some consider $ZrMo_2O_8$ as possessing a structure based on α-ZrW_2O_8 where there is evidence that this is not the case. It was found in this study that the ambient structure of $ZrMo_2O_8$ is best described by a model based on the β-ZrW_2O_8, which was an assertion not made by either Wilkinson *et al*.[3] or Varga et al (2009). In disagreement with the study by Wilkinson *et al*.[3] the α-ZrW_2O_8 structure provides a poor fit to experimental data. There are problems with the modelling of the β-ZrW_2O_8 based structure however with PDFGui not modelling the partially occupied sites correctly. This leads to unrealistic atom-atom distances and a poor fit below 10 Å. While an adapted model provides a better fit to the first Mo-O peaks a new modelling approach is required to fit the experimental data for every length scale. While these issues will also affect data presented in Chapters 3-5, they do not affect any

discussion surrounding the first Ti-O peak. Even with these problems the α-ZrW_2O_8 based structure provides a much worse fit to experimental PDFs of $ZrMo_2O_8$.

The PIA of $ZrMo_2O_8$ is made complex when the partially occupied sites are considered, it is unclear if there is any ordering of these sites on a local scale and how the different configurations affect the mechanism of PIA. Until the local structure of $ZrMo_2O_8$ is confirmed a truly accurate discussion of PIA is not possible.

It has also been shown however, that as pressure increases the amorphisation process involves a lengthening of Mo-O bonds. The Zr-O bonds are compressed initially but then lengthen slightly up to 1.74 GPa, after this pressure bond length appears to remain relatively constant. This lengthening of all the Zr-O bonds could be a result of 7 co-ordinate Zr atoms but there is no evidence for any change in Zr co-ordination above 1.72 GPa.

M-M distances show changes up to at least 8.41 GPa. As pressure is increased there is an introduction of three new atom-atom distances at 4.1 Å, 3.6 Å and 3.3 Å. While it is likely that these are mainly due to changes in Zr-Mo distances, there is evidence that these distances may also have contribution from other atom-atom distances being introduced in these ranges.

With all the atom positions in the PDF being relative to each other it is difficult to draw any firm conclusions of any weak bonding between the O1, O3 and metal atoms. The lengthening of the Mo-O bonds throughout up to 11 GPa suggests that the average Mo co-ordination number is increasing all the way up to the highest pressure. It is not certain at what pressure the structural changes would cease but these changes are not a simple densification of the structure.

If density of the sample was known as pressure is increased then this would allow an accurate RDF to be produced for each pressure, which would then give insight on co-ordination for

each atom-atom distance, specifically it would give an insight in relative areas of each peak. Unfortunately ρ_0 was unknown for all pressures which made this difficult. It may have been possible to estimate this value as pressure was increased using the initial estimated value calculated by PDFGui in the ambient pressure refinements but these values would not been exact so would provide unreliable co-ordination numbers.

High pressure neutron PDFs would complement the xPDF data and give more insight on relative oxygen positions and also reduce artificial ringing at low r assuming Q_{max} values ≥ 30 were still accessible.

References

1. S. M. Sharma and S. K. Sikka, *Progress in Materials Science*, 1996, **40**, 1-77.
2. R. Speedy, *Journal of Physics: Condensed Matter*, 1997, **8**, 10907.
3. A. P. Wilkinson, B. K. Greve, C. J. Ruschman, K. W. Chapman and P. J. Chupas, *Journal of Applied Physics*, 2012, **112**, 023511(023516).
4. J. S. O. Evans, T. A. Mary, T. Vogt, M. A. Subramanian and A. W. Sleight, *Chemistry of Materials*, 1996, **8**, 2809-2823.
5. J. S. O. Evans, W. I. F. David and A. W. Sleight, *Acta Crystallogr*, 1999, **B55**, 333-340.
6. D. A. Keen, A. L. Goodwin, M. G. Tucker, M. T. Dove, J. S. O. Evans, W. A. Chrichton and M. Bruneli, *Physical Review Letters*, 2007, **98**, 225501(225504).
7. T. Varga and A. P. Wilkinson, *Physical Review B*, 2009, **79**, 224119(224115).
8. D. A. Keen, A. L. Goodwin, M. G. Tucker, J. A. Hriljac, T. D. Bennet, M. T. Dove, A. K. Kleppe, A. P. Jephcoat and M. Bruneli, *Physical Review B*, 2011, **2011**, 064109(064106).
9. C. Lind, A. P. Wilkinson, Z. Hu, S. Short and J. D. Jorgensen, *Chemistry of Materials*, 1998, **10**, 2335-2337.
10. C. Lind, D. W. VanDerveer, A, J. Chen, M. Vaughan and D. Weldner, *Chem. Mater.*, 2001, **13**, 487-490.
11. E. Lorch, *Journal of Physics C: Solid State Physics*, 1969, **2**, 229-237.
12. T. A. Mary, J. S. O. Evans, T. Vogt and A. W. Sleight, *Science*, 1996, **272**, 90-92.

7. THE PHASE TRANSITION OF IRON AT HIGH PRESSURE

7.1 Introduction

The phase diagram of iron has been subject to a number of previous studies due to its importance to Earth science. The Earth's core is primarily made up of iron, thus understanding the phase diagram of iron is important to understanding various properties of the Earth's core. For example, seismic anisotropy has been discovered in the Earths inner core with seismic waves traveling faster along the vertical axis of the Earth than the equatorial plane.[1, 2] Pressures and temperatures up to 340GPa and 4700 K, respectively, are present in the Earth's inner core so there has been a focus on investigating the full pressure-temperature phase diagram of iron and iron alloys.

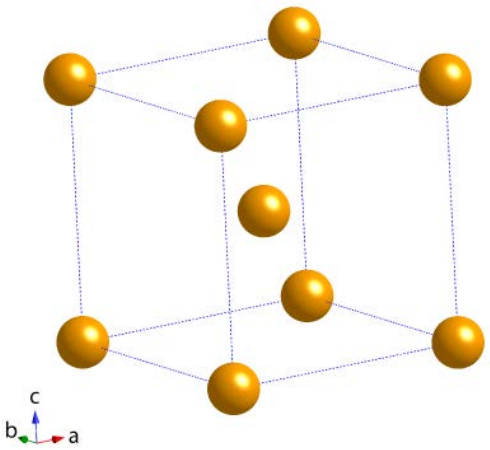

Figure 7.1: bcc α-iron.

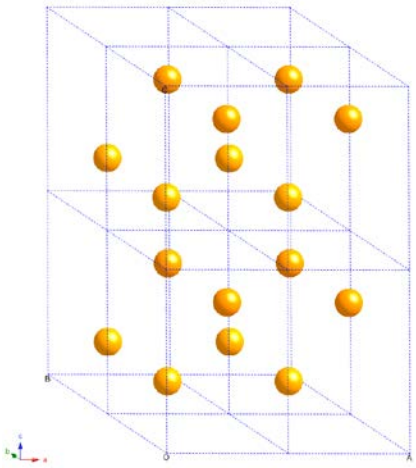

Figure 7.2: hcp ε-iron.

At ambient pressure and temperature iron is ferromagnetic and adopts a body-centred cubic structure (bcc) which is known as alpha α-iron or ferrite. Shock compression tests showed that at around 13GPa α-iron transformed into a phase with a slightly increased density.[3] An initial high pressure x-ray diffraction study suggested that this phase adopted a hexagonal close packed (hcp) structure.[4] This structure was later confirmed by further x-ray diffraction studies

and this new phase was named ε-iron. [5-7] Mossbauer spectroscopy has shown that ε-iron is paramagnetic at room temperature.[8]

This new phase was an important discovery at the time due the possibility that at extremely high pressures and temperatures in the Earth's core, there was potential for ε–iron to be the stable phase. After these initial x-ray diffraction studies, a pressure-temperature phase diagram was produced from thermocouple and voltage probes, which includes the high temperature face-centred cubic (γ-iron) phase (Figure 7.3).[9]

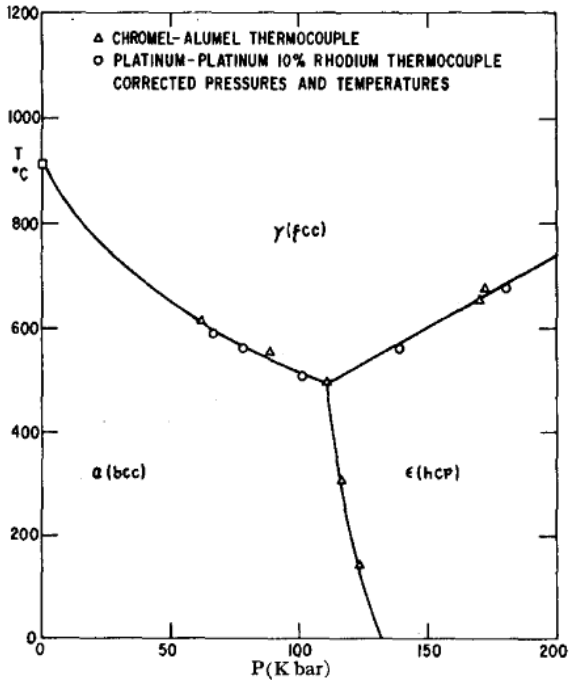

Figure 7.3: Pressure-Temperature phase diagram of iron. [9]

An initial mechanism for the transformation from the bcc to the hcp phase was suggested based on x-ray diffraction data.[7] This mechanism is representative of a displacive transition with the bcc phase transformed due to the application of pressure along the (001) plane resulting in expansion along the $(1\bar{1}0)$ plane.

Upon compression along the [001] direction, the *d*-spacing of the bcc (002) plane is reduced to form the hcp $(1\bar{2}10)$ plane.[10] This compression also results in the expanding of the *d*-spacing of the bcc (110) plane to form the hcp (100) plane. The *d*-spacings of the hcp (002) plane are kept equal to that of the *d*-spacings of the bcc (110) plane.

Another x-ray diffraction study, using synchrotron radiation, further investigated this proposed mechanism. [10] The study showed that the phase transition started at roughly 10GPa and was complete above 21GPa, with a co-existence of phases in the pressures in between. During this phase transition the two phases exert a stress on the other resulting in each phase being elastically deformed. This explains the observed anomaly in the *c*/*a* ratio of the hcp phase, with *a* being unusually small and *c* being unusually large.[10] XAFS has shown that the lattice constants of each phase are anomalous when their relative amounts are small. [11] That is to say that the bcc phase behaves anomalously as pressure is increased and the amount is reduced and the hcp phase behaves anomalously at the onset of the α–ε phase transition. It has been suggested that the transition mechanism may involve an intermediate fcc phase which could explain this unusually large value of *c*.[11] Molecular dynamic simulations suggest that the grains are irregular and the fcc atoms would then transform to the hcp phase or become grain boundaries between hcp phases and thus introduce fcc stacking faults between grains.[12]

While iron has been shown to not possess any texture at ambient conditions, α–iron has been shown to possess texture as pressure is increased between 2.8 and 12.4 GPa, developing two fiber components, a major component at (100) and a secondary component at (111).[13, 14] During the α–ε phase transition the hcp phase is said to inherit this texture, which persists well past the transition pressure. In an initial x-ray diffraction study using a rotated DAC the ε-iron phase has been shown to possess a strong (0001) texture with crystals aligning parallel to the compression direction, resulting in the *c*-axis aligning parallel to the axis of an

diamond-anvil cell.[15] In a later study ε-iron crystals were shown to initially align orthogonally to the compression axis giving rise to a (1120) texture and then only aligning parallel to the compression direction as pressure was increased.[13] This was then built on further by a study which showed that the hcp phase initially develops a maxima in the $(01\bar{1}0)$ direction, which broadens as pressure is increased to give the previously observed (1120) maximum.[14] This was explained by the <0110> hcp direction corresponding to the <112> bcc and grains with {112} perpendicular to the compression direction transforming first, resulting in the maximum at $(01\bar{1}0)$ hcp. As pressure is increased the (100) bcc and (111) bcc transform to give the observed (1120) hcp maximum. This has been used as an explanation for the seismic anisotropy observed in the Earth's inner core.

Large hysteresis is observed in the ε–α transition as pressure is released, with the hcp phase still being observed as low as 3 GPa on unloading. [10, 16, 17] Upon decompression, ε-iron begins to lose the $(11\bar{2}0)$ texture and develops a (1000) texture which increases during decompression and the bcc phase possess a maximum at (112) as pressure is reduced until the transformation back to the bcc phase is complete at which point orientation becomes random once more.[14]

There have been a number of studies that present PDF data of pure iron and there are many more than look at iron alloys. Shen *et al* in 2004 presented PDFs of amorphous iron up to 67GPa but only obtained a Q_{max} value of 8Å^{-1} so despite accessing very high pressures, the PDFs were low resolution.[18, 19] Although other studies have presented PDFs of bcc iron[20] no PDF study was found that presented a high pressure investigation into the structure of ε -iron.

The exact mechanism of the transformation from α to ε phases is still subject to much debate with different ones still being suggested.[21] While both bcc and hcp structures are relatively

very simple it is clear the phase transition mechanism is complex and has a large effect on the structure of the high pressure phase. It is unclear how texture in would affect the PDFs for ε-iron. Texture can be modelled in Rietveld refinements but there is no such feature in PDFGui. The literature has no discussion on how texture may affect a PDF and how this could be modelled. The only reference to texture in previous studies are that the authors avoided having texture in any samples. PDF analysis may provide insights into the phase transition mechanism and about any local disorder present in ε-iron however, and clearly iron is a topical system with lots of research still on going in various iron related systems.

7.2 Experimental

The data presented in Section 7.3 were collected in two separate visits to beamline I-15 at Diamond Light Source. The first data collection focussed on the phase transition of iron powder up to 21.45GPa and the second focussed on exploring the high pressure ε-iron phase up to 50GPa.

The first data collection was completed in November 2011 and twelve data sets were collected between 0 and 21.45GPa. A cell with small culets (0.4mm in diameter) was used with a W gasket pre-indented to 35μm in thickness. A hole of 150μm was then drilled in the centre of the gasket for the sample to be loaded. The beam energy was 72KeV (0.1722Å) and the sample-detector distance was refined to be 233.298mm from a silicon calibration in the DAC. This allowed for an accessible Q_{max} of 20Å^{-1} in the production of PDFs. For the background data collection, twenty four images were collected and each image consisted of 300 x 2 second exposures summed together. These images were then averaged to produce the final background image.

Rubies were loaded into the gasket hole and were used to measure pressure and these measurements show that the pressures obtained were 0.66, 3.73, 8.58, 89, 10.2, 11.5, 13.16, 14.62, 15.51, 16.97, 19.12 and 24.45GPa. At each pressure six images were collected to be averaged and again each image consisted of 300 x 2 second exposures summed together.

After the data collection at 11.50GPa the DAC slipped in the holder so was re-clamped and the experiment continued. This meant that after the experiment a new background collection had to be conducted for the cell in its new position. This was done using the same exposure times as before.

The second data collection was conducted in March 2012 at 71.45KeV (0.1735Å). The same cell was used as the previous data collection with a W gasket pre-indented to 35μm in thickness, but the hole was this time 125μm in diameter. A silicon calibration was again completed which gave a refined sample to detector distance of 212.075mm and an accessible Q_{max} of 22Å^{-1}. Forty seven background images were collected and averaged together, each consisted of 300 x 2 second exposures summed together. Six pressures were collected between 0 and 50.07GPa (0, 18.84, 22.97, 26.29, 37.62, 43.54 and 50.07GPa) and another 0GPa data collection was conducted post-decompression. Rubies were again loaded into the gasket hole with the sample but upon compression the pressure calibrated from one ruby was slightly different to rubies sat elsewhere in the hole. This showed that there was a variation in pressure in the sample from one point to the next, a phenomenon observed in other studies of iron in a DAC.[22] A ruby was located roughly in the centre of the gasket hole and all pressure measurements were made using this ruby for all pressures. The pressures presented above and in Section 7.3.2 were calculated from the equation of state of iron presented by Mao *et al* (1967) based on the lattice parameters for the hcp phase calculated from Rietveld refinements of the diffraction data. A circular 50μm beam was used, which is much smaller than the

gasket hole but it is unclear if the pressure gradient would have any effect on the data collected.

Iron powder was also loaded into a kapton capillary 1mm in diameter and 5 images, each consisting of 60 x 2 second exposures, were summed together,averaged and integrated in Fit2D. A refined sample to detector distance of 211.904mm was obtained from a silicon calibration which allowed for a Q_{max} of 25Å^{-1} to be accessed.

7.3 Results and Discussion

7.3.1 The bcc-hcp Phase Transition

7.3.1.1 Rietveld Analysis of X-ray Diffraction Data

Rietveld analysis was undertaken of the diffraction patterns of iron collected between 0.66 and 21.45GPa in November 2011. As a very high angle is not needed for Rietveld analysis, ideally the detector would have been moved further away from the sample to allow for better resolution of the Bragg peaks at lower values of two theta but due to time constraints this was not possible. A good fit of the diffraction pattern at the lowest pressure was still obtained however (Figure 7.4), with data above two theta of 30^{o} excluded from refinements.

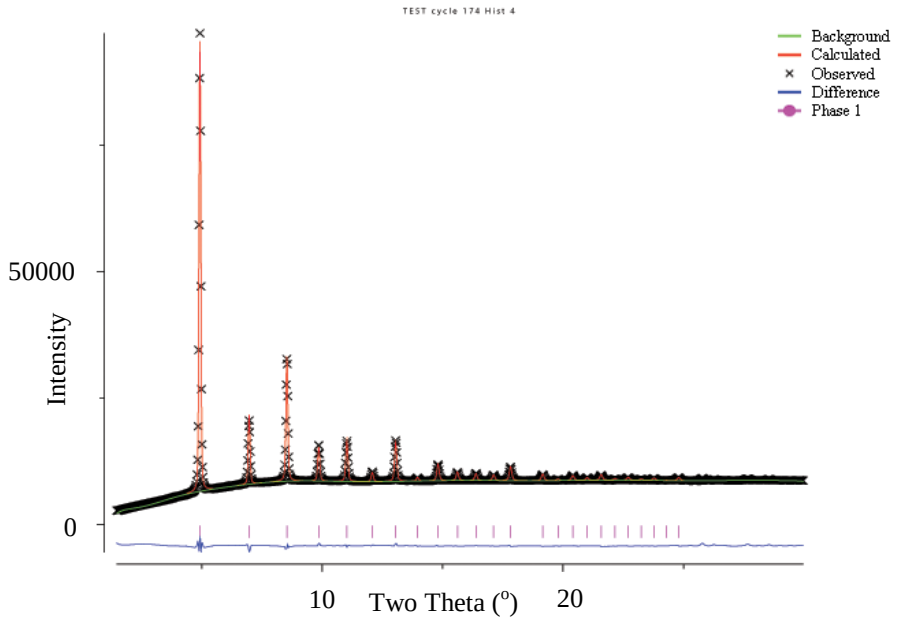

Figure 7.4: Rietveld Analysis of Iron at 0.66GPa using a bcc model.

The α-iron model provided a good fit to experimental data up to 14.62GPa but at 15.51GPa the data became best fit by a two phase refinement which included both α- and ε-iron (Figures 7.5a and b).

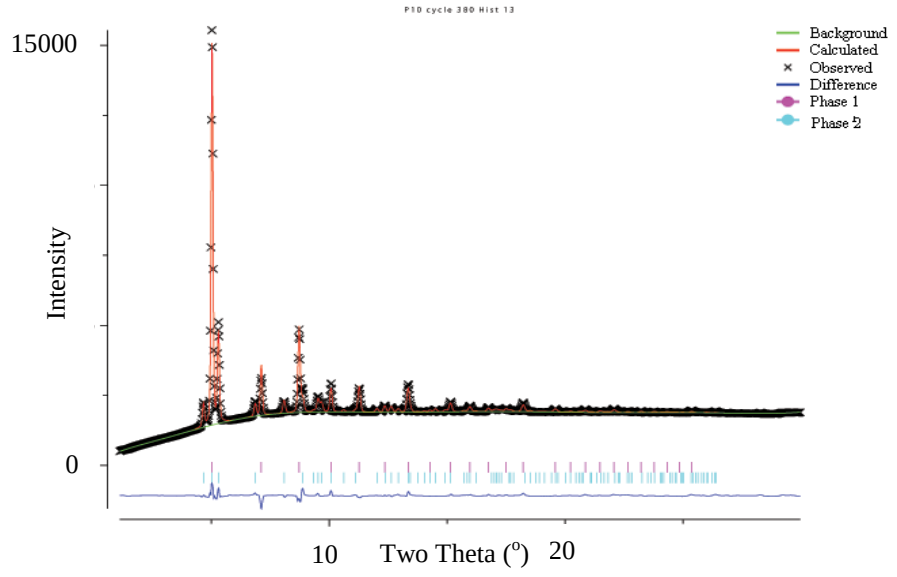

Figure 7.5a: Two phase refinement of data collected at 15.51GPa including bcc (Phase 1) and hcp models (Phase 2) of iron between 0 and 30°.

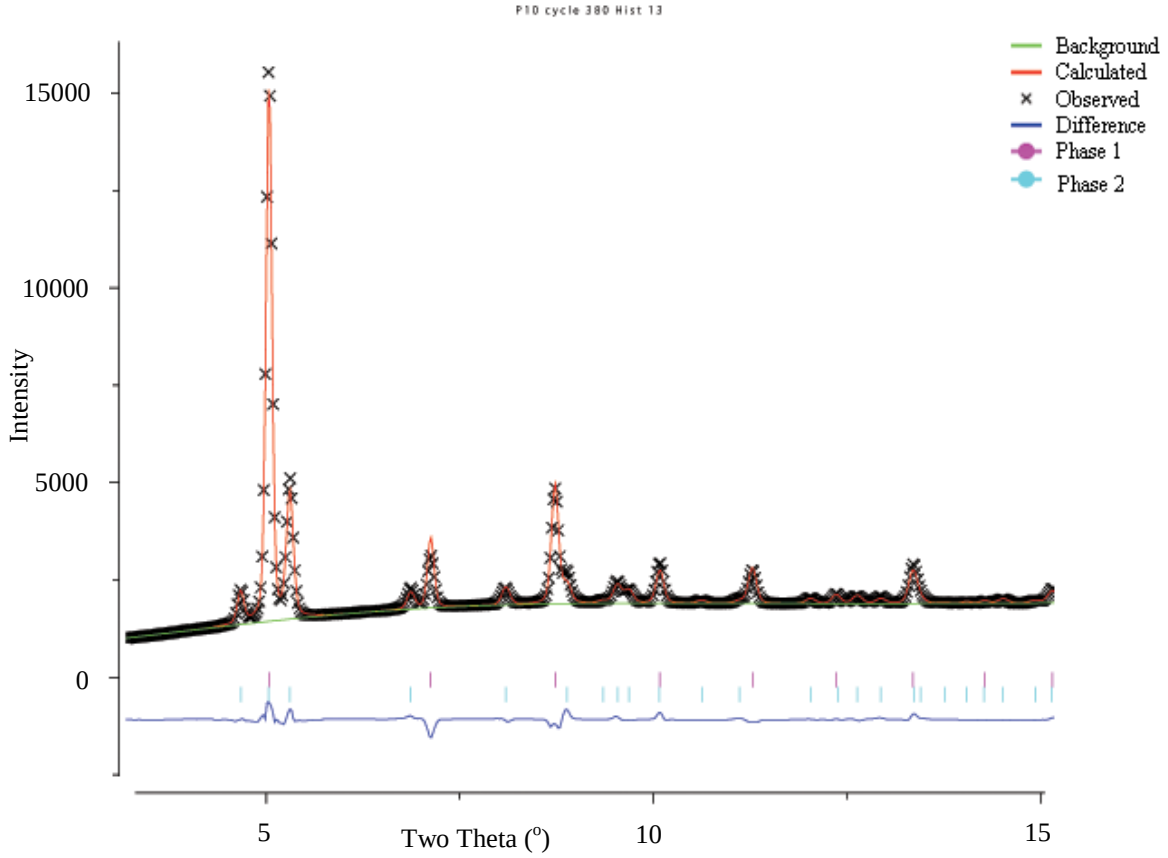

Figure 7.5b: Two phase refinement of data collected at 15.51GPa including bcc (Phase 1) and hcp models (Phase 2) of iron between 3 and 15°.

Figure 7.5b shows the co-existence of α- and ε-iron at 15.51GPa and the relative phase fractions changes as pressure was increased. All signs of α-iron in the diffraction patterns had disappeared by 21.45GPa. At this pressure the diffraction was best fit by a ε-iron model apart from one peak (Figure 7.6a and b).

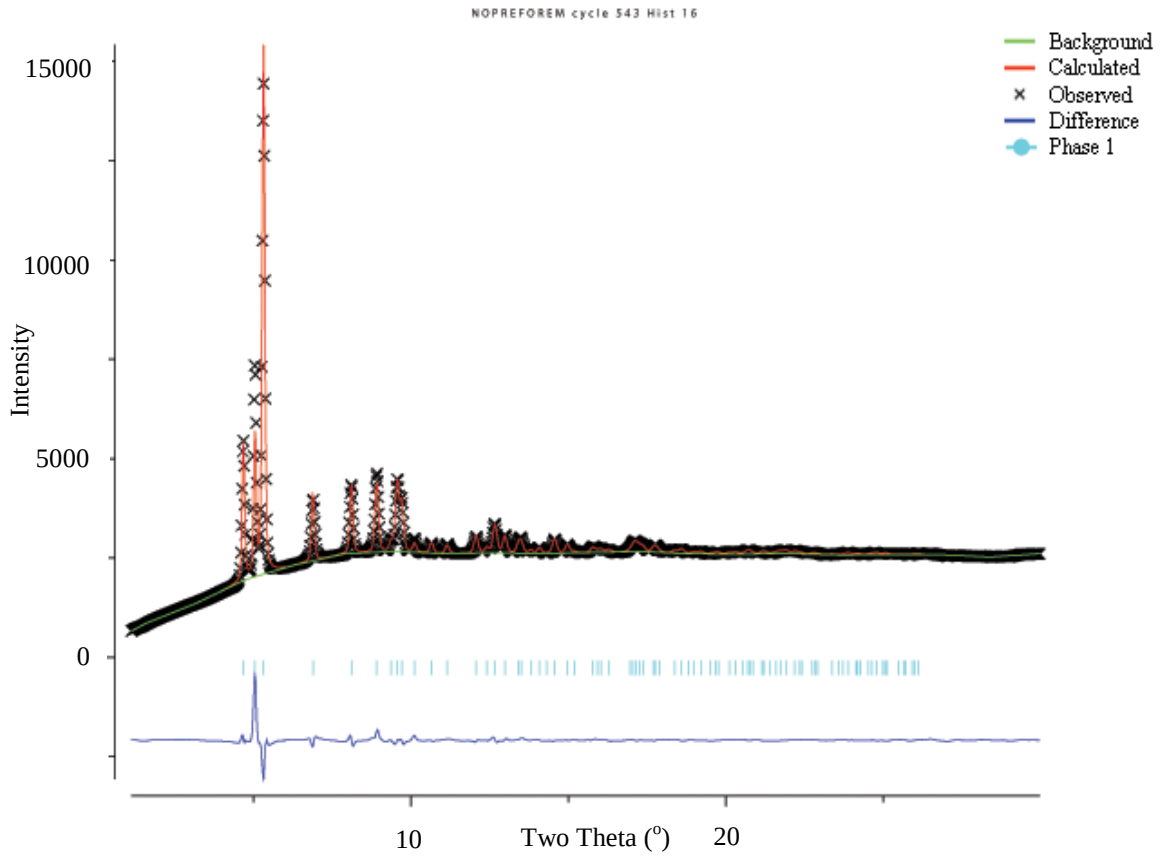

Figure 7.6a: Rietveld Analysis of Iron at 21.45GPa using a hcp model with no correction for preferred orientation.

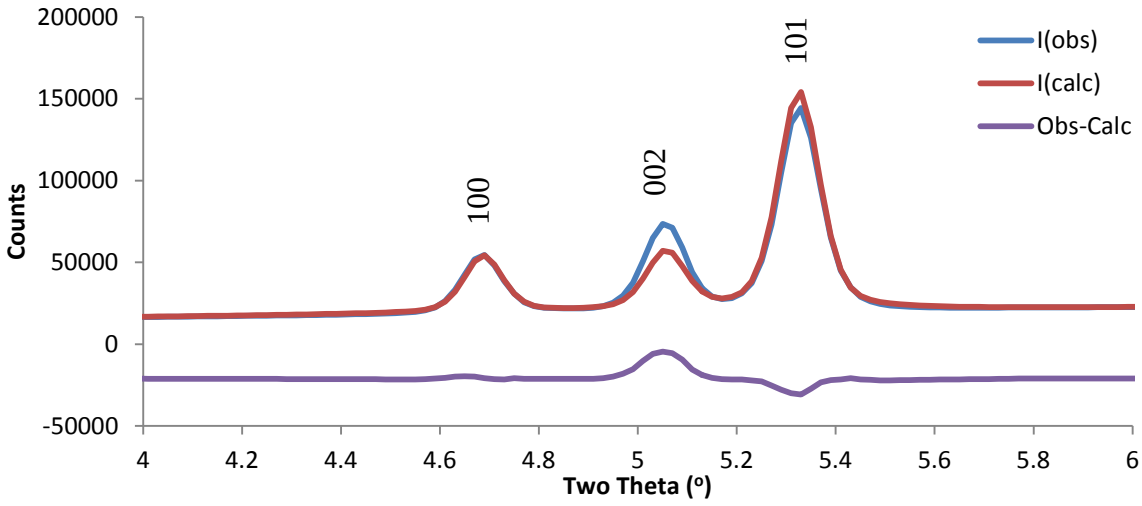

Figure 7.6b: Rietveld fit of Iron at 21.45GPa using a hcp model between 4 and 6°.

The (002) reflection was more intense that the calculated model predicts. With previous studies showing that ε-iron possess preferred orientation (Section 7.1) this preferred orientation was modelled in GSAS along the (001) plane and a better fit was obtained (Figure 7.7).

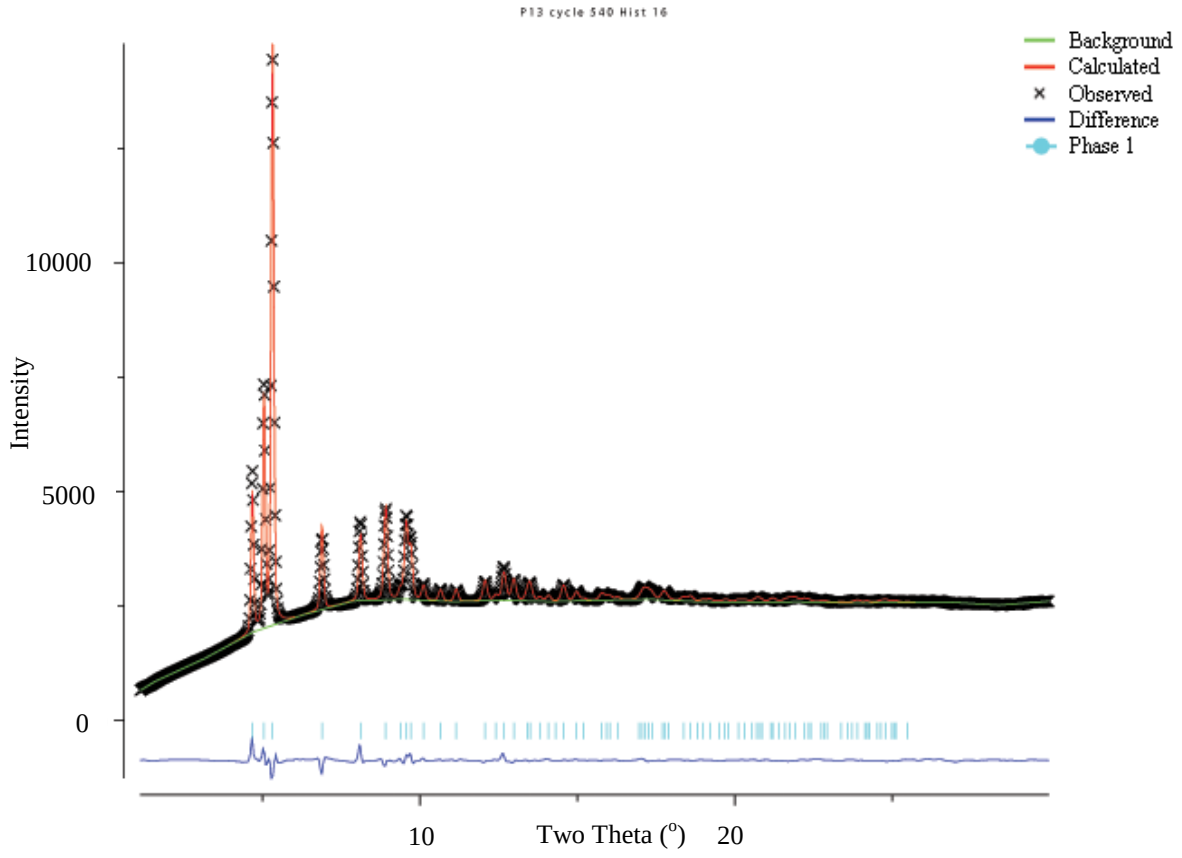

Figure 7.7: Rietveld Analysis of Iron at 21.45GPa using a hcp model with correction for preferred orientation in the (001) plane).

The calculated phase fractions from Rietveld refinements (Table 7.1) clearly show the increase in ε-iron and decrease in α–iron as pressure is increased and the phase transition appears complete at 21.45GPa. The Fe U_{iso} values appear fairly constant, with the exception of the α-iron phase during the phase transition.

Table 7.1: Refined parameters from Rietveld analysis of Iron up to 21.45GPa.

Pressure (GPa)	*wRp*	α –iron (bcc)			ε-iron (hcp)			
		a (Å)	Fe U_{iso} (Å^{-2})	Phase Fraction	*a* (Å)	*c* (Å)	Fe U_{iso} (Å^{-2})	Phase Fraction
0.66	0.0216	2.8346(1)	0.0027(2)					
3.73	0.0105	2.82578(9)	0.0032(1)					
8.58	0.0109	2.80513(9)	0.0032(1)					
8.90	0.0109	2.80163(9)	0.0031(1)					
10.20	0.0109	2.795654(9)	0.0029(1)					
11.50	0.0112	2.7866(1)	0.0029(1)					
13.16	0.0130	2.77842(1)	0.0028(2)					
14.62	0.0152	2.76496(1)	0.0057(2)					
15.51	0.0166	2.7720(2)	0.0062(2)	7.7120	2.4406(3)	3.923(1)	0.002(1)	3.2894
16.97	0.0195	2.7700(3)	0.0097(5)	5.9588	2.4394(4)	3.921(1)	0.0026(5)	6.9089
19.12	0.0157	2.7724(7)	0.003(2)	2.5094	2.4389(4)	3.9153(7)	0.0028(4)	9.8576
21.45	0.0129				2.4319(3)	3.9051(4)	0.0024(4)	13.0130

With good Rietveld fits to the diffraction patterns, data appeared of high enough quality to produce viable PDFs. It was hoped that the PDFs would provide some insight into the phase transition mechanism although it was not clear what effect preferred orientation would have on the patterns. Previous studies have indicated that there is also preferred orientation in α –iron during the phase transition, however there was no obvious signs of any preferred orientation from the Rietveld analysis.

7.3.1.2 PDF analysis of X-Ray Diffraction data

The bcc model provided an excellent fit to the experimental PDF for iron powder in the kapton capillary (*Rw*=0.048). PDF analysis was then conducted on PDFs produced from the same diffraction data that was modelled in the previous section. An α-iron model was fit to the experimental data at 0.66GPa and a good fit was obtained (Figure 7.8).

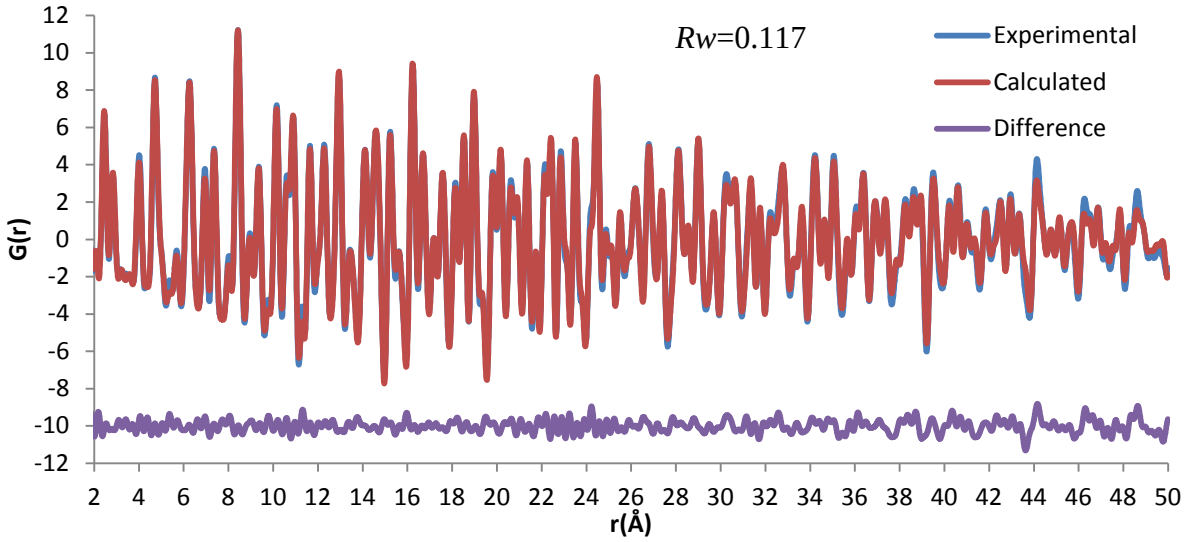

Figure 7.8: bcc model iron fit to experimental PDF data between 1.5 and 50Å at 0.66GPa.

With a good fit obtained for the α-phase, in order to investigate the phase transition mechanism it is important to understand exactly which Fe-Fe distances the peaks correspond to. The modelling shown in Figure 7.8 is again shown in Figure 7.9 but only up to 10 Å and each peak (from Fe-Fe distances shown in Figure 7.10) has been labelled with their exact distances calculated from the modelling in PDFGui.

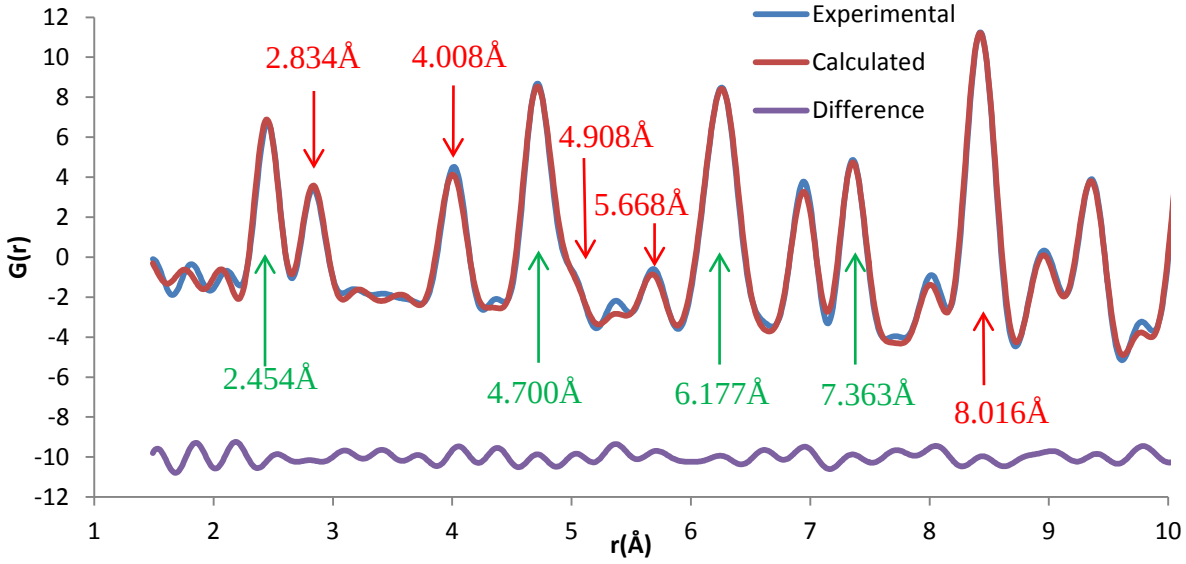

Figure 7.9: Fit from Figure 7.8 shown between 1.5 and 10Å.

The structure of bcc iron can be seen in Figure 7.10 and is presented looking down the *c*-axis but the model would look identical regardless of axis chosen. The distances between Fe1 and Fe2 are marked in green and the Fe1-Fe1/Fe2-Fe2 distances in red. The Fe1-Fe2 distance at 7.363Å corresponds to a Fe-Fe distance in the (111) direction.

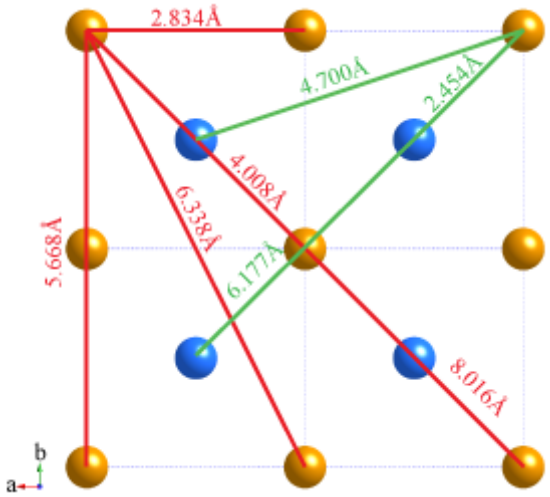

Figure 7.10: Atom-Atom distances within the bcc phase of iron.

As pressure is increased up to 14.62GPa the α-iron model still provides a good fit to experimental data from 1.5 to 50 Å (Figure 7.11). The PDFs collected up to this pressure (Figure 7.12) show a steady decrease in volume as pressure is increases and Fe-Fe distances reduced but there are no signs of any disorder or the onset of the bcc-hcp phase transition.

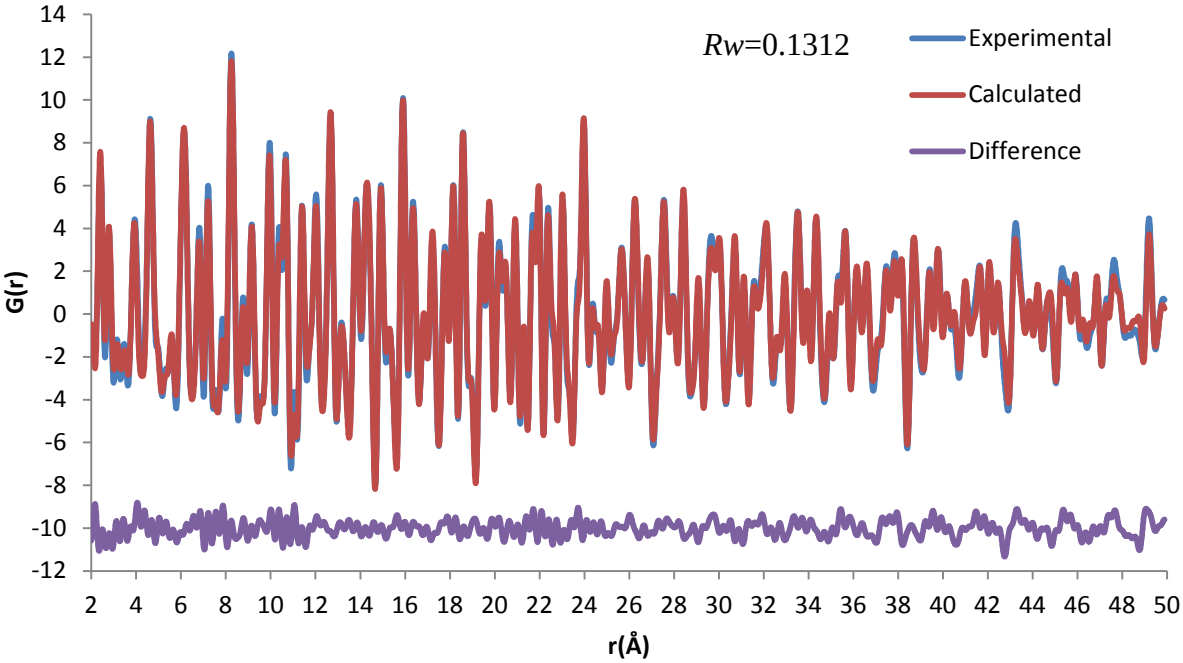

Figure 7.11: bcc model of iron fit to experimental PDF data between 1.5 and 50Å at 14.62GPa.

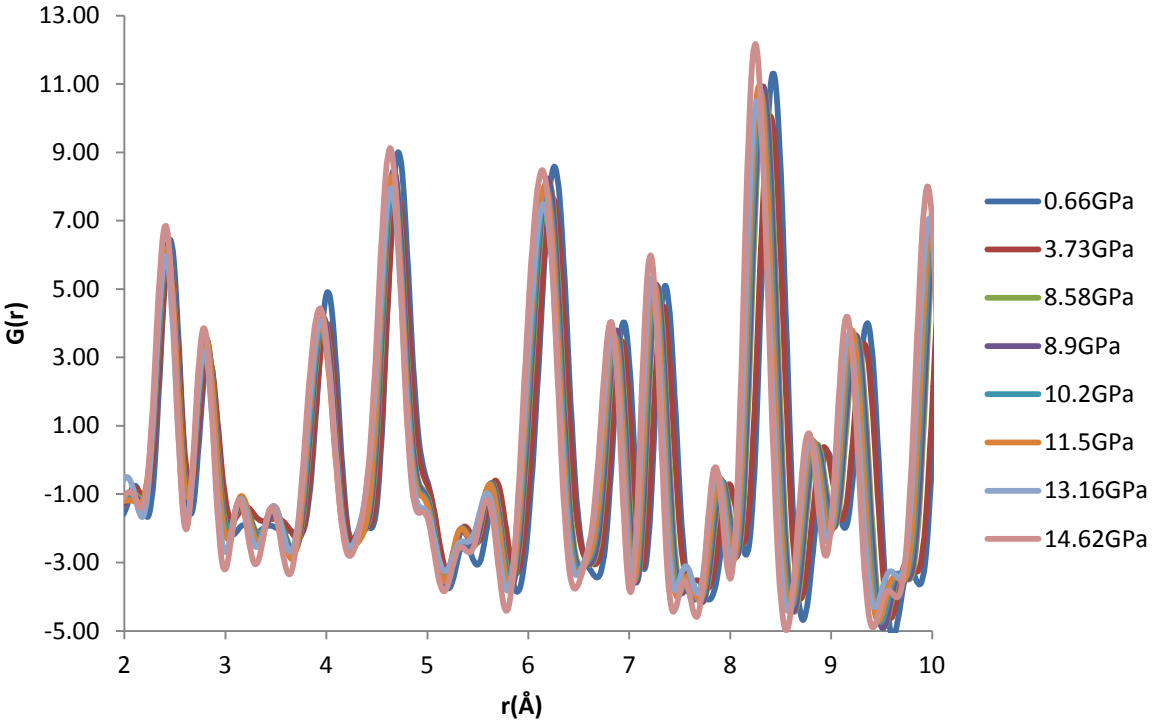

Figure 7.12 Experimental PDFs produced from diffraction data of iron between 0.66 and 14.62GPa.

In order to compare PDF and Rietveld refinement results, refinements were conducted on the eight pressures that showed no sign of any phase transition. Data were refined between 1.5 and 50 Å and refined parameters can be seen in Table 7.2.

Table 7.2: Refined parameters from modelling PDFs in PDFGui between 0.66 and 14.62GPa.

	α –iron (hcp)			
Pressure (GPa)	*Rw*	*a* (Å)	Volume (Å^3)	Fe U_{iso} (Å^{-2})
0.66	0.117	2.8340	22.762	0.0051
3.73	0.113	2.8252	22.550	0.0053
8.58	0.118	2.8045	22.058	0.0051
8.9	0.119	2.8010	21.976	0.0051
10.2	0.120	2.7950	21.835	0.0051
11.5	0.121	2.7891	21.696	0.0051
13.16	0.127	2.7815	21.520	0.0049
14.615	0.131	2.7764	21.402	0.0049

Lattice parameters are comparable to Rietveld analysis (Table 7.1) and thermal parameters are also consistent throughout meaning there is no sign of disorder present in the sample. *Rw* values for 13.15GPa and 14.62GPa are higher than the other data sets but this is most likely attributable to these PDFs being normalised against a different background data collection (Section 7.2).

At 21.45GPa the Rietveld analysis shows that the sample has been completely converted to ε-iron (hcp). Before investigating the intermediate pressures it was important to understand the PDF of ε-iron so a hcp model was fit to experimental data collected at 21.45GPa and refined between 1.5 and 50Å (Figure 7.13).

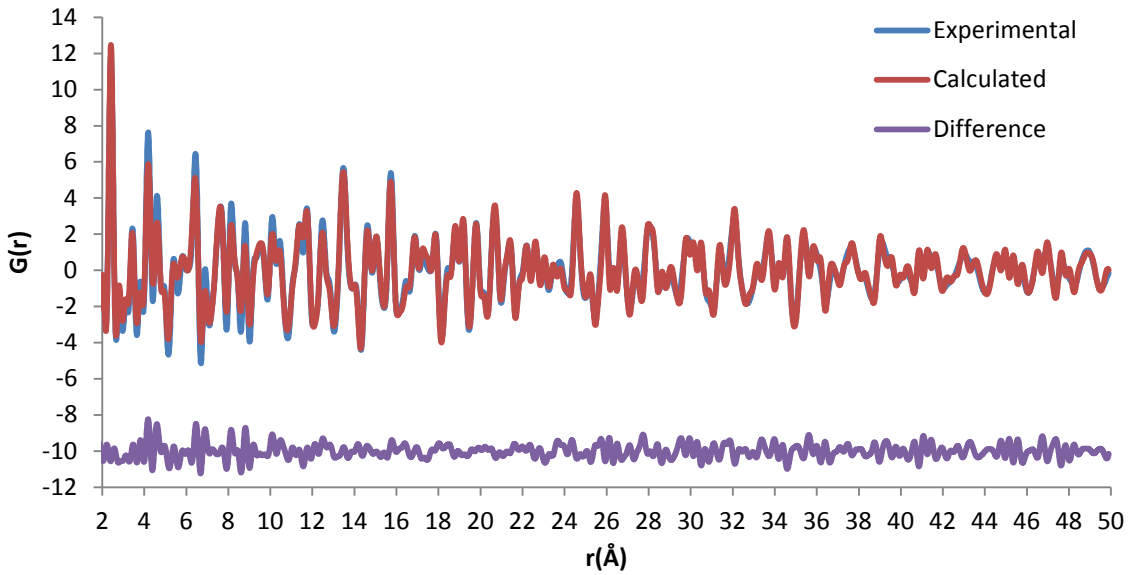

Figure 7.13: hcp model of iron fit to experimental PDF data between 1.5 and 50Å at 21.45GPa (*Rw* = 0.223).

While the *Rw* is acceptable it is much higher than the lowest pressure bcc phase (Table 7.2). The fitting below ~10Å looks particularly poor and this region is expanded in Figure (7.14)

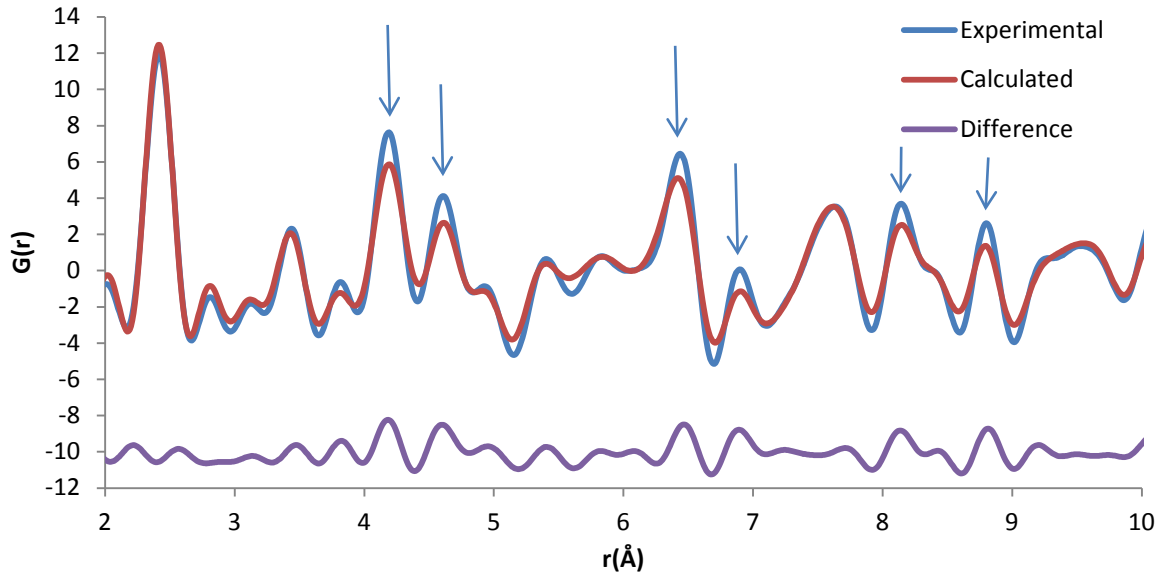

Figure 7.14: Fit presented in Figure 7.13 between 2 to 10 Å (Blue arrows indicate some poorly fit peaks).

There are certain peaks in the pattern that appear to be fitted poorly by the hcp model, while others appear to be fitted fairly well. Hcp iron possesses a ABABA stacking sequence so there will be Fe-Fe distances within layers and separate Fe-Fe distances between the layers. To investigate this the atom-atom distances were calculated from the fit in PDFGui and then assigned to either intralayer distances (Within layers A or B) or interlayer distances (A to A), (B to B) or (A to B). A diagram for all the Fe-Fe distances within a layer can be seen in Figure 7.15.

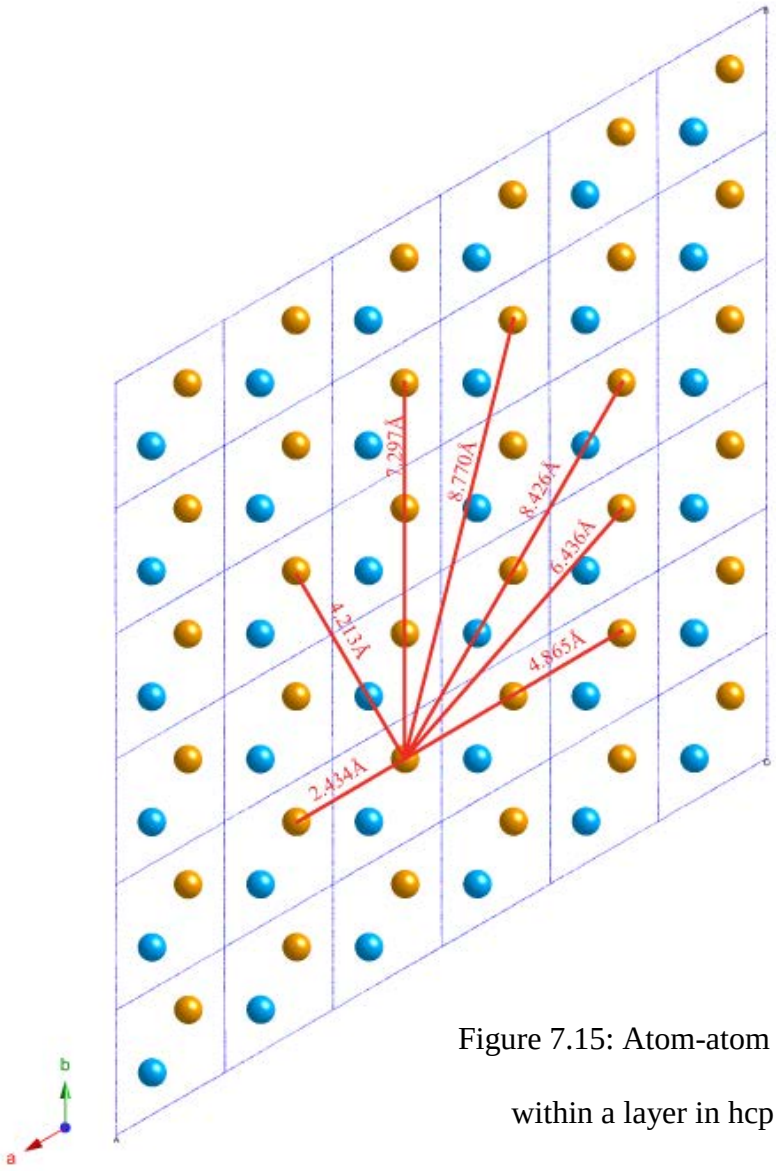

Figure 7.15: Atom-atom distances within a layer in hcp iron.

How all the atom-atom distances below 9Å correspond to the PDF pattern are presented in Figure 7.16. The peak at 2.4 Å consists of two Fe-Fe distances, one short distance at 2.403Å which corresponds to Fe1-Fe2 and one longer distance at 2.434Å corresponding to Fe1-Fe1 and Fe2-Fe2 distances.

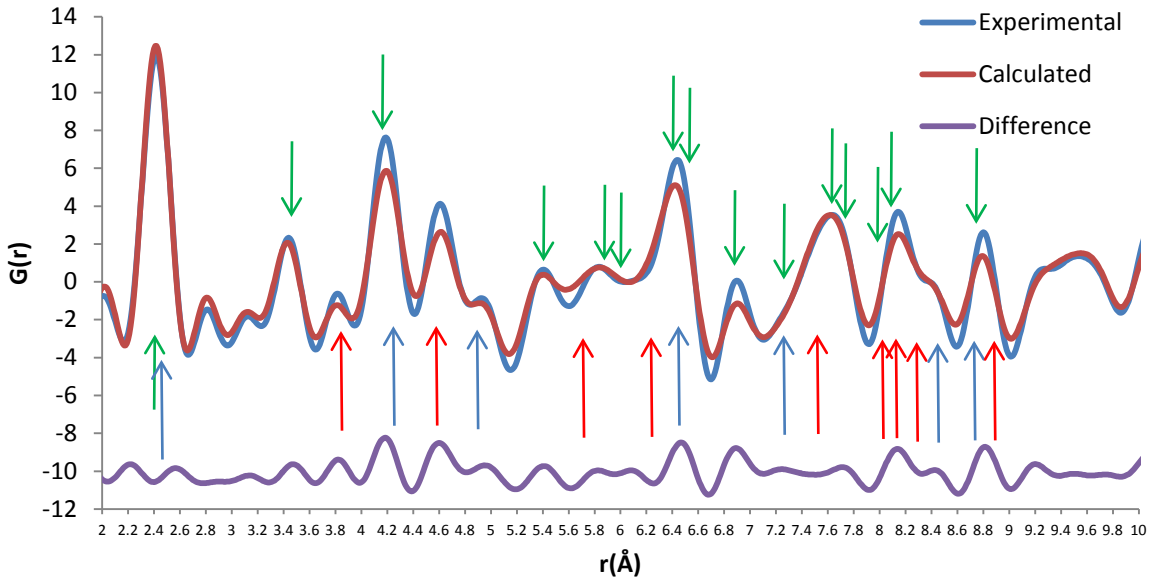

Figure 7.16 Green Arrows= Interlayer (A-B), Blue Arrows = Intralayer (A-A and B-B), red arrows Interlayer (A-A and B-B).

Stacking faults will show up as extra interlayer peaks/distances and existing interlayer peaks being poorly fit. There are no obvious trends in the peaks that are fit poorly or signs of extra Fe-Fe distances so there are no clear signs of stacking faults at these length scales, which may be shown up as poor fitting of the interlayer distances.

The Rietveld analysis (Figures 7.6 and 7.7) show that there is preferred orientation in the sample (along (100)) which may result in distances strongly along *c* (interplanar) having more intensity relative to others perpendicular (intraplanar). Any Fe-Fe distance that possesses some component in *c* would presumable be affected (green and red distances from Figure

7.16) and those without (blue distances) would not. PDFGui could chose to fit the intralayer peaks correctly and the interlayer peaks incorrectly or *vice versa*. With most peaks consisting of overlapping Fe-Fe distances it is not possible to draw any firm conclusions on the effect of preferred orientation based on Figure 7.16.

With the best possible model for hcp iron refined against this data and Fe-Fe distances calculated it is possible to use this information to investigate the phase transition as pressure is increased from 14.62GPa. At 15.51GPa the PDF begins to show signs of the phase transition that is shown by the Rietveld analysis presented in the previous section. The PDFs collected between 15.51GPa and 21.45GPa are presented in Figure 7.17.

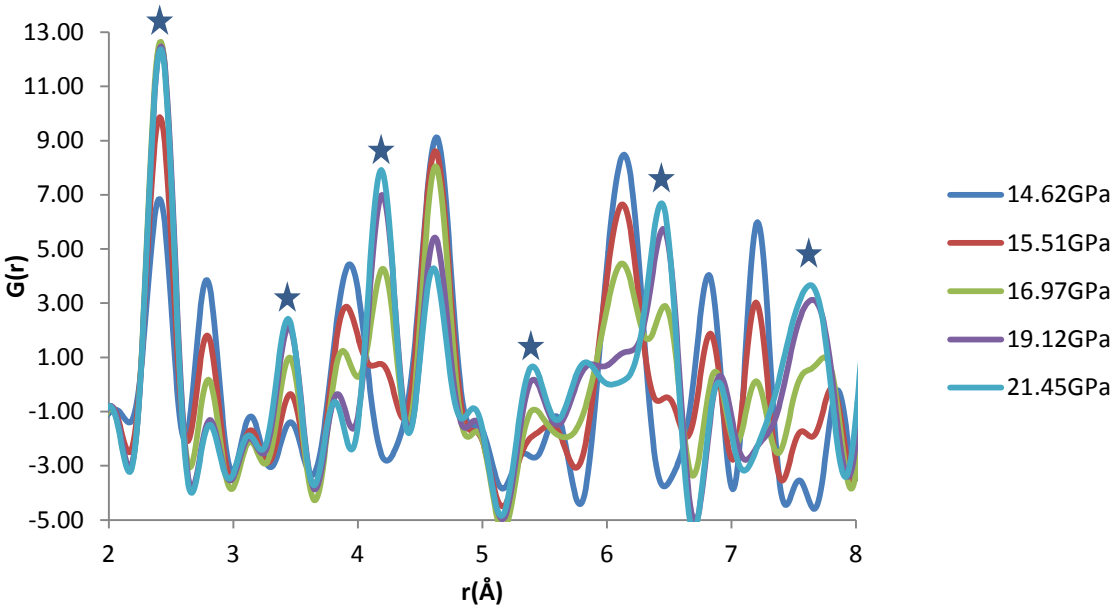

Figure 7.17: Experimental PDFs produced from diffraction data of iron between 14.62 and 21.45GPa. Peaks increasing due to hcp iron are marked with stars.

The main new hcp Fe-Fe distances introduced are labelled and it appears that every peak can be assigned to either the bcc or hcp phases. There is no evidence for any stable intermediate phase as part of the phase transition mechanism. In an attempt to model the local structure of

iron during phase transition, PDFs between 14.62 and 19.12GPa were fit to data from 1.5 to 10Å using a dual phase refinement.

Table 7.3: Refined parameters from modelling PDFs in PDFGui between 15.51 and 21.45GPa.

	α –iron (hcp)				ε-iron (hcp)				
Pressure (GPa)	*Rw*	*a* (Å)	Fe U_{iso} (Å^{-2})	Scale Factor	*a* (Å)	*c* (Å)	*c/a*	Fe U_{iso} (Å^{-2})	Scale Factor
15.51	0.109	2.7717	0.0043	0.405	2.4452	3.9213	1.604	0.0042	0.232
16.97	0.118	2.7699	0.0050	0.288	2.4420	3.9220	1.606	0.0035	0.440
19.12	0.110	2.7659	0.0079	0.103	2.4373	3.9143	1.606	0.0032	0.545
21.45	0.117				2.4320	3.9024	1.605	0.0033	-

The dual phase refinement fits the data between 0 and 10Å remarkably well, even the 21.45GPa data that fit poorly over the larger 1.5 to 50Å range. Fits for the modelling at 16.97GPa and 21.45GPa are presented in Figures 7.18 and 7.19.

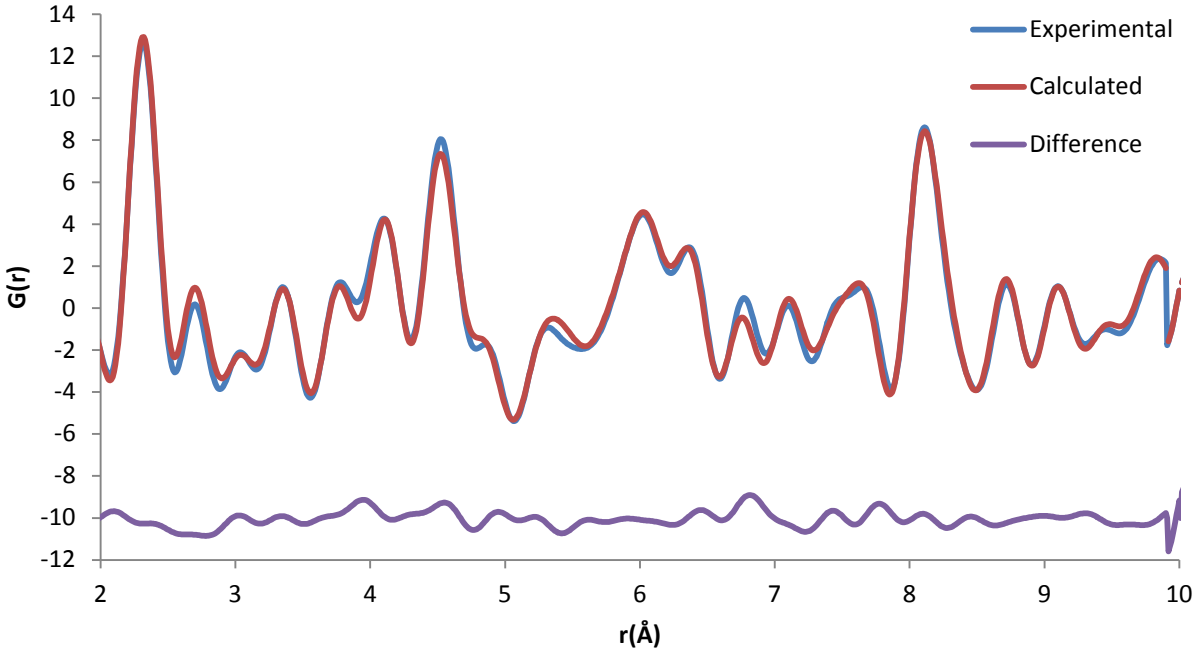

Figure 7.18: Dual phase fit to experimental data between 1.5 and 10 Å at 16.96GPa.

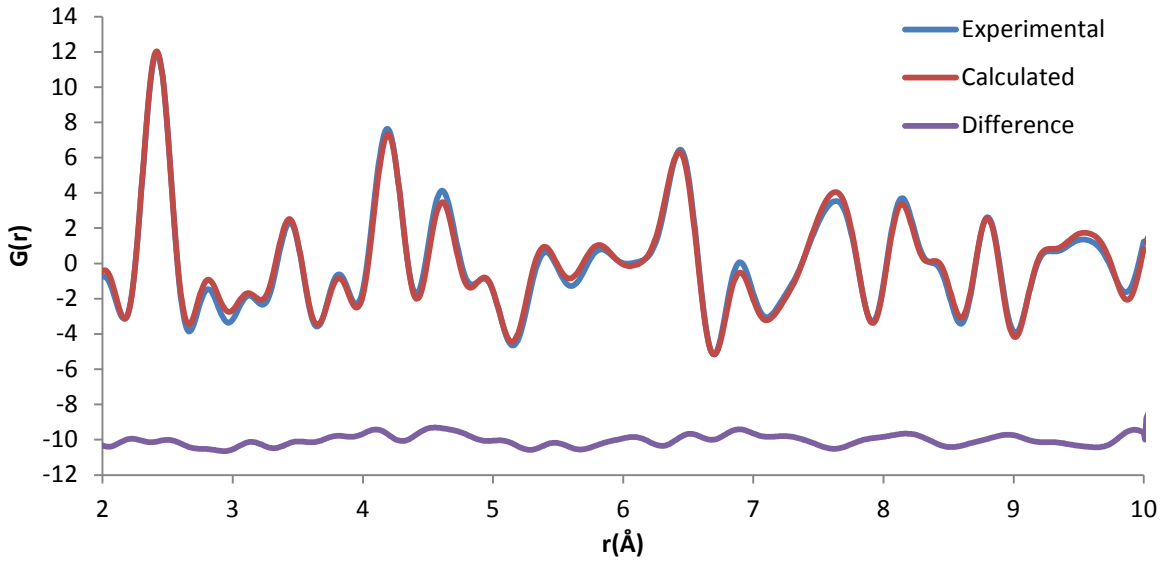

Figure 7.19: hcp model fit to experimental data between 1.5 and 10 Å at 21.45GPa.

(*Rw* = 0.117).

Both fits show good agreement with the experimental PDF but the improved fit when refining between 1.5 and 10Å for the hcp model at 21.45GPa is interesting as there are very few refined parameters (*Scale factor, Delta 2, a, c* and Fe U_{iso}). The difference between refining the data between 1.5 and 10 Å and 1.5 and 50 Å is that the Fe U_{iso} value is higher when all the data is included (Table 7.4).

Table 7.4: Refined values of Fe U_{iso} at different length scales.

Data Range for Refinement	Fe U_{iso}
1.5 to 10Å	0.0033Å^{-2}
1.5 to 50Å	0.0055Å^{-2}

To investigate this further the value for U_{iso} was fixed at 0.0033Å^{-2} for refinements of the 1.5 to 50Å data and it was found that above ~16Å the fit became much worse (Figures 7.20 and 7.21).

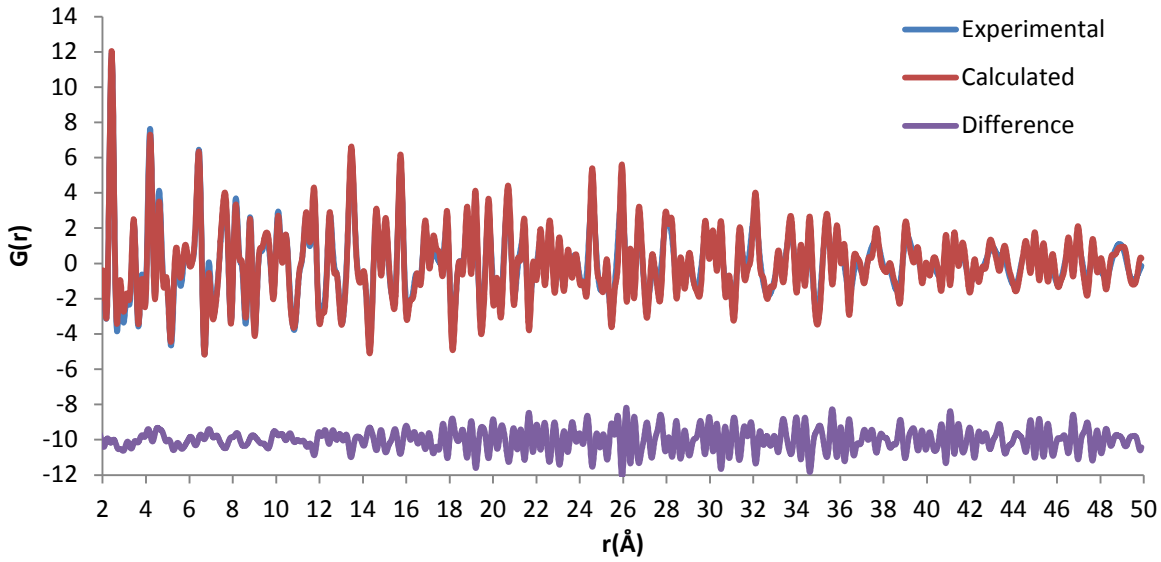

Figure 7.20a: hcp model fit to experimental data between 1.5 and 50 Å with the Fe U_{iso} value fixed from the refinements at 1.5 to 10 Å for data collected at 21.45GPa.

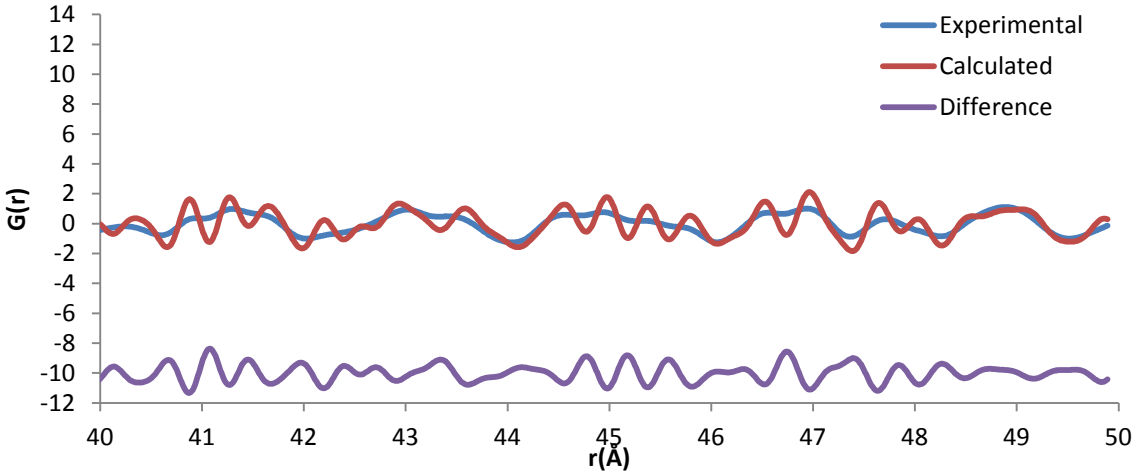

Figure 7.20b: Fit presented in Figure 7.19a shown between 40 and 50 Å.

It can be seen in Figure 7.20b that the peaks in the experimental PDF are much broader than the model (with fixed U_{iso} values) allows. These broader peaks at longer r values are leading to an increased value for U_{iso} for refinements on all the data. This shows that the actual Fe-Fe distances at longer r are more distributed than the model allows. This issue when fitting the

full range data was found in all data sets where hcp iron was present. This effect could be explained by the elastic deformation of each phase during the transition but at the highest pressure there is no longer any observable bcc phase that could deform the hcp structure.

There has been evidence provided by previous studies that stacking faults are likely to be present in hcp iron (Section 7.1). If the stacking faults were irregular enough then the pattern at short range would be dominated by hcp iron distances but the introduction of a stacking fault layer would result in interlayer distances becoming more distributed. This would thus broaden the peaks at longer range and PDFGui would attempt to model this using a pure hcp phase by increasing the Fe U_{iso} value.

PDF analysis can also give information on domain size. There is a more rapid drop-off in peak intensity as r increases at the higher pressures and as the instrument resolution is not changing this may indicate the domain size is decreasing as pressure increases (Figure 7.21).

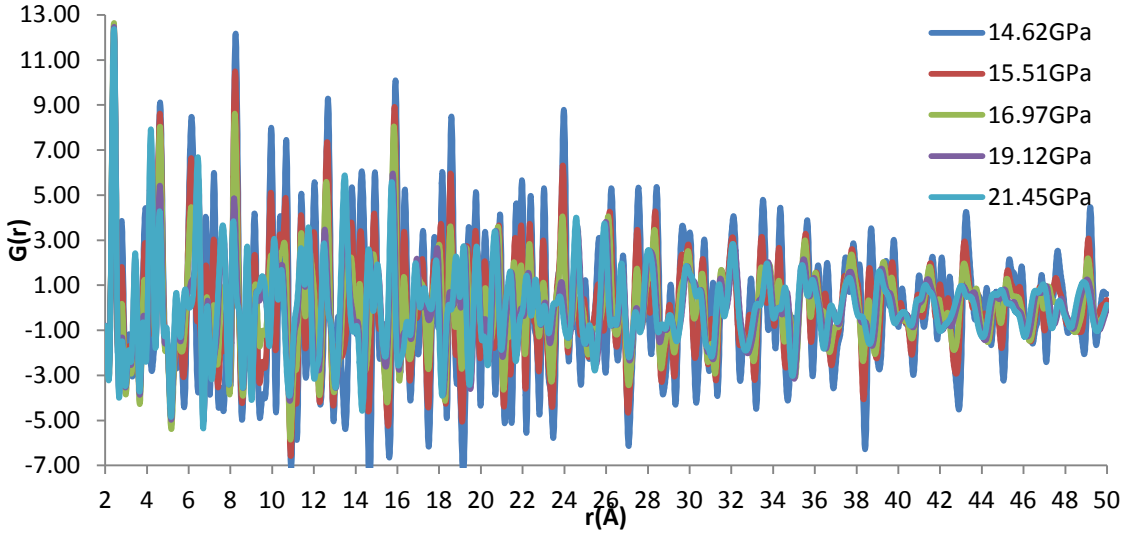

Figure 7.21: Experimental PDFs produced from diffraction data of iron collected between 14.62GPa and 21.45GPa.

If the particle size is refined for 21.45GPa then the value refines to 192Å but the fit is not noticeably improved. The diffraction pattern of hcp iron at 21.45GPa shows that the intensity of the Bragg peaks appear to diminish more quickly with increasing *Q* in comparison to bcc iron (Figure 7.22).

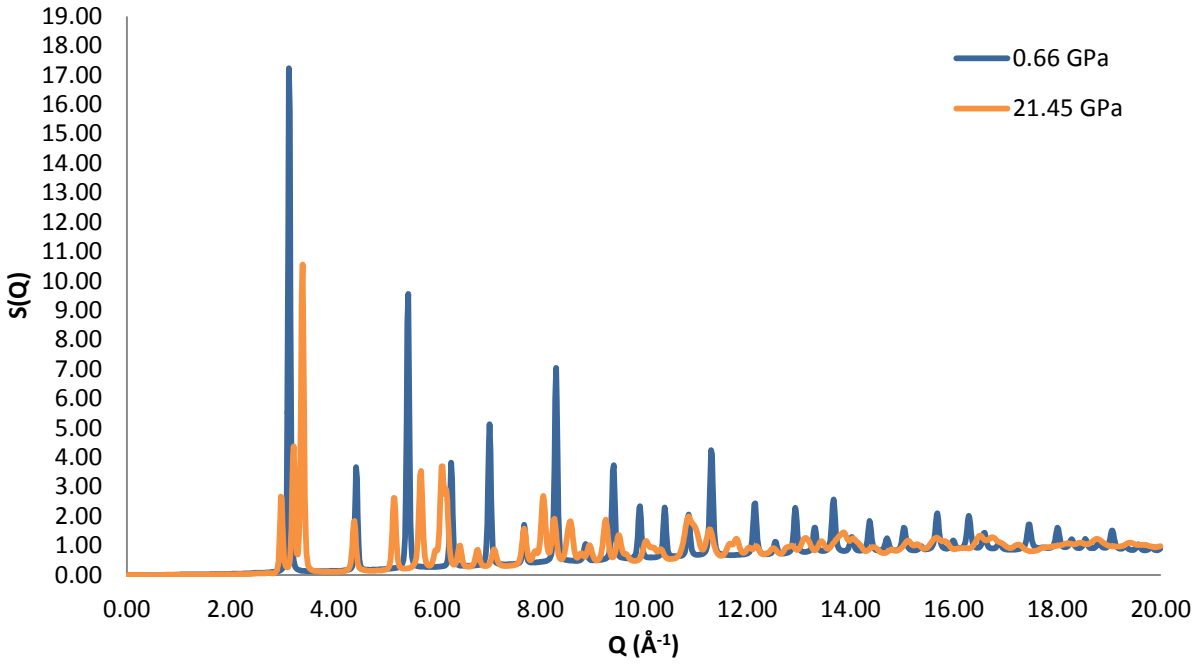

Figure 7.22: Normalised *S*(*Q*) for Fe at 0.66 and 21.45GPa.

This effect could simply be a result of increased strain in the sample which has been shown to increase the Debye-Waller factor and thus lead to the scattering intensity of the Bragg peaks dropping off more rapidly at higher *Q* values (Section 1.2).[23] It could also be a result of a reduction in domain size and the introduction of disorder into the system. It has been shown that there can be sizeable pressure variation across Fe compressed in a DAC[22] which may lead to a broadening of peaks as lattice parameters would be different at different pressures. This is not reflected in the refined Fe U_{iso} values obtained from Rietveld analysis which shows no broadening of the peaks in the Bragg diffraction pattern.

7.3.2 Analysis Of ε–iron Above 20GPa

In Section 7.4.3 only one PDF of ε–iron was collected so in order to investigate the structure of ε–iron further another data collection was undertaken to much higher pressures. Typically high pressure PDF studies use pressures below ~10GPa. While there have been PDFs reported above 60 GPa they are typically produced from low values of Q_{max} in the $S(Q)$ or the study does make reference to the normalisation process so the Q_{max} utilised is unknown. While the work of Chapman *et al* (2011) has allowed for the production of high quality PDFs at high pressure using a DAC it is unclear as to what at the highest pressures that have been accessed using PDF analysis. It has been found that drilled diamonds have a maximum operating pressure of around 10GPa and as a result they are not suitable for PDF studies above this pressure.

The experimental set up is outlined in Section 7.1.1 and it is assumed that the PDFs produced in this Section represent high quality PDFs produced at the highest pressures to date. A literature search was conducted in order to verify this assumption and no study was found with PDFs produced with comparable quality and pressure. It is very possible however that there could be a study(s) that were not found during the search of literature so caution should be given to stating the data presented here represents a new record in high pressure PDF analysis.

Initially Rietveld refinements were conducted on the diffraction pattern collected for each pressure and then the exact pressure was determined from the unit cell volumes (Section 7.2). Refined parameters produced from these refinements are presented in Table 7.5. Preferred orientation was modelled using the March-Dollase (MD) correction (Section 2.4).

Table 7.5: Rietveld analysis of diffraction data of hcp iron between 18.84 and 50.07GPa.

Pressure (GPa)	*wRp*	*MD Ratio*	ε-iron (hcp) *a* (Å)	*c* (Å)	*c/a*	Volume cm^3/mol	Fe U_{iso} ($Å^{-2}$)
18.84	0.0069	-	2.44907(9)	3.9320(3)	1.6055	6.1501	0.0006(6)
22.97	0.0078	1.044	2.4375(3)	3.9100(5)	1.6040	6.0580	0.0017(7)
26.29	0.0090	1.171	2.42980(8)	3.8904(3)	1.6011	5.9893	0.0031(8)
37.62	0.0094	1.233	2.4024(4)	3.8432(7)	1.5998	5.7843	0.0039(8)
43.54	0.0100	1.282	2.3907(6)	3.8187(6)	1.5973	5.6915	0.0042(5)
50.07	0.0163	1.315	2.3791(7)	3.793(1)	1.5951	5.5982	0.0035(4)

The two most noticeable trends from Table 7.5 are that the Rietveld fit becomes worse and the Fe U_{iso} value increases as pressure is increased. The Rietveld fit for the diffraction data collected at 50.07GPa is presented in Figure 7.23.

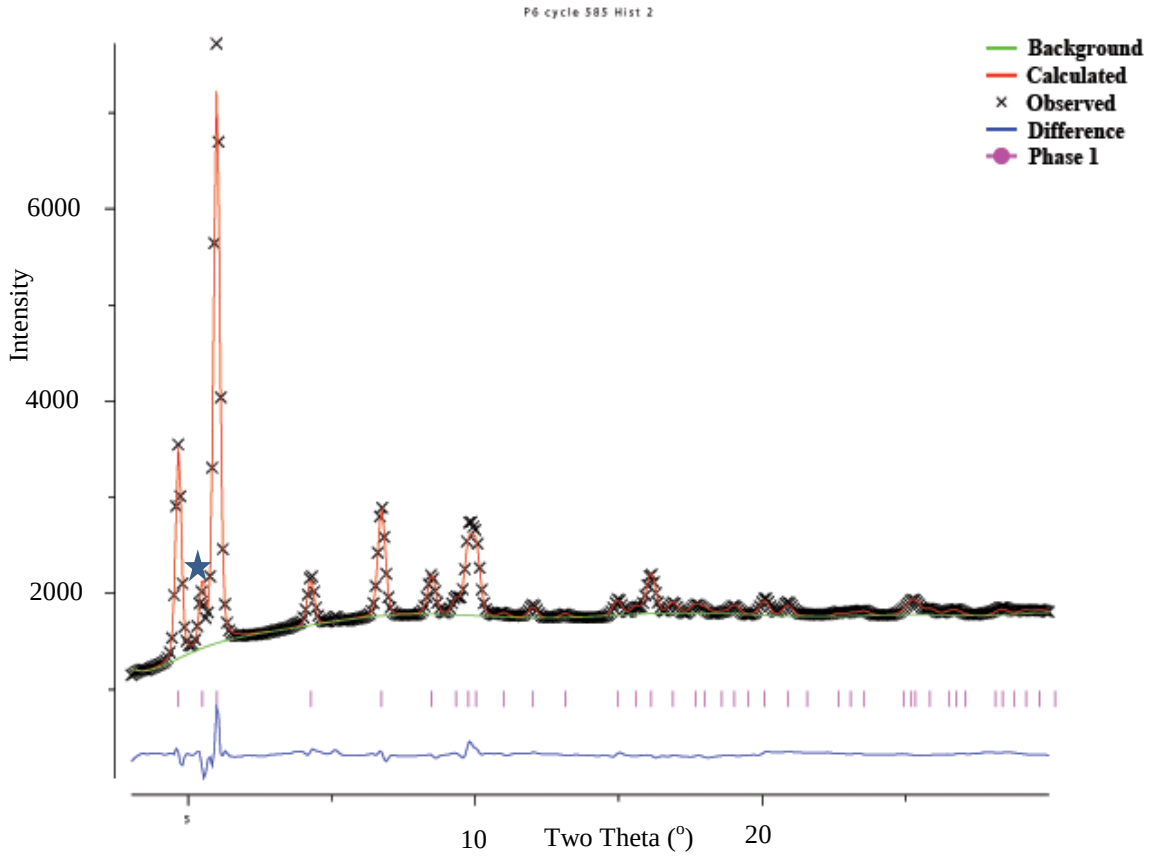

Figure 7.23: Rietveld fit to diffraction data collected at 50.07GPa using a hcp model of iron.

The noticeable difference between the diffraction pattern presented in Figure 7.23 and the normalised $S(Q)$ collected at 21.45GPa is that the relative intensity of the (002) reflection (marked with a star in Figure 7.22). The ratio of preferential orientation of the (001) plane in GSAS increases so this means that the amount of texture in the sample is increasing with pressure (Table 7.5), consistent with previous studies.[13] As a result the PDFs should reflect the increase in texture as pressure. PDFs were produced from the normalised $S(Q)$s using a Q_{max} of 22 Å^{-1} and these are presented in Figure 7.24.

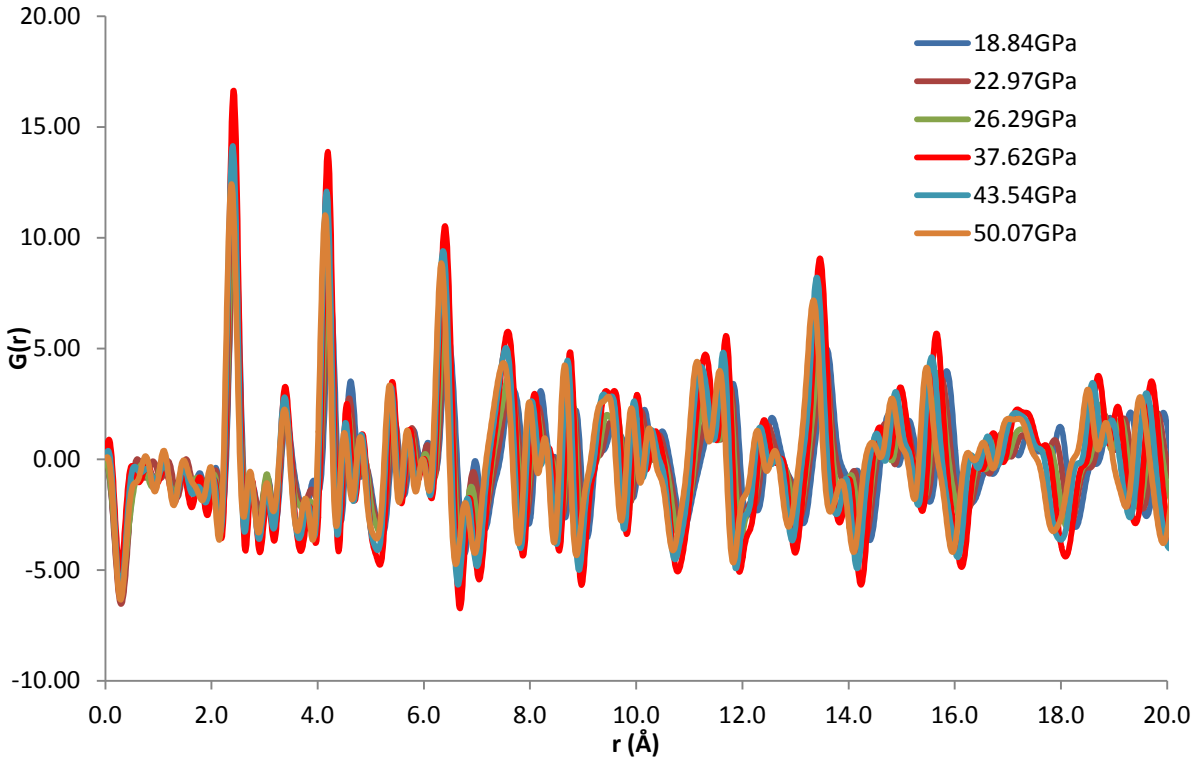

Figure 7.24: PDFs of iron up to 50.02GPa.

The PDFs show the overall reduction of atom-atom distances as pressure is increased, which makes investigating the differential PDFs difficult due to all the peak positions shifting. There are a number of peaks that appear to be affected by the increase in pressure outside of a simple reduction of atom-atom distances. Recall Figure 7.16 which outlined the Fe-Fe atom

distances each peak corresponds to in a pure hcp model of the high pressure phase, this gave an idea of the different Fe-Fe distances in the PDFs. There are clear differences in the PDFs in the first few peaks (Figure 7.25).

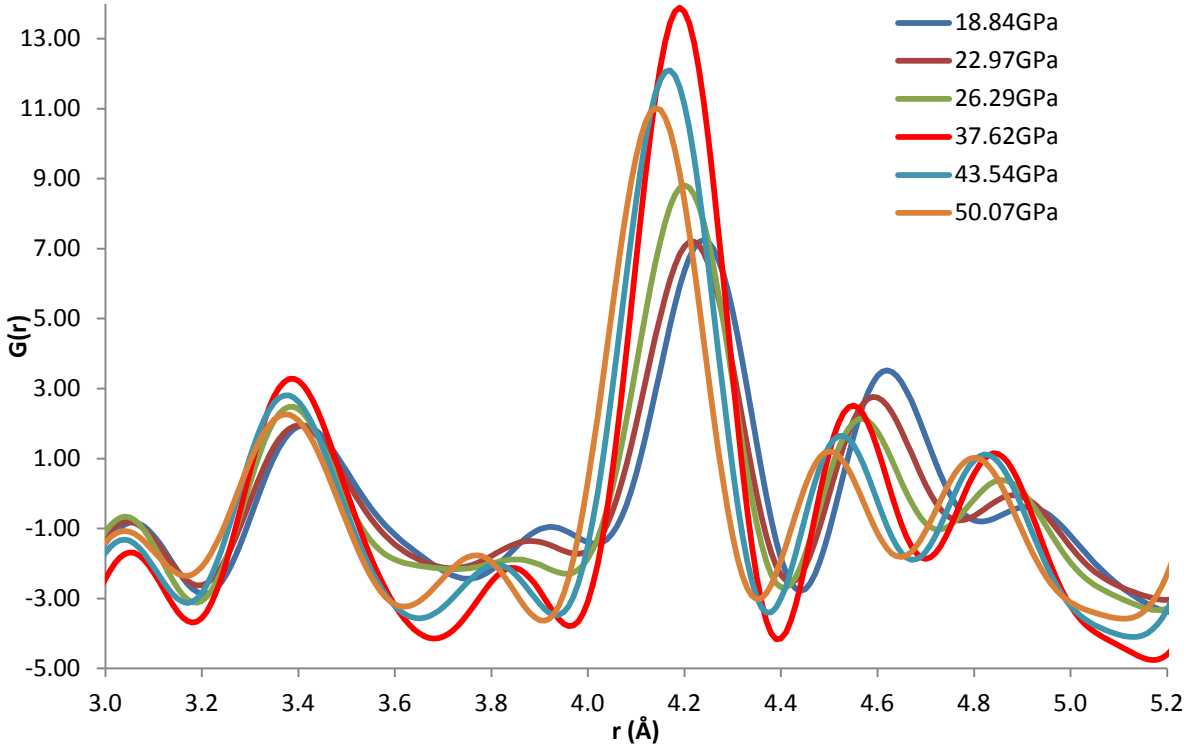

Figure 7.25: PDFs of iron between 18.84 and 50.70GPa shown between 3 and 5.2Å.

The peak at ~3.4 Å that should represent a layer A to layer B atom distance sharpens up as pressure is increased and this peak below 26.29GPa appears to consist of more than one distance between layers. In a pure hcp phase this would be expected to be a single Fe-Fe distance. The peak at ~4.2GPa which represents both A-A/B-B and A-B distances appears to potentially sharpen as pressure is increased up to 37.62GPa then either lose area or broaden as pressure increases up to 50GPa. The peaks at 4.6 (Interlayer distances) and 4.8Å (intralayer distances) also show changes as pressure is increased with the peak at 4.6Å decreasing in intensity relative to the peak at 4.8Å. With the intralayer distances being perpendicular to the

c-axis, this would cast doubt on the assertion that there should be a decrease in these distances relative to distances along the *c*-axis (the peak at 4.6Å).

An attempt was made to model the PDFs in PDFGui and the refinement results can be seen in Table 7.6.

Table 7.6: Refined parameters from PDFGui using a hcp model of iron.

	ε-iron (hcp)				
Pressure (GPa)	*Rw*	*a* (Å)	*c* (Å)	*c/a*	Fe U_{iso} (Å^{-2})
18.84	0.223	2.4504	3.9273	1.6027	0.0054
22.97	0.257	2.4393	3.9036	1.6003	0.0052
26.29	0.308	2.4307	3.8840	1.5979	0.0046
37.62	0.337	2.4245	3.8724	1.5972	0.0050
43.54	0.367	2.4120	3.8483	1.5955	0.0048
50.07	0.398	2.3999	3.8249	1.5938	0.0044

Refinements show that the fit is gradually getting worse as pressure is increased. Whereas the Rietveld refinements show that the Fe U_{iso} is increasing with pressure, refinements in PDFGui do not show this trend. The fit to the PDF produced from diffraction data at 50.07GPa is presented in Figure 7.26 and the peaks at longer ranges are too sharp to fit the experimental data which is the same issue found in the data presented in Figure 7.20b.

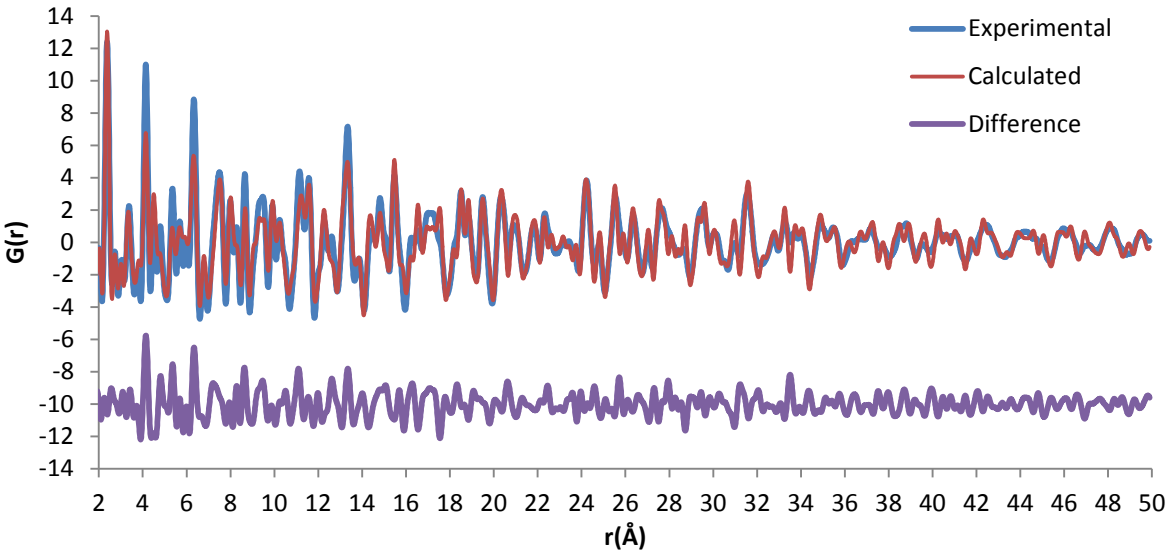

Figure 7.26: A hcp model of iron fit to PDF data produced from diffraction data collected at 50.07GPa.

The fit is poor at all length scales at this pressure and the shorter range data is fit particularly poorly. As shown in Section 7.3.1.2 if the data is refined at shorter length scales than 1.5 to 50Å the fit can be improved due to the ability of the Fe *U*iso values to be unaffected by the longer range data. A refinement was conducted between 1.5 and 10 Å on the 50.07GPa to see if the same was true at these pressures (Figure 7.27).

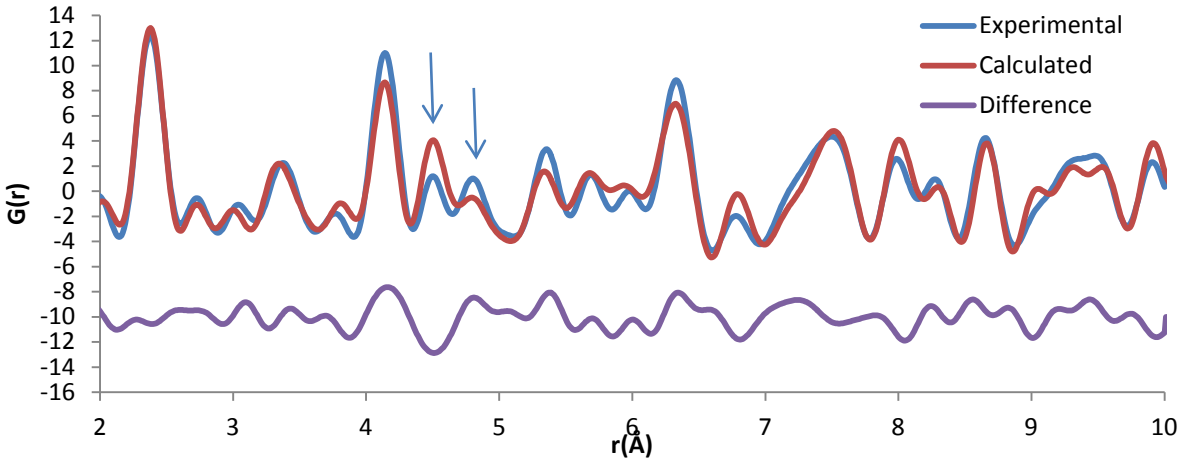

Figure 7.27: A hcp model of iron refined between 1.5 and 10Å on data collected at 50.02GPa.

Fitting of the short range data is no longer improved by excluding data above 10 Å and the Fe U_{iso} (0.0047Å^{-2}) actually increased slightly in comparison to the refinements between 0 and 50 Å. The peak at ~4.6 Å was fit very poorly with the model suggesting there should be more atom-atom distances at the length scale that the PDF suggested. In contrast the peak at ~4.71Å suggests there are more intralayer distances (Figure 7.15) than the model suggests.

A stacking fault could potentially increase the interlayer distance and result in a reduction in atom-atom distances at 4.6Å. Extensive modelling was conducted in PDFGui using a variety of different stacking fault models (growth and deformation) with different configurations of stacking faults at different length scales (i.e how many layers of perfect hcp layers before a staking fault). Hundreds of refinements were conducted using different models at different length scales yet none could provide a good description of the entire PDF pattern. Some were able to provide a better (but still poor) fit to data between 0 and 10Å but then would fall down when an attempt was made to refine the model at longer length scales. Attempts were also made to model a fcc phase but these also proved no help on fits, if there are small amounts of fcc present it is likely that PDFGui is unable to model these simply by adding in another phase into the refinement however, so this does not exclude the existence of some form of fcc phase at these pressures.

Despite the clear changes in PDF patterns as pressure was increased, it was decided that without either an accurate description of how preferred orientation impacted on PDF patterns or even better, a way of accounting for preferred orientation in PDFGui refinements it was unlikely that a reliable model could be deduced. The PDFs normalised well in PDFGetX2 and upon decompression back to 0GPa an excellent fit to bcc iron was once again obtained so there are few doubts about data quality.

7.4 Conclusions and Further Work

The PDF analysis presented in Section 7.3.1.2 shows a clear increase in the amount of ε-iron as pressure increases with an associated decrease in the amount of α–iron. There is no evidence for any stable intermediate phase using PDF analysis of the bcc-hcp phase transition but there is evidence for stacking faults being introduced based on the broad peaks at longer *r*-ranges but the short range data still being modelling well.

There is preferred orientation in the sample in the hcp phase which is likely affecting the modelling in PDFGui, but with most PDF studies actively avoiding preferred orientation effects it is not clear if there will be impetus for these issues to be resolved in the future. It is with regret that definitive answers have not been obtained in the study of the hcp phase however, if/when progress is made in modelling or explaining preferred orientation effects then the data presented in this chapter could and should be re-analysed. Currently there is uncertainty as to what changes in the PDF pattern are due to preferred orientation and which are structural changes as pressure increases. While the bcc and hcp systems appear relatively simple the phase transition is clearly quite complex which in itself would make analysing PDFs difficult by itself.

What has been demonstrated by this work is that it is possible to produce high quality PDFs, with good peak resolution ($Q_{max} = 22$ Å^{-1}) up to 50GPa and there is potential that other systems could be investigated to these high pressures, without falling foul of preferred orientation in the sample.

References

1. A. Morelli, A. M. Dzeiwonski and J. H. Woodhouse, *Geophysical Research Letters*, 1986, **13**, 1545-1548.
2. P. M. Shearer, *Journal of Geophysical Research*, 1994, **99**, 19647-19659.

3. D. Bancroft, E. L. Peterson and S. Minshall, *Journal of Applied Physics*, 1956, **27**, 291-298.
4. J. C. Jamieson and A. W. Lawson, *Journal of Applied Physics*, 1962, **33**, 776-780.
5. T. Takahashi and W. A. Basset, *Science*, 1964, **145**, 483-486.
6. R. L. Clendenen and H. G. Drickamer, *Journal of Physics and Chemistry of Solids*, 1964, **25**, 865-868.
7. H. Mao, W. A. Basset and T. Takahashi, *Journal of Applied Physics*, 1967, **38**, 272-276.
8. D. Pipkorn, C. Edge, P. Debrunner, G. De Pasquali, H. Drickamer and H. Frauenfelder, *Physical Review*, 1964, **135**, A1604.
9. F. P. Bundy, *Journal of Applied Physics*, 1965, **36**, 616-620.
10. W. A. Bassett and E. Huang, *Science*, 1987, **238**, 780-783.
11. F. M. Wang and R. Ingalls, *Physical Review B*, 1998, **57**, 5647-5654.
12. B. T. Wang, J. L. Shao, G. C. Zhang, W. D. Li and P. Zhang, *22*, 2010, 495702(495708).
13. S. Merkel, H. Wenk, P. Gillet, H. Mao and R. J. Hemley, *Physics of the Earth and Planetary Interiors*, 2004, **145**, 239-251.
14. L. Miyagi, M. Kunz, J. Knight, J. Nasiatka and M. Voltolini, *Journal of Applied Physics*, 2008, **104**, 103510.
15. H. Wenk, S. Matthles, R. J. Hemley, H. Mao and J. Shu, *Nature*, 2000, **405**, 1044-1047.
16. D. L. Williamson, S. Bukshpan and R. Ingalls, *Physical Review B*, 1972, **6**, 4194-4206.
17. R. D. Taylor, M. P. Pasternak and R. Jeanloz, *Journal of Applied Physics*, 1991, **69**, 6126-6128.
18. G. Shen, M. L. Rivers, S. R. Sutton, N. Sata, V. B. Prakapenka, J. Oxley and K. S. Suslick, *Physics of the Earth and Planetary Interiors*, 2003, **143-144**, 481-495.
19. B. Shyam, K. W. Chapman, M. Balasubramanian, R. J. Klingler, G. Srajer and P. J. Chupas, *Angewandte Communications*, 2012, **51**, 4852-4855.
20. K. Nemeth, K. W. Chapman, M. Balasubramanian, B. Shyam and P. J. Chupas, *Journal of Chemical Physics* 2012, **136**, 074105-074101.
21. B. Dupe, B. Amadon, Y. Pellegrini and C. Denoual, *Physical Review B*, 2013, **87**, 0241103(0241105).
22. Y. Ma, E. Selvi, V. I. Levitas and J. Hashemi, *Journal of Physics: Condensed Matter*, 2006, 1075-1082.
23. M. Ingaki, H. Furuhash, T. Ozeki and S. Naka, *Journal of Materials Science*, 1973, **8**, 312-316.

8. CONCLUSIONS AND FURTHER WORK

8.1 Summary

A study into a simple system led to a long and extensive study into a system that was anything but "simple". This system was $BaTiO_3$ and this project began with the aims of completing an analysis of this system before moving to other problems such as the PIA of zeolites. While it would take far too long to obtain an exact figure, thousands of refinements were conducted on $BaTiO_3$ at both high pressures and temperatures and many different approaches were taken to modelling this system using PDFGui. There was initially compelling evidence for the local structure of $BaTiO_3$ being orthorhombic at all temperatures and pressures from x-ray data, but over time refinement approaches were developed and improved that led to more robust, realistic analysis of the PDFs.

One of the lessons learnt during this project was that modelling has to make physical and chemical sense and that a good fit to experimental data does not necessarily mean that a model provides a good description of the actual structure. There are times when refined parameters can mask effects, such as the thermal parameters being unrealistically large. The questions always have to be *"are these values realistic?"* and *"does this model make sense?"*, if the answers are yes then there can be more confidence in the results produced.

The production of high pressure PDFs is often an intricate technique with patience required in loading DACs under microscopes and the requirement for consistent backgrounds and experimental set ups. The study of $BaTiO_3$ at high pressure demonstrated that sometimes, no matter how much you investigate a system using a particular technique, there may not be the conclusive answers at the end of it all. The questions raised from the high pressure study of BTO then led to the variable temperature investigation of the same system however, with neutron refinements clearly showing that the average structure can only describe the Ti

displacement in the lowest temperature orthorhombic phase. This study also showed the advantages of investigating PDFs at different length scales when considering local disorder, including showing how much information can be extracted from investigating only one peak and indeed how important the shortest atom-atom distances can be to describe local structure.

Changes in the first atom-atom peak were extremely clear in the doped $BaTiO_3$ samples but these systems showed where refinements in PDFGui can be of limited value. At the same time it shows how much information is available in a single PDF and how PDFGui should not be considered the only technique that should be used to analyse PDF patterns. These doped systems also highlighted how complex local disorder can be in comparison to a diffraction pattern that can be indexed using a cubic space group.

PDFGui has been shown to be limited when refining partially occupied sites, which can affect modelling of peaks at different length scales. Although these issues can be "got around", it would be useful for these to be resolved to prevent lengthy alternatives such as the building of altered super cells containing hundreds of atoms.

As long as peaks in the PDF pattern can be assigned to specific atom-atom distances, analysis can be undertaken even if the crystal structure is unknown. Analysis of these peaks as pressure and/or temperature varies can also yield information about how structure changes.

Finally attempts were made to push the limits of the experimental technique of collecting high pressure PDFs when looking at the phase transition of iron. If nothing else, this investigation shows the viability of collecting high quality PDF patterns at pressures in excess of 40GPa. Due to the topical nature of the system and the quality of PDFs produced a lot of time was spent trying to model disorder in hcp iron. Ultimately this has not yet been fully successful, but is has made it fairly clear that there is a lot of information about the hcp phase present in the PDFs produced.

This work hopefully presents a variety of different data analysis approaches that can be useful when analysing PDFs in different situations. A single PDF can spawn several different analyses that can complement each other to give a clearer understanding of the experimental data.

The I-15 beamline has proven itself capable of routinely producing high quality PDFs and the dedicated beamline at the APS has been running successfully for a number of years and it is safe to say that collection of high quality PDFs at high pressure is now routine, mainly thanks to the development work completed before this project began. Over the coming years, collection of high quality PDFs for UK based users will be made even easier due to the xPDF beam line which is being built as a side station to the I-15 beam line at Diamond Light Source.

8.2 Future Work

With data collection become easier and quicker, the attention should turn to resolving some of the issues with the data reduction and analysis of PDFs. New software is being developed all the time, with PDFGetX3 and GSASII being made available to download within the past few months. With the very quick data collections times associated with the production of high quality PDFs, the slowest part of investigating systems using PDF methods is the data analysis stage. The collection of data was never an issue with this project, the issue was always producing a robust data analysis for each system. There were a few systems that data analysis only progressed to early stages and some systems where the analysis was never attempted, such is the sheer volume of data that can be collected in a single trip to a synchrotron source.

It is very likely that the process of getting from diffraction pattern to PDF will be streamlined significantly in the coming years, indeed the normalisation process in PDFGetX3 has been

automated. This will speed up and simplify data reduction further with it being possible to produce PDFs from high pressure data as the data is being collected for each pressure. This still requires the laborious process of producing masks for each pressure which is a process that, while it is explained in the literature, is still a relatively difficult process to learn without guidance from someone with experience.

Recently Diamond Light Source ran a Total Scattering Training School aimed at helping people learn how to reduce data collected from image detectors. It is hoped that these schools will help new users get to grips with the current software associated with PDF analysis and aid the community in utilising PDF analysis in their work.

There is also work being done to remove “the elephant in the room” which is the lack of ESDs on the various data points. Within the coming years there will hopefully be a replacement for the very functional, but outdated, Fit2D program with early work being undertaken at Diamond to this effect. One of the aims of this project is to produce valid ESDs on integrated area detector images.

It would also be useful to tackle the issue of preferred orientation, how it affects PDF analysis and ways this could be accounted for when modelling various systems. Following on from producing PDFs up to 50GPa it would be interesting to investigate a system that would not show preferred orientation at these pressures, although it is not certain if this system exists.

Due to time restraints it was not possible to investigate the viability of using RMCprofile to investigate some of the systems presented in this work. The program has already proved itself very useful when looking at related systems, such as the PIA of $ZrWO_2O_8$ At the time of writing RMCprofile analysis was on going (through collaboration) on the variable temperature BTO and doped BTO data. It is hoped that this approach will shed further light

on all the analysis presented in Chapters 3 to 7 it will be interesting to see if sensible models are produced using the “big box” approach.